

Flow of Anisotropic Colloids in Microfluidic Channels and Jets

Dissertation

zur Erlangung des akademischen Grades eines

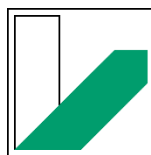
Doktors der Naturwissenschaften

(Dr. rer. nat.)

an der

Bayreuther Graduiertenschule für Mathematik

und Naturwissenschaften (BayNAT) der Universität Bayreuth



**UNIVERSITÄT
BAYREUTH**

vorgelegt von

M.Sc. Mathias Schlenk

geboren in Bayreuth

Bayreuth 2018

Die vorliegende Arbeit wurde in der Zeit von August 2013 bis Februar 2018 in Bayreuth am Lehrstuhl Physikalische Chemie I unter Betreuung von Herrn Professor Dr. Stephan Förster angefertigt.

Vollständiger Abdruck der von der Bayreuther Graduiertenschule für Mathematik und Naturwissenschaften (BayNAT) der Universität Bayreuth genehmigten Dissertation zur Erlangung des akademischen Grades eines Doktors der Naturwissenschaften (Dr. rer. nat.).

Dissertation eingereicht am: 03.05.2018

Zulassung durch das Leitungsgremium: 16.05.2018

Wissenschaftliches Kolloquium: 05.10.2018

Amtierender Direktor: Prof. Dr. Dirk Schüler

Prüfungsausschuss:

Prof. Dr. Stephan Förster (Gutachter)

Prof. Dr. Georg Papastavrou (Gutachter)

Prof. Dr. Seema Agarwal (Vorsitz)

Prof. Dr. Mirijam Zobel

„In den Verallgemeinerungen steckt der Teufel.“

Georges Bernanos

„Tout vient à point à qui sait attendre.“

Margarete von Navarra

***Meiner Familie und meiner Loulou
gewidmet in Dankbarkeit und Liebe***

*„Wer glaubt, etwas zu sein,
hat aufgehört, etwas zu werden.“*

Sokrates

*“Wer kämpft, kann verlieren,
wer nicht kämpft, hat schon verloren.“*

Bertolt Brecht

Contents

Zusammenfassung	1
Summary	3
List of Publications	5
1 Introduction.....	7
1.1 Motivation	7
1.2 Microfluidics	9
1.3 References	13
2 Fundamentals	17
2.1 Microfluidic Devices	17
2.1.1 Design, Fabrication, and Application	17
2.1.2 Fluid Dynamics in Microchannels and Jets	21
2.2 Self-Assembly of Amphiphiles	33
2.3 Microscopic and Scattering Methods	37
2.3.1 3D Confocal Laser Scanning Microscopy	37
2.3.2 Small Angle X-Ray Scattering	40
2.4 References	53
3 Thesis Overview	61
3.1 Synopsis.....	61
3.2 Individual Contributions to Joint Publications	73
4 Publications	75
4.1 Parallel and Perpendicular Alignment of Anisotropic Particles in Free Liquid Microjets and Emerging Microdroplets	75
4.2 Splitting and Separation of Colloidal Streams in Sinusoidal Microchannels	109
4.3 Strategies for the Selective Loading of Patchy Worm-Like Micelles with Functional Nanoparticles	137
Acknowledgements/Danksagung	169
Declaration/Erklärung.....	173

Abbreviations and Symbols

Abbreviations

2D	two dimensional
3D	three dimensional
μPIV	micro particle image velocimetry
μSAXS	submicron small angle X-ray scattering
ABS	acrylnitril-butadien-styrol-copolymer
AOTF	acousto-optic tunable filter
ASICs	application-specific integrated circuits
BCC	body-centered cubic
CAD	computer aided design
CCD	charge-coupled device
CFD	computational fluid dynamics
CLSM	confocal laser scanning microscopy
CMC	critical micelle concentration
CMOS	complementary metal-oxide-semiconductor
cryo-TEM	cryo-transmission electron microscopy
FCC	face-centered cubic
FDM	fused deposition modeling
FEM	finite element method
FITC	fluorescein isothiocyanate
FM	focusing medium
FWHM	full width half maximum
HEX	hexagonal packed
HPC	hybrid photon-counting
LAM	patterns and lamellar
LNPs	lipid nanoparticles
LSPR	localized surface plasmon resonance
MC	main channel
MF	microfluidics
MSR	microstructured reactor
NOA	Norland optical adhesive

NPs	nanoparticles
PDDF	pair-distance distribution function
PDEs	partial differential equations
PDI	polydispersity index
PDMS	polydimethylsiloxane
PE	polyethylene
PEB	post exposure bake
PEG	polyethylene glycerol
PEO	polyethylene oxide
PI	polyisoprene
PI-<i>b</i>-PEO	polyisoprene- <i>block</i> -polyethylene oxide
PLA	polylactide
PMTs	photomultiplier tubes
PNIPAM	poly- <i>N</i> -isopropylacrylamide)
PS	poly styrene
PTFE	polytetrafluoroethylene
PUMA	polyurethane methacrylate
Rhod B	rhodamine B
SANS	small angle neutron scattering
SAXS	small angle X-ray scattering
SC	side channel
SEM	scanning electron microscopy
SEMs	polystyrene- <i>b</i> -polyethylene- <i>b</i> -poly(methyl methacrylate) triblock terpolymers
SFA	surface force apparatus
SiH	hydrosilane groups
SLA	stereolithography
SLS	selective laser sintering
TEM	transmission electron microscopy
THV	tetra hexafluoro vinylidene
TPE	thermoset polyester
USAXS	ultra small-angle X-ray scattering
UV	ultraviolet
WAXS	wide-angle X-ray scattering
wCCMs	wormlike crystalline-core micelles
XRD	X-ray diffraction

Symbols

A	amplitude, cross-sectional area
a	acceleration, hydrophilic-hydrophobic interfacial area
c	concentration
d	thickness, characteristic length, layer distance
d_i	initial diameter
D	diffusion coefficient, diameter
De	Deborah Number
D_m	mass diffusivity
Dn	Dean Number
ζ	order parameter
E	energy
El	elasticity Number
F	force
γ	surface tension
$\dot{\gamma}$	shear rate
h	hours, shortest distance, Planck constant
H	mean curvature
I	modified Bessel function
I_0	incident intensity
I_1	detector read-out intensity
I_s	scattering intensity
J	diffusive flux
k	consistency, perturbation wavelength, wave vector
K	Gaussian curvature
l	jet diameter, hydrophobic block length
L	length
λ	wavelength, slip or Navier length
λ_{opt}	optimal wavelength
m	mass
μ_A	viscosity of the liquid jet
μ_B	viscosity of the external fluid
η	dynamic viscosity
η_0	viscosity at zero shearing

η_{∞}	high-shear viscosity
n	flow index, power law exponent, refraction index, integer multilayer
NA	numeric aperture
θ	contact angle, scattering angle
P	packing parameter
ρ	density
q	scattering vector, momentum transfer
Q	volume flow, flow rate
QE	quantum efficiency
Δp	pressure drop
Pe	Péclet Number
r_i	initial radius
R	fluidic resistance of the microchannel, radius
R_c	radius of curvature of the channel path
Re	Reynolds Number
S	orientation parameter
S_0	energetic ground state
S_1	excited electronic state
Sc	Schmidt Number
σ	surface tension, Thomson factor
t	time
T	temperature
τ	shear stress
τ_c	internal relaxation time
τ_{Flow}	flow time scales
τ_P	polymeric relaxation time
ϕ	azimuth angle
V	volume
ν	velocity, kinematic viscosity, volume of hydrophobic block, frequency
ν_x	flow velocity tangential
w	channel width
ω	perturbation growth rate
We	Weber Number
Wi	Weissenberg Number
∇	Nabla operator

Zusammenfassung

Anisotrope Kolloide sind von enormer Bedeutung sowohl in der Grundlagenforschung, als auch in der Industrie für viele Anwendungen. Diese kolloidalen Partikel beeinflussen entscheidend die Eigenschaften und das Verhalten verschiedener flüssiger und fester Materialien und Substanzen. Die Mikrofluidik ist eine moderne Technologie, die es ermöglicht viele unterschiedliche Experimente u.a. an solchen anisotropen Kolloiden unter sehr kontrollierten und definierten Bedingungen durchzuführen. Die mikrofluidischen Bauelemente, die in der vorliegenden Arbeit verwendet werden, verdeutlichen die ganze Spannweite dieser Methode: Von der Bestimmung der Partikelorientierung diverser anisotroper Kolloide im extrem schnellem Fluss, über ein komplexes Mikrochipdesign zur Partikeltrennung, bis hin zu einem chemikalienbeständigen Mikrochip aus Polytetrafluorethylen (PTFE) zur Untersuchung der *in situ* Beladung von wurmartigen Kolloiden mit Nanopartikeln.

All diese Beispiele zeigen das Leistungsvermögen und die Vielseitigkeit einer solchen mikrofluidischen Versuchsumgebung. Für ein detailliertes Verständnis der jeweiligen Versuche sind aber auch entsprechend spezifische und leistungsfähige Messtechniken nötig.

In **Kapitel 4.1** wurde die Orientierung anisotroper Kolloide in schnellen Flüssigkeitsstrahlen und -tröpfchen untersucht. Hierfür wurden Synchrotron-Röntgen-Streuexperimenten durchgeführt, da diese eine Fokussierung des Röntgenstrahls im μm -Bereich erlauben. Diese Mikrostrahl-Kleinwinkel-Röntgenstreuung (μSAXS) ermöglicht die mikrometeregenaue Untersuchung aller Abschnitte entlang eines Mikroflüssigkeitstrahls, beginnend innerhalb der Glas-Mikrodüse, über den Freistrahle und schließlich bis in die Mikrotröpfchen. In allen Teilbereichen zeigen die Experimente unerwartete Änderungen in der Strömungsorientierung anisotroper Partikel, welche allgemein für zylindrische und scheibenförmige Partikel über einen weiten Bereich von Achsenverhältnissen gezeigt werden konnte. Durch zusätzliche fluiddynamische Simulationen konnte die beobachtete Partikelflussrichtung auf die sich ändernden Flussgeschwindigkeitsfelder innerhalb der Mikrostrahlen und -tröpfchen zurückgeführt werden. Diese Erkenntnisse verbessern das Verständnis der Teilchenorientierung in freien Strahlen sowie Tröpfchen und bieten sogar die Grundlage für eine Kontrolle der Teilchenausrichtung in Herstellungs- und Beschichtungsprozessen, sowie diverser Drucktechniken, die auf Flüssigkeitsstrahlen beruhen.

Über die präzise Bestimmung der Partikelorientierung hinaus können Mikrochips auch zur Partikelauftrennung eingesetzt werden. In diesem Zusammenhang wurde in **Kapitel 4.2** dieser Arbeit ein neuer Strömungspaltungseffekt entdeckt, der durch Fluoreszenz-, Polarisations- und konfokaler Laser Raster Mikroskopie (CLSM) mit einem ultraschnellen Resonanzscanner für

3D-Bildgebung dynamischer Strömungssysteme detailliert analysiert wurde. Damit konnte eine ungewöhnliche Strömungspaltung von anisotropen wurmartigen, aber auch von kugelförmigen Kolloiden in vier Teilströme innerhalb sinusförmiger Mikrokanäle beobachtet werden. Die Spaltung trat dabei erst auf, sobald die Ströme mit viskoelastischer nicht-Newtonscher Polymerlösung fokussiert wurden. Dieser Effekt konnte schließlich dazu genutzt werden, um anisotrope wurmartige Mizellen von isotropen Kolloiden, als auch sphärische Partikel unterschiedlicher Größe voneinander zu trennen. Durch Variation der experimentellen Bedingungen: 2D- oder 3D- Fokussierung, gerade oder sinusförmige Kanäle, Sinusperiode und Amplitude, Molekulargewicht, sowie nicht-Newtonsche oder Newtonsche Flüssigkeiten, konnten die essentiellen Voraussetzungen für die Strömungsspaltung bestimmt werden. Diese Aufspaltung ergab sich schließlich aus der Kombination von Zonen mit hoher Dehnungs- und Scherrate bei Anwesenheit eines elastischen transienten Polymernetzwerkes, was auch mit anderen Experimenten auf diesem Forschungsgebiet übereinstimmt.

In **Kapitel 4.3** wird das Potential von Mikrofluidiksystemen bezüglich der Kontrolle chemischer Reaktionen aufgezeigt. Der Vorteil mikrofluidischer Kanäle liegt in der kontinuierlichen Durchführung der Synthese unter laminaren Strömungsbedingungen, welche zu wohldefinierten und reproduzierbaren Misch-, Transport- und Reaktionsprozesse führen. Eine Herausforderung bei dieser Synthese ist die chemische Beständigkeit des Chipmaterials. In dieser Arbeit wurde daher ein Mikrofluidikchip entwickelt, der aus einem PTFE-basierten Doppelfokuskreuz und einer Mikroglaskapillare als Auslasskanal besteht. Auf diese Weise konnte eine kontinuierliche *in situ* Beladung von segmentierten Wurmmizellen mit Metallnanopartikeln durchgeführt werden. Die Verwendung von mikrofluidischen Kanälen erlaubt die Untersuchung sehr kleiner Flüssigkeitsmengen und ermöglicht eine schnelle Variation der Reaktionsparameter zur Optimierung des selektiven Beladungsprozesses. Daher konnten die Beladungskapazität und die Nanopartikelgröße in Abhängigkeit der Flussraten individuell eingestellt und gesteuert werden, was eine hohe Variabilität und bedeutende Verbesserungen zur Realisierung eines maßgeschneiderten Ladeprozesses im Vergleich zu anderen selektiven Beladungsmethoden mit sich bringt.

Zusammenfassend zeigt diese Arbeit das große Leistungsvermögen und die Vielseitigkeit von mikrofluidischen Systemen mit Blick auf ein breites Materialspektrum (Polymere, anorganische Materialien, Komposite) und zusätzlich einen Vergleich zweier unterschiedlicher Strömungsbedingungen zwischen einem freien Flüssigkeitsstrahl und einer geschlossenen Mikrokanalumgebung. Die einzelnen Untersuchungen anisotroper Kolloidpartikel liefern in Kombination mit modernen, leistungsfähigen Analysegeräten neue Einblicke in die Orientierungs-, Beladungs-, Herstellungs- und Trennprozesse unterschiedlichster Forschungsgebiete.

Summary

Anisotropic colloids are of extraordinary interest in a wide variety of fundamental research fields, but also basis for many sophisticated applications in industry. These specific particles influence significantly the properties and behavior of various liquid and solid materials and substances. The modern technology microfluidics makes it possible to perform highly diverse experiments e.g. on anisotropic colloids in a very controlled and defined manner. Thus, the microfluidic devices employed in this thesis vary from a setup for the distributional orientation analysis of different anisotropic colloids in ultrafast flow, over a complex microchip design for the separation of anisotropic and isotropic particles, to a highly chemical resistant polytetrafluoroethylene (PTFE) microchip for the investigation of the *in situ* loading of wormlike colloids with nanoparticles.

Such diverse experiments show the potential of a microfluidic environment, but also demand specific and powerful measurement techniques. Consequently, all experiments have been carried out in combination with tailor-made analytical methods.

The detailed orientation analysis within fast liquid microjets and droplets, studied in **chapter 4.1**, was performed by using the high quality of brilliant X-ray scattering instruments at synchrotron sources. These instruments have the possibility to focus intense X-ray beams down to a few microns in diameter. Hence, microbeam small angle X-ray scattering (μ SAXS) enables a micrometer precise investigation along a microjet. Those parts span the micro sized nozzle made of a glass capillary, the freejet area and finally the microdroplet region. In all parts, the study reveals unexpected changes in the flow-alignment of anisotropic particles which was generally shown for cylindrical and discoidal particles over a wide range of axial ratios. By additional fluid dynamic simulations, the observed particle flow-alignment could be related to the changing flow velocity fields within the micro-jets and -droplets. These findings enhance our understanding of particle orientation in free jets as well as droplets and even provide the basis for a control of particle alignment in liquid jet-based fabrication, coating and printing techniques.

Beyond the precise determination of particle orientation via microfluidics, microchips can also be applied for particle separation. In this context, a new stream splitting effect was discovered and analyzed via fluorescence-, polarization- and confocal laser scanning microscopy (CLSM) that exhibits modern ultrafast resonance scanners for the detailed 3D imaging of dynamic flow systems, as shown in **chapter 4.2**. This unique stream splitting of anisotropic wormlike but also of spherical colloids into four substreams was recovered within sinusoidal microchannels. The splitting just occurred when the streams were focused with a viscoelastic non-Newtonian

polymer solution. This effect could finally be used to separate anisotropic wormlike micelles from isotropic colloids but also spherical particles of different sizes. By variation of the experimental conditions: 2D- vs. 3D-focusing, straight vs. sinusoidal channels, sine period and amplitude, molecular weight and Newtonian vs. non-Newtonian fluids, it was possible to reveal the essential preconditions for the stream splitting effect. This splitting is caused by a combination of high extensional and shear rate zones with the presence of an elastic transient polymer network, which is consistent with other experiments in this field of research.

The potential of microfluidic devices to run highly controlled chemical reactions is the focus of **chapter 4.3**. Microfluidic channels offer the advantage to perform continuous syntheses under laminar flow conditions which give rise to well-defined and reproducible mixing, transport, and reaction processes. A challenge, however, is the chemical resistance of the microchip material. In this work, a microdevice was developed by combining a PTFE-based double-focused cross and a micro glass capillary as outlet channel. In this way, it was possible to perform continuous *in situ* loading of patchy wormlike micelles with metal nanoparticles. The use of microfluidic channels therefore allows the investigation of very low amounts of liquids and enables a rapid screening of reaction parameters to optimise the selective loading process. Hence, the loading capacity and the nanoparticles' size could be individually adjusted and easily controlled by varying the flow rates. Said control in turn provides significant flexibility and improvement in realizing a tailor-made loading process compared to other selective loading strategies.

In summary, this thesis demonstrates the great potential and versatility of microfluidic platforms with respect to a broad material spectrum (polymers, inorganic materials, composites) on the one hand and gives a comparison of two different flow conditions between a free liquid microjet and a closed microchannel environment on the other hand. The individual studies of anisotropic colloidal particles in combination with powerful analytical instrumentation reveals novel insights into the orientation, loading, synthesis and separation processes in highly diverse research fields.

List of Publications

This thesis is based on publication [1], [2] and [3], that are adapted as **chapters 4.1, 4.2 and 4.3.**

- [1] **M. Schlenk**, E. Hofmann, S. Seibt, S. Rosenfeldt, L. Schrack, M. Drechsler, A. Rothkirch, W. Ohm, J. Breu, S. Gekle, S. Förster
„Parallel and Perpendicular Alignment of Anisotropic Particles in Free Liquid Microjets and Emerging Microdroplets”
Langmuir, **2018**, 34 (16), 4843-4851
- [2] **M. Schlenk**, M. Drechsler, M. Karg, W. Zimmermann, M. Trebbin, S. Förster
„Splitting and Separation of Colloidal Streams in Sinusoidal Microchannels”
Lab on a Chip, **2018**, 18 (20), 3163-3171
- [3] J. Schöbel, C. Hils, A. Weckwerth, **M. Schlenk**, C. Bojer, M.C.A. Stuart, J. Breu, S. Förster, A. Greiner, M. Karg, H. Schmalz
„Strategies for the Selective Loading of Patchy Worm-Like Micelles with Functional Nanoparticles”
Nanoscale, **2018**, 10 (38), 18257-18268

Further publications that were prepared in collaboration with fellow scientists and coworkers:

- [4] S. Rosenfeldt, M. Stöter, **M. Schlenk**, T. Martin, R.Q. Albuquerque, S. Förster, J. Breu
„In-Depth Insights into the Key Steps of Delamination of Charged 2D Nanomaterials”
Langmuir, **2016**, 32 (41), 10582-10588
- [5] J. Decock, **M. Schlenk**, J.-B. Salmon
„In-Situ Photo-Patterning of Pressure-Resistant Hydrogel Membranes with Controlled Permeabilities in PEGDA Microfluidic Channels”
Lab on a Chip, **2018**, 18 (7), 1075-1083
- [6] A.C.G. Weiss, K. Krüger, Q. Besford, **M. Schlenk**, K. Kempe, S. Förster, F. Caruso
„In Situ Characterization of Protein Corona Formation on Silica Microparticles Using Confocal Laser Scanning Microscopy Combined with Microfluidics”
ACS Applied Materials & Interfaces, in revision

1 Introduction

1.1 Motivation

Material science is a remarkable field of research which has fascinated mankind since the dawn of time. However, as portrayed in “Faust”, the magnum opus of the world-famous naturalist and writer Johann Wolfgang von Goethe, the human desire for the universal understanding of what our entire world consists of remains unfulfilled. I too, as a child, remember being impressed and inspired by nature I wanted to know how materials are fundamentally structured and built-up. Today, as a scientist and after years of learning in a bid to understand, I am able to apply myself at least a little to explore new materials and to do my part to improve and understand our surrounding world.

Based on nature’s fundamental growth and hierarchical structuring principles, as nucleation, growth, and self-assembly, advanced material sciences as well as condensed matter physics are governed by nanometer to micrometer length scale to finally create complex high-performance materials made of several molecules.^{1,2} The study of the underlying building principles and the resulting highly-ordered composite structures demands for an interdisciplinary technology that is capable of controlling the experimental chemical and physical conditions while at the same time enabling modern *in situ* analysis techniques.³⁻⁵

Microfluidics is a revolutionary methodology that brought up precise control of substances within laminar flow conditions on microliter scale and nowadays even down to nanoliter scale.⁶⁻⁸ Thus, microfluidics provides different parameters for adjusting ideal conditions to create tailor-made super-structured assemblies, respectively colloids and moreover to obtain perfect oriented anisotropic particles within for example multi-compound systems.⁹⁻¹¹

The advantage of modern microscopy, e.g. confocal laser scanning microscopy (CLSM) enable ultrafast, precise and detailed micrometer scanning via sophisticated resonant scanners possible.^{12,13} The state-of-the-art achievements in synchrotron technology, like the free electron lasers are capable of time-resolved *in situ* experiments using a highly brilliant source for submicron small angle X-ray scattering (μ SAXS).¹⁴⁻¹⁶

In this thesis, combinations of different home-built microfluidic setups and current analysis technics are used for several investigations of flowing wormlike micelles and further anisotropic colloids (**Figure 1**) within microchannels and -jets. Anisotropic colloids like the wormlike micelles assemble from polymeric block copolymers and are of highest interest as carrier

structures for drug delivery or as integral part of high-performance composite materials in which the orientation plays a key role.¹⁷⁻¹⁹ We developed various microfluidic methodologies. The first one was devised to analyze the reorientation of different anisotropic particles within liquid microjets and microdroplets. The second setup was evolved to investigate a colloid separation process within sinus-shaped microchannels and the third one to simultaneously synthesize and load nanoparticles continuously on wormlike micelles by running a specific, highly-controllable *in situ* microfluidic process within a double focus chip made of polytetrafluoroethylene (PTFE).

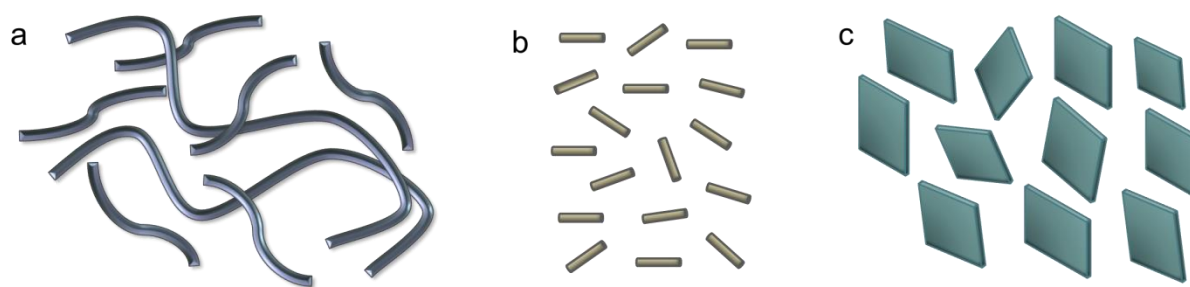


Figure 1 | Sketch of anisotropic colloid systems. (a) Wormlike micelles synthesized out of a flexible block copolymer. (b) Nanorods that could be made of various stiff metals like gold. (c) Nanoplatelets like inorganic layered silicates.

The following **chapter 1.2** will give an overview about the microfluidic essentials and preliminary work as well as the combinable analysis technologies which have already been done in these fields of research.

1.2 Microfluidics

Employing a microfluidic setup, it is possible to carry out experiments in very different conditions. You can run chemical reactions for synthesis, assembly or loading processes within a closed microfluidic channel at moderate flow rates.¹⁰ Moreover, there are jet devices available using ultra-high flow velocities which often result in an open free jet environment after passing a nozzle outlet. These aforementioned examples (see **Figure 2**) are two of several possibilities that aim to show the versatility of microfluidics. Both conditions, the closed channel system as well as the open liquid jet system, are used in this work.

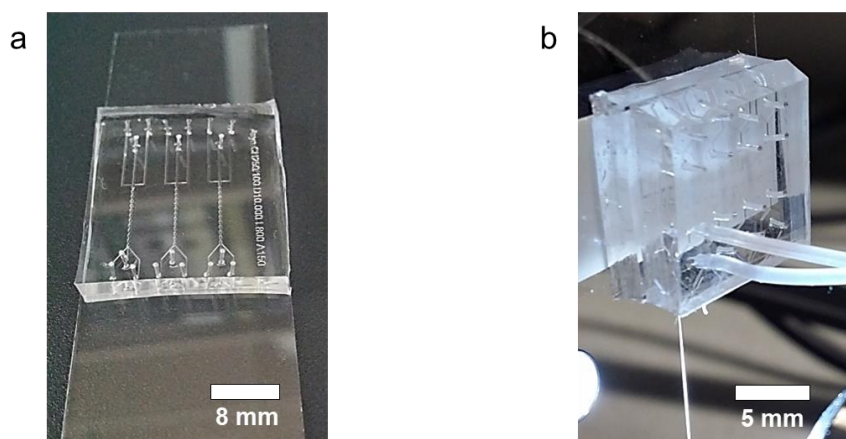


Figure 2 | Images of two basic microfluidic methodologies. (a) Closed microchannel chip design. (b) Nozzle-chip for free liquid microjet systems.

Microfluidics is based on the treatment and control of very small volumes of liquids or gases via specific devices.²⁰ As these volumes are on a microliter scale or less, the physical laws concerning the flow behavior are completely different from those on macro scale. Consequently, the flow in a microfluidic setup is laminar and not turbulent which basically leads to very well controllable conditions regarding the treatment of chemicals. But what are the specific parameters influencing laminar flow in microfluidic devices? One of the basic parameters is the channel dimension that finally restricts scaling down to micrometer and leads to micro scale properties. Aside from the channel dimension, the flow rate and the viscosity of the liquid, or the gas, respectively, play a key role. Generally, the flow is laminar for lower flow rates as well as for higher viscosities and the mixing of compounds can be achieved by simple diffusion. A measure for the amount of turbulence is given by the dimensionless Reynolds-Number (Re) which is fully explained in chapter 2.2.2. Based on simple parameters, microfluidics can provide well-defined model environments which makes it adaptable to many fields of science such as chemistry, biology, pharmacy, medicine and any other analytical or technological field.

The ability to carry out quantitative and qualitative analysis with high resolution and sensitivity while using very small amounts of substances led to the rise of microfluidics during the last decade of the 20th century.^{21,22} After the growing interest on low cost and fast analytical processes as well as the emergence of lithographical and rapid prototyping processes during that time, microfluidics became quite attractive for industry and science.^{23,24} One of the first and certainly the most famous pioneer on scientific microfluidics is George M. Whitesides who introduced poly(dimethylsiloxane) (PDMS) as a polymeric fabrication material on which a huge majority of the following research was carried out.^{25,26} The next decades, much scientific work was done on microfluidic setups especially for drug delivery and drug targeting systems. Here, the synthesis, assembly and loading processes as well as effective separation methods are the main focus of this research field.

Many studies on synthesis in microfluidic devices have been carried out using biomaterials, nanoparticles or enzymes.²⁷⁻²⁹ Currently, especially nanoparticles are of highest interest because they can be synthesized via microfluidics with a huge variety of functionalized groups in order to create for example lipid nanoparticles (LNPs) that have a higher circulation time in the blood stream, low cytotoxicity, good biocompatibility and transfection efficiency.^{30,31} However, nanoparticles can also be used to load different types of super-structured and self-assembled systems by employing a microfluidic chip in order to increase their pharmaceutical efficiency as drug-targeting systems.^{32,33} Such self-emulsifying delivery systems, liposomes, polymeric nanoparticles, microemulsions and micellar solutions can be compounded within complex and individually designed microfluidic chip labs. Those labs on a chip are predestinated for mixing different substances and particle systems under highly controlled laminar flow conditions.^{9,34} In this context, hydrodynamic flow focusing is indispensable to achieve a good quality for the reaction process of these colloidal systems. Such processes encompass nucleation, growth by aggregation, stabilization, or self-assembly.³⁵ Consequently, colloids of various shape and elasticity, e.g. microdroplets and vesicles, core-shell structures, or Janus particles are available at high monodispersity.

Another important topic is flow- as well as shear-induced orientation and the associated separation. Thus, a given polydisperse colloidal system can be sorted by size for instance.^{11,36} This separation in turn increases the quality of drug delivery and the manufacturing process of high-performance materials like composite materials in which the different particle systems need to have maximized alignment within a matrix. In most cases, batch synthesized particles have rather high polydispersities which calls for effective post-processing. This processing may include particle separation with respect to their size, shape or elasticity. The goal is to finally

receive one homogeneous species for effective drug targeting and mechanical material enhancement.³⁷⁻³⁹ Microfluidic colloid separation is diverse and ranges from active sorting processes via chemical, electrical or magnetic impact to gentle passive systems using various physical forces without the need of modifications of the particle itself.⁴⁰⁻⁴² For that, many different microchannel geometries have already been tested with several colloids to figure out the best method for their separation.⁴³⁻⁴⁵ Nevertheless, there is still room for improvement to achieve maximum efficacy for all kinds of particles. A basic prerequisite to particle separation is to understand why colloids are going to flow on certain trajectories.⁴⁶ Here, very often the size-, shape- and elasticity-induced orientation behavior of each particle plays an important role.⁴⁷ Knowledge about colloidal distribution and orientation helps to improve particle separation as well as sorting and also offers a powerful tool to adjust particle order in process engineering for many soft matter and material applications.

To attain all these specific requirements, this work presents two major microfluidic setups that are mainly used to perform tailor-made experiments. The first and common system is a closed microchannel chip device which gives maximum control of liquid or gaseous flows. Today, there is a huge variety of channel designs including 2D- but also highly complex 3D-channel structures which leads to a great flexibility for all kinds of experiments. However, channel walls are found to be critical as they may cause agglomeration of particles which ultimately leads to clogging of the device. Moreover, chemicals leeching from the chip material might interfere with highly sensitive analytical methods. For example, commonly used PDMS is not X-ray transparent thus making an experimental investigation via SAXS impossible. A solution to these problems is a modern free liquid jet system – the second setup. Free jets lack channel walls over a wide range except for the inlet part consisting of a nozzle.^{48,49} Consequently, virtually every analytical method can be used without any disturbance.⁵⁰ However, the flow conditions are slightly different when comparing closed streams and free jets: a higher flow rate is necessary to achieve a free jet and the missing walls change the originally no-slip conditions to free-slip conditions which again enable new possibilities.

As mentioned above, a fully established methodology requires powerful analytical methods. Ideally, an elaborated microfluidic platform should be used on which you can integrate different techniques of analysis such as optical, scattering or spectroscopic methods potentially used simultaneously and *in situ*.⁵¹ State-of-the-art devices are designed to be mobile microfluidic platforms that can be integrated temporarily in intense synchrotron sources like DESY, ESRF, MAX or Diamond to achieve effective time management, as illustrated in following **Figure 3**.

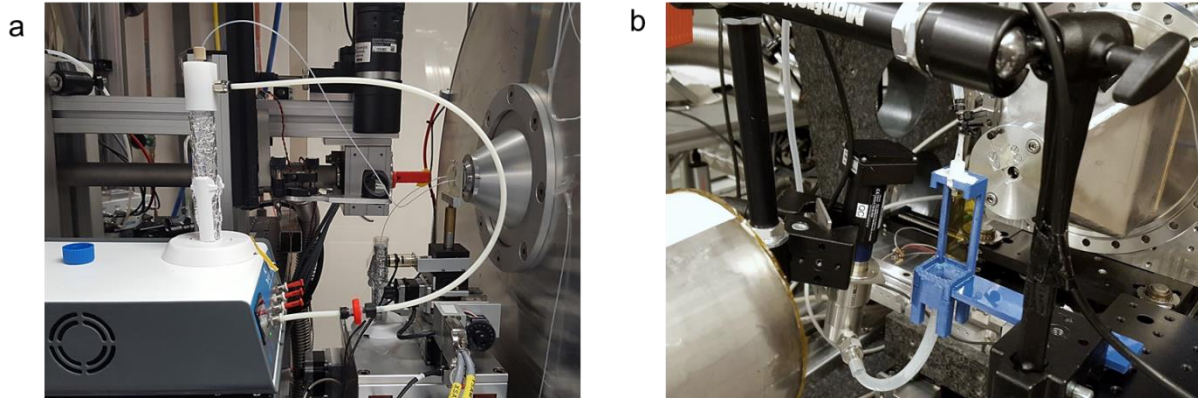


Figure 3 | Portable complex microfluidic platforms for simultaneous *in situ* analysis techniques at intern and extern research institutions like synchrotrons. (a) Pressure-based pump setup for a closed microchannel chip system. (b) Micro gear pump recycling built-up for free liquid microjets.

1.3 References

1. Fratzl, P. & Weinkamer, R. Nature's hierarchical materials. *Progress in Materials Science* **52**, 1263-1334, (2007).
2. Antonietti, M. & Förster, S. Vesicles and Liposomes: A Self-Assembly Principle Beyond Lipids. *Advanced Materials* **15**, 1323-1333, (2003).
3. Lopez, C. G., Saldanha, O., Huber, K. & Köster, S. Lateral association and elongation of vimentin intermediate filament proteins: A time-resolved light-scattering study. *Proceedings of the National Academy of Sciences* **113**, 11152-11157, (2016).
4. Saldanha, O., Brennich, M. E., Burghammer, M., Herrmann, H. & Köster, S. The filament forming reactions of vimentin tetramers studied in a serial-inlet microflow device by small angle x-ray scattering. *Biomicrofluidics* **10**, 024108, (2016).
5. Trebbin, M. *Microfluidics at high-intensity X-ray sources: from microflow chips to microfluidic liquid jet systems*, University of Bayreuth, (2013).
6. Brennich, M. E. & Köster, S. Tracking reactions in microflow. *Microfluidics and Nanofluidics* **16**, 39-45, (2014).
7. Schoch, R. B., Han, J. & Renaud, P. Transport phenomena in nanofluidics. *Reviews of Modern Physics* **80**, 839-883, (2008).
8. Squires, T. M. & Quake, S. R. Microfluidics: Fluid physics at the nanoliter scale. *Reviews of Modern Physics* **77**, 977-1026, (2005).
9. Thiele, J., Steinhäuser, D., Pfohl, T. & Förster, S. Preparation of Monodisperse Block Copolymer Vesicles via Flow Focusing in Microfluidics. *Langmuir* **26**, 6860-6863, (2010).
10. Whitesides, G. M. The origins and the future of microfluidics. *Nature* **442**, 368-373, (2006).
11. Trebbin, M. *et al.* Anisotropic particles align perpendicular to the flow direction in narrow microchannels. *Proceedings of the National Academy of Sciences* **110**, 6706-6711, (2013).
12. Xi, P., Liu, Y. & Ren, Q. *Scanning and image reconstruction techniques in confocal laser scanning microscopy*. (Intech, Peking University and Shanghai Jiao Tong University China, 2011).
13. Kimura, T., Shintate, M. & Miyamoto, N. In situ observation of the evaporation-induced self-assembling process of PS-b-PEO diblock copolymers for the fabrication of titania films by confocal laser scanning microscopy. *Chemical Communications* **51**, 1230-1233, (2015).
14. Chapman, H. N. *et al.* Femtosecond X-ray protein nanocrystallography. *Nature* **470**, 73-77, (2011).
15. Als-Nielsen, J. & McMorrow, D. *Elements of Modern X-ray Physics*. (Wiley, Chichester, 2011).
16. Daubersies, L., Leng, J. & Salmon, J.-B. Steady and out-of-equilibrium phase diagram of a complex fluid at the nanolitre scale: combining microevaporation, confocal Raman imaging and small angle X-ray scattering. *Lab on a Chip* **13**, 910-919, (2013).

17. Younghoon, K., Paul, D., David, A. C. & Dennis, E. D. Polymeric worm micelles as nano-carriers for drug delivery. *Nanotechnology* **16**, S484, (2005).
18. Suarez, S. A., Gibson, R. F., Sun, C. T. & Chaturvedi, S. K. The influence of fiber length and fiber orientation on damping and stiffness of polymer composite materials. *Experimental Mechanics* **26**, 175-184, (1986).
19. Förster, S., Konrad, M. & Lindner, P. Shear Thinning and Orientational Ordering of Wormlike Micelles. *Physical Review Letters* **94**, 017803, (2005).
20. Franke, T. & Wixforth, A. Das Labor auf dem Chip: Mikrofluidik. *Physik in unserer Zeit* **38**, 88-94, (2007).
21. Gravesen, P., Branebjerg, J. & Jensen, O. S. Microfluidics-a review. *Journal of Micromechanics and Microengineering* **3**, 168, (1993).
22. Brody, J. Y., P.; Goldstein, R.; Austin, R. Biotechnology at Low Reynolds Numbers. *Biophysical Journal* **71**, 3430-3441, (1996).
23. Ramsey, J. M., Jacobson, S. C. & Knapp, M. R. Microfabricated chemical measurement systems. *Nature Medicine* **1**, 1093, (1995).
24. McDonald, J. C. *et al.* Fabrication of microfluidic systems in poly(dimethylsiloxane). *Electrophoresis* **21**, 27-40, (2000).
25. Whitesides, G. M. & Xia, Y. Soft lithography. *Annu. Rev. Mater. Sci.* **28**, 153-184, (1998).
26. Whitesides, G. M. & Xia, Y. Soft Lithography. *Angewandte Chemie International Edition* **37**, 550-575, (1998).
27. Hung, L.-H. & Lee, A. *Microfluidic devices for the synthesis of nanoparticles and biomaterials.* (2006).
28. Luckarift, H. R., Ku, B. S., Dordick, J. S. & Spain, J. C. Silica-immobilized enzymes for multi-step synthesis in microfluidic devices. *Biotechnology and Bioengineering* **98**, 701-705, (2007).
29. Jahn, A. *et al.* Preparation of nanoparticles by continuous-flow microfluidics. *Journal of Nanoparticle Research* **10**, 925-934, (2008).
30. Maeki, M. *et al.* A strategy for synthesis of lipid nanoparticles using microfluidic devices with a mixer structure. *RSC Advances* **5**, 46181-46185, (2015).
31. Kim, Y. *et al.* Single Step Reconstitution of Multifunctional High-Density Lipoprotein-Derived Nanomaterials Using Microfluidics. *ACS Nano* **7**, 9975-9983, (2013).
32. Valencia, P. M. *et al.* Microfluidic Platform for Combinatorial Synthesis and Optimization of Targeted Nanoparticles for Cancer Therapy. *ACS Nano* **7**, 10671-10680, (2013).
33. Hood, R. R., Vreeland, W. N. & DeVoe, D. L. Microfluidic remote loading for rapid single-step liposomal drug preparation. *Lab on a Chip* **14**, 3359-3367, (2014).
34. Karnik, R. *et al.* Microfluidic Platform for Controlled Synthesis of Polymeric Nanoparticles. *Nano Letters* **8**, 2906-2912, (2008).
35. Zhang, Y., Chan, H. F. & Leong, K. W. Advanced materials and processing for drug delivery: The past and the future. *Advanced Drug Delivery Reviews* **65**, 104-120, (2013).
36. Mukherjee, S. & Sarkar, K. Lateral migration of a viscoelastic drop in a Newtonian fluid in a shear flow near a wall. *Physics of Fluids* **26**, 103102, (2014).

37. Nam, J., Lim, H., Kim, D., Jung, H. & Shin, S. Continuous separation of microparticles in a microfluidic channel via the elasto-inertial effect of non-Newtonian fluid. *Lab on a Chip* **12**, 1347-1354, (2012).
38. Kagalwala, T. E. *Continuous Size-Based Separation of Microparticles in Straight Channels*, University of Cincinnati, (2011).
39. Yang, S. *et al.* Deformability-selective particle entrainment and separation in a rectangular microchannel using medium viscoelasticity. *Soft Matter* **8**, 5011-5019, (2012).
40. Fukui, Y., Iiguni, Y., Kitagawa, S. & Ohtani, H. Continuous-flow Size-based Separation of Microparticles by Microchip Electromagnetophoresis. *Analytical Sciences* **31**, 197-203, (2015).
41. Ahn, S. W., Lee, S. S., Lee, S. J. & Kim, J. M. Microfluidic particle separator utilizing sheathless elasto-inertial focusing. *Chemical Engineering Science* **126**, 237-243, (2015).
42. D'Avino, G., Hulsen, M. A. & Maffettone, P. L. Separation of particles in non-Newtonian fluids flowing in T-shaped microchannels. *Advanced Modeling and Simulation in Engineering Sciences* **2**, 9, (2015).
43. Gossett, D. R. *et al.* Label-free cell separation and sorting in microfluidic systems. *Anal. Bioanal. Chem.* **397**, 3249-3267, (2010).
44. Bhagat, A. A. S., Kuntaegowdanahalli, S. S. & Papautsky, I. Continuous particle separation in spiral microchannels using dean flows and differential migration. *Lab on a Chip* **8**, 1906-1914, (2008).
45. Gossett, D. R. & Carlo, D. D. Particle Focusing Mechanisms in Curving Confined Flows. *Analytical Chemistry* **81**, 8459-8465, (2009).
46. Di Carlo, D. Inertial microfluidics. *Lab on a Chip* **9**, 3038-3046, (2009).
47. Hur, S. C., Henderson-MacLennan, N. K., McCabe, E. R. B. & Di Carlo, D. Deformability-based cell classification and enrichment using inertial microfluidics. *Lab on a Chip* **11**, 912-920, (2011).
48. Trebbin, M. *et al.* Microfluidic liquid jet system with compatibility for atmospheric and high-vacuum conditions. *Lab on a Chip* **14**, 1733-1745, (2014).
49. Acero, A. J., Ferrera, C., Montanero, J. M. & Gañán-Calvo, A. M. Focusing liquid microjets with nozzles. *Journal of Micromechanics and Microengineering* **22**, 065011, (2012).
50. Nelson, G. *et al.* Three-dimensional-printed gas dynamic virtual nozzles for x-ray laser sample delivery. *Optics Express* **24**, 11515-11530, (2016).
51. Chen, X. *et al.* Simultaneous SAXS/WAXS/UV-Vis Study of the Nucleation and Growth of Nanoparticles: A Test of Classical Nucleation Theory. *Langmuir* **31**, 11678-11691, (2015).

2 Fundamentals

2.1 Microfluidic Devices

2.1.1 Design, Fabrication, and Application

The fabrication of microfluidic devices starts ordinarily with the design of the microchip and its microchannel structures. Nowadays, computer-aided design (CAD) software allows to draw and finally manufacture precise channel structures with errors less than a few nanometers. In this thesis, all fabricated microchannel structures have been designed via AutoCAD software (Autodesk Inc.). Also, 3D printed sample holders made of polylactide (PLA) or acrylnitril-butadien-styrol-copolymer (ABS) have been drawn using the 3D functions of AutoCAD. The devices were home-fabricated by the additive manufacturing technology of an Ultimaker 2 (Ultimaker B.V.) that is working via fused deposition modeling (FDM), visible in **Figure 4**.

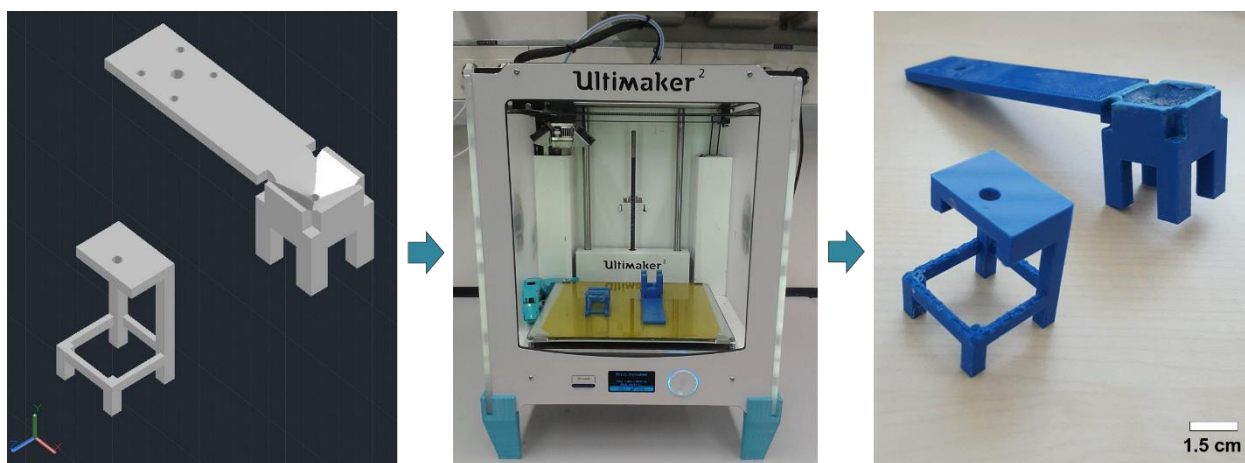


Figure 4 | 3D AutoCAD design for a 3D printed sample holder that consists of two separate pieces and is made of PLA by the FDM method of an Ultimaker 2. The sample holder is created to employ liquid microjets within a micro gear pump recycling setup which is mobile and able to be installed at synchrotron measurement stations.

Beyond the FDM method, other 3D printing technologies, like stereolithography (SLA) or selective laser sintering (SLS), have already been developed during the 1980s for various materials like plastics, resins, ceramics or metals.^{1,2} Today, all these 3D printing technologies are based on CAD-data and represent versatile systems for rapid prototyping processes. During the last decade, 3D fabrication advanced extremely fast and to astonishing precision down to the micrometer scale. Nowadays, a complete microfluidic chip can be produced in one step.^{3,4} Still, depending on the 3D printing process and the required mechanical and chemical properties of the

chip material, the resolution can only be a few hundred micrometers for the channel size. As processes like photo- and soft lithography can achieve even nano-sized master devices as casting forms, they are still often preferred.⁵⁻⁷

In this thesis, the microfluidic master devices are fabricated within a cleanroom via a contact mask aligner MJB4 (SÜSS MicroTec SE, see **Figure 5**). The aligner is working with UV light ($\lambda = 365 \text{ nm}$) and high-resolution film photomasks, respectively chromium-glass masks to achieve a resolution of $1 \mu\text{m}$ produced by JD Photo Data. After getting the photomasks, the actual photolithography starts by spin-coating a silicon wafer with a photoresist. For the applications in this thesis, a 3 inch silicon wafer (Silicon Materials Inc.) was sufficient and spin-coated (Cee 200X, Brewer Science Inc.) with a thin layer of the commercially available negative photoresist SU-8 from MicroChem Corporation.⁸ The layer thickness of this epoxy-based resist is adjustable to $0.5\text{-}150 \mu\text{m}$ by varying the viscosity depending on the amount of solvent γ -butyrolactone for a certain spin-speed in a range of $1000\text{-}4000 \text{ rpm}$. The structures on the photomask were transferred to this layer of SU-8 by exposing through the transparent parts of the mask and hereby cross-linking the photoresist in the exposed areas. Upon exposure, cross-linking proceeds in a first step, the formation of a strong acid during the exposure, and is followed by a second step, the acid-catalyzed and thermally driven epoxy cross-linking during post exposure bake (PEB).⁹ The finally obtained master contains the inverted positive structure of the desired microchannel network and can be reused and replicated over many cycles, allowing rapid prototyping at low cost. By employing only one layer of photoresist the common and so-called 2D microchannel chip designs are available. However, if a more complex channel network with 3D fluid focusing was required, the previous steps of spin-coating and exposure were repeated to build up additional layers whereby a precise alignment of different photomasks to the substrate was necessary, as illustrated in **Figure 5**. In the following development step, the uncured photoresist was removed with 1-methoxy-2-propanyl acetate (mr-Dev 600, micro resist technology GmbH).

After the photolithographical process within a cleanroom, also the soft lithography is carried out in a dust-free environment,¹⁰ within a laminar flow box (ScanLaf, Mars Safety Class 2) from LaboGeneTM. Here, the master is casted with polydimethylsiloxane (PDMS) to form the actual microchip with its channel structures by replica molding. For the replication of the microstructured master, a 10:1 mixture (monomer : curing agent) of PDMS (Sylgard 184 kit, Dow Corning Corp.) was poured onto the master and degassed as well as baked for 1.5 h at $75 \text{ }^\circ\text{C}$. During heating, the terminal vinyl groups ($\text{SiCH}=\text{CH}_2$) of the dimethyl-siloxane oligomer basic

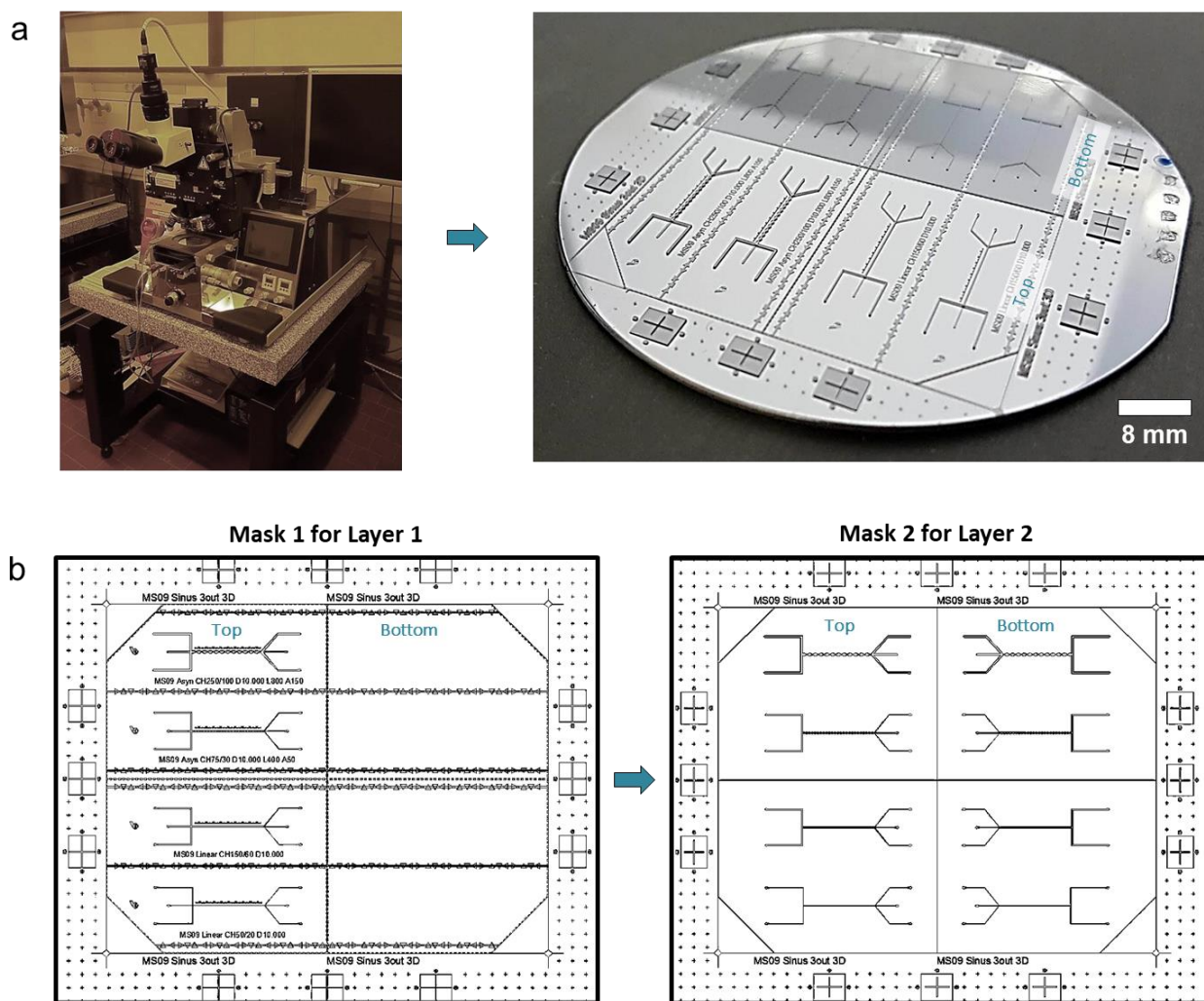


Figure 5 | Equipment for photolithography. (a) Mask aligner MJB4 (SÜSS MicroTec SE) within the cleanroom of the physical chemistry chair of the University of Bayreuth in order to fabricate Si-master devices as casting forms. (b) Layout of the high-resolution photomasks for multilayer master devices.

component and the hydrosilane groups (SiH) of the hydrogen-methylsiloxane cross-linker component, which also contains a platinum-catalyst, are reacting via hydrosilylation to create the cross-linked polymer network PDMS. After demolding, the PDMS replica was cut with a razor blade along predefined grooves into individual parts. Inlet ports for the later polyethylene (PE) tube connection were punched into the PDMS with an Integra[®] Miltex[®] biopsy punch (1 mm, Integra LifeSciences Corp.). The pattern surface of the resulting PDMS chip parts can easily be characterized via scanning electron microscopy (SEM) in order to determine the exact channel height and to identify defects that could disrupt the laminar microflow later on. Then, the hydrophobic surface of the PDMS chip halves were activated by air plasma treatment (MiniFlecto[®], plasma technology GmbH) that led to the generation of hydrophilic silanol groups. These silanol groups can be used to initiate a condensation reaction resulting in a covalent

bonding between the both PDMS chip halves.¹¹ Apart from a thin unstructured piece of PDMS acting as bottom part for a 2D microchip, also a glass slide could be used to seal the structured PDMS half. If a 3D microfluidic chip with a 3-dimensional fluid focusing channel design has been fabricated, two structured PDMS microchip parts are needed to create the channel network. A small drop of ultrapure water (Milli-Q, Merck KGaA) was added to generate a thin film of water which enabled the alignment of the two individual parts prior to the final bonding. After bringing both parts in close contact, integrated orientation structures allowed to snap in and to align the microstructures automatically. If necessary, fine adjustments were carried out under a microscope. Removing the water in an oven at 35 °C for 12 h resulted in a permanent covalent bonding of the microfluidic chip. The fabricated PDMS microfluidic devices used in this thesis are based on quasi-two- and three-dimensional focusing channel networks which are illustrated in **Figure 6** and developed for the investigation of particle separation phenomena.

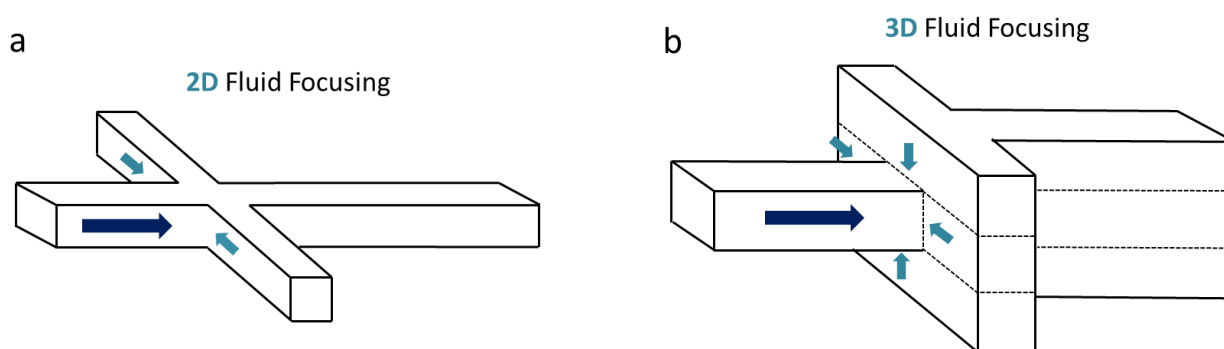


Figure 6 | Comparison 2D and 3D microfluidic devices. (a) Lateral 2D focusing flow cross with three inlet and one outlet channels. (b) Surrounding 3D focusing cross also with three inlets and one outlet however the two side channels as well as the outlet channel are more than twice as high as the main inlet channel.

Microfluidic chips made of elastomer PDMS have many advantages like an easy fabricating process,¹²⁻¹⁴ good temperature stability between -50 and 200 °C as well as an excellent transparency to visible light between 240 and 1100 nm for all optical methods of analysis.¹⁵ Its low toxicity and high gas permeability is well-suited for cell culturing and growth studies.¹⁶ Additionally, the elasticity of PDMS can be controlled by the ratio of the oligomer and crosslinker. PDMS is electrically insulating and allows the integration of electrodes in order to manipulate the fluid flow by electric fields.^{17,18} However, this soft material has also significant drawbacks e.g. its chemical resistance only against aqueous solutions and a small number of polar organic solvents like ethanol, isopropanol or acetone.¹⁵ Due to the fact that PDMS is hydrocarbon-based, organic solvents with solubility in hydrocarbons are able to swell and deform PDMS resulting ultimately in a collapse of the microfluidic channel.¹⁹ By fabricating

microchannels with extreme aspect ratios (channel height h divided by channel width d , and $h/l \leq 0.2$ or $h/l \geq 8$), strong deformation of the channel structures will occur.²⁰ Moreover, unspecific adsorption of biomolecules can lead to bio-fouling of the hydrophobic PDMS surface.¹⁵ Consequently, other materials like thermoplastic, UV-curable perfluoropolyether and fluorinated terpolymers (Dyneon™ THV),²¹⁻²³ polyimides²⁴ and poly(methyl methacrylates),²⁵ but also thermoset polyester (TPE),²⁶ polyurethane methacrylate (PUMA) and Norland optical adhesive (NOA) have been tested by research groups for building up microfluidic devices, even though these materials demand for more complex manufacturing methods, such as high precision injection and compression molding, hot embossing or laser ablation.²⁷

Like PDMS, however, many of these materials suffer from their low X-ray transparency. Yet, for an *in situ* analysis of growth kinetics and orientation of colloids within microchips small angle X-ray scattering (SAXS) is a highly desired tool.²⁸⁻³¹ For such X-ray applications, just acrylate-based NOA and the specific liquid fluoroelastomer SIFEL (produced by Shin-Etsu Chemicals Co.) are suitable.³² SIFEL contains more small fluorine atoms instead of silicon atoms, to increase X-ray transparency. In this context, also developing hybrid materials, like combinations of SIFEL or polyimide foils (Kapton®) and PDMS are of growing interest.^{33,34} Another possibility is to employ a free liquid microjet device by using a micro nozzle system that could be fabricated out of a micro glass capillary or an individually designed microfluidic nozzle chip.^{35,36} The advantage of free liquid microjets is that the analyzed volume is not surrounded by any chip material, which results in no background scattering for SAXS analysis.³⁷ Additionally, a fast microjet shortens the time X-rays are in contact with sensible samples. For instance, analyzing cells, free jets reduce the possibility of damage as well as enable a better and faster decoding of the proteins.^{38,39}

2.1.2 Fluid Dynamics in Microchannels and Jets

The confinement of fluids in micro-scale dimensions enables access to fluid flow phenomena which are not noticeable in a macroscopic environment. As a consequence, viscous dissipation as well as pressure effects dominate over inertia and result in a laminar flow without any turbulences.^{40,41} Moreover, as explained in **chapter 2.1.1**, microfluidic devices have become more and more complex, which increases the need for fluid flow simulations to further improve chip design.⁴² Computational fluid dynamics (CFD) is the standard tool for modeling fluid flow by solving numerically partial differential equations (PDEs) that describe the transport of momentum, mass and energy in moving fluids.⁴³ The most common method today is the finite

element method (FEM) that has evolved as a powerful simulation tool due to recent advances in computer power. Nowadays, FEM enables highly accurate modeling of fluid behavior within the flow geometry by handling complex mesh structures.⁴⁴ Such FEM analyses have been made for certain applications employed in this thesis using COMSOL Multiphysics (v4.3).⁴⁵

Navier-Stokes equation The exact motion of fluids is mathematically described and governed by the Navier-Stokes equation, which describes the velocity field in a Newtonian fluid by deriving the Newton's second law of motion $\vec{F} = m\vec{a}$ to a finite element of a fluid.^{41,46} Basically, the Navier-Stokes equation is a set of two second order PDEs and can be written as:⁴⁷

$$\rho \left[\frac{\partial v}{\partial t} + (v \cdot \nabla)v \right] = \eta \nabla^2 v - \nabla p + F \quad (1)$$

Here, the fluid density is denoted as ρ , the dynamic viscosity as η and v expresses the velocity vector of the fluid flow. The Nabla-Operator is termed with ∇ and F represents additional long-range forces per unit volume directed on the fluid, like centrifugal forces or gravity. The rest of the equation on the right-hand side expresses the stress forces per unit volume due to a pressure gradient ∇p and the viscosity $\eta \nabla^2 v$.⁴² The inertial terms on the left side express the acceleration in terms of the velocity field.

Since, in microfluidic flow, inertial forces and other body forces are negligible, therefore, the Navier-Stokes equation can be linearized omitting its time dependency (because fluid flow in microfluidic devices is symmetric in time).⁴⁶ Consequently, under low Reynolds number conditions, the motion of the fluid is reversed and the initial state of the fluid can be recovered, if forces and pressure acting on a fluid are also reversed.⁴⁸ This behavior is characteristic in case of laminar flow and not possible in turbulent flow.⁴⁹ Additionally, by assuming an incompressible liquid as a continuum material and neglecting its molecular nature, the following continuity equation is obtained:⁴²

$$\nabla \cdot v = 0 \quad (2)$$

In this context, slowly flowing fluids with almost constant density (as is the case for water), can be categorized as incompressible materials. Therefore, the mass of an inflowing and outflowing finite volume of liquid must be the same over a certain time.⁴²

Reynolds number The conception "fluid" is defined in fluid mechanics as a substance that sets no resistance to a discretionary slow shearing and therefore exhibits endless viscosity.⁵⁰ The definition combines the behavior of liquids as well as gases which are quite similar in this consideration. If the characteristic length of the fluid flow decreases to the size of the fluid

transport system (like in micro-sized channels), a fundamental change in hydro-dynamics occurs, i.e. viscous forces start to dominate over inertial forces. This phenomenon causes the typical laminar flow pattern in microfluidics and expresses a stationary flow with constant flow speed. To measure a laminar flow, the Reynolds number (Re) was established and relates inertial forces $\rho(v \cdot \nabla)v$ and viscous forces $\eta \nabla^2 v$:^{41,51,52}

$$Re = \frac{\text{inertial forces}}{\text{viscous forces}} = \frac{|\rho(v \cdot \nabla)v|}{|\eta \nabla^2 v|} = \frac{v \rho d}{\eta} \quad (3)$$

Here, v is the flow velocity, d a characteristic length of the system represented by the microchannel diameter, ρ is the density and η the viscosity of the fluid.⁵³ For microfluidic applications Re tends to be very small, which signifies a higher importance of viscous forces that again describe the resistance of fluids under shear stress due to small microchannel geometries, low flow rates and/or high viscosities.⁴⁸ In consequence, the inertial term can be neglected because the flow velocity varies on the scale of the channel diameter d and therefore the Reynolds number decreases to $Re \ll 1$.^{41,54} This leads to phenomena like turbulence-free flow, fast evaporation and the increased importance of surface tension.⁴⁶

In this work, most of the microfluidic devices were operated with water or solvents that have approximately the same density and viscosity, typical flow velocities of $v = 0.1 - 5000$ mm/s, and channel dimensions between 50 and 1000 μm . These microfluidic conditions lead to Reynolds numbers in a range of $Re \approx 0.01 - 100$, where the fluid flow is always laminar and mixing of liquids is limited to diffusion processes.^{41,55} Turbulences occur in low Reynolds number flow starting at a value of $Re = 2040 \pm 10$.⁵⁶

Fick's laws of diffusion The diffusion effect is defined as a movement of particles along a concentration gradient, from an area of high concentration to an area of low concentration.^{57,58} Fick's first law of diffusion covers the proportionality of the concentration gradient and a so-called diffusive flux J that measures the number of molecules moving through an area per time interval. In order to describe the diffusion at a certain point in the microfluidic channel, Fick's second law is used to give the relation between the concentration gradient ∇c and the alteration rate of concentration by diffusion, whereby D denotes the diffusion constant:^{46,59}

$$\frac{\partial c}{\partial t} = -\nabla \cdot J = \nabla \cdot (-D \nabla c) \quad (4)$$

Diffusion is a non-linear process and the average time $t_{\text{diffusion}}$ necessary for two substances to diffuse into each other is governed by the Einstein-Smoluchowski equation:^{60,61}

$$t_{diffusion} = \frac{d^2}{D} \quad (5)$$

with the characteristic length d for the diffusive process. The mixing time based on advection depends on flow velocity v and is given by following equation:⁴²

$$t_{advection} = \frac{d}{v} \quad (6)$$

Comparing both convection times, the required time for a species to diffuse scales quadratically with the distance of diffusion d that is represented by the channel diameter in this work. Thus, species exchange by diffusion is not effective on the centimeter scale but enable effective mixing in small microchannels at low Reynolds numbers within very short times.^{46,62} In combination with stationary fluid motion, this enables a time-resolved *in situ* monitoring of diffusion-based convection with a temporal resolution down to microsecond in micro-sized channels. Thereby, a precise determination of the reaction kinetics and concentration of the molecules or fluorescent dyes in microfluidic devices can be obtained by hydrodynamic fluid focusing,⁴² as illustrated in **Figure 6** of **chapter 2.1.1**. The monitoring can be carried out with microscopic or scattering methods,⁶³ as shown in this thesis using confocal laser scanning microscopy (CLSM) and small angle X-ray scattering (SAXS).

Péclet number A central parameter for the description of transport phenomena is the dimensionless Péclet number (Pe). Pe represents the ratio between advective transport (i.e. fluid flow) and diffusive transport (i.e. diffusion):⁴¹

$$Pe = \frac{advection}{diffusion} = \frac{vd}{D} = Re \cdot Sc \quad (7)$$

with D the diffusion coefficient, v as flow velocity and d as channel diameter. The Péclet number is also the product of Re and the Schmidt (Sc) number and defined as ratio between the viscous diffusion rate as well as molecular (mass) diffusion rate. Sc is given by the ratio of the kinematic viscosity ν and the mass diffusivity D_m .⁴¹ At high Pe numbers, advection is the dominant convection process contributing to the transport of the substance and happens in microfluidic devices just downstream. Therefore, diffusion is the only mixing process across the channel and the mass flux perpendicular to the flow is completely diffusive. For an aqueous solution flowing at an average velocity of $v = 0.01$ m/s in a microfluidic channel with a characteristic length $L = 100$ μ m, the Pe number is about 1000.⁴⁹

Convection in microfluidic devices can be achieved by different techniques, as common T- or Y-shaped channel designs. However, more complex convoluted or curved mixing geometries are

also available today.⁶⁴ In this work, diffusion-based mixing techniques employing with a cross-shaped channel design are in focus. Here, the convection can be accelerated by e.g. sinus shaped microchannels, as it is shown in the work of **chapter 4.2**. Using a cross-shaped geometry for the channel entrance, one liquid is guided through the center channel (MC) and hydrodynamically focused by another liquid from the side channels (SC1). This setup is shown in **Figure 6** in **chapter 2.1.1**. The cross-shape geometry allows to focus flow and to manipulate the thickness of the middle liquid layer. Thus, very fast diffusive mixing for kinetic experiments, can be carried out as exemplified by the work in **chapter 4.3**. The use of a double-cross polytetrafluoroethylene (PTFE) chip prevents wall agglomeration of reaction products (e.g. growing nanoparticles), by water flowing from the two additional side channels (SC2), as shown in **Figure 7**. The layer thickness of each stream can be adjusted by varying the flow rates:⁴⁹

$$\frac{d_{MC}}{d_{SC1}+d_{SC2}} = \frac{\eta_{MC}}{\eta_{SC1}+\eta_{SC2}} \cdot \frac{Q_{MC}}{Q_{SC1}+Q_{SC2}} \quad (8)$$

where d is the thickness of the relevant layer, η is the viscosity and Q the volume flow. The equation shows that the layer thickness of two, four or more merging streams are proportional to their viscosity and their volumetric flow rate, if the fluids are Newtonian and the viscosity does not change during the experiment. Moreover, the microchannel geometry has to be rectangular and the height is the same in all inlet and outlet channels. As indicated by **equation 5**, mixing time is inversely proportional to the square of the diffusion path length. Therefore, decreasing the stream width d , the mixing time can be reduced significantly.⁴⁹

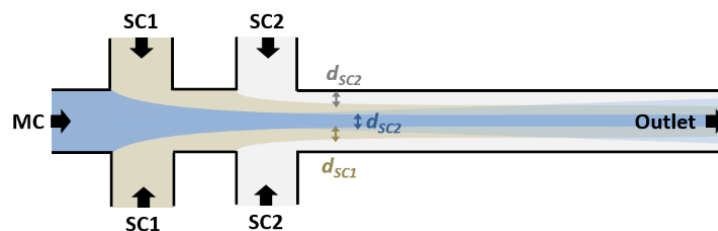


Figure 7 | Double focus microchannel design with two flow crosses. Two sets of two side channels each (SC1, SC2) allow a hydrodynamic focusing of the fluid stream from the center channel (MC).

No-slip condition The phenomenon of particle wall agglomeration is based on the fact that on the micro scale surface properties become more and more important as the surface to volume ratio increases.⁶⁵ Consequently, the influence of the channel walls on the liquids becomes much more pronounced and defines the flow profile within the microchannel which also results in a small Reynolds number Re .⁴⁹ This hydrodynamic interaction between solids and liquids can be described using the Navier boundary conditions. Those conditions assume that the flow velocity v_x tangential to the surface is proportional to the shear stress at the surface:⁶⁶⁻⁶⁸

$$v_x = \lambda \frac{dv_x}{dy} \quad (9)$$

Here, λ is the slip, or Navier length, which can be illustrated as distance between the surface and an imaginary point inside the solid wall, where the velocity profile extrapolates to zero (shown in **Figure 8**).⁴² If $\lambda = 0$, no slip is present, which is widely accepted as suitable boundary condition to describe the interaction of a fluid and a solid wall in microfluidics.⁶⁶ It should be noted that the no-slip boundary condition remains an assumption, which is rather based on experimental findings than physical principles. The depth of fluid slip depends on many parameters, such as the roughness and wettability properties of the surface as well as dissolved gas in the fluid stream.⁶⁹ Micro particle image velocimetry (μ PIV) and surface force apparatus (SFA) experiments have demonstrated that the velocity close to the wall is not exactly zero. More likely, a velocity component remains, as soon as hydrophilic species are in contact with strongly hydrophobic or nanostructured materials.^{66,68,70,71} For systems of ethanol or aqueous samples that flow in PDMS-based microfluidic channels with untreated surfaces, however, the no-slip condition is a good approximation.⁶⁶

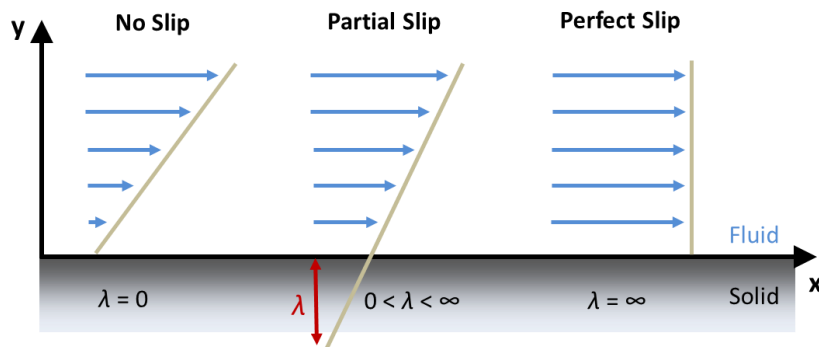


Figure 8 | Sketch of the slip length λ for different boundary conditions, adapted from the literature.^{42,66,69}

As a consequence, the flow velocity v_x is highest in the center and much smaller with $v_x \approx 0$ at the surface of the microchannel. Hence, a parabolic flow profile is established across the channel's cross section with a lower speed of particles next to the wall and therefore a higher probability to stick and agglomerate. The volumetric flow rate Q and the maximum flow velocity v_{max} in circular channels can be calculated using the Poiseuille equation:⁷²

$$Q = \frac{\pi d^4 \Delta p}{128 \eta L} \quad v_{max} = \frac{d^2 \Delta p}{16 \eta L} \quad (10)$$

where d is the diameter of the pipe and η the fluid viscosity. The pressure drop is denoted as Δp along the channel length L , which follows the fluidic resistance of the microchannel $R = Q/\Delta p$.⁶⁵ In case of Poiseuille flow, the mean flow velocity is $1/2$ of the maximum velocity.⁴⁶

When employing a free liquid jet microfluidic device, the parabolic flow profile is turning into a plug flow profile after passing the nozzle outlet. This form represents a simplified flow profile because boundary layers become negligible due to the lack of channel walls. In a free jet, the solid channel walls are replaced by an interface with air. That interface has lower friction with the fluid and can be accelerated in flow direction. Thus, the flow velocity is generally homogeneous across the jet cross-section which results in a so-called plug flow. The effect of plug flow is especially pronounced in the case of shear thinning fluids or fluids with high viscosity.⁴⁹ A comparison of the parabolic and plug flow profile is illustrated in **Figure 9**.



Figure 9 | Illustration of velocity flow profiles for parabolic (left) and plug (right) flow.

Dean number As soon as a straight microchannel is modified to include curvatures, those will cause the initially existing Poiseuille flow to change its main direction of motion. Due to an arising adverse pressure gradient generated by the curvature, a decrease in velocity will occur close to the convex wall.⁷³ A contrary effect will appear towards the outside of the pipe and gives finally rise to a secondary motion superimposed on the primary flow. That motion will sweep the fluid towards the outside of the bend and simultaneously the fluid near the channel wall will return towards the inside of the bend. This secondary motion within a laminar flow is expected to appear as a pair of counter-rotating cells, which are called Dean vortices.⁷⁴ The probability for such Dean-vortices to arise, depend on the curvature of a channel and is given by the dimensionless Dean number (Dn or De):⁷⁵

$$Dn = \frac{\sqrt{(\text{inertial forces})(\text{centrifugal forces})}}{\text{viscous forces}} = \frac{\sqrt{\frac{1}{2}(\rho d^2 R_c \frac{v^2}{d})(\rho d^2 R_c \frac{v^2}{R_c})}}{\mu \frac{v}{d} R_c} = \frac{\rho D v}{\mu} \sqrt{\frac{d}{2 R_c}} = Re \sqrt{\frac{d}{2 R_c}} \quad (11)$$

where d is the channel diameter, ρ the density, and μ the dynamic viscosity of the fluid. The axial velocity scale is denoted as v and the radius of curvature of the channel path is R_c . **Equation 11**, also shows that the Dean number is the product of Reynolds number (Re) and the square root of the curvature ratio. Hence, the creation of Dean vortices is stronger as the viscosity of the used fluid is lower.⁷⁶

The Dean number plays an important role in particle separation phenomena in sinusoidal microchannels as will be shown in **chapter 4.2**. A convergent-divergent cross section of the

microchannel causes mixing due to Dean vortices as well as expansion vortices in the divergent section based on the amplitude and wavelength of the sinusoidal shape.⁷⁷ This behavior results in the off-motion of particles from their straight trajectories and therefore allows separation of particles within fluids. These kinds of micro vortices within laminar flow conditions at low Dean and Reynolds numbers are illustrated in **Figure 10**.

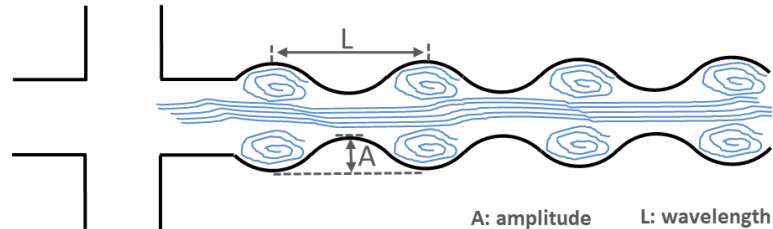


Figure 10 | Sketch of stream trajectories due to Dean micro vortices on horizontal mid-plane of a sinusoidal microchannel.

Further parameters In polymeric dispersions, i.e. non-Newtonian, shear thinning fluids, the Weissenberg (Wi) and Deborah (De) number are important to compare the polymeric relaxation time τ_P within a fluid to another specific time range. Wi is connected to the shear rate time γ^{-1} :⁴⁹

$$Wi = \tau_P \gamma \quad (12)$$

A small value for Wi expresses that the polymer relaxes before flow deforms it significantly. When Wi becomes 1, the polymer does not have enough time to relax and gets deformed due to shear stresses.⁴¹ The Deborah number, however, compares τ_P with other relevant flow time scales τ_{Flow} :

$$De = \tau_P / \tau_{Flow} \quad (13)$$

which is very useful for the characterization of a fluid's response to a stimulus of a given duration.⁴¹ The time scale of such a stimulus could be given by changes of the flow geometries at a given flow rate, like the fluid's flow through a sinusoidal microchannel, or its passing of a micro nozzle outlet.⁷⁸

In order to determine the influence of elastic vs inertial effects, the Elasticity number (El) can be used. It is defined as the ratio of Deborah and Reynolds number:⁴¹

$$El = \frac{De}{Re} = \frac{\tau_P \eta}{\rho h^2} \quad (14)$$

with h as shortest distance setting the shear rate. This dimensionless number depends therefore only on material properties and the geometry, but not on flow velocity.⁴¹

Non-Newtonian fluids In contrast to simple linear systems, where the input is proportional to the output, most of the systems existing in nature have complicated non-linear behavior. Such natural systems very often are of highest interest research because precious resources like material costs, man-power and especially time can be saved.⁷⁸

This thesis is based on the investigation of the flow of non-Newtonian fluids within microfluidic devices that can be considered a non-linear problem. Anisotropic colloids as wormlike micelles, entangled polymer networks and inorganic nanosheets have been used. All of which change their viscosity under the influence of shear or elongation. The viscosity of non-Newtonian fluids can increase and cause in shear thickening (“dilatant”) or decrease to cause shear thinning (“pseudoplastic”).⁷⁹ Both characteristics are displayed in the diagrams of **Figure 11** and compared to the shear independent behavior of Newtonian fluids. Newtonian fluids show a linear connection between shear stress τ and shear rate $\dot{\gamma}$, whereas non-Newtonian behavior can be described by the law of Ostwald and de Waele using k as consistency and n as flow index.⁸⁰

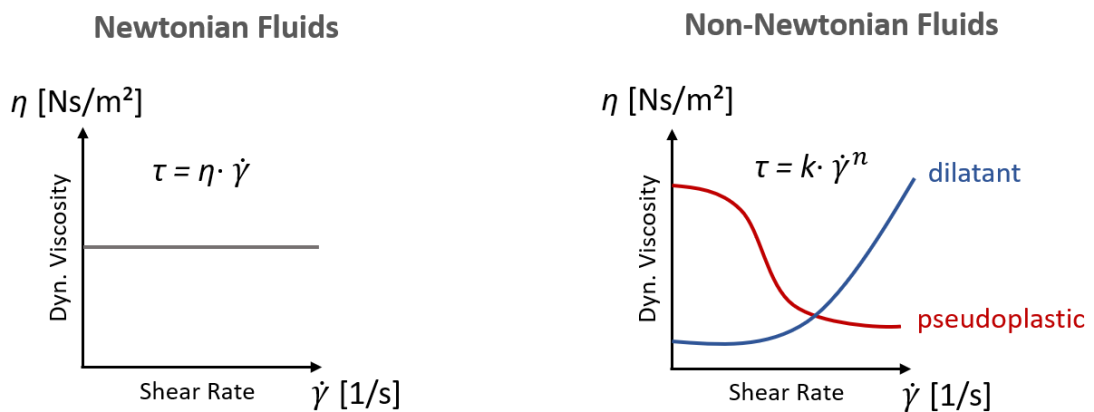


Figure 11 | Comparison between a Newtonian (left) and a non-Newtonian (right) fluid with respect to their dynamic viscosity η vs shear rate $\dot{\gamma}$.

The systems investigated in this thesis all show non-Newtonian behavior. The fluids decrease of viscosity η is based on parallel shear-oriented nanosheets, macromolecules or wormlike micelles that had been entangled and not yet pre-aligned without shearing. This complex non-Newtonian behavior can be described following the Cole-Cole-, or Cross-equation:⁸¹⁻⁸³

$$\eta = \eta_{\infty} + \frac{\eta_0 - \eta_{\infty}}{1 + (\tau_c \dot{\gamma})^n} \quad (15)$$

where η_0 is the viscosity at zero shearing and η_{∞} the high-shear viscosity. The internal relaxation time τ_c and the power law exponent n characterize the shear thinning between η_0 and η_{∞} .²⁹ By coupling this equation with the Navier-Stokes equations (eq. 1 and 2) of an incompressible fluid, the fluid flow of non-Newtonian fluids can be calculated via FEM-based CFD-simulations.⁷⁸

Rayleigh jets and droplet generation The investigation of liquid microjets (due to their aforementioned advantages with respect to scattering techniques) requires a thorough understanding of their basics. Considering the starting conditions – a micro nozzle – the volume flow rate Q divided by the cross-sectional area A of the nozzle outlet gives the initial flow speed v . Additionally, the law of continuity for incompressible fluids, also known as Venturi effect, states that the fluid density ρ is the same at each position in the channel.⁸⁴ Due to the connection $m = \rho \cdot V$ of mass m and volume V , the mass as well as volume flow have to be constant. Thus, reducing the nozzle diameter, the flow speed of the fluid will be increased at a given volume flow.

For analytical reasons, it is important to generate a stable microjet without any movement over the entire distance of interest until droplet breakup. Hence, the hydrodynamic stability of the liquid jet has to be locally and temporally investigated with respect to its initial moment of droplet generation.⁸⁵ The first work on this field was done by Plateau in 1873 and Rayleigh in 1887 who investigated an incompressible non-viscous fluid cylinder that showed an oscillating surface.^{86,87} Rayleigh discovered an optimal wavelength λ_{opt} that yields maximum jet instability where the jet length is minimal. This basic time-dependent and so-called Plateau-Rayleigh instability is valid when only inertial and surface tension effects are present and is defined as:⁸⁷

$$\lambda_{opt} = 9.016 \cdot \frac{d_i}{2} \quad (16)$$

with d_i as initial diameter of the unperturbed fluid. Unstable Rayleigh modes are only possible when the product of the wave number of perturbation k and the initial radius r_i is less than unity ($k \cdot r_i < 1$). Hence, a non-viscous water jet will break up into drops if its wavelength is greater than about 3.18 times its diameter.⁸⁸ The driving force of the Rayleigh instability is that liquid jets tend to minimize their surface area and break up into smaller fractions with the same volume due to the virtue of their surface tensions.⁸⁹ The result of this perturbation might be a steady stream of droplets. These tiny perturbations are always present, no matter how smooth the stream is, and can be subdivided into sinusoidal components,⁹⁰ as visible in **Figure 12**. At the trough of the sinus wave, the radius of the stream is smaller, and the Laplace pressure is increased.⁹¹ The Young-Laplace equation gives the pressure difference Δp as a function of the surface tension γ :⁹²

$$\Delta p = \frac{2\gamma \cos \theta}{r} \quad (17)$$

with the contact angle θ between the fluid and the surface. Therefore, the surface tension is inversely proportional to the microchannel, or micro nozzle dimension. This effect alone predicts

that the higher pressure in the trough squeezes liquid into the lower-pressure region in the peak, and so causes the wave's amplitude to grow over time.⁹⁰

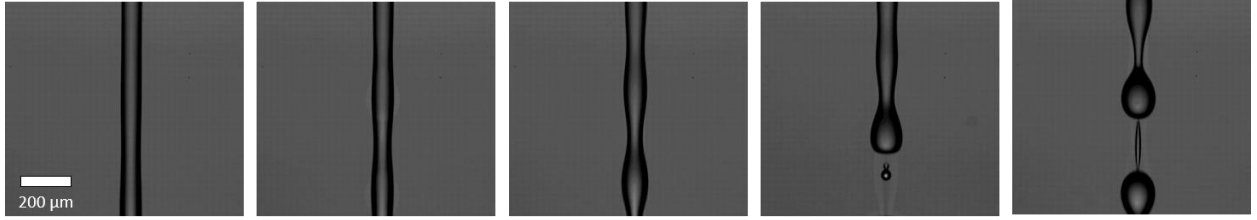


Figure 12 | Series of highspeed camera images from a liquid microjet with a flow rate of $v = 385 \text{ mL/h}$ and a diameter of about $100 \mu\text{m}$ that show the sinusoidal jet movement until droplet breakup taken by a Phantom v1612 (Vision Research).

Next to the temporal stability analysis, however, the local stability analysis is also very important since the amplitude of the sinusoidal movement of the jet is increasing in direction of the stream.⁹³ Furthermore, fluid density and viscosity play a key role in detailed fluid dynamics.⁹⁴ For instance, the Weber (We) number gives the ratio between the inertia of the fluid compared to its surface tension, which is expressed by:^{41,47}

$$We = \frac{\rho v^2 l}{\sigma} \quad (18)$$

where ρ is the fluid density, v the velocity, l the jet diameter and σ the surface tension. In a free liquid microjet system must, the viscosity of the liquid jet μ_A as well as the viscosity of the external fluid μ_B must be included.⁹⁵ In this thesis, the liquid microjet is generated in air where it undergoes jet breakup. In this case, the perturbation growth rate ω is only a function of the initial jet radius r_i , the surface tension σ as well as the viscosity of the jet μ_A , and the perturbation wavelength k :⁹⁵

$$\omega = \frac{\sigma(k^2 r_i - 1)}{2 r_i \mu_A} \frac{1}{k^2 r_i^2 + 1 - k^2 r_i^2 I_0^2(k r_i) / I_1^2(k r_i)} \quad (19)$$

where I is the modified Bessel function of the first kind. As visible in the **equation 19**, the viscosity only determines how fast a given perturbation will grow or decay. Including the viscosity of the liquid jet and its surrounding fluid, it is possible to explain the process of atomization due to jetting.⁹⁶ This kind of droplet breakup creates a spray with extremely small drops and is called Taylor mode.⁹⁷

The aim of this thesis, however, was to generate stable liquid microjets. Based on the **equations 16 – 19**, their stability regimes (steady jetting) can be finally mapped out using Weber- and Reynolds number diagrams to avoid early droplet formation.^{98,99} Thus, a stable microjet is observed when the fluid outruns the instabilities convectively.¹⁰⁰

2.2 Self-Assembly of Amphiphiles

Nature's fundamental principle of self-assembly drives components of a system to form ordered structures or patterns out of a pre-existing chaotic arrangement.⁴⁹ This autonomous organization represents a basic process not just in our immediate environment but also on a galaxy scale.¹⁰¹ Saturn's rings,¹⁰² for instance, or the human body that again are built-up by even smaller macromolecules.¹⁰³⁻¹⁰⁶ Both of these examples employ the principle of bottom-up assembly on very different length scales to form ordered superstructures with an energetic minimum.^{106,107} Concerning the process of droplet breakup of a liquid jet in **chapter 2.1.2**, the reduction of surface tension is the driving force for reaching a more favorable energy level.⁸⁹ A similar principle based on a fast adaptable and effective energy balance can be observed on macro scale for penguins: their body size is decreasing approaching the equator where the climate is warmer.¹⁰⁸ Due to their greater surface to volume ratio, they can easily use the heat of the sun to keep up their body temperature, but at the same time also cool down much more effectively.¹⁰⁹ In very cold regions, like Antarctica, however, they need to keep their energy in form of heat, which is working better with a bigger body because the volume increases cubic, whereas the surface rises just quadratic.¹¹⁰

This thesis focuses on self-assembled anisotropic colloids, as wormlike micelles shown in the cryo-transmission electron microscopy (cryo-TEM) images of later **Figure 13**. The process of static self-assembly is thermodynamically reversible and needs little to no activation energy from an external source. Self-assembly is the result and can be controlled by the design of the components, which makes an attractive method for the formation of nanomaterials, drug delivery systems or other superstructures with new properties.¹⁰¹

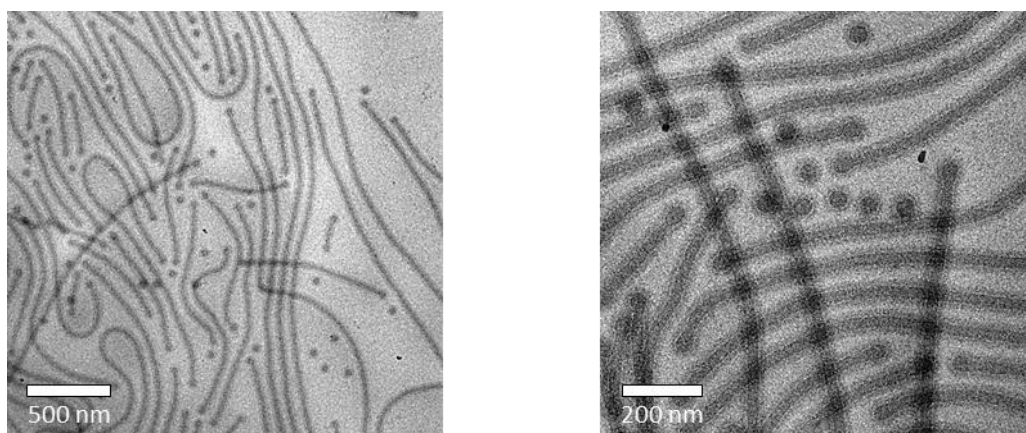


Figure 13 | Cryo-transmission electron microscopy (cryo-TEM) images of wormlike micelles that have self-assembled out of the diblock copolymer polyisoprene-*block*-polyethylene oxide (PI-*b*-PEO).

In chemistry, well-known types of substances that carry out autonomous organization are amphiphilic molecules, which consist of both a lipophilic as well as hydrophilic part. Here, the most famous examples are molecular surfactants used in soap to form soap bubbles out of micelles via self-assembly as soon as the critical micelle concentration (*CMC*) is reached.⁴⁹ The self-assembly process aims to minimize the surface area between the solvent and an insoluble block, as well as the immiscible blocks.¹¹¹ Self-assembly phenomena create new systems with higher order, therefore, a theoretical description using an order parameter ζ was found to be useful.⁴⁹ This parameter defines the degree of order of a system, where a completely chaotic system would have the order parameter of $\zeta = 0$ and a perfectly ordered one would reach a value of $\zeta = 1$.¹⁰⁷ A prerequisite for the formation of organized domains are specific forces between molecules. A balance of short-range attractive as well as long-range repulsive forces is required to form specific structure patterns. Such short-range forces can be covalent or ionic bonds, while coulomb repulsion, hydrophobic interactions or chemical incompatibility of polymers appear as long-range forces.¹⁰⁷

Micelles created out of copolymers, like the used wormlike micelles in **Figure 13**, are also a well-known product of self-assembly. Such copolymers that can be synthesized adjustable and tailor-made via living polymerization exhibit micellar superstructures. Thus, this field of chemistry is predestined for constructing a great variety of components as building blocks for assembly processes.¹¹² Hence, block copolymers, consisting of two or more immiscible or functionalized blocks of chemically different polymeric moieties covalently bound together, extend the possibilities to create new materials for medical, catalytical, or photoelectric and ceramic applications.^{107,113} Most common are diblock copolymers with an insoluble block that forms the micellar core and a soluble block wrapped around it. Copolymers with a soluble block larger than the insoluble one always self-assemble to spherical micelles.¹¹⁴ Apparently, not all copolymers self-assemble to spherical shapes. There are certain requirements with respect to composition and structure of self-assembling copolymers.¹¹⁵ The size and shape of the micelle depends on length and ratio of the polymer blocks.⁴⁹ And based on the size and shape of the building block, it is possible to manipulate the interface to create an interfacial curvature. This relation is described by the micelle's mean curvature H and its Gaussian curvature K , both of which are specified by the two radii of curvature R_1 and R_2 , based on the following equations:^{116,117}

$$H = \frac{1}{2} \left(\frac{1}{R_1} + \frac{1}{R_2} \right) \qquad K = \frac{1}{R_1 R_2} \qquad (20)$$

The resulting interfacial curvature in turn is related to the dimensionless packing parameter P that dictates the molecular shape of copolymer molecules in solution. Thus, P determines the morphology of the corresponding self-assembled copolymer aggregate upon phase separation of the hydrophobic and hydrophilic block.¹¹⁸ P is defined as the size of the hydrophobic block relative to the hydrophilic block and connected to the interface curvature as follows:¹¹⁶

$$P = \frac{v}{a \cdot l} = 1 - H \cdot l + \frac{K \cdot l^2}{3} = 1 - \frac{l}{2} \left(\frac{1}{R_1} + \frac{1}{R_2} \right) + \frac{l^2}{3R_1 \cdot R_2} \quad (21)$$

where v is the volume of the hydrophobic block, a the hydrophilic-hydrophobic interfacial area, and l the hydrophobic block length normal to the interface, as shown in **Figure 14**. For instance, employing symmetric copolymers with a larger core compared to the corona, leads to the generation of cylindrical micelles.¹¹⁹ This is the case for the wormlike micelles studied in this thesis which have a packing parameter of $P = 0.5$ and therefore assume a cylindrical shape. The respective diblock copolymer polyisoprene₁₁₀-*block*-polyethylene oxide₁₉₈ (PI₁₁₀-PEO₁₉₈) was synthesized via living anionic polymerization, where $K = 0$, and $H = 1/2r$ turns into $1/2l$ and yield to $P = 0.5$ which represents a cylindrical shape.⁴²

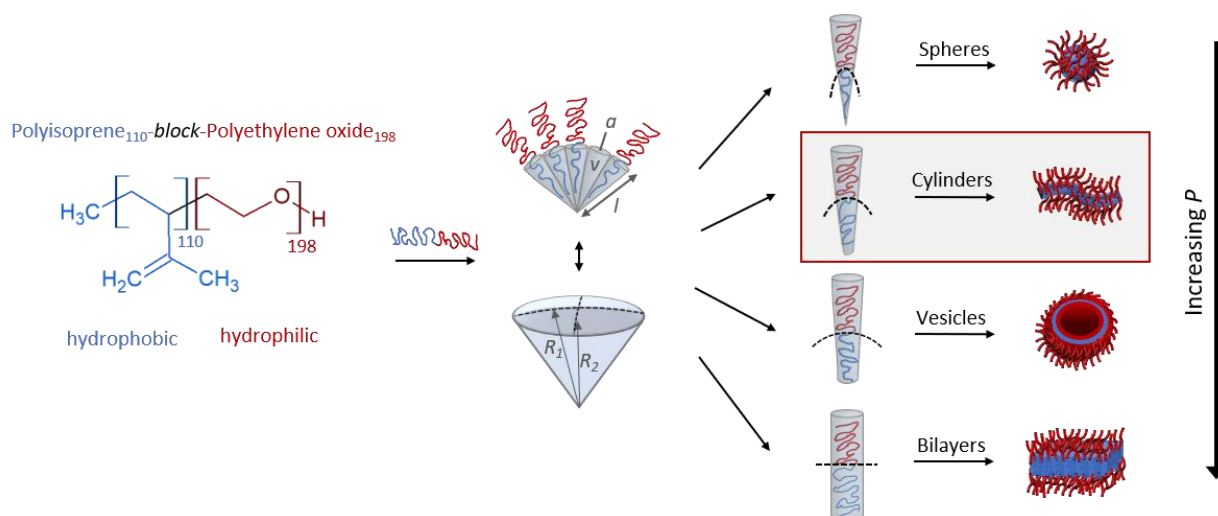


Figure 14 | Chemical formula of the used diblock copolymer PI₁₁₀-PEO₁₉₈ and illustration of the packing parameter P with the related geometric parameters known from equations (20) and (21) as well as the various structures attainable by self-assembly of the block copolymers. PI₁₁₀-PEO₁₉₈ forms wormlike micelles represented by a cylindrical shape for P .

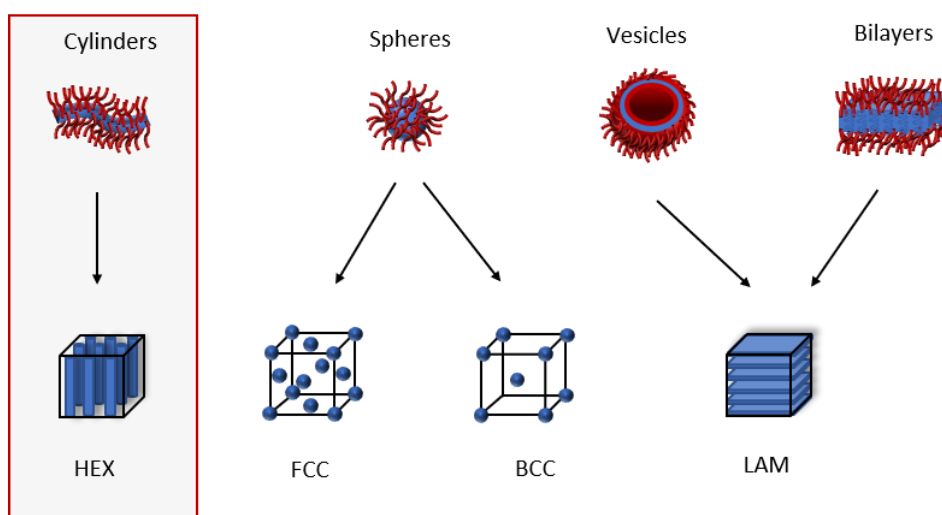
Increasing values of P turn the morphology of the assembly from spherical over cylindrical and vesicular to planar bilayer aggregates. This transition is illustrated in **Figure 14** and supported by the theoretical values in following **Table 1**:

Table 1 | Packing parameter P of different aggregated structures as well as their corresponding mean curvature H and Gaussian curvature K .¹¹⁸

Shape	$P = \frac{v}{a \cdot l}$	R_1	R_2	H	K
Sphere	$P < \frac{1}{3}$	R	R	$1/R$	$1/R^2$
Cylinder	$\frac{1}{3} \leq P < \frac{1}{2}$	R	∞	$1/2R$	0
Vesicle	$\frac{1}{2} \leq P < 1$	R	∞	$1/2R$	0
Bilayer	$P = 1$	∞	∞	0	0

In comparison to low molecular weight amphiphiles, micelles formed by polymeric amphiphiles are kinetically and thermodynamically much more stable. Therefore, they provide a variety of applications, such as colloid stabilization or emulsion polymerization.¹²⁰

In diluted solutions, mainly individual particles like micelles or vesicles are formed. In contrast, in higher concentration cubic phases of spherical micelles develop and can arrange into even higher ordered body-centered cubic (BCC) or face-centered cubic (FCC) phases.¹²¹ Moreover, there are known hexagonal packed (HEX) patterns and lamellar (LAM) phases from the used wormlike or cylindrical micelles in bulk with domains sizes over several micrometers.¹⁰⁷ An overview of some of the modulated or porous phases that can be generated in bulk is shown in **Figure 15**.

**Figure 15** | Illustration of different structures attainable by self-assembly of block copolymers in dilute solutions (top) as well as favored orders with higher concentration in bulk (bottom).

2.3 Microscopic and Scattering Methods

2.3.1 3D Confocal Laser Scanning Microscopy

3D confocal laser scanning microscopy (3D CSLM) is a powerful optical imaging technique mainly applied in biological science, genetics and microbiology.¹²² Furthermore, it is increasingly used to analyze dynamic systems, like general flow profiles or particle flow in microfluidics as shown in this work. In 1957, the principle of confocal imaging presented by Marvin Minsky was shown to overcome the resolution limitations of traditional wide-field fluorescence microscopes.¹²³ The first confocal laser scanning microscope was built by William Bradshaw Amos and John Graham White in Cambridge in the mid-1980s. There, some manufacturers have started to fabricate CLSMs commercially from the 1990s on.¹²⁴ After the advent of ultra-fast resonant scanners, it is possible, for instance, to detect the growth of nanoparticles flowing along a microchannel as a function of their excitation wavelength with a multichannel lambda mode.

Generally, a CLSM is a specialized fluorescence microscope and therefore, requires the use of fluorescence dyes or autofluorescent specimen to detect the target. As visible in **Figure 16**, the phenomenon of fluorescence is based on short-time and spontaneous emission of light due to the transition from an excited electronic state (S_1) back to the lower energetic ground state (S_0). Light emitted from this transition shifts to lower energy and a longer wavelength compared to the absorbed light, which is known as stokes-shift.¹²⁵ The excited electronic state arises from the excitation of valence electrons of chromophores by the absorption of a light photon as it is possible with fluorescence dyes.¹²⁶ A certain amount of the excitation energy will decay in a non-radiative oscillating relaxation process before fluorescence can appear.⁵⁷ Fluorescent transitions are spin-allowed and occur only between states with the equal spins according to the transition rule $\Delta S = 0$.¹²⁷ Therefore, only coherent light with a certain wavelength (e.g. lasers), can provide photons with the relevant energy $E = h \cdot \nu$ to achieve an excitation of valence electrons to a higher state.¹²⁸ The Franck-Condon principle states that these transitions can only occur vertically.⁵⁷ The mechanism of fluorescence can be illustrated by a Jablonski diagram:¹²⁹

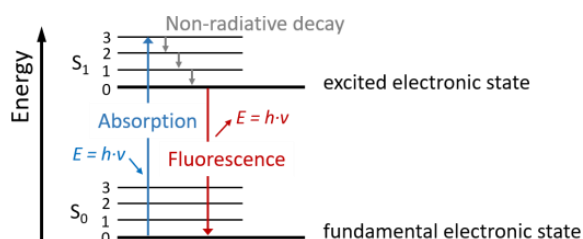


Figure 16 | Jablonski diagram for absorption, non-radiative decay and fluorescence, adapted from⁵⁷.

In a CLSM, a spatial pinhole blocks out-of-focus light in image formation and leads to an increasing optical resolution and contrast.¹³⁰ 3D objects can be reconstructed via optical sectioning, i.e. capturing multiple 2D images at different depths in a sample.¹³¹ In this work, a Zeiss LSM 710 and a Leica TCS SP8, which is visible in **Figure 17**, have been used to reconstruct 3D-images of the flow profiles along various-designed microchannels.

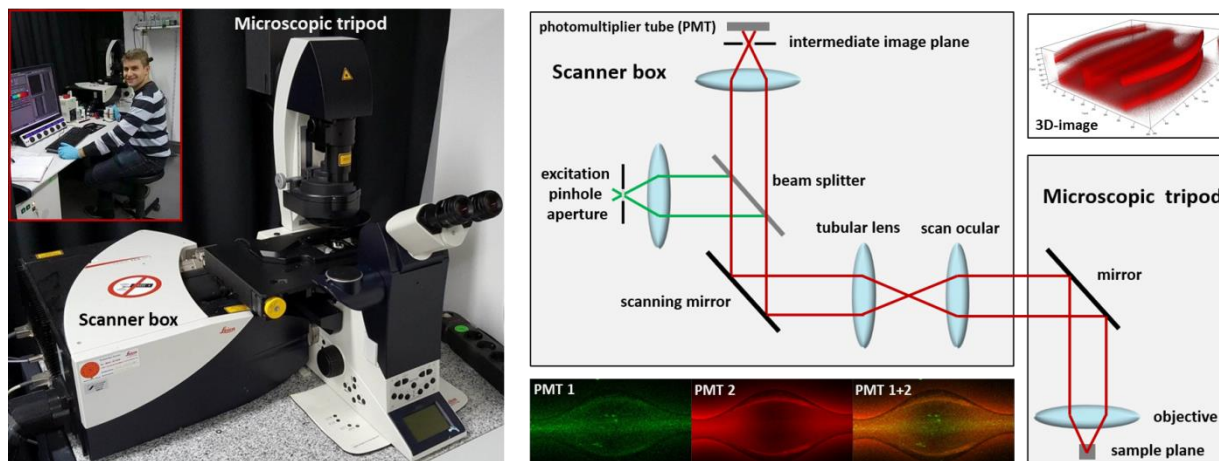


Figure 17 | Leica TCS SP8 CLSM used in this thesis (left), a schematic built-up of the scanner box as well as microscopic tripod adapted from the Leica user manual¹³² and recorded images of various flowing colloids in microchannels (right).

In a conventional fluorescence microscope, the entire sample is illuminated and all parts in the optical path are excited simultaneously. The resulting fluorescence is detected by a camera including a large unfocused background contribution.¹³³ The advantage of a CLSM, is that only a very small beam of light can be focused by a pinhole (point illumination) in all three dimensions at a given time.¹³⁰ A modern CLSM is equipped with several lasers of different excitation wavelengths, which can be used to excite various dyes independently from each other and detect their signals by two or three different photomultiplier tubes (PMTs). The Leica TCS SP8 used in this thesis is an incident light microscope that works with an objective for illumination and detection at the same time. It is equipped with a diode laser of 405 nm, an argon-ion laser of 488 and 514 nm, and a helium-neon laser of 552 as well as 638 nm.¹³² The coherent laser light is coupled into the scanner box via fiber optic cables and directed onto a dichroitic mirror. This mirror acts as a beam splitter as it reflects the excitation wavelength and can be penetrated by the fluorescence light. The optical path is detailed in **Figure 17**. The reflected excitation light is guided by various optical components and focused on the sample. Fluorescent light emitted from the sample is guided back and can pass the dichroitic beam splitter due to its longer wavelength and be detected. The point in the middle of the focus plane and the illuminated point in the sample are “confocal” to each other, which means that they are in focus simultaneously.¹²³

As only light generated by fluorescence very close to the focal plane can be detected, the optical resolution of the image is much better than that of a conventional wide-field microscope.¹³³ The lateral and axial resolution of a modern CLSM is determined by the “full width half maximum” (*FWHM*) of the light intensity and is represented by:¹³⁴

$$FWHM_{lateral} = \frac{0.51\lambda}{NA} \qquad FWHM_{axial} = \frac{0.88\lambda}{n - \sqrt{n^2 - NA^2}} \quad (22)$$

where *NA* is the numeric aperture of the objective which is defined as $n \cdot \sin \alpha$ with the opening angle α . The wavelength of the irradiated light is λ and n is the refraction index of the immersion medium. The wavelength should be estimated as an average wavelength of the excitation and emission wavelength:¹³⁴

$$\bar{\lambda} \approx \sqrt{\lambda_{excitation} + \lambda_{emission}}. \quad (23)$$

The resolution can be further improved by reducing the diameter of the focus plane, which can vary depending on the fluorescence intensity of the dye and the required resolution. Depending on the amount of fluorescent light blocked at the pinhole, the resolution can be enhanced at the cost of decreased signal intensity, which in turn requires longer exposure times.¹³¹ Another factor limiting the resolution of confocal microscopy is the signal-to-noise ratio as only a small number of photons is typically available in fluorescent systems. Increasing the number of photons could be achieved by an increased laser intensity, which on the other hand, bears the risk to bleach or damage the sample.¹³⁰ Therefore, laser intensity is regulated by an acousto-optic tunable filter (AOTF) and detected by very sensitive detectors. Usually PMTs or ultra-sensitive hybrid detectors are used to convert light intensity into an electrical signal that can be processed by a computer.¹³²

CLSM is a scanning microscopy technique. Thus, at a given time only one spot in the sample is illuminated and the signal detected. To reconstruct a 2D image, the sample is subdivided in a raster and the laser is scanned on the horizontal plane using several oscillating scanning mirrors. This scanning method has a short reaction latency and the scan speed can be varied. Naturally, a slower scan speed provides a better signal-to-noise ratio and hence, better contrast and higher resolution.¹³⁰ The default scan frequency of the Leica TCS SP8 is 1400 Hz but can be increased by an ultra-fast resonant scanner to 12,000 Hz.¹³² Such an increased speed is necessary to investigate fast dynamic systems like the flow of colloids in a microchannel.

For one focus plane the pixel dwell time and the horizontal spacing of the pixels defines the temporal and spatial resolution.¹³⁴ The highest resolution possible for the Leica CLSM is

512 x 512 pixels. To create a 3D image, successive focal planes (generated by horizontal scanning) are stacked vertically (along the z-axis). An algorithm to generate such an image is implemented in the software “Leica Application Suite X” (LAS X) from Leica Microsystems.¹³² The sample holder is positioned on a motorized table which enables a scan of the whole distance of a microchannel spanning several centimeters.

2.3.2 Small Angle X-Ray Scattering

Small angle X-ray scattering (SAXS) is one of the most powerful techniques to characterize colloids regarding their internal structure, averaged size, shape and orientation. This chapter will give an overview over the theoretical background of SAXS, the instrumentation and the analysis relevant for this thesis.

Sample materials for SAXS can be solid, liquid or a combination of both and they can even have gaseous domains. Insightful investigations have been conducted on polymers and colloids, biological materials, metals, minerals, nanocomposites, food and pharmaceuticals.¹³⁵ The resolution allows particle or structure characterization in a size range from 1 to 100 nm in a setup with the typical angle of 0.1 to 10°. ¹³⁶ The investigated length scale can furthermore be extended to both bigger and smaller structures. Bigger structures require smaller angles (using ultra small-angle X-ray scattering (USAXS)) and smaller structures require larger angles (using wide-angle X-ray scattering (WAXS) or X-ray diffraction (XRD)).¹³⁷ The sample concentration can range between 0.1 wt.% and 99.9 wt.%, where structures made from materials with high atomic numbers exhibit higher contrast and vice versa.¹³⁵

Absorption and scattering are the first processes in any technique that uses radiation, like also in the already described microscopy of previous **chapter 2.3.1**. Thus, the interaction between matter and electromagnetic radiation is a universal basis for the investigation of materials. In that context, absorption is the basis for microscopy and scattering the basis for SAXS analysis.¹³⁵ The results, however, are different as the contrast in SAXS arises due to the various electron densities of the particles compared to the surrounding matrix.¹³⁶ In contrast, an optical micrograph is the reconstruction of the specimen from the scattering pattern with the help of lenses (which are not available for X-ray radiation used in SAXS).¹³⁷ Hence, the scattering pattern must be recorded and mathematically reconstructed in an indirect and not an optical way.¹³⁵ In the recording process, the phases of the detected waves are lost. Therefore, direct 3D holographic representation of the sample is not possible (in contrast to lens-based optical systems).¹³⁷

Nevertheless, the resolution criteria in SAXS are the same as those in microscopy: large distance between sample and lens, and smaller aperture or scattering angle allow for larger objects to be observed.¹³⁶ On the other hand, the closer the lens to the specimen and the larger the aperture or the scattering angle, the smaller are the details that can be resolved.¹³⁵ The fundamental setup of a scattering experiment is illustrated in **Figure 18**:

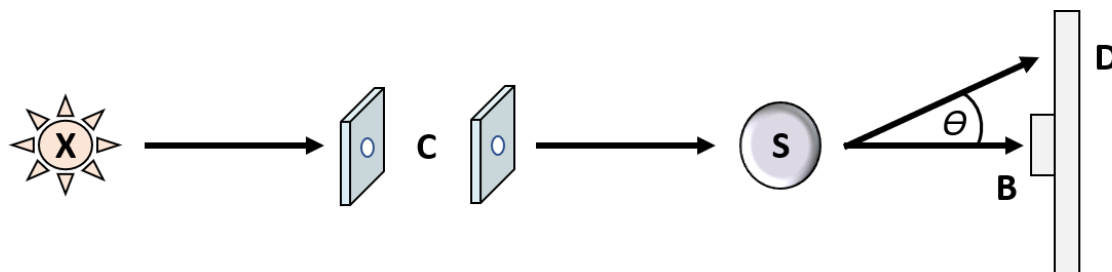


Figure 18 | Scheme of the basic elements of a scattering experiment. The X-ray source (X) emits light that passes through a collimator (C) and the sample with its sample holder (S). The scattering pattern is recorded by a detector (D) depending on the scattering angle θ while the primary beam is blocked out using a beamstop (B), image adapted from⁷⁸.

The elementary components of all SAXS instruments are a source (X) that emits close to monochromatic X-rays, a collimator (C) to narrow the X-ray beam, a sample holder (S), a beamstop (B) that prevents the intense primary beam from over exposure and destroying the detector (D) which measures the radiation scattered by the sample depending on the angle θ .⁷⁸

The source (X) most commonly is a sealed X-ray tube with an optional rotating anode as well as a microfocus beam. Alternatively, synchrotron sources can be used which are aimed to have a higher photon flux or various wavelengths.¹³⁵ An X-ray tube contains a filament (wire) and an anode (target) placed in an evacuated housing. In a first step, electrical current heats up the filament so that electrons are emitted into the tubes, as shown in **Figure 19**:¹³⁵

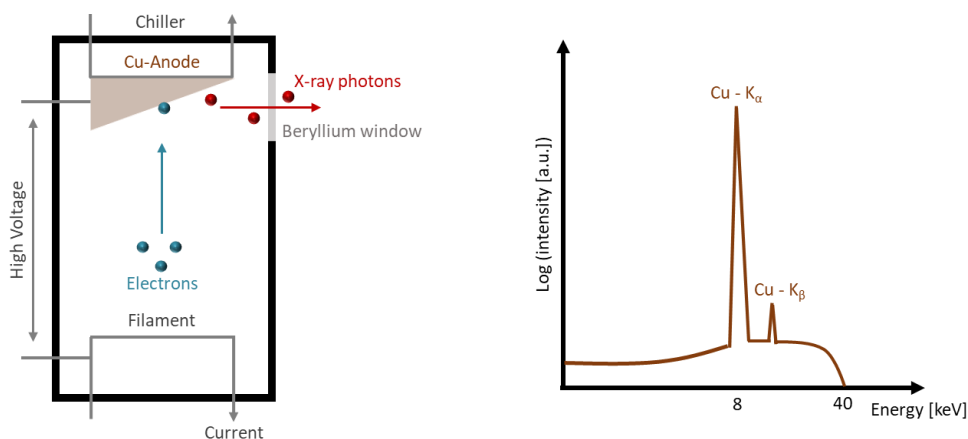


Figure 19 | Fundamental scheme of a sealed tube (left) and the emitted wavelength spectrum of a copper anode operated at 40 kV (right), adapted from¹³⁵.

High voltage between 30 – 60 kV is applied within the tube to accelerate the electrons towards the anode.¹³⁶ As soon as the electrons hit the anode they are decelerated and emit X-rays with characteristic wavelengths specific to the anode material (“Bremsstrahlung”).¹³⁸ This radiation covers a broad spectrum of wavelengths with energies not exceeding the applied high voltage.¹³⁶ For example, a copper tube operated at 2 kW with a current set to 50 mA and a high voltage of 40 kV, limits the electrons’ maximum energy to 40 keV.¹³⁵ The intensity of the X-ray tube is controlled by the number density of electrons (current) that impact the anode.¹³⁸ X-rays are electro-magnetic waves (similar to visible light) with much shorter wavelengths below 300 nm.¹³⁷ The waves propagate as an electric field associated with a perpendicular magnetic field.¹³⁶ Moreover, X-rays can also be modeled according to their particle character as so-called photons. Therefore, every interaction between light and matter can be represented by two models, the oscillator model (wave) and the impulse-transfer model (photon).¹³⁷

The shelling of the anode material with electrons causes senescent effects like grooves or holes and ultimately causes the break-down of the X-ray tube. Therefore, an enhancement of the lifetime of the X-ray sources is highly desired.¹³⁵ A more sustainable option is e.g. a rotating wheel that evenly distributes the bombardment of the anode over its whole area and to reduce the wear per area. Additionally, the rotating anode also increases the electron current and thus the intensity output up to a 10 times higher photon flux as compared to a sealed tube.¹³⁵ An optional microfocus beam allows to focus the electrons in one spot of the anode. Thus, the emission of X-rays can be restricted to a very small area (20 to 50 μm in diameter) and therefore the beam profile can be narrowed.¹³⁹ Micro sources are usually powered by only 30 to 50 watts which makes ordinary water circulators or even air cooling sufficient.¹³⁵

The best and brilliant X-ray sources, however, are synchrotrons that generate a continuous wavelength spectrum as a by-product when forcing charged particles to move along various trajectories at high speed, see **Figure 20**.¹⁴⁰ This radiation has an enormous photon flux because the charged particles move in pulsed bunches.¹³⁵ Thus, the intensity at synchrotrons is not stable over time which explains the need to refresh new electrons by injecting them occasionally.¹⁴⁰

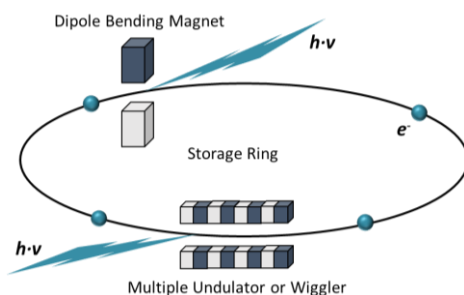


Figure 20 | Sketch of a synchrotron radiation accelerator with $h\cdot\nu$ as photon source and e^- as electrons.

One of the biggest challenges in SAXS is to separate the primary beam from the scattered radiation at small angles less than 0.1° .¹³⁵ The divergence of the incoming beam has to be kept smaller than the small-angle requirement in order to distinguish the relatively weak intensity of the scattering pattern from the much more intense primary beam.¹³⁸ For that purpose, a collimation system (**C**) out of slits (line collimation) or pinholes (point collimation) narrows the beam by forcing it to pass an orifice of about $300 \times 300 \mu\text{m}$ (see **Figure 18**).¹³⁵ While a small collimator reduces the intensity of the incident beam significantly, a bigger pinhole causes more instrumental broadening, which is called slit smearing.¹³⁹ Furthermore, X-rays that are emitted by a synchrotron source are polychromatic, which leads to various angles for the scattered photons and additionally causes wavelength smearing.¹⁴⁰ Multilayer optics can be used to monochromatize the beam according to Bragg's law $n \cdot \lambda = 2d \cdot \sin(\theta/2)$. Using a n integer multilayer with a d -spacing of about 4 nm, a wavelength λ can be selected by tilting the multilayer mirror by an angle θ with respect to the direction of the incoming beam.¹³⁵

The sample holder for the sample (S) has to be tailored for each experiment. In this thesis, a 3D-printer was used to design and fabricate a sample holder meeting the specific requirements, as shown in **Figure 4** of **chapter 2.1.1**. As many samples cannot tolerate the vacuum, for instance, it is necessary to keep background scattering as low as possible. Moreover, many investigations focus on a systems response to a stimulus, e.g. to a change of the environment such as temperature, pressure, flow and shear rate, strain, humidity, projection angle others.¹³⁵ Especially the freejet experiment in this thesis had special requirements concerning the integration in a synchrotron setup.

The beam stop (B) prevents the primary beam from hitting the detector. Although many detectors are capable of high intensities, a beam stop is essential to suppress strong background scattering particularly when analyzing samples with weak scattering.¹³⁵ There are two types of beam stops: one consists of dense materials like lead or tungsten and fully blocks of the primary beam. The other uses transparent materials which mitigate the beam to an intensity not harmful to the detector.¹³⁸ Commonly, transparent beam stop materials are used in synchrotrons to adjust and monitor the intensity of the direct beam simultaneously with the sample scattering.¹⁴⁰

The detector (D). Various types of detectors are in use, e.g. wire detectors, charged-coupled device (CCD) detectors, imaging plates or complementary metal-oxide-semiconductor (CMOS) detectors. There are 5 general specifications that must be considered when selecting a suitable detector:¹³⁵

- The resolution in pixels

- The linear dynamic range to precisely convert photon flux to intensity with a high stability of the read-out intensity
- The sensitivity for effective photon counting (quantum efficiency, QE)
- The dark-count rate detected when the X-ray beam is switched off
- The frame rate as number of scattering patterns recorded per second

Since 2006, detectors operating in 1D single photon counting mode have drastically changed basic research at synchrotron facilities.¹⁴⁰ Recently, 2D digital hybrid photon-counting (HPC) pixel detectors (i.e. Pilatus 1M) are becoming a revolutionary technology for almost all X-ray scattering instruments in the energy range from 2 to 30 keV.¹⁴¹ The main reason for this success is the accurate determination of scattering patterns at the level of individual photons over an extremely high dynamic range that are based on semiconductor sensors and coupled to application-specific integrated circuits (ASICs) using modern CMOS processes.¹⁴¹

If X-rays hit a sample, a fraction will pass through and a fraction will be absorbed as well as transformed into other forms of energy (like fluorescence radiation or heat) and a fraction will be scattered to various directions.¹³⁵ To interpret scattering results, a basic model picture of the process is quite helpful: X-rays interact with a sample, then they cause the sample's electrons to resonate and emit secondary waves of the same frequency.⁷⁸ Such a process is called elastic because incident and scattered photons have the same energy.¹³⁷ The scattered X-rays are coherent but have a phase difference due to the different spatial positions of the scattering centers thus resulting in interference patterns.⁷⁸ The fundamental principle of the wave's interference can be described by the Bragg equation:^{139,142}

$$2d \sin(\theta) = n \cdot \lambda \quad (24)$$

where an intensity maximum can be found if the wave's path difference is a n integer of the wavelength λ the prerequisite for constructive interference.⁷⁸ The path difference is determined by the scattering planes d and the scattering angle 2θ , as illustrated in the following **Figure 21**.

Summarizing all scattered waves with respect to their amplitude and phase,⁷⁸ one obtains a 2D pattern of the sample which is an angle-dependent intensity distribution that is characteristic for the given sample structure. The scattering curve is given as the measured intensity vs the scattering vector's absolute length \vec{q} . Here, \vec{q} is based on the difference of an incident \vec{k}_1 and a reflected \vec{k}_2 wave vector.¹³⁸

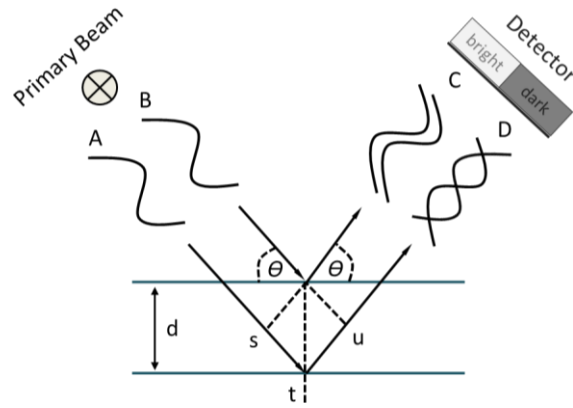


Figure 21 | Illustration of the Bragg relation with the lattice distance d , the half scattering angle θ and the path difference of the wave given by $\Delta = \overline{st} + \overline{tu}$. The intensity of interfering waves depends on the distance of the scattering atoms and on the angle of the incident waves A, B and scattered waves C, D. Hence, waves in phase (constructive, C) lead to high intensity whereas waves out of phase (destructive, D) canceled out, adapted from¹⁴³.

For elastic X-ray scattering with similar wavelengths for the wave vectors according to $|\vec{k}_1| = |\vec{k}_2| = \frac{2\pi}{\lambda}$, the scattering vector q is given by:¹³⁹

$$q = |\vec{q}| = \frac{4\pi}{\lambda} \sin \frac{\theta}{2} \quad (25)$$

Here, instead of the scattering angle θ , also the azimuth angle ϕ can be used. Adversely, each distance is measured relative to the wavelength λ of the applied radiation, wherefore it is better to present the scattering pattern as function of the here described wavelength independent q -value.¹³⁸ \vec{q} is a reciprocal length (units 1/nm) and consequently, a scattering pattern is called a “structure in reciprocal space”.¹³⁵ The absolute value of q can be expressed as s in correspondence to the Bragg equation, depending on q and θ . The inverse of s gives the distance between lattice planes in a crystal:^{78,135}

$$s = \frac{q}{2\pi} = \frac{2}{\lambda} \sin \frac{\theta}{2} \quad (26)$$

The intensity or efficiency by which X-rays are scattered depends on the number of electrons per illuminated material volume. Each electron contributes the same amount of scattered radiation.¹³⁵ This value is expressed by the so-called scattering cross-section (“Thomson factor”) as $\sigma = 7.93977 \cdot 10^{-26} \text{ cm}^2$, which is the energy produced by an incident beam of unit energy per unit area.¹⁴⁴ The X-rays are detected by methods using an absorption process in the first step. The second step comprises acceleration, multiplication as well as amplification processes that lead to electric pulses. These electric pulses are counted and finally given as scattering intensity

or count rates via $I_0 = I_0 \cdot \sigma$.¹⁴¹ Thus, the accumulated energy is proportional to the number of photons that hit the detector. However, whatever the type of the detector, the amplitude cannot be measured and the scattering intensity is only accessible by the squared amplitude of all summed up waves via $I_s = |\overline{E_s}|^2$, finally resulting in the interference scattering pattern.¹³⁸ The more electrons are placed in a sample volume, the more waves are scattered and if the specimen is just one particle of volume V_1 with an electron density of ρ_1 , then $V_1 \cdot \rho_1$ wave amplitudes are scattered. The received detector's read-out intensity I_1 is the square of all of them and finally amounts to:¹³⁵

$$I_1(q) = I_0 \cdot \rho_1^2 \cdot V_1^2 \cdot P(q) \quad (27)$$

The form factor $P(q)$ and the way the obtained pattern oscillates is characteristic of the shape of the particles. The scattering curve of the pattern is described as a function that is given by:⁷⁸

$$I(q) = I_0 \cdot P(q) \quad (28)$$

where the form factor $P(q)$ is determined as $P(q) = |\overline{E_s}(q)|^2$.¹³⁵ In this context, the curve slope of the form factor at small angles is primarily determined by the overall size, whereas the final slope at large angles bears the information of the surface and the oscillating part in the middle section gives the shape as well as internal density distribution.¹³⁶ An approximate subdivision into globular, cylindrical and lamellar shape can be done by investigating the power law of the form factor at small angles on a double logarithmic plot with a slope of 0, -1 or -2, as shown in succeeding **Figure 22a**.

The oscillating part of the form factor can be analyzed by a Fourier-transformation into “real space” due to the calculation of $p(r)$ from an experimental $P(q)$ via the general equation:¹⁴⁵

$$P(q) = 4\pi \int_0^\infty (p)r \frac{\sin(qr)}{qr} dr \quad (29)$$

The resulting curve $p(r)$ is called “pair-distance distribution function” (PDDF) and represents a histogram of distances that can be found inside the particle, as it is shown in **Figure 22b**, further details of the PDDF calculations can be found in the original literature.¹⁴⁵ Here, one of the simpler equations of the PDDF is based on the form factor of spherical particles with radius r and a homogeneous shape, which have a constant scattering length distribution.¹⁴⁶ Moreover, rigid cylinders as an example of simple anisotropic particles can be specified by succeeding formula that uses r as cylinder radius and L for its length:^{147,148}

$$P(q) = \frac{L\pi}{q} \cdot \left(4\rho^2 r^2 \left(\frac{\sin(qr)}{qr} \right)^2 \right) \quad (30)$$

The flexible wormlike micelles that have been investigated in this work, the equation has to be modified by the wormlike chain model of Kratky and Porod, which is introduced by the subsequent form factor:¹⁴⁹

$$P(q) = \int_0^L (L-r) \cdot e^{-q^2 C^2 \frac{\sin Bq}{Bq}} dr \quad (31)$$

with B and C as parameters that are available in original literature.¹⁴⁹ In this equation, another important role regarding the wormlike micelles plays the Kuhn length l_k and the persistence length l_p that are explained, like form factors of other colloid shapes, in further literature.^{146,147}

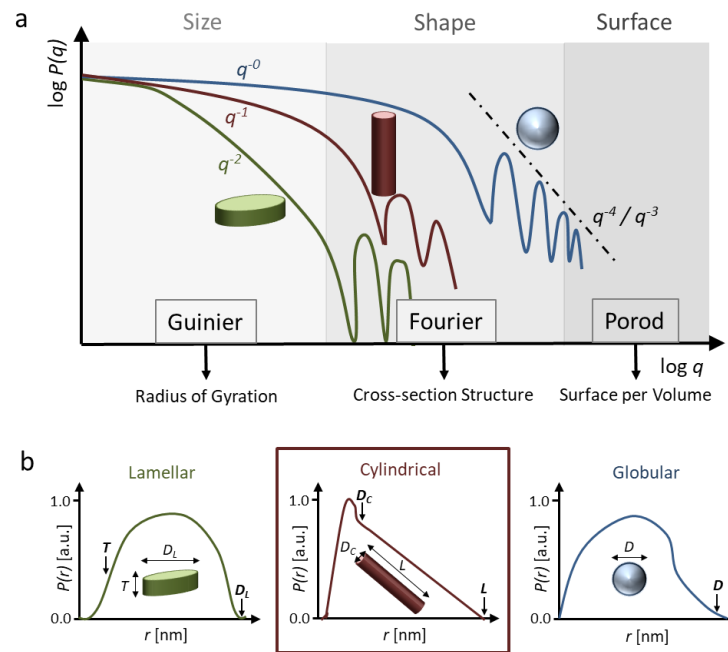


Figure 22 | Form factor. (a) Graph outlining the information domains of a particle form factor and (b) the key features of the pair-distance distribution function (PDDF), which are indicative for the particle shape. Both images are adapted from¹³⁵.

If the sample is dilute, the experimental scattering pattern is the form factor $P_i(q)$ multiplied by the number of particles i that are in the X-ray beam.¹³⁵ However, if the particles have different sizes, all N summed up form factors present an averaged scattering pattern of the entire polydisperse sample with non well-defined minimums.¹³⁸ The same smearing appears with a polymorphous sample of various shapes or a two-phase system where the summation also gives an averaged form factor that can be received by an averaged scattering intensity:¹³⁵

$$\Delta I(q) = I_0 \cdot \sum_{i=1}^N (\Delta\rho)_i^2 \cdot V_i^2 \cdot P_i(q) \quad (32)$$

The structure factor $S(q)$ is added from the form factor the other parameter to characterize substances. The structure factor, however, can only be determined, if the sample concentration is high enough to get densely packed particle systems. Here, the distances relative to each other (interparticular relations) come into the same order of magnitude as the distances inside the particle (intra-particular relations) and therefore the interference pattern will also contain elements from the neighboring particles.^{150,151} Consequently, this further interference pattern appears as an additional factor $S(q)$ in the scattering intensity equation by multiplication with the form factor $P(q)$:

$$I(q) = I_0 \cdot P(q) \cdot S(q) \quad (33)$$

whereby the structure factor $S(q)$ is specified as^{78,150}

$$S(q) = 1 + \int_0^\infty [g(r) - 1] \frac{\sin(qr)}{qr} 4\pi^2 dr \quad (34)$$

The structure factor $S(q)$ is also called lattice factor because it contains the information for the positions of the particles with respect to each other.¹³⁵ This expression is also valid for isotropic systems that form cubic lattices such as spheres.⁷⁸ For rising concentrations and more ordered systems, this factor creates peaks with exponential decay due to repulsive interaction potentials, which are indicated by an intensity drop at small angles respectively low q -values along with the raising of a first peak.¹³⁵ The peak intensity increases with higher concentrations and higher order of the system. The peak is then called Bragg peak whose position for the maximum q_{Peak} indicates the distance d_{Bragg} between the aligned particles by Bragg's law $d_{Bragg} = 2\pi/q_{Bragg}$.¹⁴² Strongly diluted or disordered systems will again be described solely by the form factor $P(q)$ because the structure factor $S(q)$ becomes 1.⁷⁸

As soon as the scattering systems start to form long-range structures that are similar to lattices in crystals (like in liquid crystalline or lyotropic substances), Bragg peaks can appear in the scattering pattern.⁷⁸ Hence, principles of classical crystallography can be applied for this system's description while the above-mentioned scattering principles are still valid.¹⁴² In that the particles can be regarded as an ordered series of interfering scattering centers using a unit cell with defined periodic edge length a , b and c as well as corresponding angles α , β and γ , the particles' scattering can then be applied to extend periodic structures.¹²⁴ The planes of the crystal lattice, which is defined by this unit cell, can be uniquely identified by the Miller indices h , k and l .¹⁴² The indices denote the planes orthogonal to a direction in the basis of the reciprocal lattice vectors while their greatest common divisor should be 1.⁷⁸ In this regard, for example, the unit

cell coordinate system of a cubic lattice is orthogonal with $a = b = c$ and presents a special case where lattice plane distance d_{hkl} and peak positions s_{hkl} are given by:¹⁴²

$$d_{hkl} = \frac{a}{\sqrt{h^2+k^2+l^2}} \quad s_{hkl} = \frac{\sqrt{h^2+k^2+l^2}}{a} \quad (35)$$

Wormlike micelles for instance which pack hexagonally, would be represented by a hexagonal lattice with $a = b$ and $\gamma = 120^\circ$, where only the planes parallel to the c -axis ($= hk0$) are of interest.⁷⁸ However, the wormlike micelles solutions used in this thesis have a quite low concentration between $c = 1$ and 10 wt.%, which is why the peaks in the curve of the 1D analysis are not completely sharp and show smearing due to the ability of position moving of the slightly packed wormlike micelles.

The detailed model-based analysis of experimental scattering data from ordered systems requires further parameters. The entire structure factor for ordered systems is given as:¹⁵²

$$S(q) = 1 + \left(\frac{(2\pi)^{d-1}}{c_d V_d n_0} \sum_{hkl} \left(m_{hkl} |F_{hkl}|^2 \frac{L_{hkl}(q)}{q_{hkl}^{d-1}} \right) - 1 \right) E(q) \quad (36)$$

with the number of structure elements n_0 (spheres, cylinders or lamellae) per unit cell, the dimensionality d (3 for spheres, 2 for cylinders and 1 for lamellae) as well as the dimension-dependent volume V_d . The parameter c_d has a value of 1 for lamellae, 2π for cylinders and 4π for spheres. The factor m_{hkl} considers the multiplicity of peaks that stem from lattice plane multitudes with identical peak positions while the factor F_{hkl} contains any extinction rules.⁷⁸ The profile $L_{hkl}(q)$ determines the peak shapes as well as locations and $E(q)$ is a correlation function, both are described in literature.¹⁵³

The complex data analysis for the 1D scattering curves and the modelling of 2D scattering patterns are made in this thesis with the software “scatter”, written by Förster *et al.*¹⁵⁴ A screenshot of this software while doing parameter adjustments for the modelling of 2D scattering patterns is shown in the following **Figure 23**.

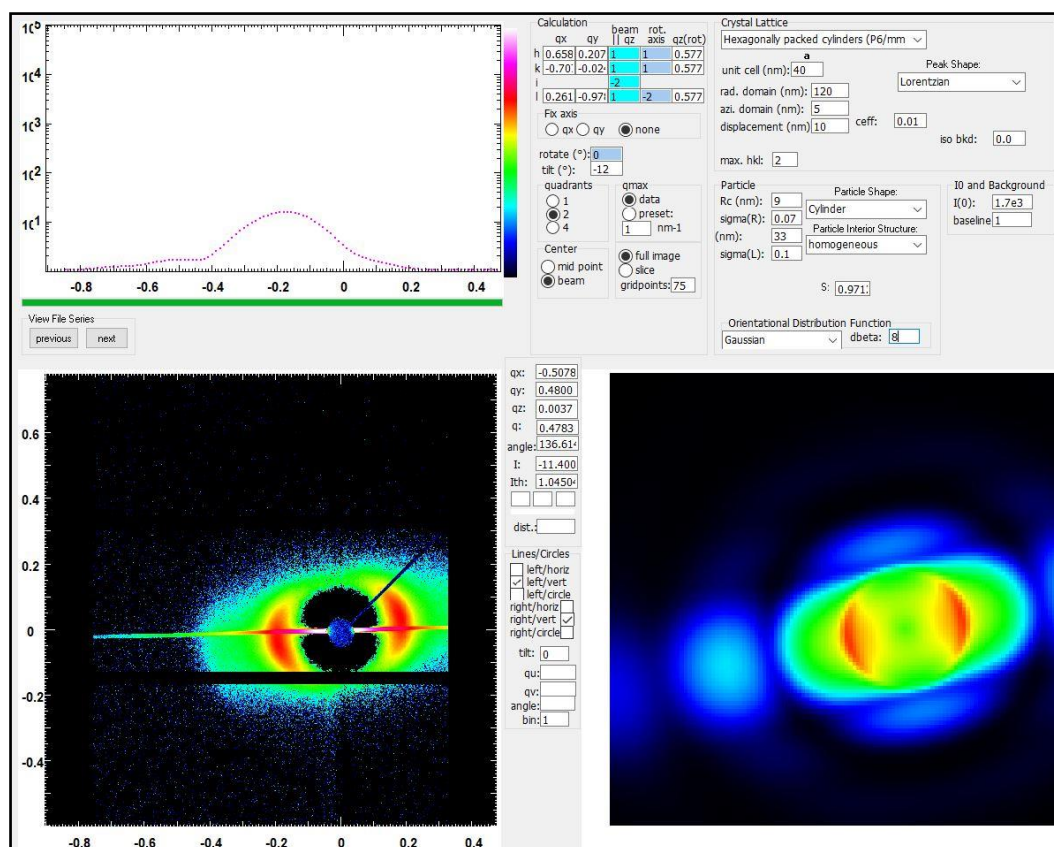


Figure 23 | Software layout of “scatter” that is used in this thesis to simulate the measured 2D scattering patterns (left screen) by adjusting various parameters in order to get the model (right screen).

Such 2D models can be calculated for many other particle shapes, sizes and orientations.¹⁴⁷ In this thesis, it was done for wormlike micelles, nanoplatelets as well as nanorods in a liquid microjet and examples for their measured and simulated 2D scattering patterns are shown in **Figure 24**. As visible, all these flowing liquids have no intensive spots and rather smeared rings are observable around the center of the scattering pattern which again has to do with their low concentrations below 10 wt.% and therefore their lower degree of an order system.

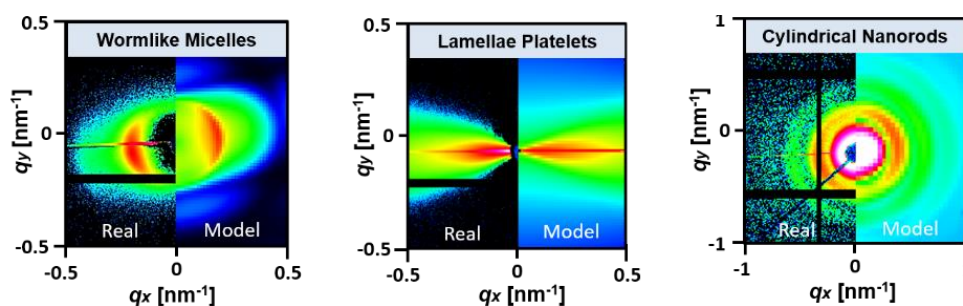


Figure 24 | Measured (left part) and modeled (right part) 2D scattering patterns of wormlike micelles, nanoplatelets and nanorods in dependence of their q -value and azimuthal orientation angle.

The orientation of anisotropic particles along a certain direction, however, was not yet considered in the above discussion. However, within a stream or a microjet, such anisotropic

particles have a high tendency to orientate in flow direction due to applied shear or strain.²⁹ The azimuthal profiles of randomly oriented samples or just spherical particles have a constant intensity along a circular path centered at the primary beam position.¹³⁵ Consequently, this behavior is represented as ring-like, isotropic scattering patterns on 2D detectors of just radially averaged scattering curves.⁷⁸ As soon as some preferred orientation is introduced into the sample, the intensity profile starts to oscillate or peaks at certain azimuth angles.¹³⁵ It is therefore clear that both components of the scattering vector q_x and q_y need to be considered in the analysis and the amplitudes of the oscillation are useful to quantify the degree of orientation.⁷⁸ Of course, the angle of the preferred orientation is also of interest.¹³⁸

Good examples for anisotropic scattering patterns are SAXS studies of shear-oriented wormlike micelles flowing out of a micro capillary, as carried out in this thesis and shown in the first 2D scattering pattern of previous **Figure 24**. Within the capillary, the wormlike micelles are oriented towards the flow direction according to the flow-induced shear and extensional forces. These physical parameters are controlled by the experimental parameters such as flow speed, particle concentration and diameter as well as the geometry of the micro nozzle.^{29,35} By using high precision syringe micro pumps, the setup enables highly reproducible flow conditions. Hence a very good correlation between structural- and orientation information from SAXS studies in combination with fluid dynamic studies from other methods such as high-speed video analysis, particle image velocimetry or polarization microscopy is received.⁷⁸

Instead of splitting the scattering vector into its components q_x and q_y , it is more beneficial to use the polar coordinate system. Here, the scattering vector is described by its absolute value and the angle β between cylinder axis and the scattering vector.¹⁴⁷ This results in the following equation for scattering intensity of oriented cylindrical micelles:¹⁵⁵

$$I\langle q_x, q_y \rangle = N \int S(q, \beta) P(q, \beta) h(\beta) d\beta \quad (37)$$

with the number of micelles N , the structure factor S , the form factor P and the fraction of micelles $h(\beta)$ with the angle β . The form factor is further defined as:^{147,152}

$$P(q, \beta) = \int_0^\pi \langle F_R^2(q, R, \beta) \rangle \langle F_L^2(q, L, \beta) \rangle h(\phi) \sin \phi d\phi \quad (38)$$

The distribution function $h(\phi)$ describes the cylindrical micelle orientation with the angle ϕ between the cylinder axis with the base vector and the direction of the shear field. The expression F_R and F_L are yielded from the factorization of the scattering amplitude into cross section- as well as length-contribution and the pointed brackets indicate the averaging across the

corresponding size distributions of cylinders and radii.¹⁵² As described above, it is possible to express F_R for typical block copolymers by using hypergeometric functions that are described in further detail in the original literature.^{78,152} These block copolymers like those in this work have a core-shell structure and a density-profile. The orientation of anisotropic particles can then be described by a range of distribution functions $h(\phi)$ such as Gauß, Boltzmann, Maier-Saupe, Onsager or Heaviside.¹⁴⁷ Among these functions, the Maier-Saupe and Onsager distributions can be pointed out because they are the most important for the description of particle orientations in cylindrical and wormlike micelles solutions but also in lyotropic and liquid-crystalline systems.⁷⁸ For example, the Onsager (first) and Maier-Saupe (second) distribution functions $h(\phi)$ are given by following equations:¹⁴⁷

$$h(\phi) = e^{\frac{-\sin \phi}{\phi}} \quad h(\phi) = e^{\left(\frac{\cos \phi}{\phi}\right)^2} - 1 \quad (39)$$

The resulting mean deviation angle between cylinders and the director can take on values between 0° and 90° (see **Figure 25**) and is defined as:^{78,147}

$$\langle \phi \rangle = c_h \int_0^{\pi/2} \phi h(\phi) \sin \phi d\phi \quad (40)$$

The final orientaton parameter S can then take on values between 0 and 1 and for dilute solutions, like in this thesis, it is defined for a known distribution function as follows:^{147,155}

$$S = \left\langle \frac{3\cos^2 \phi - 1}{2} \right\rangle \quad (41)$$

To conclude, as shown in this whole **chapter 2.3.2**, small-angle X-ray scattering is a powerful and variable analytical method for a huge variety of particles. Nevertheless, in addition to SAXS, it is indispensable to use microscopic methods as well, because their results are complementary and therefore help to finally get a complete picture of an unknown sample.

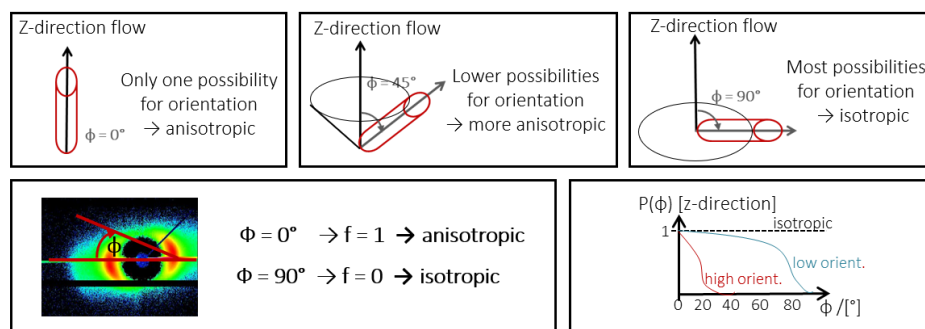


Figure 25 | Theoretical background of the mean deviation angle ϕ and its determination between the cylinders and the z-director of the flow direction based again on a 2D scattering pattern of shear-orientated wormlike micelles in a liquid microjet.

2.4 References

1. Gebhardt, A. *Rapid Prototyping - Werkzeuge für die schnelle Produktentwicklung*. (Hanser, München, 2002).
2. Fastermann, P. *3D-Druck/Rapid Prototyping: Eine Zukunftstechnologie - kompakt erklärt*. (Springer Vieweg, Berlin/Heidelberg, 2012).
3. Reza, A. *et al.* 3D-printed microfluidic devices. *Biofabrication* **8**, 022001, (2016).
4. Bishop, G. W. *3D Printed Microfluidic Devices*. (Springer International Publishing, Cham, 2016).
5. Hwang, H., Kang, G., Yeon, J. H., Nam, Y. & Park, J.-K. Direct rapid prototyping of PDMS from a photomask film for micropatterning of biomolecules and cells. *Lab on a Chip* **9**, 167-170, (2009).
6. Kim, S. H. *et al.* Simple fabrication of hydrophilic nanochannels using the chemical bonding between activated ultrathin PDMS layer and cover glass by oxygen plasma. *Lab on a Chip* **11**, 348-353, (2011).
7. Haywood, D. G., Saha-Shah, A., Baker, L. A. & Jacobson, S. C. Fundamental Studies of Nanofluidics: Nanopores, Nanochannels, and Nanopipets. *Analytical Chemistry* **87**, 172-187, (2015).
8. Zhang, J., Tan, K. L., Hong, G. D., Yang, L. J. & Gong, H. Q. Polymerization optimization of SU-8 photoresist and its applications in microfluidic systems and MEMS. *Journal of Micromechanics and Microengineering* **11**, 20, (2001).
9. MicroChem. *NANOTM SU-8 Negative Tone Photoresist Formulations 50-100*, Access 2014.
10. Whitesides, G. M., Ostuni, E., Takayama, S., Jiang, X. & Ingber, D. E. Soft Lithography in Biology and Biochemistry. *Annual Review of Biomedical Engineering* **3**, 335-373, (2001).
11. Bhattacharya, S., Datta, A., Berg, J. M. & Gangopadhyay, S. Studies on surface wettability of poly(dimethyl) siloxane (PDMS) and glass under oxygen-plasma treatment and correlation with bond strength. *Journal of Microelectromechanical Systems* **14**, 590-597, (2005).
12. Friend, J. & Yeo, L. Fabrication of microfluidic devices using polydimethylsiloxane. *Biomicrofluidics* **4**, 026502, (2010).
13. McDonald, J. C. & Whitesides, G. M. Poly(dimethylsiloxane) as a Material for Fabricating Microfluidic Devices. *Accounts of Chemical Research* **35**, 491-499, (2002).
14. Zhao, X.-M., Xia, Y. & Whitesides, G. M. Soft lithographic methods for nanofabrication. *Journal of Materials Chemistry* **7**, 1069-1074, (1997).
15. Mukhopadhyay, R. When PDMS isn't the best. *Analytical Chemistry* **79**, 3248-3253, (2007).
16. Michael, J., Greg, L., Mark, E. & Bruce, G. Bubble inclusion and removal using PDMS membrane-based gas permeation for applications in pumping, valving and mixing in microfluidic devices. *Journal of Micromechanics and Microengineering* **19**, 095011, (2009).

17. Thorsen, T., Maerkl, S. J. & Quake, S. R. Microfluidic Large-Scale Integration. *Science* **298**, 580-584, (2002).
18. Ng, J. M. K., Gitlin, I., Stroock, A. D. & Whitesides, G. M. Components for integrated poly(dimethylsiloxane) microfluidic systems. *Electrophoresis* **23**, 3461-3473, (2002).
19. Lee, J. N., Park, C. & Whitesides, G. M. Solvent Compatibility of Poly(dimethylsiloxane)-Based Microfluidic Devices. *Analytical Chemistry* **75**, 6544-6554, (2003).
20. Whitesides, G. M. & Xia, Y. Soft Lithography. *Angewandte Chemie International Edition* **37**, 550-575, (1998).
21. Priola, A. *et al.* UV-curable systems containing perfluoropolyether structures: Synthesis and characterisation. *Macromolecular Chemistry and Physics* **198**, 1893-1907, (1997).
22. Rolland, J. P., Van Dam, R. M., Schorzman, D. A., Quake, S. R. & DeSimone, J. M. Solvent-Resistant Photocurable "Liquid Teflon" for Microfluidic Device Fabrication. *Journal of the American Chemical Society* **126**, 2322-2323, (2004).
23. Ren, K., Dai, W., Zhou, J., Su, J. & Wu, H. Whole-Teflon microfluidic chips. *Proceedings of the National Academy of Sciences of the United States of America* **108**, 8162-8166, (2011).
24. Metz, S., Holzer, R. & Renaud, P. Polyimide-based microfluidic devices. *Lab on a Chip* **1**, 29-34, (2001).
25. Galloway, M. *et al.* Contact Conductivity Detection in Poly(methyl methacrylate)-Based Microfluidic Devices for Analysis of Mono- and Polyanionic Molecules. *Analytical Chemistry* **74**, 2407-2415, (2002).
26. Fiorini, G. S., Jeffries, G. D. M., Lim, D. S. W., Kuyper, C. L. & Chiu, D. T. Fabrication of thermoset polyester microfluidic devices and embossing masters using rapid prototyped polydimethylsiloxane molds. *Lab on a Chip* **3**, 158-163, (2003).
27. Sollier, E., Murray, C., Maoddi, P. & Di Carlo, D. Rapid prototyping polymers for microfluidic devices and high pressure injections. *Lab on a Chip* **11**, 3752-3765, (2011).
28. Barrett, R. *et al.* X-ray microfocussing combined with microfluidics for on-chip X-ray scattering measurements. *Lab on a Chip* **6**, 494-499, (2006).
29. Trebbin, M. *et al.* Anisotropic particles align perpendicular to the flow direction in narrow microchannels. *Proceedings of the National Academy of Sciences* **110**, 6706-6711, (2013).
30. Pollack, L. *et al.* Compactness of the denatured state of a fast-folding protein measured by submillisecond small-angle x-ray scattering. *Proceedings of the National Academy of Sciences* **96**, 10115-10117, (1999).
31. Pollack, L. *et al.* Time Resolved Collapse of a Folding Protein Observed with Small Angle X-Ray Scattering. *Physical Review Letters* **86**, 4962-4965, (2001).
32. Renckens, T. J. A. *et al.* Micromolding of solvent resistant microfluidic devices. *Lab on a Chip* **11**, 2035-2038, (2011).
33. Dootz, R., Evans, H., Köster, S. & Pfohl, T. Rapid Prototyping of X-Ray Microdiffraction Compatible Continuous Microflow Foils. *Small* **3**, 96-100, (2007).
34. Bong, K. W., Lee, J. & Doyle, P. S. Stop flow lithography in perfluoropolyether (PFPE) microfluidic channels. *Lab on a Chip* **14**, 4680-4687, (2014).

35. Trebbin, M. *et al.* Microfluidic liquid jet system with compatibility for atmospheric and high-vacuum conditions. *Lab on a Chip* **14**, 1733-1745, (2014).
36. Nelson, G. *et al.* Three-dimensional-printed gas dynamic virtual nozzles for x-ray laser sample delivery. *Optics Express* **24**, 11515-11530, (2016).
37. Polte, J., Erler, R., Thunemann, A. F., Emmerling, F. & Kraehnert, R. SAXS in combination with a free liquid jet for improved time-resolved in situ studies of the nucleation and growth of nanoparticles. *Chemical Communications* **46**, 9209-9211, (2010).
38. Brennich, M. E. *et al.* Dynamics of intermediate filament assembly followed in micro-flow by small angle X-ray scattering. *Lab on a Chip* **11**, 708-716, (2011).
39. Trachsel, F., Günther, A., Khan, S. & Jensen, K. F. Measurement of residence time distribution in microfluidic systems. *Chemical Engineering Science* **60**, 5729-5737, (2005).
40. Atencia, J. & Beebe, D. J. Controlled microfluidic interfaces. *Nature* **437**, 648, (2004).
41. Squires, T. M. & Quake, S. R. Microfluidics: Fluid physics at the nanoliter scale. *Reviews of Modern Physics* **77**, 977-1026, (2005).
42. Thiele, J. *Fabrication of Polymersomes using microfluidic Devices*, University of Bayreuth, (2011).
43. Chung, T. J. *Computational Fluid Dynamics*. (Cambridge University Press, Cambridge, 2002).
44. Kämmer, G., Franek, H. & Recke, H.-G. *Einführung in die Methode der finiten Elemente*. (Carl Hanser Verlag, München, 1990).
45. COMSOL. COMSOL Multiphysics User's Guide. *Version 4.3*, 1-1292, (2012).
46. Brody, J. Y., P.; Goldstein, R.; Austin, R. Biotechnology at Low Reynolds Numbers. *Biophysical Journal* **71**, 3430-3441, (1996).
47. Baerns, M. *et al.* *Technische Chemie*. (Wiley-VCH Verlag, Weinheim, 2006).
48. Purcell, E. M. Life at low Reynolds number. *American Journal of Physics* **45**, 3-11, (1977).
49. With, S. *Microfluidics as a method to follow dynamic assembly of colloidal systems*, University of Bayreuth, (2015).
50. Bird, R. B., Stewart, W. E. & Lightfoot, E. N. *Transport Phenomena*. (Wiley, New York, 2006).
51. Reynolds, O. XXIX. An experimental investigation of the circumstances which determine whether the motion of water shall be direct or sinuous, and of the law of resistance in parallel channels. *Philosophical Transactions of the Royal Society of London* **174**, 935-982, (1884).
52. Reynolds, O. IV. On the dynamical theory of incompressible viscous fluids and the determination of the criterion. *Philosophical Transactions of the Royal Society of London. (A.)* **186**, 123-164, (1895).
53. Guyon, E., Hulin, J.-P., Petit, L. & Mitescu, C. D. *Physical Hydrodynamics*. (Oxford University Press, Oxford, 2001).
54. Groisman, A. & Quake, S. R. A Microfluidic Rectifier: Anisotropic Flow Resistance at Low Reynolds Numbers. *Physical Review Letters* **92**, 094501, (2004).

55. deMello, A. J. Control and detection of chemical reactions in microfluidic systems. *Nature* **442**, 394, (2006).
56. Avila, K. *et al.* The Onset of Turbulence in Pipe Flow. *Science* **333**, 192-196, (2011).
57. Atkins, P. W. & de Paula, J. *Physikalische Chemie*. (WILEY-VCH Verlag GmbH & Co. KGaA, Weinheim, 2006).
58. Mialdun, A. *et al.* A comprehensive study of diffusion, thermodiffusion, and Soret coefficients of water-isopropanol mixtures. *The Journal of Chemical Physics* **136**, 244512, (2012).
59. Was, G. S. *Fundamentals of Radiation Materials Science - Metals and Alloys*. (Springer, Berlin Heidelberg, 2007).
60. Islam, M. A. Einstein–Smoluchowski Diffusion Equation: A Discussion. *Physica Scripta* **70**, 120, (2004).
61. Philibert, J. One and a Half Century of Diffusion: Fick, Einstein, Before and Beyond. *Diffusion Fundamentals* **4**, 1-19, (2006).
62. Knight, J. B., Vishwanath, A., Brody, J. P. & Austin, R. H. Hydrodynamic Focusing on a Silicon Chip: Mixing Nanoliters in Microseconds. *Physical Review Letters* **80**, 3863-3866, (1998).
63. Schmölder, S., Gräbner, D., Gradzielski, M. & Narayanan, T. Millisecond-Range Time-Resolved Small-Angle X-Ray Scattering Studies of Micellar Transformations. *Physical Review Letters* **88**, 258301, (2002).
64. Capretto, L., Cheng, W., Hill, M. & Zhang, X. *Micromixing Within Microfluidic Devices*. (Springer Berlin Heidelberg, Berlin, Heidelberg, 2011).
65. David J. Beebe, Glennys A. Mensing, a. & Walker, G. M. Physics and Applications of Microfluidics in Biology. *Annual Review of Biomedical Engineering* **4**, 261-286, (2002).
66. Cottin-Bizonne, C., Barrat, J.-L., Bocquet, L. & Charlaix, E. Low-friction flows of liquid at nanopatterned interfaces. *Nature Materials* **2**, 237, (2003).
67. Navier, C. L. M. H. Sur les lois du mouvement des fluids. *Mémoires de l'Académie des sciences de l'Institut de France* **6**, 389-440, (1823).
68. Tretheway, D. C. & Meinhart, C. D. Apparent fluid slip at hydrophobic microchannel walls. *Physics of Fluids* **14**, L9-L12, (2002).
69. Lauga, E., Brenner, M. P. & Stone, H. A. *Handbook of Experimental Fluid Dynamics*. (Springer, New York, 2007).
70. Baudry, J., Charlaix, E., Tonck, A. & Mazuyer, D. Experimental Evidence for a Large Slip Effect at a Nonwetting Fluid–Solid Interface. *Langmuir* **17**, 5232-5236, (2001).
71. Santiago, J. G., Wereley, S. T., Meinhart, C. D., Beebe, D. J. & Adrian, R. J. A particle image velocimetry system for microfluidics. *Experiments in Fluids* **25**, 316-319, (1998).
72. S P Suter, a. & Skalak, R. The History of Poiseuille's Law. *Annual Review of Fluid Mechanics* **25**, 1-20, (1993).
73. S A Berger, L Talbot, a. & Yao, L. S. Flow in Curved Pipes. *Annual Review of Fluid Mechanics* **15**, 461-512, (1983).
74. Dean, W. R. XVI. Note on the motion of fluid in a curved pipe. *The London, Edinburgh, and Dublin Philosophical Magazine and Journal of Science* **4**, 208-223, (1927).

75. Dean, W. R. LXXII. The stream-line motion of fluid in a curved pipe (Second paper). *The London, Edinburgh, and Dublin Philosophical Magazine and Journal of Science* **5**, 673-695, (1928).
76. Kalpakli, A. *Experimental study of turbulent flows through pipe bends* PhD thesis, Royal Institute of Technology KTH Mechanics, (2012).
77. Mohsen Khosravi, P. & Faramarz, H. Experimental and CFD modeling of fluid mixing in sinusoidal microchannels with different phase shift between side walls. *Journal of Micromechanics and Microengineering* **24**, 065018, (2014).
78. Trebbin, M. *Microfluidics at high-intensity X-ray sources: from microflow chips to microfluidic liquid jet systems*, University of Bayreuth, (2013).
79. Tropea, C., Yarin, A. L. & Foss, J. F. *Springer Handbook of Experimental Fluid Mechanics*. (Springer, 2007).
80. Brummer, R. *Rheologische Messmethoden zur Charakterisierung kosmetischer Produkte*. (Beiersdorf AG, Doktorandenseminar Bayreuth, 2013).
81. Cole, K. S. & Cole, R. H. Dispersion and Absorption in Dielectrics I. Alternating Current Characteristics. *The Journal of Chemical Physics* **9**, 341-351, (1941).
82. Cole, K. S. & Cole, R. H. Dispersion and Absorption in Dielectrics II. Direct Current Characteristics. *The Journal of Chemical Physics* **10**, 98-105, (1942).
83. Cross, M. M. Rheology of non-Newtonian fluids: A new flow equation for pseudoplastic systems. *Journal of Colloid Science* **20**, 417-437, (1965).
84. Herschel, C. *Measuring water*. (Builders Iron Foundry, Providence, R.I., 1895).
85. Jens, E. & Emmanuel, V. Physics of liquid jets. *Reports on Progress in Physics* **71**, 036601, (2008).
86. Plateau, J. A. F. *Statique expérimentale et théorique des liquides soumis aux seules forces moléculaires*. (Gauthiers-Villars, Paris, 1873).
87. Rayleigh, L. On The Instability Of Jets. *Proceedings of the London Mathematical Society* **s1-10**, 4-13, (1878).
88. Papageorgiou, D. T. On the breakup of viscous liquid threads. *Physics of Fluids* **7**, 1529-1544, (1995).
89. Eggers, J. Nonlinear dynamics and breakup of free-surface flows. *Reviews of Modern Physics* **69**, 865-930, (1997).
90. de Gennes, P.-G., Brochard-Wyart, F. & Quere, D. *Capillarity and Wetting Phenomena*. (Springer-Verlag, New York, 2004).
91. Young, T. III. An essay on the cohesion of fluids. *Philosophical Transactions of the Royal Society of London* **95**, 65-87, (1805).
92. Batchelor, G. K. *An Introduction to Fluid Dynamics*. (Cambridge University Press, Cambridge, 2000).
93. Keller, J. B., Rubinow, S. I. & Tu, Y. O. Spatial instability of a jet. *The Physics of Fluids* **16**, 2052-2055, (1973).
94. Chandrasekhar, S. *Hydrodynamic and Hydromagnetic Stability*. (Dover Publications, Dover, 1981).

95. Tomotika, S. On the instability of a cylindrical thread of a viscous liquid surrounded by another viscous fluid. *Proceedings of the Royal Society of London. Series A - Mathematical and Physical Sciences* **150**, 322-337, (1935).
96. Taylor, G. I. *The Scientific Papers of Geoffrey Ingram Taylor*. (Cambridge University Press 3, Cambridge, 1963).
97. Lin, S. P. & Kang, D. J. Atomization of a liquid jet. *The Physics of Fluids* **30**, 2000-2006, (1987).
98. Gañán-Calvo, A. M., Herrada, M. A. & Montanero, J. M. How does a shear boundary layer affect the stability of a capillary jet? *Physics of Fluids* **26**, 061701, (2014).
99. Leib, S. J. & Goldstein, M. E. The generation of capillary instabilities on a liquid jet. *Journal of Fluid Mechanics* **168**, 479-500, (2006).
100. Leib, S. J. & Goldstein, M. E. Convective and absolute instability of a viscous liquid jet. *The Physics of Fluids* **29**, 952-954, (1986).
101. Whitesides, G. M. & Grzybowski, B. Self-Assembly at All Scales. *Science* **295**, 2418-2421, (2002).
102. Greenberg, R. & Brahic, A. *Planetary Rings*. (Arizona University Press, Tucson, 1984).
103. Fialkowski, M. *et al.* Principles and Implementations of Dissipative (Dynamic) Self-Assembly. *The Journal of Physical Chemistry B* **110**, 2482-2496, (2006).
104. Klages, N. & Strubin, M. *Stimulation of RNA polymerase II transcription initiation by recruitment of TBP in vivo*. (1995).
105. Agalarov, S. C. *et al.* Structure of the S15,S6,S18-rRNA Complex: Assembly of the 30S Ribosome Central Domain. *Science* **288**, 107-112, (2000).
106. Cademartiri, L. & Ozin, G. A. *Concepts of Nanochemistry*. (WILEY-VCH Verlag GmbH & Co. KGaA Weinheim, 2012).
107. Förster, S. & Plantenberg, T. From Self-Organizing Polymers to Nanohybrid and Biomaterials. *Angewandte Chemie International Edition* **41**, 688-714, (2002).
108. Stonehouse, B. in *Advances in Ecological Research* Vol. 4 131-196 (Academic Press, 1967).
109. Stahel, C. D. & Nicol, S. C. Temperature regulation in the little penguin, *Eudyptula minor*, in air and water. *Journal of comparative physiology* **148**, 93-100, (1982).
110. Thomas, D. B. & Fordyce, R. E. Biological Plasticity in Penguin Heat-Retention Structures. *The Anatomical Record* **295**, 249-256, (2012).
111. Hentze, H. P. *et al.* Lyotropic Mesophases of Poly(ethylene oxide)-b-poly(butadiene) Diblock Copolymers and Their Cross-Linking To Generate Ordered Gels. *Macromolecules* **32**, 5803-5809, (1999).
112. Mai, Y. & Eisenberg, A. Self-assembly of block copolymers. *Chemical Society Reviews* **41**, 5969-5985, (2012).
113. Riess, G. Micellization of block copolymers. *Progress in Polymer Science* **28**, 1107-1170, (2003).
114. Gummel, J., Sztucki, M., Narayanan, T. & Gradzielski, M. Concentration dependent pathways in spontaneous self-assembly of unilamellar vesicles. *Soft Matter* **7**, 5731-5738, (2011).

115. Sai, H. *et al.* Hierarchical Porous Polymer Scaffolds from Block Copolymers. *Science* **341**, 530-534, (2013).
116. Hyde, S., T. Curvature and the Global Structure of Interfaces in Surfactant-Water Systems. *J. Phys. Colloques* **51**, C7-209-C207-228, (1990).
117. Israelachvili, J. N., Mitchell, D. J. & Ninham, B. W. Theory of self-assembly of hydrocarbon amphiphiles into micelles and bilayers. *Journal of the Chemical Society, Faraday Transactions 2: Molecular and Chemical Physics* **72**, 1525-1568, (1976).
118. Antonietti, M. & Förster, S. Vesicles and Liposomes: A Self-Assembly Principle Beyond Lipids. *Advanced Materials* **15**, 1323-1333, (2003).
119. Lund, R. *et al.* Structural and thermodynamic aspects of the cylinder-to-sphere transition in amphiphilic diblock copolymer micelles. *Soft Matter* **7**, 1491-1500, (2011).
120. Förster, S., Zisenis, M., Wenz, E. & Antonietti, M. Micellization of strongly segregated block copolymers. *The Journal of Chemical Physics* **104**, 9956-9970, (1996).
121. Bates, F. S. *et al.* Fluctuations, conformational asymmetry and block copolymer phase behaviour. *Faraday Discussions* **98**, 7-18, (1994).
122. Stockert, J. C. & Blazquez-Castro, A. *Fluorescence Microscopy in Life Sciences*. (2017).
123. Minsky, M. Memoir on Inventing the Confocal Scanning Microscope. *Scanning* **10**, 128-138, (1988).
124. Feigin, L. A. & Svergun, G. I. *Structure Analysis by Small-Angle X-ray and Neutron Scattering*. (Plenum Press, New York, 1987).
125. Rost, F. W. D. *Fluorescence Microscopy*. (Camebridge University Press, 1992).
126. Lakowicz, J. R. *Principles of Fluorescence Spectroscopy*. (Plenum Press, New York, 1983).
127. Condon, E. A Theory of Intensity Distribution in Band Systems. *Physical Review* **28**, 1182-1201, (1926).
128. Franck, J. & Dymond, E. G. Elementary processes of photochemical reactions. *Transactions of the Faraday Society* **21**, 536-542, (1926).
129. Jablonski, A. Efficiency of Anti-Stokes Fluorescence in Dyes. *Nature* **131**, 839, (1933).
130. Pawley, J. *Handbook of Biological Microscopy*. (Springer US, New York, 2006).
131. Sheppard, C. J. R. & Shotton, D. M. *Confocal Laser Scanning Microscopy*. (BIOS Scientific Publishers Limited, Oxford, 1997).
132. Leica-Microsystems-GmbH. *User Manual Leica TCS SP8*. (Leica Microsystems CMS GmbH, 2014).
133. White, J. G. An evaluation of confocal versus conventional imaging of biological structures by fluorescence light microscopy. *The Journal of Cell Biology* **105**, 41-48, (1987).
134. Cox, G. & Sheppard, C. J. Practical limits of resolution in confocal and non-linear microscopy. *Microscopy research and technique* **63**, 18-22, (2004).
135. Anton-Paar-GmbH. *The SAXS Guide*. (Anton Paar GmbH, Austria, 2013).
136. Guinier, A. & Fournet, G. *Small-Angle Scattering of X-rays*. (Wiley, New York, 1955).
137. Kerker, M. *The Scattering of Light and Other Electromagnetic Radiation*. (Academic, New York, 1969).

138. Glatter, O. & Kratky, O. *Small-Angle X-ray Scattering*. (Academic, London, 1982).
139. Lindner, P. & Zemb, T. *Neutron, X-rays and Light. Scattering Methods Applied to Soft Condensed Matter*. (North Holland, 2002).
140. Davies, R. J., Burghammer, M. & Riekel, C. An Overview of the ESRF's ID13 Microfocus Beamline. *Synchrotron Radiation in Natural Science* **5**, 96-99, (2006).
141. Jaeschke, E., Khan, S., Schneider, J. & Hastings, J. *Synchrotron Light Sources and Free-Electron Lasers*. (Springer, Cham, 2015).
142. Giacobazzo, C. *et al. Fundamentals of crystallography*. (Oxford University, Oxford, 1992).
143. Plantenberg, T. *Strukturbildung und Wechselwirkung geladener amphiphiler Blockcopolymermizellen*, University of Hamburg, (2001).
144. Schmitz, W. International Tables for X-ray Crystallography, vol. IV (Ergänzungsband). Herausgegeben von der International Union of Crystallography. The Kynoch Press, Birmingham, England, 1974, 366 Seiten einschließlich Tabellen und Sachwortverzeichnis. *Kristall und Technik* **10**, K120-K120, (1975).
145. Glatter, O. A new method for the evaluation of small-angle scattering data. *Journal of Applied Crystallography* **10**, 415-421, (1977).
146. Pedersen, J. S. Analysis of small-angle scattering data from colloids and polymer solutions: modeling and least-squares fitting. *Advances in Colloid and Interface Science* **70**, 171-210, (1997).
147. Förster, S. *et al.* Calculation of scattering-patterns of ordered nano- and mesoscale materials. *Advances in Colloid and Interface Science* **163**, 53-83, (2011).
148. Kratky, O. & Porod, G. Diffuse small-angle scattering of x-rays in colloid systems. *Journal of Colloid Science* **4**, 35-70, (1949).
149. Kratky, O. & Porod, G. Röntgenuntersuchung gelöster Fadenmoleküle. *Recueil des Travaux Chimiques des Pays-Bas* **68**, 1106-1122, (1949).
150. Weyerich, B., Brunner-Popela, J. & Glatter, O. Small-angle scattering of interacting particles. II. Generalized indirect Fourier transformation under consideration of the effective structure factor for polydisperse systems. *Journal of Applied Crystallography* **32**, 197-209, (1999).
151. Brunner-Popela, J. & Glatter, O. Small-Angle Scattering of Interacting Particles. I. Basic Principles of a Global Evaluation Technique. *Journal of Applied Crystallography* **30**, 431-442, (1997).
152. Konrad, M. *Wurmartige Blockcopolymermizellen als Strukturbausteine*, University of Hamburg, (2003).
153. Förster, S. & Burger, C. Scattering Functions of Polymeric Core-Shell Structures and Excluded Volume Chains. *Macromolecules* **31**, 879-891, (1998).
154. Förster, S., Apostol, L. & Bras, W. Scatter: software for the analysis of nano- and mesoscale small-angle scattering. *Journal of Applied Crystallography* **43**, 639-646, (2010).
155. Förster, S., Konrad, M. & Lindner, P. Shear Thinning and Orientation Ordering of Wormlike Micelles. *Physical Review Letters* **94**, 017803, (2005).

3 Thesis Overview

After the motivation for this work (**chapter 1**) and the introduction of the fundamentals (**chapter 2**), on which this thesis is built, the later **chapter 4** will present the experimental findings and their interpretation. Said part is comprised of three publications in total given in **chapter 4.1** to **4.3**. These publications contribute to the methodical advancement of microfluidic devices for the treatment and investigation of anisotropic particles in microchannels and -jets.

The present **chapter 3** gives short summaries of the aforementioned publications (**chapters 4.1** through **4.3**) and elucidates their role in the superordinate theme of this thesis.

3.1 Synopsis

The primary aim of this thesis was the design of sophisticated microfluidic devices for the detailed handling and analysis of anisotropic particles flowing in microchannels and microjets.

Microfluidic is prevalent in more and more research fields like modern medicine, biology or chemistry. The small volume on micrometer scale in thin channels with laminar flow comprises several advantages such as low costs in combination with defined and controlled conditions for a wide variety of complex experiments on a reduced scale with various functional elements.

This work benefits from the advancements of scattering and microscopic methods which led to the development of powerful sub-micrometer free-electron lasers of synchrotrons as well as ultrafast confocal laser scanning microscopes. A sophisticated microfluidic device based on state-of-the-art lithographic methods provides a significant tool for the detailed analysis of colloids on sub-micrometer scale. In this context, we handle wormlike micelles within microfluidic channels and jets to investigate their dynamic reorientation, carry out their separation or load them by an *in situ* microfluidic process with different kinds of nanoparticles.

The first publication, that is presented in **chapter 4.1**, deals with the development of a methodology to determine for the first time the local reorientation of anisotropic colloids such as wormlike micelles, silicate nanoplatelets and gold nanorods within liquid micro-jets. Microfocus X-ray scattering (μ SAXS) of a synchrotron source was used to detect the different orientation within the micro-jet and micro-droplet areas. This led to a good comparison and comprehension of the influences of differently shaped, sized and stiff anisotropic colloids on the gradually loss of orientation and especially on the unexpected biaxial realignment of the particles during droplet formation. All results are supported by additional simulations.

In the second publication of **chapter 4.2**, a useful colloidal stream-splitting effect was found in sinusoidal microchannels for anisotropic and spherical particle separation of polydisperse samples. Here, a 2D flow focusing with polyethylene glycol (PEG) as shear thinning fluid was carried out at the flow cross of the channel entrance. Wavy stream lines caused by the modulated channel side walls induce, near to the ceiling and floor, channel boundaries cross-streamline migration of colloidal particles away from the primary colloidal stream. 3D confocal laser scanning microscopy proved a controllable particle migration that can be influenced by flow rates, microchannel geometries, colloid shapes, deformability as well as molar mass and composition of the carrier fluid. Hence, this developed microfluidic setup can be used not just for the passive separation of particles with various shapes such as wormlike micelles from core-shell particles but also for the sorting of spherical colloids with different sizes.

The third publication of **chapter 4.3** presents various methodologies to load selectively patchy wormlike micelles with functional nanoparticles. Via a sophisticated tailor-made microfluidic setup, it was possible to carry out a selective *in situ* loading of functional wormlike crystalline-core micelles (wCCMs) with nanoparticles in a continuous and well-controllable way. The PTFE microfluidic chip was fixed to a glass capillary and exhibits a double flow-cross with one main and four side channels to run controlled fluid focusing with any kinds of aggressive solvents and to avoid particle agglomeration. The laminar flow allows a very precise regulation of all reactants by varying the flow rate. The wormlike micelles have been run by the main channel, the gold acid via the first two and the L-selectride via the second two side channels for a direct nanoparticle synthesis and *in situ* loading of the micelles at the same time. Compared to a batch synthesis, we could significantly increase the loading capacity. Moreover, by varying the flow rates for the various reactants, it was possible to adjust the nanoparticle size.

Publication of Chapter 4.1

Parallel and Perpendicular Alignment of Anisotropic Particles in Free Liquid Microjets and Emerging Microdroplets

In **chapter 4.1**, the generation of stable liquid micro-jets of anisotropic colloid suspensions have been conducted and analyzed by microfocus synchrotron X-ray scattering (μ SAXS). The setup consisted of a micro glass capillary and a micro-gear pump for recycling the liquids back to the capillary via tubes. Vertically aligned capillaries with an inner radius of 300 μm have been used to run liquid micro-jets with a flow rate of $Q = 750 \text{ mL/h}$ as well as the radius of the capillary. The resulting jet velocity is determined at $v \approx 1 \text{ m/s}$ and exhibited a stability of about 15 mm in

length until the microdroplet breakup started due to the Rayleigh instability. By scanning with a $20 \times 20 \mu\text{m}$ X-ray beam across a raster of 7 – 20 horizontal as well as 5 vertical positions from the capillary downstream the nozzle, free jet and microdroplets, the local orientational distribution of the dispersed particles could be determined for all the named positions. In **Figure 1a** and **1b**, the relevant SAXS scanning positions are illustrated for the various areas.

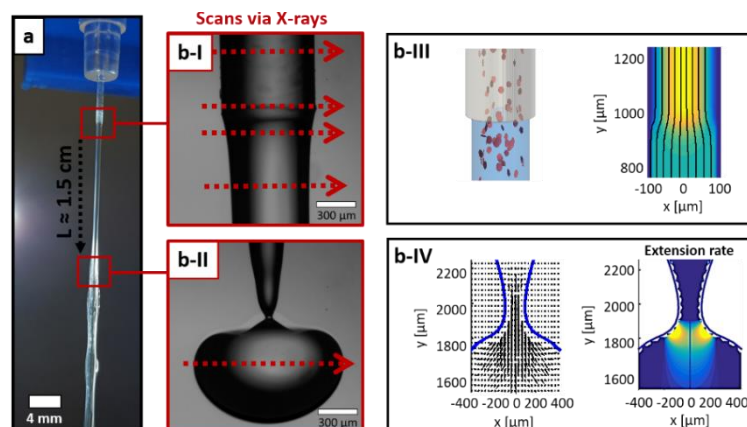


Figure 1 | (a) Dimensions of the free liquid microjet in a 3D-printed sample holder out of a micro glass capillary. (b) High-speed camera images of the generated microjet with the different μSAXS scan positions across as well as along the capillary/ freejet (b-I) and droplet breakup (b-II). Furthermore, Lattice-Boltzmann simulations for platelet reorientation during jet ejection at the outlet of the capillary (b-III) and potential-flow boundary-integral simulations for the droplet breakup position (b-IV).

The appearing flow profiles and velocities have been analyzed by high-speed cinematography (HSC) in combination with microparticle image velocimetry (μPIV) as well as simulated via Lattice-Boltzmann simulations. By applying the above described setup, three different particle systems have been investigated: first layered silicates as an example for 2D nanoplatelets, second wormlike micelles as 1D flexible, long cylinders and finally stiff, short gold nanorods with small axial ratios. For all three particle systems it was discovered a sudden and significant loss of orientation directly after passing the outlet of the microcapillary and a surprising reorientation within the microdroplets that will be generated after freejet breakup due to Rayleigh instability. This behavior is shown in the later microjet scheme and 2D SAXS patterns of **Figure 2**. Here, the highest orientation parameter could be determined next to the wall within the capillary where shear flow dominates, and all types of anisotropic particles remain orientated in flow direction. In this context, the determination of the orientation parameter was carried out by the software “scatter”. For the better understanding of the observed decreasing orientation parameter immediately after passing the outlet, Lattice-Boltzmann simulations have been conducted, as demonstrated in **Figure 1b-III**. Thus, the slightly decreasing inclination angle and the instant loss of particle orientation visible in the 2D SAXS patterns (see **Figure 2**) can be fully

understood by inspecting the stream lines of the simulated flow velocity field. Here, the conditions at the liquid surface changes from no-slip boundary conditions of a Poiseuille flow at the glass wall of the capillary to free-slip boundary conditions of a homogenous plug flow at the liquid/air-interface of the free jet. The resulting local velocity differences cause a transition zone due to an acceleration of fluid volume elements in the outer jet region and a deceleration in the center of the micro-jet. For the satisfaction of mass conservation, the fluid needs to flow radially from the inner to the outer region and therefore carries along the anisotropic particles. The shorter the relaxation time of anisotropic particles is, the faster the loss of orientation can be. The reestablishment of a purely axial flow after the transition zone then partly reorients the platelets parallel to the streamlines thereby leading to near zero inclination angles.

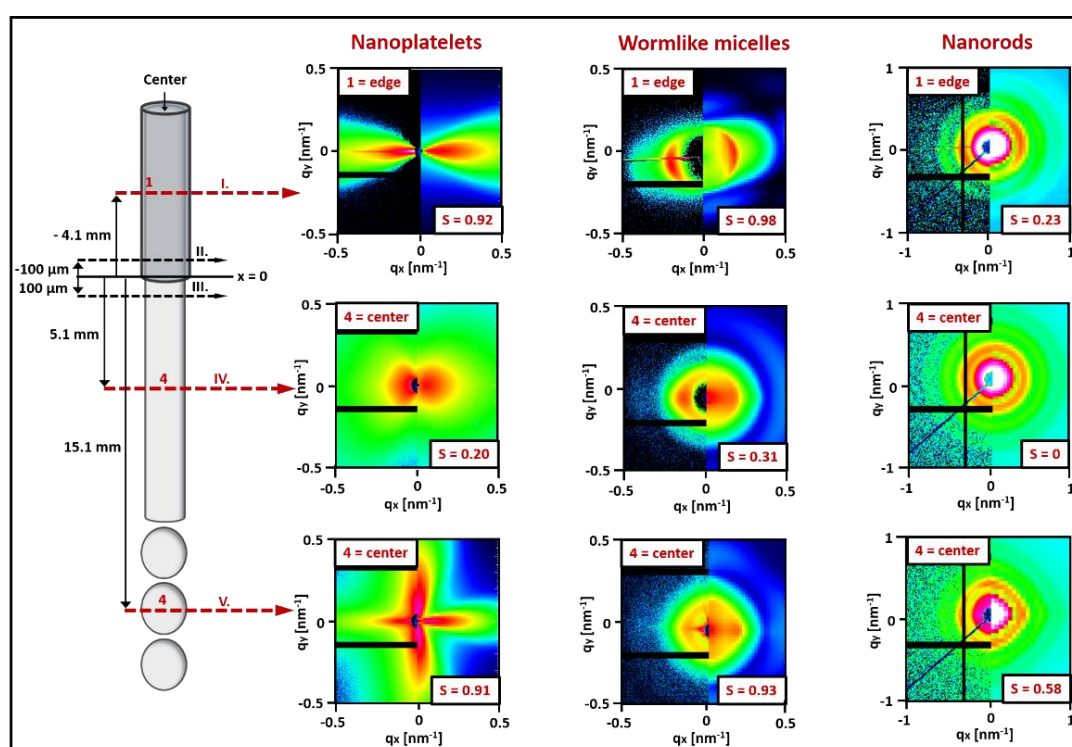


Figure 2 | Overview of the μ SAXS scan positions for the various microjet areas with its corresponding 2D SAXS patterns for the ejected watery dispersions of nanoplatelets, wormlike micelles and nanorods. In addition to it, a simulated model of the measured 2D SAXS patterns and the orientation parameter, which both were calculated by the software “scatter”, are represented at the right half of each image.

However, along the freejet the orientation reduction carries on but starts at the center of the freejet due to a decelerating of flow velocity of the homogeneous plug flow profile with vanishing shear rates. These decreasing shear rates cause lower shear-induced flow alignment by central rotational diffusion. As visible in **Figure 2**, the differences such as the persistence of a high orientational order in the freejet for the wormlike micelles, for instance, are related to the stronger positional and orientational correlations of a higher concentration as well as more elastic

particles with higher relaxation times. Consequently, the short and stiff nanorods with the lowest concentration showed the fastest loss of orientation along the free liquid microjet.

This general orientation behavior for various anisotropic particles still applies to the second finding, the reorientation within microdroplets which finally appear from microjets. This effect is verified by a cross-shaped high intensity region in the 2D SAXS patterns that is displayed in **Figure 2**. Almost equal fractions of the platelets are oriented parallel to the flow direction, with the platelet normal in the equatorial plane, and perpendicular to the flow direction with the platelet normal parallel to the flow direction. To understand the evaluation of this biaxial orientation, simulations of the flow profile in the liquid jet during droplet breakup have been executed. Since this requires to explicitly consider the dynamics of the free micro-jet surface, including the thinning of the neck and the final droplet pinch-off, boundary-integral simulations have been used. These simulations are shown in the last two diagrams of previous **Figure 1b-IV**. As visible, the simulations of the droplet breakup, which have been performed using the same conditions with a micro-jet radius of 300 μm and a flow rate of $Q = 750 \text{ mL/h}$, are in good agreement with the experimentally determined break-up. After passing the thin neck and entering the droplet, the fluid enters an expansion zone with high extension rates (see right image of **Figure 1b-IV**) and significant radial outward flow. Within the high extensional rate zone, the platelets are oriented perpendicular to the flow direction and after formation of the final droplet shape the extensional rates become zero and the platelets remain in their biaxial orientation. The experiments for the nanoplatelets, wormlike micelles and gold nanorods thus showed that the observed reorientation effects, particularly the unusual biaxial distribution in the micro-droplets after droplet break-up, are generally occurring for anisotropic particles.

Publication of Chapter 4.2

Splitting and Separation of Colloidal Streams in Sinusoidal Microchannels

In **chapter 4.2**, a cross-stream migration of anisotropic as well as spherical soft and hard colloid suspensions is explored in sinusoidal microchannels by using fluorescence-, polarization- and confocal laser scanning microscopy (CLSM). The streams of the colloidal solutions were hydrodynamically focused into the center of microchannels at low Reynolds numbers using non-Newtonian fluids like polyethylene glycol (PEG). Following this, a surprising phenomenon of a symmetrical splitting of the central stream into four side streams moving towards the outer wall of the microfluidic channel has been discovered. This observed stream splitting and separation can be controlled via flow rates, microchannel geometries, colloid shape and

deformability as well as the rheological properties of the focused liquid. The aim of this study was to investigate the flow of anisotropic colloids, in this case wormlike micelles, in sinusoidal microchannels. A diagram of the channel design is displayed in the following **Figure 1a**.

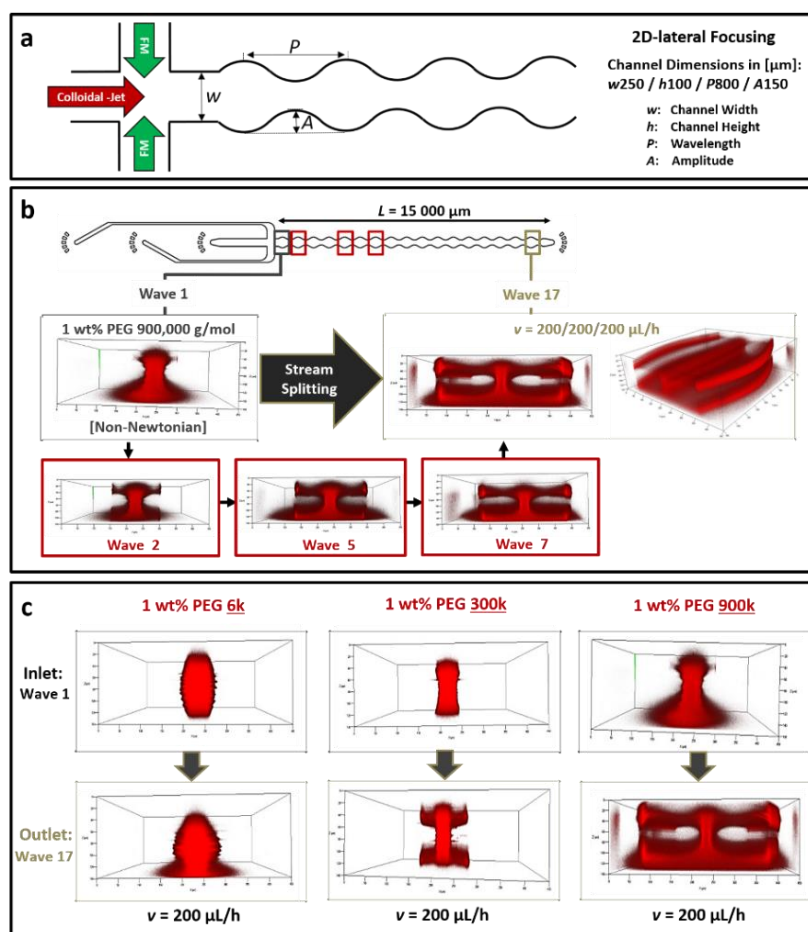


Figure 1 | (a) Diagram of the sinusoidal microchannel with its parameter dimensions. (b) 3D CLSM front view images of a Nile red dyed 1 wt% wormlike micelles solution that is 2D-focused by a non-Newtonian 1 wt% PEG-solution. Just with non-Newtonian PEG, the stream-splitting effect happens next to the channel floor and ceiling where the colloids are near to the walls. The front view images of wave 2, 5 and 7 show the subsequent rising of the stream-splitting with each sine wave. (c) 3D CLSM front view images at the channel inlet and outlet of the flow profiles of the same sample but using various molar mass of the non-Newtonian 1 wt% PEG-solution ($M = 6,000$ g/mol, $300,000$ g/mol and $900,000$ g/mol) as focusing fluid at a constant flow velocity of $v = 200 \mu\text{L/h}$ for all three inlets.

An aqueous solution of wormlike micelles ($c = 1$ wt%) was focused by two side streams of non-Newtonian PEG ($M = 900,000$ g/mol, $c = 1$ wt%) into an outlet channel that had periodic sinusoidal variations of the channel width. The wormlike micelles were formed by self-assembly of poly(isoprene-*b*-ethylene oxide) block copolymers (PI-PEO) that spontaneously occurs when dissolving the block copolymer in water. The channel width was $w = 250 \mu\text{m}$ for both the central and the two side channels, was identical to the average width of the sinusoidal outlet channel. A

typical flow rate in the central and side channels was $Q = 200 \mu\text{L/h}$ which leads to a flow rate of $Q = 600 \mu\text{L/h}$ in the outlet channel. The most interesting question was how the central stream of wormlike micelles would respond to periodic extension and contraction. Therefore, wormlike micelles have been labelled with the fluorescent dye Nile Red to follow the focused stream in the sinusoidal outlet channel using fluorescence microscopy. As visible in the 3D confocal laser scanning microscopy (3D CLSM) images in the previously shown **Figure 1b**, the stream of the wormlike micelles splits into four side streams. The CLSM image on the left shows the central stream in the first sine period, where it is already slightly extended at the bottom and the floor of the channel. The two CLSM images on the right show the central stream in the 17th sine period, where it has split symmetrically into four substreams which are located close to the left and the right wall at the channel floor and channel ceiling. Three additional images in **Figure 1b** show the increasing separation of the four streams in the 2nd, 5th, and 7th sine period. The part of the central stream located in the middle between the floor and the ceiling of the outlet channel, does not split.

As shown in **Figure 1c**, the influence of PEGs of smaller molecular weights that show less pronounced shear thinning, eventually becoming near Newtonian at very low molecular weights, has been investigated. The corresponding experiment with PEG of different molecular weights were performed again under standard conditions with a 1 wt% solution of wormlike micelles, a channel height $h = 100 \mu\text{m}$, an average channel width of $w = 250 \mu\text{m}$, a sine period of $L = 800 \mu\text{m}$, an amplitude of $A = 150 \mu\text{m}$, and a volumetric flow rate of $Q = 600 \mu\text{L/h}$ in the outlet channel. In previous **Figure 1c**, CLSM-images of the central stream shapes in the first and the 17th sine period are compared for PEG-solutions with PEG molecular weights of 6, 300, and 900 kg/mol. Whereas the 6 kg/mol low molecular weight PEG-solution showed (like also tested Newtonian water) no indications of stream splitting in the 17th sine period, the 300 kg/mol PEG-solution lead to a small, but clearly observable splitting. The 900 kg/mol PEG-solution lead to a very pronounced splitting of the central stream, as already described. This indicates that the molecular weight of the polymer, which is used in the focusing fluid, must be sufficiently large to induce stream-splitting. Additionally, the effect of the flow rates has been analyzed because for shear-thinning non-Newtonian fluids the solution viscosity depends on the shear rate. In a range of a flow rate of $10 - 520 \mu\text{L/h}$, that corresponds to a mean velocity of $0.1 - 6 \text{ mm/s}$, there is no observable stream splitting at the lowest flow rate of $10 \mu\text{L/h}$, but a small significant splitting at $80 \mu\text{L/h}$ and a further increasing splitting up to a flow rate of $520 \mu\text{L/h}$.

Moreover, to clarify other necessary conditions for the achievement of the stream splitting effect, the channel geometry with respect to the influence of the channel floor and ceiling was

investigated. Here, a 3D-focusing design was employed in such a way that the central stream was focused into the center of the outlet channel with considerable distance from the channel floor, ceiling and both side walls. The 3D-focusing channel design is schematically shown in **Figure 2a**. The CLSM images on the right clearly prove that under these conditions no splitting of the central stream is observed. This suggests that the proximity of the channel floor and ceiling is necessary for the splitting and separation of the central stream. Furthermore, a comparison of the sinusoidal channel to a straight one of the same total length of $L = 1.5$ cm, the same height of $h = 100$ μm , and the same average width $w = 250$ μm was carried out. The sinusoidal channel had a period of $P = 800$ μm and an amplitude of $A = 150$ μm . The results are presented in subsequent **Figure 2b-I/II**, which shows the CLSM side view and top view images. When using the 1 wt% PEG(900k)-solution for flow-focusing, in the straight channel the central stream width was 75 μm . This width remained constant over the entire length of the channel (1.5 cm). When using the sine channel, the central stream with an original width of 75 μm splits into four substreams with a separation that increases by about 25 μm for each sine wave until the limit of $h = 250$ μm due to the channel walls is reached. The increasing splitting and separation of the main stream at selected downstream positions is illustrated in **Figure 2b-I**. However, also the sine period and amplitude influence the separation of the substreams. Decreasing each the sine-period from $P = 800$ to 400 μm and increasing the amplitude from $A = 150$ to 300 μm lead to a considerably larger separation, e.g. from 200 to 350 μm at the 12th sine period for instance. Hence, strong extensional forces in y -direction, as in the sine expansion sections, lead to large stresses in this direction. In addition to fluid elasticity, shear-thinning generates a lift force towards the channel wall such that a migration in this direction is expected in regions of high extensional forces and shear rates. On a local scale this relates to flow-induced polymer stretching and alignment that is locally different across the particle or polymer network.

As cross-stream migration is an effective mechanism for particle separation, the possibility to separate colloids of different size in the splitting streams was also investigated. Therefore, a binary mixture of spherical silica-PNIPAM core-shell particles has been used: ones fluorescently labeled fluorescein with a diameter of $d = 600$ nm and the other ones rhodamine B labeled with a diameter of $d = 1000$ nm. In the CLSM images of **Figure 2c-I**, the 1000 nm rhodamine-labeled colloids are well separated from the central stream and visible in the four red-coloured substreams in the top- and front views of the last sine-period. The 600 nm fluorescein-labeled colloids remain in the central stream even at the end of the channel. The 600 nm ones could also be separated from wormlike micelles, see following **Figure 2c-II**.

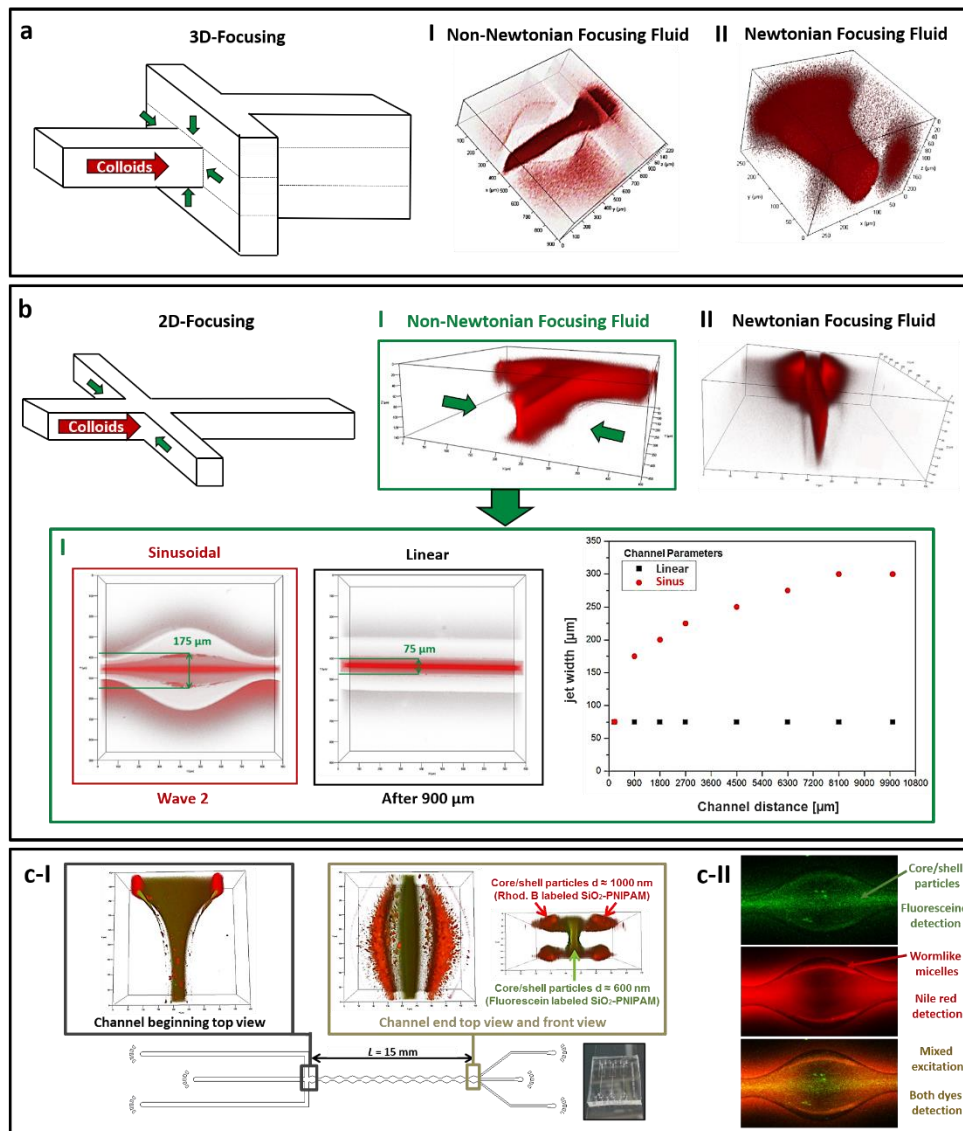


Figure 2 | (a) 3D CLSM images of a 3D sinusoidal microchannel for 3D-focusing where no emerging stream-splitting appears independent from using Newtonian (I) or non-Newtonian (II) focusing fluids. (b) 3D CLSM images of the subsequent stream-splitting effect by using 2D-focusing for a Nile red dyed 1 wt% wormlike micelles solution in combination with non-Newtonian (I) and without Newtonian (II) focusing fluids. (b-I) Top view images of the stream-splitting in a sinus-shaped and a linear channel as well as a comparative diagram regarding their sub-stream spreading distances. (c-I) Sine channel with three outlets for particle separation and 3D CLSM images at channel cross and end. The device is used for non-Newtonian 1 wt% PEG(900 k)-focusing of a binary mixture of spherical SiO₂-PNIPAM core-shell particles with a diameter of $d = 1000$ nm and 600 nm. At the channel end, the two particle sizes are separated into a green center stream with fluorescein (FITC) labeled 600 nm particles and into four red sub-streams at the channel edges with rhodamine B (Rhod B) labeled 1000 nm particles. (c-II) Tripartite CLSM image at the channel end of the separation of a mixture of spherical core-shell particles $d = 600$ nm (FITC) and anisotropic wormlike micelles $d = 20$ nm (Rhod B) with polydisperse lengths focused by the same PEG-solution. Here, two detected emission wavelengths are shown, FITC (top) and Rhod B (mid) but also the overlay from both (bottom).

Publication of Chapter 4.3

Strategies for the Selective Loading of Patchy Worm-Like Micelles with Functional Nanoparticles

In **chapter 4.3**, a microfluidic setup for the facilitated selective loading of anisotropic wormlike crystalline-core micelles (wCCMs) with nanoparticles (NPs) was employed in a continuous way by a well-controllable parameter screening. The advantage in microchannels is the presence of a laminar flow without turbulences and therefore a diffusion-controlled reaction process for the chemicals. Thus, an individually designed microfluidic device based on a home-made polytetrafluoroethylene (PTFE) chip with a double-focusing cross was fabricated. This microchip was made up of four side channels and finally connected to a glass capillary via the outlet channel, as illustrated in the CAD-design of **Figure 1a**. The double-focusing design is used to add the reactants for the nanoparticle synthesis separately to avoid an uncontrolled reaction beforehand and to get the formed NPs in contact with the micelles simultaneously just by *in situ* reduction, as schematically shown in **Figure 1b**. In a continuous flow, the amidated polystyrene-*block*-polyethylene-*block*-poly(methyl methacrylate) triblock terpolymers (SEMs) wCCM dispersion was pumped through the main channel at a flow rate of 2000 $\mu\text{L/h}$. At the same time, $\text{HAuCl}_4 \cdot 3\text{H}_2\text{O}$ (also 2000 $\mu\text{L/h}$) was added through the first two side channels and *L*-Selectride (1000 $\mu\text{L/h}$) was fed via the second two side channels. The resulting dispersion showed a purple color, which is characteristic for the formation of Au nanoparticles.

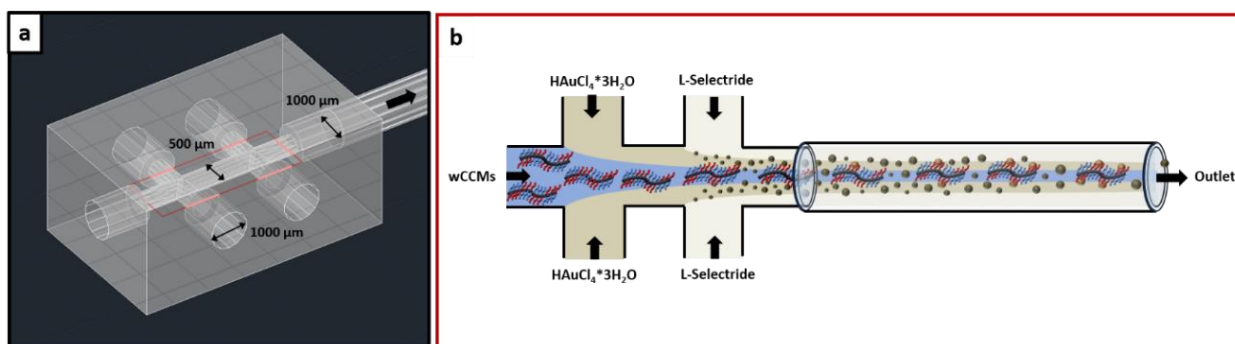


Figure 1 | (a) Detailed CAD design of the inner channel geometry of the employed microfluidic PTFE double focus chip that is connected to a glass capillary with an inner diameter of $D = 980 \mu\text{m}$. (b) Illustration of the fluid focusing of the different chemicals and the nanoparticle growth within the tailor-made microfluidic device.

The transmission electron microscopy (TEM) micrograph reveals that the PDMA patches of the wCCMs are homogeneously and densely loaded with Au NPs, which show an average diameter of $D = 4.3 \pm 1.4 \text{ nm}$ as visible in **Figure 2a** later on. Thus, the NP loading strategy by *in situ*

reduction could be successfully transferred to a continuous process that allows a more simplified parameter variation. The diameter of the observed Au NPs is comparable to the diameter of Au NPs synthesized by *in situ* batch reduction ($D = 4.7 \pm 1.2$ nm). The narrowly localized surface plasmon resonance (LSPR) at approximately $\lambda_{max} = 532$ nm and the weak absorbance at wavelengths of 700 nm and higher in the UV-Vis spectra of **Figure 2a** support the good stabilization and distribution of Au NPs by wCCMs. Compared to the Au NP hybrid wCCMs obtained by the *in situ* batch synthesis, the LSPR absorption of the Au NPs is significantly stronger indicating a higher loading density. This becomes more pronounced by comparing the specific PS absorbances at $\lambda = 250$ nm and at the LSPR in both samples. As the PS content in the wCCMs is constant and the Au NP size is comparable in the samples, the LSPR/PS absorbance ratio can be taken as a measure for the incorporated amount of Au NPs.

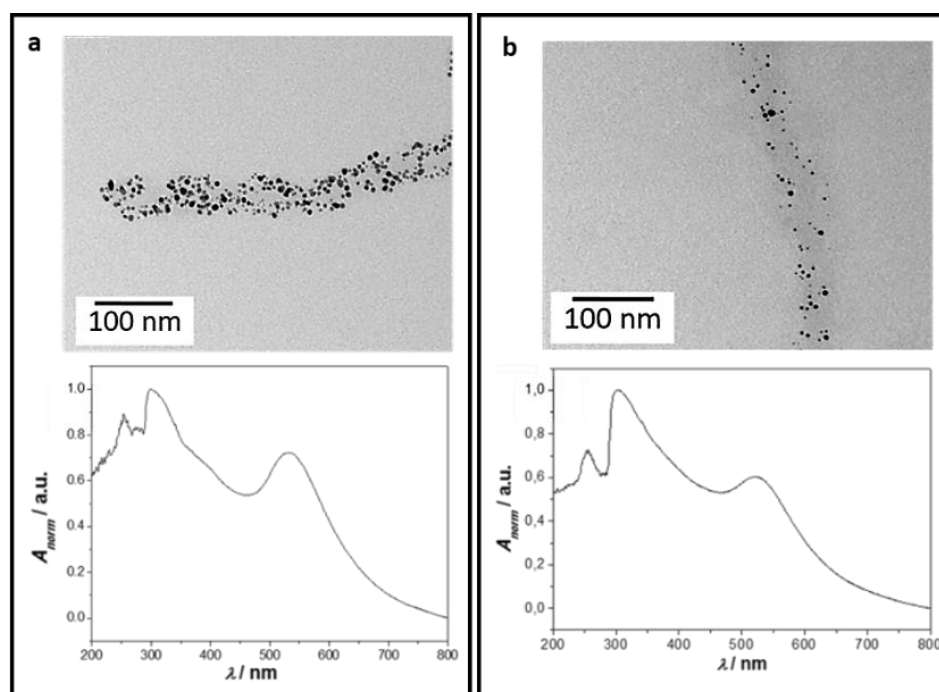


Figure 2 | TEM micrographs (top) and UV-Vis spectra (bottom) of SEDMA loaded wCCMs in a continuous microfluidic process at different flow rates: (a) wCCMs $\nu = 2000$ $\mu\text{L/h}$, $\text{HAuCl}_4 \cdot 3\text{H}_2\text{O}$ $\nu = 2000$ $\mu\text{L/h}$ and L-Selectride $\nu = 1000$ $\mu\text{L/h}$, (b) wCCMs $\nu = 2000$ $\mu\text{L/h}$, $\text{HAuCl}_4 \cdot 3\text{H}_2\text{O}$ $\nu = 1000$ $\mu\text{L/h}$ and L-Selectride $\nu = 1000$ $\mu\text{L/h}$.

The potential of this continuous loading method regarding the already mentioned advantage of a very simple parameter screening was analysed by varying the flow rates. By decreasing the flow rate of the $\text{HAuCl}_4 \cdot 3\text{H}_2\text{O}$ solution to 1000 $\mu\text{L/h}$, while keeping the other flow rates constant, the loading density of Au NPs within the SEDMA wCCMs is reduced. This finding is confirmed by TEM and UV-Vis spectroscopy, see **Figure 2b**. Thus, the lower concentration of Au salt in the total flow volume reduces the amount of growing Au NPs within the channel that results in a

lower loading density for the micelles. In addition, the decreased molar ratio of $\text{HAuCl}_4 \cdot 3\text{H}_2\text{O}$ to reducing agent (L-Selectride) led to vastly smaller Au NPs with a diameter of $D = 3.4 \pm 1.6$ nm, see **Figure 2b** compared to **Figure 2a**. These results confirm the adjustable parameters and conditions for varying the Au NP diameter and the wCCM loading density, simply by changing the flow rates.

3.2 Individual Contributions to Joint Publications

The results of this thesis presented in the scientific publications of **chapter 4**, were prepared in collaboration with fellow coworkers and scientists. My part is mostly centered on the application of microfluidics for the detailed investigation of anisotropic particles flowing in microchannels and -jets as well as the interpretation of the data. The contributions of each researcher involved to these publications are specified in greater detail below and the corresponding authors are indicated with an asterisk (*).

Chapter 4.1

This work is published in *Langmuir*, **2018**, *34* (16), 4843-4851, with the title:

„Parallel and Perpendicular Alignment of Anisotropic Particles in Free Liquid Microjets and Emerging Microdroplets“

by *Mathias Schlenk, Eddie Hofmann, Susanne Seibt, Sabine Rosenfeldt, Lukas Schrack, Markus Drechsler, Andre Rothkirch, Wiebke Ohm, Josef Breu, Stephan Gekle, and Stephan Förster**.

I performed all experiments and analyzed the data. Stephan Förster supervised the project and with him I wrote the manuscript and had scientific discussions. Eddie Hofmann helped with the 3D-printed sample holder and microparticle image velocimetry. Susanne Seibt synthesized and characterized the gold nanorods. Sabine Rosenfeld helped with the characterization of the layered silicates. Lukas Schrack and Stephan Gekle carried out the Lattice-Boltzmann and Potential-flow boundary-integral simulations. Josef Breu provided the layered silicates. Markus Drechsler carried out the colloid characterization via cryo-transmission electron microscopy. At the synchrotron beamline Wiebke Ohm and Andre Rothkirch provided technical support.

Chapter 4.2

This work is published in *Lab on a Chip*, **2018**, *18* (20), 3163-3171, with the title:

„Splitting and Separation of Colloidal Streams in Sinusoidal Microchannels“

by *Mathias Schlenk, Markus Drechsler, Matthias Karg, Walter Zimmermann, Martin Trebbin*, and Stephan Förster**.

I performed all experiments and analyzed the data. Stephan Förster was involved in the scientific discussions and corrected the manuscript. Martin Trebbin gave the idea for this project and supervised most of the parts. Matthias Karg provided the core-shell particles. Markus Drechsler run the colloid characterization via cryo-TEM. Walter Zimmermann supported with scientific discussions and corrections concerning the experiments and the manuscript.

Chapter 4.3

This work is published in *Nanoscale*, **2018**, *10* (38), 18257-18268, with the title:

„Strategies for the Selective Loading of Patchy Worm-Like Micelles with Functional Nanoparticles“

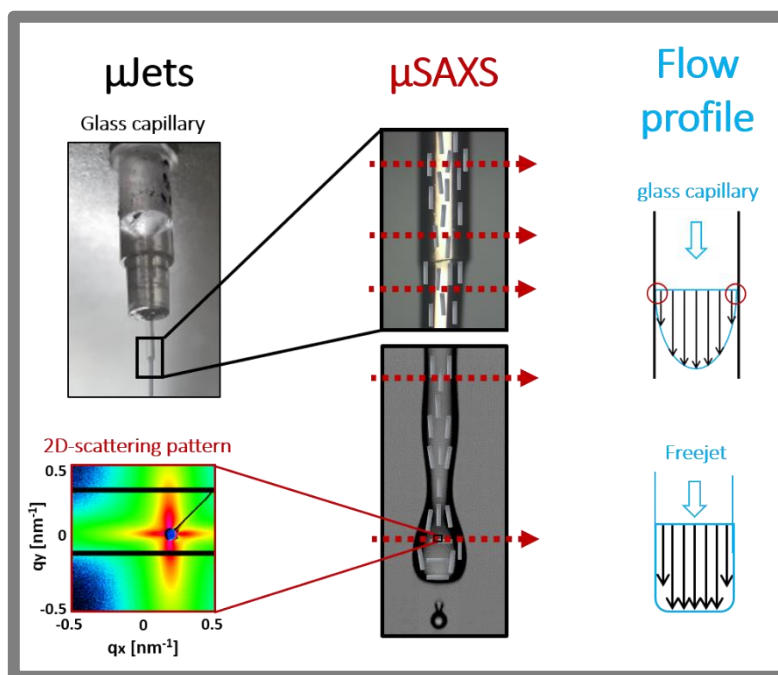
by Judith Schöbel, Christian Hils, Anne Weckwerth, Mathias Schlenk, Carina Bojer, Marc C. A. Stuart, Josef Breu, Stephan Förster, Andreas Greiner, Matthias Karg, and Holger Schmalz.*

I designed and fabricated the microfluidic device that I have built from a microfluidic PTFE chip with a double focusing mixing cross and a specifically modified glass capillary for the main outlet microchannel. Furthermore, I performed the microfluidic experiments for the continuous loading method and wrote a part of the manuscript. Judith Schöbel performed the main part of the experiments, including the functionalization of the triblock terpolymers, the self-assembly and the synthesis of hybrid materials. She was also involved in the microfluidic experiments, the co-precipitation method and wrote the manuscript together with Holger Schmalz who co-designed the experiment, supervised the project and corrected the manuscript. Christian Hils synthesized the second polymer and carried out the TEM measurements. Anne Weckwerth co-designed and conducted the main part of the experiments for the co-precipitation method. Carina Bojer synthesized the metal oxide nanoparticles and Josef Breu supervised this synthesis. Marc Stuart measured the TEM-EDX and corrected the TEM-EDX part of the paper. Stephan Förster supervised the microfluidic experiments. Andreas Greiner co-supervised the project. Matthias Karg supervised the co-precipitation experiments and corrected the manuscript.

4 Publications

The following **chapter 4** presents the three scientific publications on which this thesis is based.

4.1 Parallel and Perpendicular Alignment of Anisotropic Particles in Free Liquid Microjets and Emerging Microdroplets



Reproduced with permission from **M. Schlenk**, E. Hofmann, S. Seibt, S. Rosenfeldt, L. Schrack, M. Drechsler, A. Rothkirch, W. Ohm, J. Brey, S. Gekle, S. Förster published in *Langmuir*, **2018**, *34*, (16), 4843-4851. © **2018** American Chemical Society.

Abstract

Liquid microjets play a key role in fiber spinning, inkjet printing and coating processes. In all these applications, the liquid jets carry dispersed particles whose spatial and orientational distributions within the jet critically influence the properties of the fabricated structures. Despite its importance, there is currently no knowledge about the orientational distribution of particles within microjets and droplets. Here we demonstrate a microfluidic device that allows to determine the local particle distribution and orientation by X-ray scattering. Using this methodology, we discovered unexpected changes in the particle orientation upon exiting the nozzle to form a free jet, and upon jet break-up into droplets, causing an unusual biaxial particle

orientation. We show how flow and aspect ratio determine the flow orientation of anisotropic particles. Furthermore, we demonstrate that the observed phenomena are a general characteristic of anisotropic particles. Our findings greatly enhance our understanding of particle orientation in free jets and droplets and provide a rationale for controlling particle alignment in liquid jet-based fabrication methodologies.

Introduction

Advanced materials fabrication technologies such as fiber spinning,^{1,2} inkjet-printing,³ liquid-based coatings and microparticle fabrication,⁴⁻⁷ as well as vacuum liquid sample delivery for free electron lasers⁸ all involve the intermediate generation of liquid microjets. These liquid jets contain dispersed particles and microstructures such as polymers, fibers, pigments, microcrystals or proteins whose spatial and orientational distribution within the jets critically determine the properties of the resulting fibers, coatings, or surface patterns. It is thus essential to determine and control the particle distribution and orientation within liquid microjets. However, there is hardly any knowledge about the orientational distribution of particles within free liquid jets because this requires to develop challenging in-situ microstructure analysis methodology that so far has not been available.

Early pioneering experiments used synchrotron X-ray scattering to investigate fiber crystallization during fiber spinning.^{9,10} Although averaging over the whole fiber cross-section, it enabled to follow details of the crystallization process starting from the melt exiting the nozzle down-stream to the final solidified fiber. With microfocus X-ray beams at third-generation synchrotrons it has become possible to monitor silk fiber production¹¹ and even spray coating processes on micrometer length scales.^{4,12} However, a detailed study of particle orientations within a free microjet including its break-up into single droplets has so far not been possible.

Here we demonstrate that microfocus X-ray scattering combined with a microfluidic setup that continuously generates stable liquid microjets enables determining the spatial and orientational distribution of anisotropic particles within the jets all the way from inside the nozzle to the free micro-jet and eventually to the emerging droplets. We investigate wormlike micelles and nanoplatelets as examples of one- and two-dimensional anisotropic particles with large axial ratios, as well as gold nanorods as anisotropic particles with small axial ratios to provide general insights into the flow-induced orientation of anisotropic particles within free microjets and microdroplets. For all anisotropic particles we found characteristic changes in their uni-axial order when exiting the nozzle and within the microjets and, surprisingly, a biaxial orientational order in the droplets emerging from the liquid jet. Furthermore, we show how flow and aspect

ratio determine the flow-orientation of anisotropic particles. The obtained results provide a first fundamental understanding of particle alignment in free liquid micro-jets and micro-droplets and have important implications for liquid jet-based fiber, particle and coatings fabrication techniques.

Experimental

Synthesis of layered silicates nanoplatelets

Na_{0.5}-fluorohectorite with a nominal composition of [Na_{0.5}]inter[Mg_{2.5}Li_{0.5}]oct[Si₄]tetO₁₀F₂ (Na_{0.5}-Hec) was synthesized by melt synthesis in a gastight molybdenum crucible according to a procedure described in detail by Breu *et al.*²⁵ The material was annealed for 6 weeks at 1045°C to improve intracrystalline reactivity, charge homogeneity and phase purity as described elsewhere.²⁶ Afterwards Na_{0.5} hectorite in its one water layer hydrated form was generated by storing at 43% relative humidity in a desiccator for at least 3 days.

Synthesis of block copolymer wormlike micelles

Polyisoprene₁₁₀-*b*-ethylene oxide₁₉₈ (PI₁₁₀-*b*-PEO₁₉₈) with a weight-averaged molecular weight of $M_w = 16,000$ g/mol is synthesized by sequential living anionic polymerization, yielding an amphiphilic block copolymer with narrow polydispersity ($M_w/M_n = 1.02$). The detailed synthesis and characterization of PI₁₁₀-*b*-PEO₁₉₈ is described elsewhere.²⁷ The dry polymer is dissolved in Millipore-quality water with a resistivity of 17.9 MΩ/cm to a concentration of 20% w/w. By using an UltraTurrax T8 (IKA Werke GmbH) the solution was homogenized.

Synthesis of gold nanorods single crystals

Monodisperse gold nanorods were synthesized following a seeded growth method. For producing cetyltrimethylammonium bromide-capped (CTAB-capped) Au seeds and an equal amount of chloroauric acid (HAuCl₄, 0.5 x 10⁻³ m) and aqueous CTAB solution (0.2 x 10⁻³ m) were mixed and stirred for 10 min at room temperature. Next, a freshly prepared sodium borohydride solution (NaBH₄, 600 μL, 0.01 x 10⁻³ m) was added quickly under vigorous stirring. After 2 min, the stirring was stopped and the seeds were aged 1 h at room temperature. To finally produce the single crystal gold nanorods (AuNRs), an aqueous CTAB-solution (10 mL, 0.1 x 10⁻³ m) was mixed with HAuCl₄-solution (50 μL, 0.25 x 10⁻³ m) and silver nitrate (AgNO₃, 0.1 x 10⁻³ m) solution until all components are homogeneously dissolved. To reduce the gold acid, hydroquinone was added and the growth solution gently mixed until complete decoloration. Finally, the aged CTAB-capped Au seeds (400 μL) was added and mixed thoroughly. The Au nanorods were grown for 24 h at room temperature. The solution was purified by centrifugation

(10 min, 14000 rcf) before washing with water two times and redispersed in water (2 mL) to obtain a solution at a concentration of 4.0 mM Au, which for the nanorods corresponds to ~ 1012 nanorods/ml.

Sample preparation

The sodium hectorite solution with a concentration of 3% w/w was prepared in a closed vessel by addition of deionized water with Millipore-quality to solid Na_{0.5}-hectorite for osmotic swelling, and afterwards stored at ambient temperature. The 20% w/w stock solution of wormlike micelles was dissolved down to 10% w/w and filtered through a polytetrafluoroethylene filter with pore size of 5 μm before the microfluidic experiments could be carried out. Cryo-transmission electron microscopy (cryo-TEM) and transmission electron microscopy (TEM) images of the used concentrations of each sample are shown in electronic supplementary information (ESI Fig. S3).

Free liquid microjet

The free liquid microjet was generated using a micro glass capillary with an inner diameter of $D = 600 \mu\text{m}$ (wall thickness 50 μm) fixed in a home-built 3D-printed sample holder. By using a micro gear pump (mzr-7205G) a microfluidic recycling setup was constructed to continuously deliver liquid at high flow rates to generate the microjet. The whole setup is displayed in detail in electronic supplementary information (ESI Fig. S1).

Small-angle X-ray scattering

The microfocus small-angle X-ray scattering (SAXS) experiments were performed at the synchrotron beamline P03 at PETRAIII/DESY.²⁸ After collecting necessary background data of the pure solvent jet at different positions along the microjet (electronic supplementary information, ESI Fig. S8), the actual experiments with different type of anisotropic particles were carried out. Measurements across and along the glass capillary as well as the free jet and the droplet area are performed with a microfocused X-ray beam at wavelength of $\lambda = 0.1381 \text{ nm}$. The beam size was 20 x 20 μm² for fluorohectorite nanoplatelets as well as wormlike micelles and 105 x 63 μm² for the gold nanorods. The X ray scattering patterns were recorded with step sizes of 25 μm, respectively 100 μm behind the microjet using a Pilatus 300K, respectively 1M (Dectris Ltd.) whereby both detectors have a pixel size of 172 x 172 μm². The sample-detector distance was 5.1 m for the sodium hectorite nanoplatelets with an integration time of 10 s. The wormlike micelles were measured with the same detector distance but with an integration time of

20 s. The detector distance for the gold nanorods was shorter with 2.4 m and the integration time was 60 s.

Microparticle image velocimetry

Micro particle image velocimetry (μ PIV) was performed with a high-speed camera, a highly intense, focused light source and the open-source software package JPIV for flow profile analysis.²⁹ In combination with a long-distance microscope and a 10x magnification objective the setup allows exposure down to 1.5 μ s and frame rates up to 210,000 s^{-1} for the microfluidic experiments. These experiments allowed to determine the flow velocity profile within the glass capillary and free jet as well as the droplet area to observe changes between these different microjet regions. For more details, we refer to the electronic supplementary information.

Lattice-Boltzmann simulations for platelet reorientation during jet ejection

We conducted three-dimensional lattice-Boltzmann simulations using the open source software package ESPResSo.³⁰⁻³³ The grid size was 24 x 24 x 210 with a capillary/jet radius of 10 grid cells. Here, we were interested in modeling the re-orientation of platelets right after the exit of the capillary where the jet shape is to a very good approximation cylindrical with the same radius as the capillary. We therefore considered in our simulations a long undeformable cylinder whose left half models the capillary (no-slip boundary conditions are applied at the cylinder wall) while the right half models the free jet by imposing free-slip boundary conditions, see **Fig. 2a**. Thermal fluctuations were included into the Lattice-Boltzmann fluid.

Platelets were modeled by a grid of five vertices, each of which was frictionally coupled to the fluid.³⁴ The shape of the platelets was fixed by stiff springs to enforce (almost) constant vertex distances and angles to maintain a flat shape. In order to avoid artifacts from periodic boundary conditions, platelets were fed into the channel on the left and removed on the right end. Here, the platelet configuration at the inlet was not purely random. Instead, before the actual microjet simulation was run, we first conducted a simulation in a fully no-slip channel at the same flow rate and platelet concentration, but with periodic boundary conditions. Platelets taken from this „feeding simulation“ firstly received the orientation parameter S . They were then properly aligned and obeyed the correct radial distribution when they were fed into the microjet simulation. This platelet orientation was then quantified by the orientation parameter

$$S = \langle (3\cos^2\varphi - 1)/2 \rangle \quad (1)$$

where φ is the angle between the normal vector of the platelet surface and the flow direction. In this definition, $S = 1$ signals complete alignment in flow direction, $S=0$ corresponds to random

isotropic orientation, and $S = -0.5$ to complete alignment perpendicular to the flow direction. The calculated orientation parameters S of the ensuing microjet simulations are shown in the electronic supplementary information (ESI Fig. S9-S11) for all three particle systems.

Potential-flow boundary-integral simulations

In order to predict the shape evolution and flow field within the microjet, we required a method which is able to track the time-dependent free surface shape of the jet. We thus conducted boundary-integral simulations (**Fig. 2**) based on potential flow assuming a purely inviscid fluid. Details are given in literature.³⁴⁻³⁸ The goal of these simulations was to obtain an understanding of the flow field in the jet at droplet breakup which is why the presence of the anisotropic particles was excluded.

Results and discussion

In order to continuously produce stable liquid micro-jets that can be investigated by microfocus synchrotron X-ray scattering we developed a setup consisting of a glass capillary to generate the micro-jets and a micro-gear pump to recycle the liquid back to the glass capillary. We used vertically aligned capillaries with 300 μm inner radius and 300 μm orifice radius to generate liquid jets at a flow rate of $Q = 750$ mL/h, resulting in a jet velocity of $v \sim 1$ m/s. The micro-jet is stable over a length of 15 mm, until it breaks up into micro-droplets due to Rayleigh instability. The local orientational distribution of the dispersed particles within the micro-jet and the micro-droplets is determined by scanning with a 20 x 20 μm X-ray beam across a raster of 7-20 horizontal and 5 vertical positions from the capillary downstream the nozzle, free jet and the droplets.

Nanoplatelets

We first investigated solutions of hectorite nanoplatelets as models of two-dimensional anisotropic particles at a concentration of 3 wt%, which is sufficiently high to have a good signal-to-noise ratio, but still having low enough viscosity to continuously pump the solutions through the microfluidic device. The hectorite platelets are fully exfoliated, have a thickness of 1.0 nm and a lateral dimension of 20 μm , and thus have very large axial ratios of $2 \cdot 10^4$.¹³⁻¹⁵ Details of the synthesis, structure, and sample preparation are provided in the electronic supplementary information. For the large axial ratio hectorite nanoplatelets, we expected pronounced orientation effects upon formation of the micro-jets and micro-droplets.

To determine changes in the platelet orientation upon transition from the capillary into the free micro-jet, and upon the subsequent transition from the free micro-jet into the micro-droplets, we

performed horizontal scans at five downstream vertical positions (**Fig. 1a**): far within the capillary (**I**), 100 μm upstream and downstream the orifice (**II**, **III**), in the fully developed micro-jet (**IV**), and in the micro-droplet region (**V**).

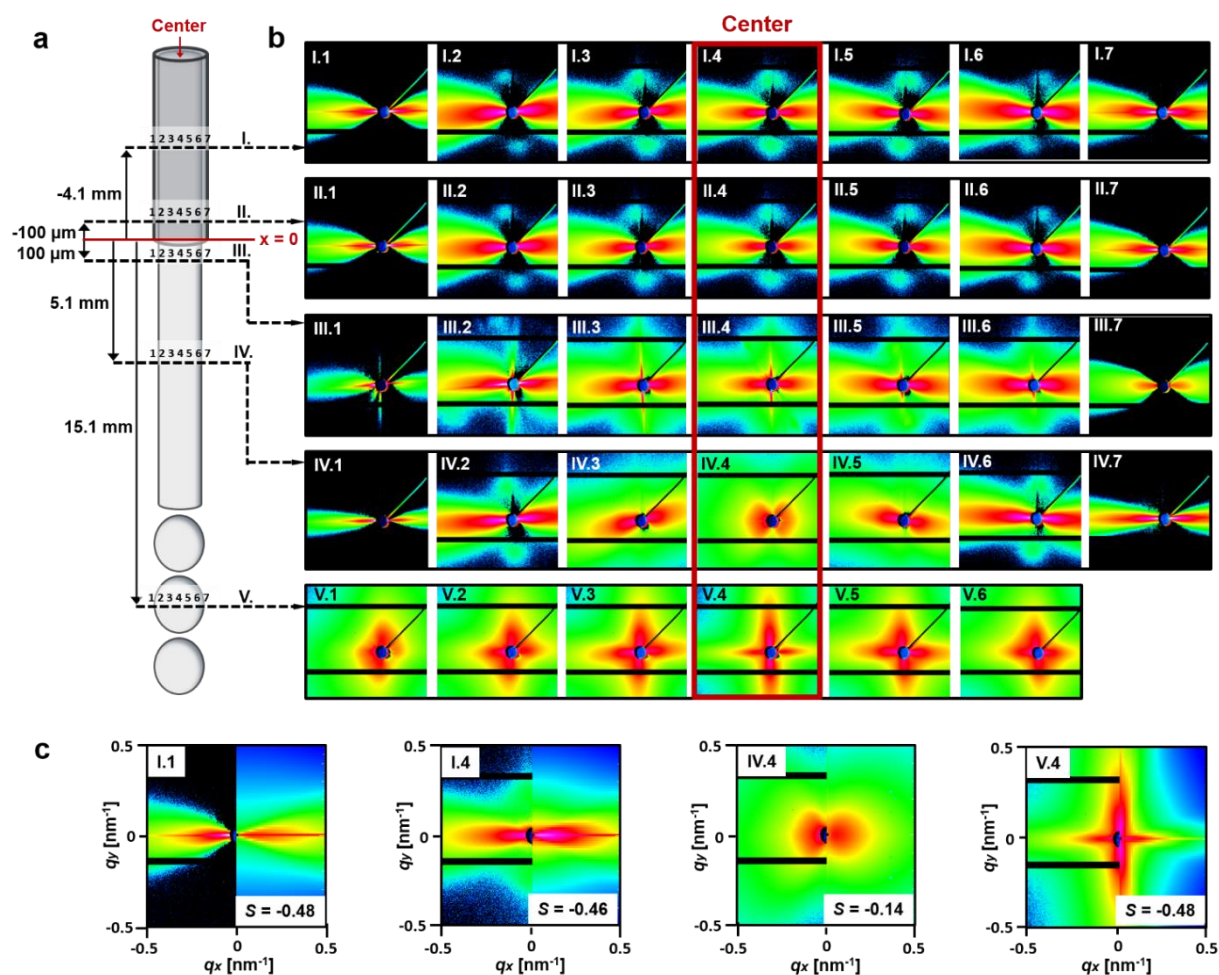


Figure 1. Scheme of the microjet and the emerging microdroplets with dispersed nanoplatelets together with the 2D-SAXS patterns measured within the jet and the droplets. (a) Scheme of the capillary, the liquid micro-jet and the micro-droplet region with the scan lines I–V where the 2D-SAXS-patterns were measured. (b) Set of scattering patterns measured for the hectorite nanoplatelets at the specified scan positions. We observe a strong anisotropy resulting from the flow-alignment of the nanoplatelets, with an unexpected biaxial orientation of the nanoplatelets in the microdroplet region (c) Comparison of experimental and calculated scattering patterns to determine the orientational order parameter of the nanoplatelets. The q -range is $-0.5 - 0.5 \text{ nm}^{-1}$.

Fig. 1b displays the small-angle X-ray scattering (SAXS) patterns for the hectorite nanoplatelets measured at different scan positions from the capillary into the free micro-jet and further downstream into the micro-droplet region. Reference scans outside the liquid and at the

air/liquid-interface are provided in the electronic supplementary information (ESI Fig. S9-S11). All scattering patterns in **Fig. 1b** show a strong anisotropy indicating pronounced shear-alignment of the nanoplatelets.

We first inspect the upper row of the scattering patterns shown in **Fig. 1b**, which was measured in the liquid stream within the glass capillary (**position I**). The first scattering pattern (**I.1**) was measured close to the left capillary inner wall. The scattering pattern is characterized by a sharp equatorial ∞ -shaped high intensity region, indicated in red. The next two scattering patterns (**I.2**, **I.3**) were measured towards the center of the capillary. They also show a ∞ -shaped high-intensity region, which is, however, inclined by an angle of $+6^\circ$ with respect to the horizontal axis. In the center of the capillary (**I.4**) the ∞ -shaped high intensity region has a perfect horizontal alignment with 0° inclination angle. The scattering patterns measured at subsequent scan positions at the right-hand side of the capillary are found to be mirror images of the left-hand side scattering patterns. This is the case for all subsequent downstream scans. In the following discussion, we thus focus only on the scattering patterns measured on the left-hand side of the capillary, micro-jet, and micro-droplets.

The observed characteristic ∞ -shaped high intensity regions result from the formfactor of the nanoplatelets which are strongly aligned in flow-direction, co-planar to the capillary wall. To quantitatively determine the orientational distribution of the nanoplatelets we calculated scattering patterns using different types of orientational distribution functions. We modelled the hectorite nanoplatelets as disks with an average thickness of 1.0 nm and an average radius of 10 μm to analytically calculate their formfactor. We obtained best agreement between calculated and measured scattering patterns when using a Gaussian orientational distribution function, for which the orientational order parameter was calculated. Details of the calculations are given in the electronic supplementary information and further in literature.^{16,17} In **Fig. 1c**, the lowest row of scattering patterns shows measured (left-half) and calculated (right-half) scattering patterns for selected characteristic scan-positions together with the orientational order parameter which is defined in Equation (16) of electronic supplementary information and gave the best agreement. We observe very good agreement between measured and calculated scattering patterns. Here, the orientation parameters are determined in the capillary and all have values of $S = -0.46$ - -0.48 , with slightly less negative values towards the center of the capillary. In this context, a value of $S = -0.5$ would declare a complete alignment in flow direction, whereas $S = 0$ corresponds to a random isotropic orientation. Thus, the result indicates an alignment of the nanoplatelets in flow-direction, with their basal plane normal vector being perpendicular to the flow direction.

The slight inclination of the scattering patterns observed towards the center of the capillary (**positions I.2, I.3**) indicates a small tilt of the flowing nanoplatelets towards the center of the capillary. The value of the inclination angle is a result of the competing effects of flow-orientation preferring the nanoplatelets to orient parallel to the streamlines, corresponding to a 0° inclination angle, and rotational diffusion allowing the particles to explore a larger angular range, resulting in larger inclination angles. For the hectorite nanoplatelets we observe rather small inclination angles indicating that shear orientation dominates over rotational diffusion. This implies that the ratio of shear rates to the rotational diffusion coefficients is much larger than unity, i.e. $\dot{\gamma} / D_{rot} \gg 1$. The value of this ratio can be estimated from the experimental flow rate and the capillary diameter, from which the wall shear rate $\dot{\gamma} = 4Q / (\pi R^3)$ can be estimated to be $\dot{\gamma} \sim 10^4 \text{ s}^{-1}$, and from the platelet radius R_D , from which a rotational diffusion coefficient¹⁸ $D_{rot} = 3kT/(32\pi R_D^3) \sim 10^{-4} \text{ s}^{-1}$ can be estimated. Thus, the condition $\dot{\gamma} / D_{rot} \sim 10^7 \gg 1$ is well fulfilled. The effects due to rotational diffusion, possibly enhanced by inter-platelet collisions, are slightly more pronounced towards the center of the capillary, where the shear rates are smaller, leading to slightly larger inclination angles and slightly reduced orientational order.

As shown by the scattering patterns in the second row in **Fig. 1b (II.1 – II.5)**, which were measured in the capillary 100 μm upstream the orifice, the observed local orientational distribution of the nanoplatelets is stable and stationary across the capillary, even until just before the capillary exit.

The third row of scattering patterns (**III.1 – III.5**) was measured in the free micro jet just 100 μm downstream after exiting the capillary orifice. As the micro-jet has a slightly smaller diameter than the orifice, the X ray beam at the first scan position (**III.1**) just touches the surface of the liquid jet. This results in a thin horizontal streak with a slight inclination due to the surface orientation of the narrowing jet, together with a weak ∞ -shaped scattering pattern from the oriented nanoplatelets. The sharp vertical streak is caused by the micro-X-ray beam which slightly touches the end of the capillary. At all scan positions across the free micro-jet we observe scattering patterns with nearly zero inclination angle indicating nearly vertical orientation of the nanoplatelets in flow direction. A slight broadening of the ∞ -shaped high-intensity region in the center of the micro jet indicates a minor loss of orientational order.

A slightly decreasing inclination angle and a minor loss of orientational order are the two characteristic features that we observe when the liquid stream exits the orifice and forms a free liquid micro jet. They accompany a fundamental change of the flow velocity field when the boundary condition at the liquid surface changes from no-slip condition at the glass wall of the capillary to free slip condition at the liquid/air-interface of the free jet. To obtain insights into

how this transition relates to the observed changes in the nanoplatelet orientation, we performed lattice-Boltzmann simulations. In the simulations the transition from the capillary into the free micro-jet is modeled by a Newtonian liquid stream flowing through a cylindrical channel, where halfway down the channel the boundary conditions change from no-slip to free-slip (**Fig. 2a**). The liquid contains dispersed platelets whose orientational distribution can be followed and analyzed along the channel. Details of the simulations are described in the Methods Section.

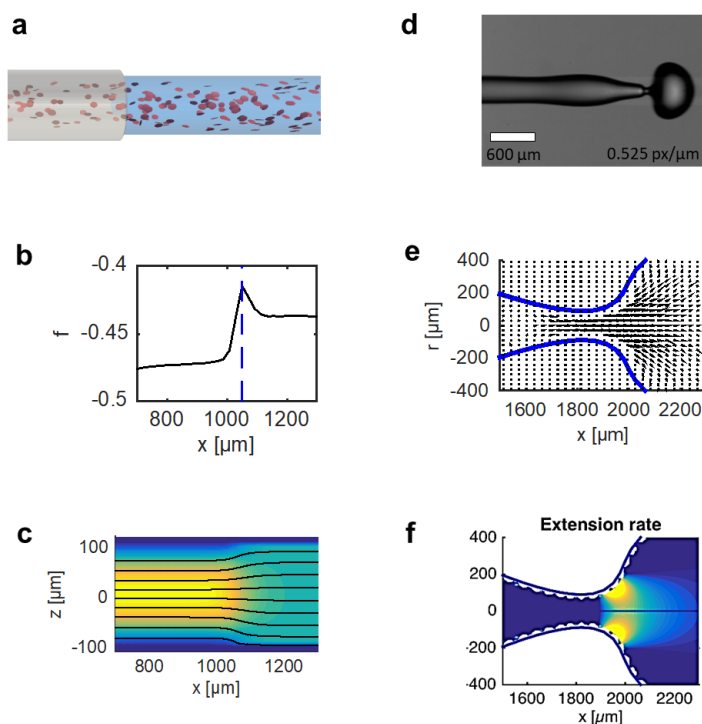


Figure 2. Simulation of the platelet orientation upon micro-jet formation and break-up into microdroplets. (a) Snapshot of a Lattice-Boltzmann simulation to determine changes of the platelet reorientation from the nozzle exit into the free jet. (b) Simulated development of the orientational order parameter from the capillary through the nozzle into the free jet with a slight loss of orientational order at the exit, marked by the dashed blue line. (c) Simulated velocity profile where the colors indicate the axial velocity and black lines represent stream lines. (d) Shape of the micro-jet just before droplet breakup imaged with a high-speed camera and (e) simulated with the potential-flow boundary-integral code. The velocity field in the frame of reference moving with the jet features an outward radial flow right after the narrow constriction before entering the droplet. This extensional flow with a high extension rate (f) causes reorientation of the platelets upon entering the droplet and leads to the biaxial orientation observed in the X-ray scattering patterns (Fig. 1b, row V).

Fig. 2b shows the evolution of the orientational order parameter downstream the channel. Within the capillary the platelets are well oriented in flow direction with a calculated orientational order

parameter $S = 0.48$ in good agreement with the experiments. We observe in the simulations that directly after the exit, when changing from no slip to free slip conditions, the order parameter slightly drops to a value of $S = 0.41$ until the nanoplatelets realign to reach a value of $S = 0.43$. The degree of order in the simulations is higher compared to the experimentally determined values, which is due to the internal flexibility of the hectorite nanoplatelets. Yet, the simulations reveal that the underlying reason for the characteristic change of the orientational distribution is the change of the velocity field, which varies from a parabolic profile characteristic for Poiseuille flow in the capillary to a homogeneous plug flow profile in the free microjet.¹⁹ This change in the flow velocity profile, illustrated in **Fig. 2c**, involves an acceleration of fluid volume elements in the outer jet region and a deceleration in the center of the micro-jet. To satisfy mass conservation fluid needs to flow radially from the inner to the outer region of the microjet in a transition zone immediately after the capillary exit which carries along platelets and leads to the observed loss of orientational order. The reestablishment of a purely axial flow after the transition zone then partly reorients the platelets parallel to the streamlines thereby leading to near zero inclination angles. The observed characteristic changes of the nanoplatelet orientation in the zone directly after the capillary exit can thus be well rationalized in terms of the changing surface boundary conditions and changing velocity profiles.

The fourth horizontal scan (**IV**) transects the free fully developed micro-jet at $x = 5.1$ mm downstream the capillary exit. At the first scan position inside the free jet (**IV.2**) we observe a narrow ∞ -shaped high intensity region indicating still high orientational order with only a slight inclination of $+5^\circ$ indicating the onset of rotational diffusion and inter-platelet collision due to the reduced surface shear rates. Both, the loss of orientational order and the increase of the inclination angle, become more significant towards the center of the free jet. The shape of the high intensity region changes from a ∞ -shape to a broad “butterfly”-shape in the center (**IV.4**), corresponding to a reduction of the orientation order parameter from $S = 0.46$ to $S = 0.14$. Due to symmetry the inclination angle in the center is zero. Off-center inclination angles, e.g. at position (**IV.3**), have values of 15° , i.e. significantly higher compared to the liquid stream in the capillary. The loss of orientational order and the increase of the inclination angle indicate that shear rates within the liquid jet, particularly in the center, have strongly decreased. Ideally, for the free micro-jet a homogeneous plug-flow profile with vanishing shear rates would be expected such that orientational order is significantly reduced by rotational diffusion.

To verify the development of a plug-flow profile we carried out microparticle image velocimetry (μ PIV) in the free micro-jet as shown in detail in the electronic supplementary information. It is experimentally impossible to determine the flow velocity profile at the outer edge of the free jet

because the jet acts as a cylindrical lens that refracts light such that the outer edge is completely dark. Yet it is possible to determine the flow profile within the micro-jet, where within experimental error we indeed observe a plug-flow profile, leading to a consistent description of the flow velocity profile and the experimentally observed changes in the nanoplatelet orientation. The last row of scattering patterns (**V**) was measured at position $x = 15.1$ mm, which is in the region where the free micro jet has broken-up into a train of micro-droplets due to Rayleigh instability.^{20,21} The micro-droplets have larger diameters than the free jet such that already at position **V.1** we probe the orientational distribution of nanoplatelets within the droplet. **Fig. 2d** shows a snapshot taken with a high-speed camera at $50.000 \text{ frames s}^{-1}$ to illustrate the development of the micro-droplet from the micro-jet. The droplet breakup occurs in a narrow region at $11 < x < 13$ mm, such that at position **V** we already probe the microdroplet region.

At all **V** scan positions the scattering patterns have an un-usual appearance characterized by a cross-shaped high intensity region. It originates from two mutually perpendicular ∞ -shaped high intensity regions, one along the horizontal axis, the other along the vertical axis. This indicates an unexpected biaxial orientational distribution of the nanoplatelets, which our scanning experiments reveal for the first time. From the scattering intensities integrated over the meridian and the equation we deduce that approximately 20% of the platelets are oriented parallel to the flow direction, with the platelet normal in the equatorial plane, and 80% perpendicular to the flow direction with the platelet normal parallel to the flow direction. In the center of the droplet the fraction of unexpectedly perpendicularly oriented nanoplatelets is significantly larger compared to the parallel oriented nanoplatelets. Compared to the upstream position in the free micro jet, the high-intensity regions are sharper, promoting increased orientational order along each of the two platelet orientation axes.

To understand the evolution of the biaxial orientation we simulated the flow profile in the liquid jet during droplet breakup. Since this requires to explicitly consider the dynamics of the free micro-jet surface, including the thinning of the neck and the final droplet pinch-off, we employed boundary-integral simulations as described in the Methods Section. As shown in **Fig. 2d/e** the simulations of the droplet break-up are in good agreement with the experimentally determined break-up. The experiments and simulations were performed for the same conditions, i.e. a micro-jet radius of $300 \mu\text{m}$ and a flow rate of $Q = 750 \text{ mL/h}$. While these simulations do not include platelet dynamics they nevertheless allow us to get a detailed insight into the local flow fields as shown in **Fig. 2e**. After passing the thin neck and entering into the droplet, the fluid enters an expansion zone with high extension rates (**Fig. 2f**) and significant radial outward flow. Within the high extensional rate zone, the platelets are oriented perpendicular to the flow direction. After

formation of the final droplet shape the extensional rates become zero and the platelets remain in their biaxial orientation. This is analogous to the recently observed perpendicular orientation of wormlike micelles in the extensional section of tapered microchannels which was similarly caused by high extensional rates perpendicular to the flow direction.²²

Thus, our scanning synchrotron X-ray experiments on free liquid micro-jets provide first insights into the orientation of dispersed platelet-shaped particles upon transition from a capillary into a free jet, and upon the subsequent transition into micro-droplets. The changing velocity fields cause characteristic reorientation effects leading to significant and unexpected changes in the platelet orientation, such as the biaxial orientation observed in the micro-droplets.

Wormlike micelles

It is interesting whether the orientational changes observed for nanoplatelets, which are examples of two-dimensional anisotropic objects, are a general characteristic for all anisotropic particles. We therefore also investigated the flow orientation of wormlike micelles, which are examples of one-dimensional anisotropic objects. We used wormlike micelles formed by the self-assembly of poly(isoprene-*b*-ethylene oxide) (PI-*b*-PEO) block copolymers in water. The micelles have a diameter of 20 nm and contour lengths of several micrometers as shown by the cryo-TEM images in the electronic supplementary information (**ESI Fig. S3b**). We used a concentration of $c = 10\%$ w/w in water where the scattering intensity is sufficiently high to quantitatively determine the orientational distribution from the measured scattering patterns. The capillary, flow rates and scanning positions were the same as for the hectorite nanoplatelets.

The first row of scattering patterns (**Fig. 3, I**) was measured across the capillary. The scattering patterns are characterized by two pronounced first order and weak second order Bragg peaks located on the equator. This indicates that the wormlike micelles are oriented in flow-direction with strong positional and orientational correlations. From the position of the Bragg-peaks one can calculate an average distance between adjacent micelles of $d = 42$ nm.

The first scattering pattern (**Fig. 3, I.1**) results from worm-like micelles that are located directly next to the capillary wall. We observe two sickle-shaped high-intensity regions with an inclination angle of 12° with respect to the equator. At subsequent scan positions towards the center of the capillary (**I.2-I.4**), the Bragg-peaks have lower intensity, a more circular shape, a smaller inclination angle, and are located on a weak Debye-Scherrer ring. This indicates that at all scan positions in the capillary the wormlike micelles are oriented in flow direction, with a significant inclination only next to the capillary wall. The weak Debye-Scherrer ring indicates the presence of a small fraction of isotropically oriented wormlike micelles. At the capillary wall, the characteristic sickle-shaped Bragg-peaks, the higher scattering intensity and the absence of a

Debye-Scherrer ring are indications of a dense, nematic phase forming a lubrication layer at the capillary wall as a result of shear-banding.²³ The small inclination angles in the center of the liquid stream indicate that rotational diffusion is very slow due to the retarded cooperative motion of the wormlike micelles.²⁴

The scattering patterns shown in the second row (II) are measured directly (100 μm) upstream the capillary exit and are very similar to the upstream position, indicating stable stationary flow conditions in the capillary. With the exception of the occurrence of the nematic phase close to the capillary wall, the observed orientational distribution for the wormlike micelles in the capillary is very similar to the one observed for the nanoplatelets.

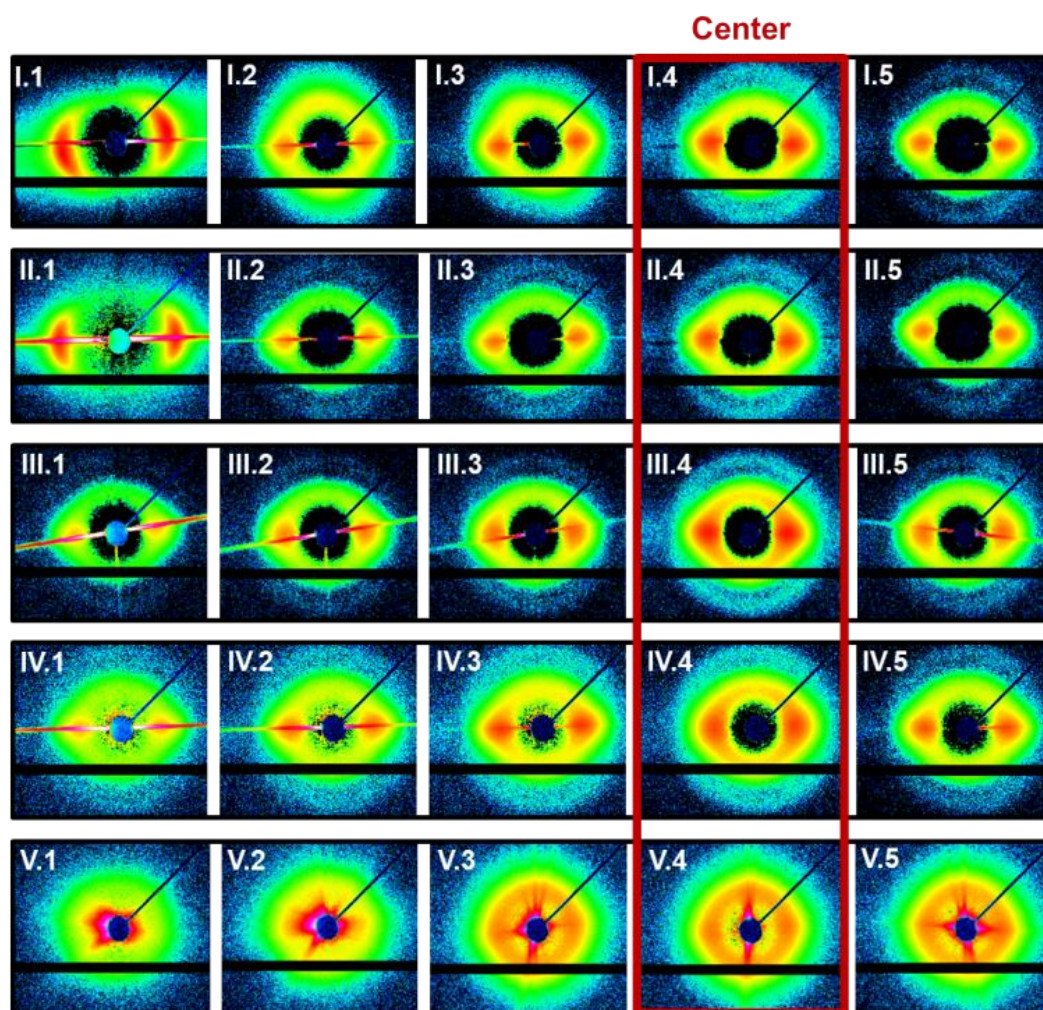


Figure 3. Set of 2D-SAXS-patterns measured within the microjet and the emerging microdroplets containing dispersed wormlike micelles. Also, for the wormlike micelles we observe pronounced flow-alignment with equatorial Bragg-peaks indicating strong intermicellar correlations. The biaxial orientation of the micelles in the microdroplet region can be observed as slight intensity modulations on the Debye-Scherrer rings (V). The q -range is $-0.5 - 0.5 \text{ nm}^{-1}$.

The third row of scattering patterns (**III**) was measured just 100 μm downstream the capillary exit in the zone of the developing free micro-jet. At the first scan position (**III.1**) the X-ray beam just touches the micro-jet resulting in a thin streak, yet the Bragg-peaks from the oriented cylindrical micelles are already apparent. At the subsequent scan positions (**III.2–III.5**) we observe Bragg peaks with increased azimuthal widths indicating some loss of orientational order, particularly towards the center of the free microjet. The inclination angles are very small, indicating a near vertical alignment of the cylindrical micelles in flow direction. The two effects, (1) the loss of orientational order towards the center of the micro-jet, and (2) the near-zero inclination angles are the same as observed for the nanoplatelets. This indicates that the transition from no-slip to free-slip boundary conditions and the related change of the flow-profile towards plug flow are characteristic for both the nanoplatelets and the wormlike micelles. The subsequent scans shown in the fourth row (**IV**) were measured in the fully developed micro-jet 5.1 mm after exiting the capillary. Compared to the previous scan (**III**) taken directly after exiting the capillary, we observe only a very minor reduction of the orientational order and still near perfect orientation in the flow direction. We conclude that effects of rotational diffusion are negligibly small for the wormlike micelles such that even at strongly reduced shear rates in the center of the free micro-jet the alignment in flow direction well persists. Compared to the nanoplatelets, which were measured in more dilute solutions and where effects of rotational diffusion are more noticeable, the wormlike micelles were measured at higher concentrations where positional and orientational correlations, as apparent from the Bragg peaks, reduce local rotational mobility.

The last row shows the scattering patterns measured in the droplet region (**V**). The signature of the particle orientation in the scattering patterns is more difficult to recognize due to streaks originating from X-ray reflections from the droplet surface. Yet, from the scan position in the droplet center (**V.4**) we observe scattering patterns with higher intensity regions on the equator and on the meridian, located on top of a pronounced Debye-Scherrer ring. This indicates a significant loss of orientational order, but with a signature of a biaxial distribution that was also observed for the nanoplatelets.

We thus observe the same characteristic changes of the orientational distribution during transitions from the capillary to the free micro-jet and subsequently from the micro-jet to the micro-droplets for both the nanoplatelets and the wormlike micelles. Observed differences such as the formation of the nematic lubrication layer and the persistence of a high orientational order in the free micro-jet are related to the stronger positional and orientational correlations of the higher concentrated wormlike micelles.

Gold nanorods

It is finally interesting, whether the observed reorientation behavior generally applies not only to anisotropic particles with large axial ratios, such as hectorite nanoplatelets and wormlike micelles, but also to anisotropic particles with much smaller axial ratios. For the latter case we expected rotational diffusion to significantly reduce shear-orientation effects but hoped that some of the observed characteristic re-orientation effects might still be observable.

Thus, we also investigated the shear-orientation of gold nanorods. We synthesized monodisperse gold nanorods with an average diameter of $D = 26$ nm and an average length of $L = 71$ nm, resulting in an axial ratio of only ~ 3 . The synthesis and the corresponding TEM images are provided in the electronic supplementary information (ESI Fig. S3c). The set of scattering patterns were measured at the same positions as for the nanoplatelets and the worm-like micelles and are shown in **Fig. 4**.

For the gold nanorods the measured scattering patterns at all scan positions are characterized by concentric rings resulting from cross-sectional form factor oscillations. High-intensity regions along the azimuth of the rings would indicate a preferred orientation. Row **(I)** shows the scattering patterns measured within the capillary. The first scattering pattern **(I.1)** was obtained directly next to the inner capillary wall. We indeed observe two increased scattering intensity regions on the formfactor rings, located on a line with an inclination angle of 25° . This indicates an alignment of the nanorods in flow direction with a quite large mean inclination angle of 25° . At all other scan positions, we observe isotropic scattering patterns indicating a completely isotropic orientational distribution resulting from the fast-rotational diffusion of the gold nanorods. The rotational diffusion coefficient for the nanorods can be estimated to be¹⁸ $D_{rot} = 3kT(\ln(2L/d)-\gamma)/\pi\eta L^3 \sim 10^5$ s⁻¹. It is thus larger than the shear rates, except at the capillary wall where the shear rate is at least of comparable magnitude, leading to the observed shear alignment with a quite large inclination angle.

When inspecting the set of scattering patterns measured at position **(II)**, close to the capillary exit, the slightly preferred orientation in flow-direction with a large inclination angle can be better recognized, not only at position **II.1**, but also at position **II.2**. As expected, the degree of orientational order of the short nanorods is generally much lower compared to the extended nanoplatelets and wormlike micelles, and nearly isotropic in the center of the capillary.

For the gold nanorods the measured scattering patterns at all scan positions are characterized by concentric rings resulting from cross-sectional form factor oscillations. High-intensity regions along the azimuth of the rings would indicate a preferred orientation. Row **(I)** shows the scattering patterns measured within the capillary. The first scattering pattern **(I.1)** was obtained

directly next to the inner capillary wall. We indeed observe two increased scattering intensity regions on the formfactor rings, located on a line with an inclination angle of 25° . This indicates an alignment of the nanorods in flow direction with a quite large mean inclination angle of 25° . At all other scan positions, we observe isotropic scattering patterns indicating a completely isotropic orientational distribution resulting from the fast-rotational diffusion of the gold nanorods. The rotational diffusion coefficient for the nanorods can be estimated to be¹⁸ $D_{rot} = 3kT(\ln(2L/d)-\gamma)/\pi\eta L^3 \sim 10^5 \text{ s}^{-1}$. It is thus larger than the shear rates, except at the capillary wall where the shear rate is at least of comparable magnitude, leading to the observed shear alignment with a quite large inclination angle.

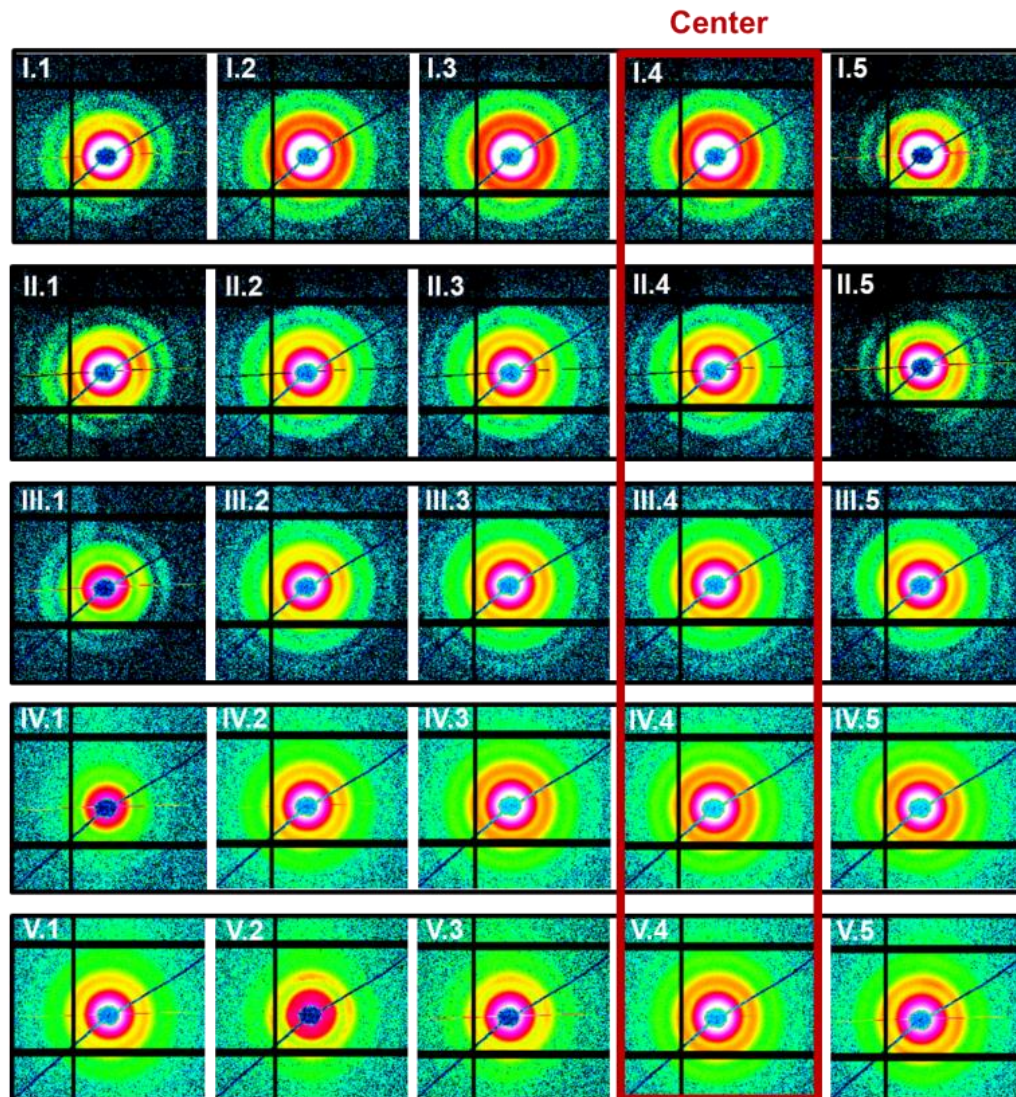


Figure 4. Set of 2D-SAXS-patterns measured within the microjet and the emerging microdroplets containing narrow disperse gold nanorods. The scattering patterns feature concentric rings due to the cross-sectional formfactor. Due to the small axial ratio the nanorods are flow-aligned only close to the capillary walls, but even for the short nanorods the biaxial alignment in the micro-droplet region is clearly visible indicating strong extensional forces during droplet-breakup. The q -range is $-1 - 1 \text{ nm}^{-1}$.

When inspecting the set of scattering patterns measured at position (II), close to the capillary exit, the slightly preferred orientation in flow-direction with a large inclination angle can be better recognized, not only at position II.1, but also at position II.2. As expected, the degree of orientational order of the short nanorods is generally much lower compared to the extended nanoplatelets and wormlike micelles, and nearly isotropic in the center of the capillary.

The first scan across the free microjet (III.1-III.5) just 100 μm downstream the capillary exit shows only slight changes of the orientational order. At the jet edge (III.1) the flow-orientation is still well observable, whereas at the center the orientational distribution is nearly isotropic. Further downstream in the fully developed microjet (IV) the orientational order is completely lost across the micro-jet as indicated by the fully isotropic concentric formfactor oscillations and scattering patterns.

The last row (V) shows the scattering patterns measured after the droplet breakup region. The off-center scattering patterns clearly show the biaxial distribution with high-intensity regions on the equator and meridian of the concentric formfactor oscillations. It is only in the center of the micro-jet that the scattering pattern is still isotropic. This shows that the extensional rates during droplet pinch-off are very large, leading to a reorientation even of the short nanorods.

Our experiments for the nanoplatelets, wormlike micelles and gold nanorods thus show that the observed reorientation effects, particularly the unusual biaxial distribution in the micro-droplets after droplet break-up, are generally occurring for anisotropic particles. The understanding of the flow-alignment of anisotropic particles is crucial for the controlled fabrication of fiber materials as demonstrated by recent in-situ SAXS experiments on the flow-alignment of biological nanofibers.^{39,40} Our experiments, which demonstrate the importance of perpendicular extensional forces in affecting particle orientation, underline the necessity to generate extensional forces in flow direction to achieve desired parallel fiber orientation needed for high performance fibers.³⁹ Thus, experiments at higher particle concentrations to generate fibers is an important next step for further experiments.

Conclusion

We have demonstrated a microfluidic setup that enabled us to investigate the flow-orientation of anisotropic particles in free liquid jets for the first time, using scanning micro-focus X-ray scattering. Our study reveals remarkable and unexpected changes in particle flow-alignment upon exiting the nozzle to form a free jet, within the free jet, and upon jet break-up into droplets, where we observed an unusual biaxial particle orientation. We show how flow and aspect ratio determine the flow-orientation of anisotropic particles. We have furthermore demonstrated that

the observed flow-alignment phenomena are a general characteristic of anisotropic particles, comprising one- and two-dimensional particle geometries. Finally, using fluid dynamics simulations we could directly relate the observed particle flow-alignment to the changing flow velocity fields within the micro-jets and micro-droplets.

The developed microfluidic setup is broadly applicable for the investigation of micro-jets and micro-droplets with dissolved particles, taking advantage of the ever smaller, even sub- μm X-ray beam diameters that become available at dedicated synchrotron beamlines. Our findings greatly enhance our understanding of particle orientation in free jets and droplets and provide the basis for a control of particle alignment in liquid jet-based fabrication, coating and printing techniques.

Conflicts of interest

There are no conflicts of interest to declare.

Acknowledgements

This work was financial supported by an ERC Advanced Grant (STREAM, #291211), by the German ministry BMBF (# 05K13WC5), and the Deutsche Forschungsgemeinschaft (SFB 840). SG and LS thank the Volkswagen Foundation for financial support and the SuperMUC system for computation time. Stephan Hauschild is gratefully acknowledged for his sustained support.

References

1. J. A. Cuculo, J. F. Hotter and Q. Zhou, *Structure Formation in Polymeric Fibers*, Hanser Gardner Publications, Munich, 2001.
2. S. Agarwal, M. Burgard, A. Greiner and J. H. Wendorff, *Electrospinning: A Practical Guide to Nanofibers*, Walter de Gruyter GmbH, Berlin/Boston, 2016.
3. H. P. Le, *J. Imaging Technol.*, 1998, **42**, 49-62.
4. S. Roth, *J. Phys.: Condens. Matter*, 2016, **28**, 403003.
5. N. Ashgriz and A. L. Yarin, *Capillary instability of free liquid jets*, Springer US, Boston, MA, 2011.
6. A. M. Gañán-Calvo, *Phys. Rev. Lett.*, 1998, **80**, 285-288.
7. S. P. Lin and R. D. Reitz, *Annu. Rev. Fluid Mech.*, 1998, **30**, 85-105.
8. U. Weierstall, *Philos. Trans. R. Soc., B*, 2014, **369**.
9. J. M. Samon, J. M. Schultz, B. S. Hsiao, S. Seifert, N. Stribeck, I. Gurke and C. Saw, *Macromolecules*, 1999, **32**, 8121-8132.
10. J. L. White and M. Cakmak, *Adv. Polym. Technol.*, 1986, **6**, 295-338.
11. C. Riekkel, B. Madsen, D. Knight and F. Vollrath, *Biomacromolecules*, 2000, **1**, 622-626.
12. S. J. S. Qazi, A. R. Rennie and J. K. Cockcroft, *Langmuir*, 2012, **28**, 3704-3713.

13. S. Rosenfeldt, M. Stöter, M. Schlenk, T. Martin, R. Q. Albuquerque, S. Förster and J. Breu, *Langmuir*, 2016, **32**, 10582-10588.
14. M. Stöter, S. Gödrich, P. Feicht, S. Rosenfeldt, H. Thurn, J. W. Neubauer, M. Seuss, P. Lindner, H. Kalo, M. Möller, A. Fery, S. Förster, G. Papastavrou and J. Breu, *Angew. Chem., Int. Ed.*, 2016, **55**, 7398-7402.
15. M. Stöter, S. Rosenfeldt and J. Breu, *Annu. Rev. Mater. Res.*, 2015, **45**, 129-151.
16. S. Förster, L. Apostol and W. Bras, *J. Appl. Crystallogr.*, 2010, **43**, 639-646.
17. S. Förster, S. Fischer, K. Zielske, C. Schellbach, M. Sztucki, P. Lindner and J. Perlich, *Adv. Colloid Interface Sci.*, 2011, **163**, 53-83.
18. A. Ortega and J. García de la Torre, *J. Chem. Phys.*, 2003, **119**, 9914-9919.
19. J. Eggers and E. Villermaux, *Rep. Prog. Phys.*, 2008, **71**, 036601.
20. L. Rayleigh, *Proc. R. Soc. London*, 1879, **29**, 71-97.
21. M. Goldin, J. Yerushalmi, R. Pfeffer and R. Shinnar, *J. Fluid Mech.*, 2006, **38**, 689-711.
22. M. Trebbin, D. Steinhauser, J. Perlich, A. Buffet, S. V. Roth, W. Zimmermann, J. Thiele and S. Förster, *Proc. Natl. Acad. Sci. U. S. A.*, 2013, **110**, 6706-6711.
23. P. D. Olmsted, *Rheol. Acta*, 2008, **47**, 283-300.
24. S. Förster, M. Konrad and P. Lindner, *Phys. Rev. Lett.*, 2005, **94**, 017803.
25. J. Breu, W. Seidl, A. J. Stoll, K. G. Lange and T. U. Probst, *Chem. Mater.*, 2001, **13**, 4213-4220.
26. M. Stöter, D. A. Kunz, M. Schmidt, D. Hirsemann, H. Kalo, B. Putz, J. Senker and J. Breu, *Langmuir*, 2013, **29**, 1280-1285.
27. S. Förster and E. Krämer, *Macromolecules*, 1999, **32**, 2783-2785.
28. A. Buffet, A. Rothkirch, R. Doehrmann, V. Körstgens, M. M. Abul Kashem, J. Perlich, M. Schwartzkopf, G. Herzog, R. Gehrke, P. Müller-Buschbaum and S. V. Roth, *J. Synchrotron Radiat.*, 2012, **19**, 647.
29. P. Vennemann, JPIV v16.08.03: Open source software package for particle image velocimetry, www.jpiv.vennemann-online.de, Accessed August 29, 2016, accessed: August, 2016.
30. C. Bächer, L. Schrack and S. Gekle, *Phys. Rev. Fluids*, 2017, **2**, 013102.
31. A. Arnold, O. Lenz, S. Kesselheim, R. Weeber, F. Fahrenberger, D. Roehm, P. Košovan and C. Holm, *ESPREsSo 3.1: Molecular Dynamics Software for Coarse-Grained Models*, Springer, Berlin/Heidelberg, 2013.
32. D. Roehm and A. Arnold, *Eur. Phys. J.: Spec. Top.*, 2012, **210**, 89-100.
33. H. J. Limbach, A. Arnold, B. A. Mann and C. Holm, *Comput. Phys. Commun.*, 2006, **174**, 704-727.
34. B. Dünweg and A. J. C. Ladd, *Lattice Boltzmann Simulations of Soft Matter Systems*, Springer, Berlin/Heidelberg, 2009.
35. W. v. Hoeve, S. Gekle, J. H. Snoeijer, M. Versluis, M. P. Brenner and D. Lohse, *Phys. Fluids*, 2010, **22**, 122003.
36. S. Gekle, J. M. Gordillo, D. van der Meer and D. Lohse, *Phys. Rev. Lett.*, 2009, **102**, 034502.

- 37 S. Gekle and J. M. Gordillo, *Int. J. Numer. Methods Fluids*, 2010, **67**, 1456-1469.
- 38 O. R. Enriquez, I. R. Peters, S. Gekle, L. E. Schmidt, D. Lohse and D. van der Meer, *J. Fluid Mech.*, 2012, **701**, 40-58.

Supporting Information

Microfluidic Device

All micro-jet experiments were performed using a newly developed microfluidic setup that allows to cycle small liquid volumes at high flow rates to continuously generate stable micro-jets. The microfluidic setup consists of a micro annular gear pump (mzr-7205G, HNP Mikrosysteme GmbH) with an electrical control terminal box (S-G05) to precisely adjust flow rates as visible in Figure S1a. The pump is connected with silicone tubes to a specially fabricated 3D-printed sample holder which was designed in AutoCAD 2013 (Autodesk) and printed in polylactide using an Ultimaker 2 (Ultimaker B.V.). The 3D-printed sample holder was fabricated to hold a micro glass capillary (Hilgenberg GmbH) with an inner diameter of $600\ \mu\text{m}$ (wall thickness $50\ \mu\text{m}$) and is constructed for long-time small angle X-ray scattering (SAXS) measurements at synchrotrons as it is shown in Figure S1b-d.

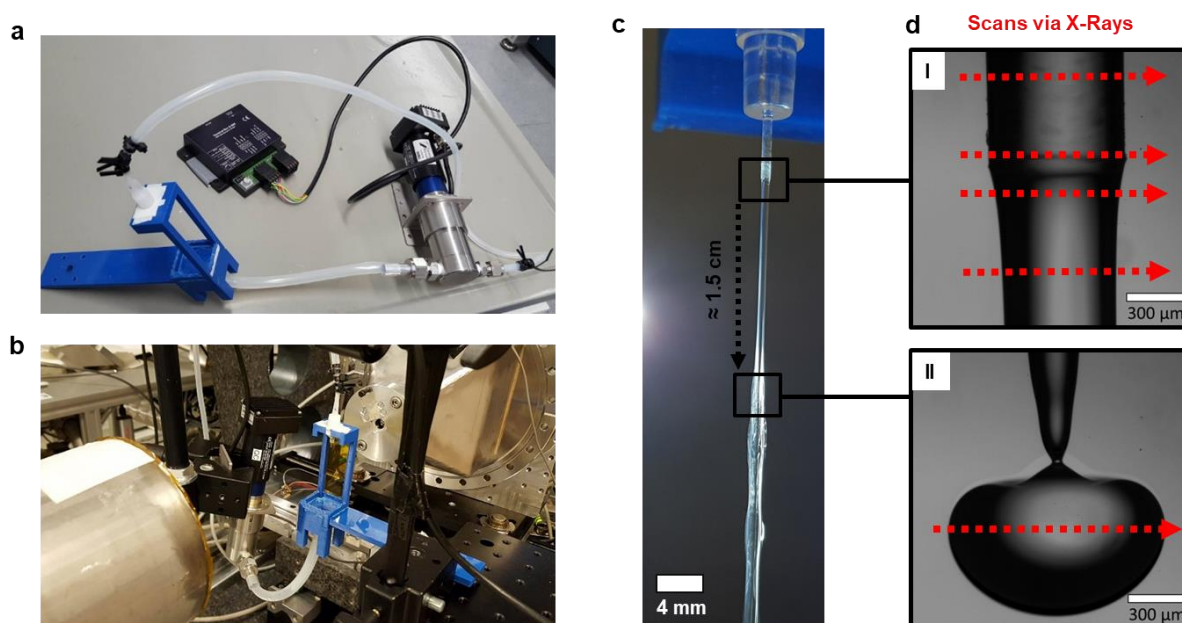


Fig. S1 Overview about the whole microjet setup. (a) 3D-printed sample holder (blue) and micro annular gear pump with control module. (b) Setup generating the microjet with a gear pump (7205G) at the synchrotron DESY, Petra III, beamline P03. (c) Video snapshot of the microjet indicating the nozzle exit as well as the droplet breakup area further downstream. Due to the extreme high flow rates and the high shutter speed of a normal camera, no drop formation is visible. (d) The droplet breakup is just visualized by a high-speed camera that can run very short exposure times between each picture, whereby the SAXS positions for scans at the nozzle exit are shown at the top image (I) and at the droplet breakup area 1.5 cm further downstream at the bottom image (II).

Determination of the droplet breakup position

Figure S2 shows the position for the droplet breakup at $\sim 13\ \text{mm}$ downstream the glass capillary with diameter of $ID = 600\ \mu\text{m}$ and a flow rate of $Q = 750\ \text{mL/h}$ that is used during the SAXS experiments.

Shown in the top row (Figure S2a) is a series of 20 subsequent 0.7 ms-snapshots of droplet breakups. Here we observe just a slight variation of the position for the droplet breakup between 0.5 – 1 mm at short time scales. The bottom row (Figure S2b) illustrates the droplet breakup over longer time scales of 1 second intervals. We observed just a small deviation from the droplet position of around 0.5 – 1 mm. All measurement positions were double checked by video microscopy to be sure about being either in the continuous jet or in the droplet regime (15.2 mm).

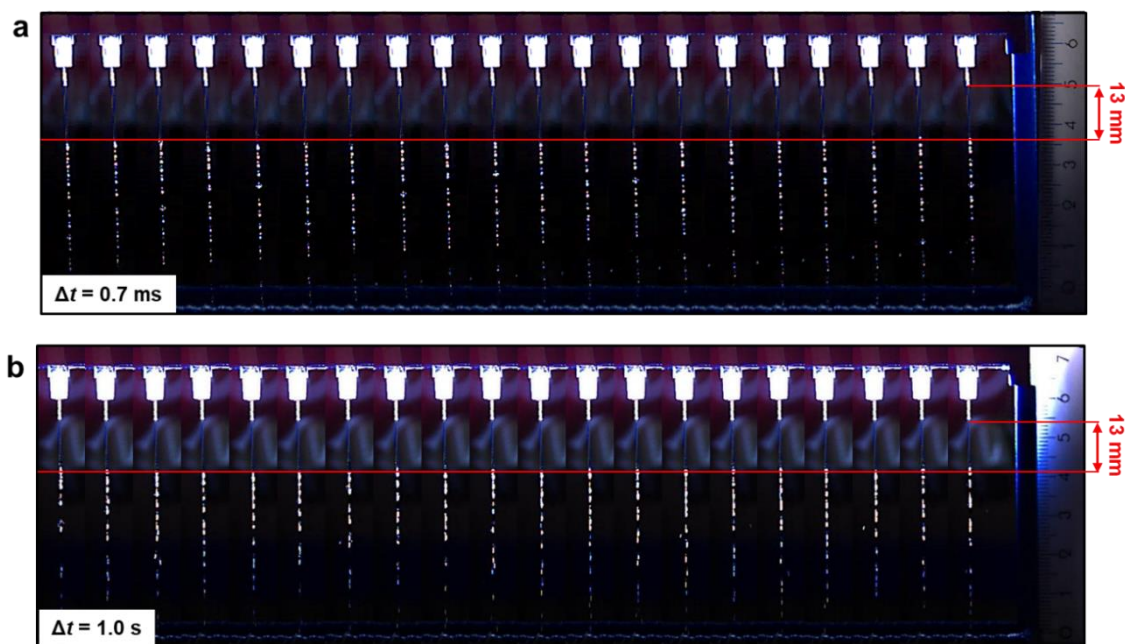


Fig. S2 Determination of the droplet breakup position. (a) Image series of the droplet breakup position for a capillary with diameter of $ID = 600 \mu\text{m}$ and a flow rate of $Q = 750 \text{ mL/h}$ for short time intervals of $\Delta t = 0.7$ ms and (b) longer time intervals of $\Delta t = 1.0$ s.

Characterization of anisotropic particles

The liquid micro-jet setup has been run with three different types of anisotropic particles. Cryo-TEM and TEM-images are shown in Figure S3. The first sample, 1% w/w sodium hectorite nanoplatelets dispersion in water, is visible in Figure S3a. The 10% w/w of wormlike micelles solution and the dispersed gold nanorods are illustrated in Figure S3b, c.

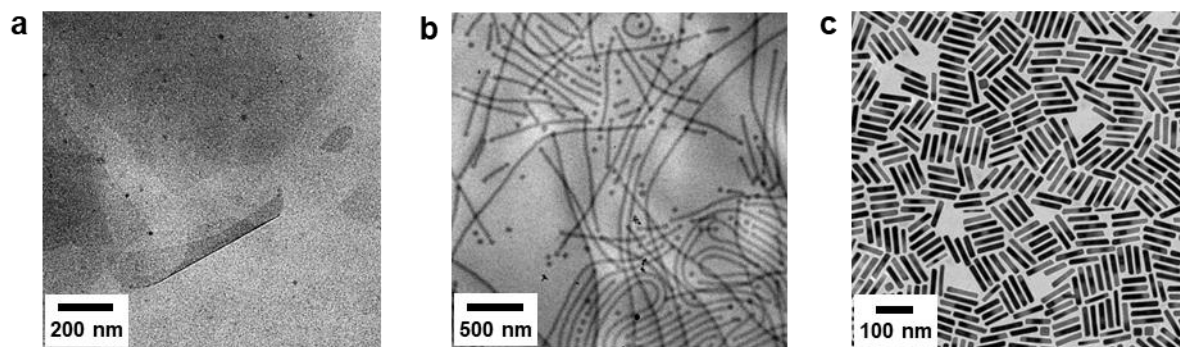


Fig. S3 Characterization of anisotropic particles via transmission electron microscopy. (a) Cryo-transmission electron microscopy (Cryo-TEM) image of $\text{Na}_{0.5}$ -hectorite nanoplatelets with a concentration of $c = 1\%$ w/w in water. The sample was milled by ultrasonic treatment to shorten the originally aspect ratio of 20.000. (b) Cryo-TEM image of PI_{110} - PEO_{198} wormlike micelles solution with a concentration of $c = 0.1\%$ w/w in water. (c) Transmission electron microscopy (TEM) image of single crystal gold nanorods (Au-Nanorods).

Microparticle Image Velocimetry

To determine the velocity profile experimentally, we used microparticle image velocimetry (μPIV). The setup consists of a Phantom v1612 high-speed camera (Vision Research), and a highly intense, focused light source Halolux LED-30 (Streppel Glasfaser-Optik oHG). In combination with a Model K1 CentriMaxTM long distance microscope (Infinity Photo-Optical Company) and a 10x /0.30 P UPlanFL N magnification objective (Olympus Corporation) the setup allows exposure down to $1.5 \mu\text{s}$ and frame rates up to $210,000 \text{ s}^{-1}$ for the performed experiments. Due to the narrow depth of focus of this kind of setup a precise vertical position control within the microjet is possible. The sample-holder was adjusted in the way that the focus distance was always set to the inner center part of the microjet and just frames of that position are taken by the high-speed camera. In total, always 30 frames are taken from exactly the same position at the center for averaging. For data collection via high-speed camera measurements the Phantom PCC v2.8.761.0 software was used. The obtained high-speed image sequence is autocorrelated and analyzed using the open-source software package JPIV. Measurements were made in pure water that contained 0.1% w/v of $4.89 \mu\text{m}$ diameter monodisperse polystyrene tracer particles (Micro Particles GmbH). The results as well as analysis of the water microjet flow profiles based on a $300 \mu\text{m}$ diameter glass capillary and the generally used flow rate of 750 ml/h is shown in Figure S4.

Concerning the μPIV experiments, analysis problems appear due to light reflexions on the curved outer free jet but especially at the curved glass capillary. As a consequence, dark areas at the edge of the glass capillary are emerging and no valid evaluation within these black regions is possible by the software since the particles are not visible anymore for tracing. However, flow profile analysis for the freejet area is possible up to a certain point. The black area is just present at the outermost edge of the freejet and thus

we can determine most of the flow profile. In Figure S4a, the freejet position 5 mm after outlet is analyzed via JPIV whereby the red marked jet edges of the dark regions are not considered. The results in Figure S4b are showing a velocity profile which is like plug flow with an average velocity of around $v_{average} = 2.0$ m/s, whereby the zero velocity directly at the edge of the freejet is not available. Additionally, we have simulated the flow profile out of a capillary with a diameter of $D = 30 \mu\text{m}$ and a flow rate of $Q = 10 \mu\text{L/h}$ at the freejet area which is visible in Figure S4c. Here, a whole plug flow profile is recognized and matches quite good to the analyzed part of the experimentally found flow profile for the freejet area. Moreover, the flow profile within a capillary has also been simulated for the same parameters and the expected parabolic flow profile was determined, as seen in Figure S4d. However, a detailed analysis of an experimental flow profile is not possible due to intense light reflexions at the glass capillary. Nevertheless, a changing from a parabolic flow profile within the capillary to a plug flow profile within the freejet is identifiable by simulations and supported by experimental data. Consequently, this drastic change of the flow profile benefits the loss of orientation within and along the free jet.

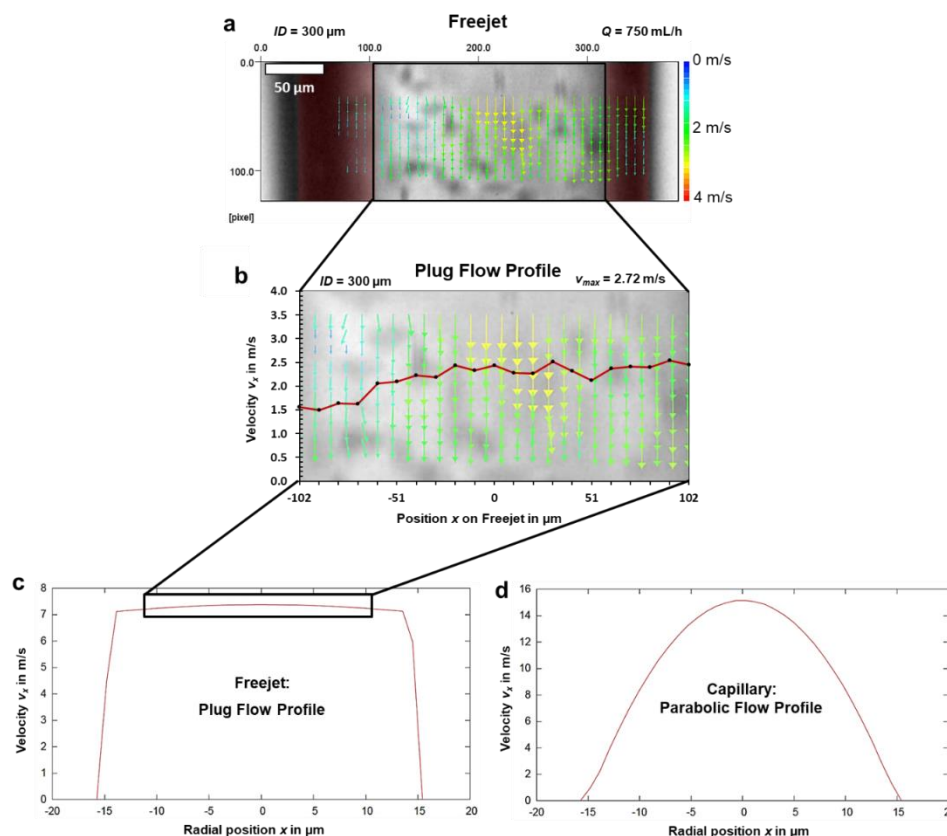


Fig. S4 Microparticle image velocimetry. (a) μ PIV measured flow profile of water including monodisperse polystyrene tracer particles which are jetting out of a glass capillary with an inner diameter of 300 μm and flow rate of $Q = 750 \text{ mL/h}$. The measurement position is on the freejet 5 mm after outlet. (b) Graph of analyzed plug flow profile with velocity V_x [m/s] versus position x on freejet in [μm]. (c) Simulated plug flow profile of the freejet out of a capillary with diameter of 30 μm and flow rate of 10 $\mu\text{L/h}$. (d) Simulated parabolic flow profile within the capillary and same flow rate.

In the further μ JPIV experiments, we present the flow profile generated by a smaller 200 μm diameter glass capillary to show the influence of the microjet diameter and velocity on the flow profile. In Figure S5, the flow profile for the experimental flow rate of $v = 750 \text{ mL/h}$ is shown for different positions on the microjet. As discussed before, the vector arrows in the dark areas of the capillary and freejet of Figure S5 are not allowed to incorporate to the consideration. Though the black areas are present at the edge of the capillary and freejet, we at least can observe a parabolic flow profile within the glass capillary (Figure S5a) and the gradual growing plug flow profile for the freejet at 5 mm after outlet (Figure S5b). As visible, the maximum velocity at the center part within the capillary amounts to $v_{max} = 3.91 \text{ m/s}$ and shows a parabolic flow profile in comparison to the rather plug flow profile for the freejet area at 5 mm after outlet, where the velocity decreased down to $v = 3.16 \text{ m/s}$. Compared to the bigger capillary in Figure S4, the maximum velocity within the smaller capillary is much higher.

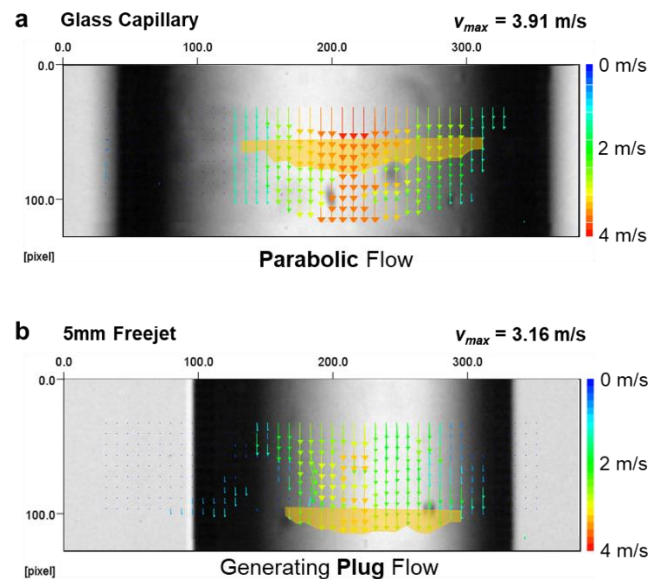


Fig. S5 μ PIV measured flow profiles of water using monodisperse polystyrene tracer particles and a flow rate of $v = 750 \text{ mL/h}$. a) Within a glass capillary of a diameter of $ID = 200 \mu\text{m}$ and b) 5 mm after the outlet within the free jet.

SAXS-pattern calculation

In the following we outline the calculation of the scattering patterns of oriented anisotropic particles, such as cylinders and disks, which are dispersed in a solvent. For such two-phase systems consisting of particles (phase “1”) with scattering length b_1 and volume fraction ϕ_1 in a solvent (phase “2”) of scattering length b_2 and a volume fraction $\phi_2 = 1 - \phi_1$, separated by sharp interfaces, the scattered intensity per unit volume is given by

$$I(\mathbf{q}, \mathbf{L}, \mathbf{R}) = (b_1 - b_2)^2 \rho_N \left\langle \left\langle F^2(\mathbf{q}, \mathbf{L}, \mathbf{R}) \right\rangle_{L,R} \right\rangle_{or} \left[1 + \beta(\mathbf{q}, \mathbf{L}, \mathbf{R}) \left(\langle Z(\mathbf{q}, \mathbf{g}) \rangle_{or} - 1 \right) G(q, g) \right] \quad (1)$$

where \mathbf{q} is the scattering vector, $\rho_N = N/V$ is the number density of the particles, $F(\mathbf{q})$ the scattering amplitude or Fourier transform of the particle form, L is equal to the length of the cylinder or the thickness of the sheet, R is equal to the cross-sectional radius of the cylinder or the lateral radius of the disk, $Z(\mathbf{q})$ is the lattice factor describing the spatial distribution of the particles, $G(q)$ is the Debye-Waller factor, and

$$\beta(\mathbf{q}, \mathbf{L}, \mathbf{R}) = \frac{\left\langle \left\langle F(\mathbf{q}, \mathbf{L}, \mathbf{R}) \right\rangle_{L,R}^2 \right\rangle_{or}}{\left\langle \left\langle F^2(\mathbf{q}, \mathbf{L}, \mathbf{R}) \right\rangle_{L,R} \right\rangle_{or}} \quad (2)$$

The effect of the ratio $\beta(\mathbf{q})$ on the scattering intensity is similar to the effect of the Debye-Waller factor $G(q)$, resulting in a decay of the Bragg peak-intensities with increasing scattering vector q . Equation (1) considers the effect of the particles - via their first and second moment of the particle size distribution - and of the lattice - via the first and second moment of the distribution of lattice points - on the scattered intensity $I(q)$.

The scattering amplitude $F_C(\mathbf{q}, \mathbf{L}, \mathbf{R})$ for cylindrical particles of cross-sectional radius R and length L can be factorized into

$$F_C(\mathbf{q}, \mathbf{L}, \mathbf{R}) = F_{C\parallel}(\mathbf{q}, \mathbf{L}) F_{C\perp}(\mathbf{q}, \mathbf{R}) \quad (3)$$

where $F_{C\parallel}(\mathbf{q}, \mathbf{L})$ is the longitudinal contribution parallel to the cylinder axis, and $F_{C\perp}(\mathbf{q}, \mathbf{R})$ is the contribution from the cross-section of the cylinder. $\mathbf{L} = L\mathbf{l}_{\parallel}$ is a vector with length L and a direction given by the unit vector parallel to the cylinder axis \mathbf{l}_{\parallel} . $\mathbf{R} = R\mathbf{l}_{\perp}$ is a vector with length R and a direction given by the unit vector perpendicular to the cylinder axis \mathbf{l}_{\perp} . The directions are shown in Figure S6. The longitudinal and cross-sectional contributions for cylinders are given by

$$F_{C\parallel}(\mathbf{q}, \mathbf{L}) = \frac{\sin(\mathbf{q}\mathbf{L}/2)}{\mathbf{q}\mathbf{L}/2} \quad (4)$$

$$F_{C\perp}(\mathbf{q}, \mathbf{R}) = \frac{2J_1(\mathbf{q}\mathbf{R})}{\mathbf{q}\mathbf{R}} \quad (5)$$

where $J_1(z)$ is the Bessel function of the first kind.

The structure of disks can be described by their lateral radius R_D and the thickness D as shown in Figure S6.

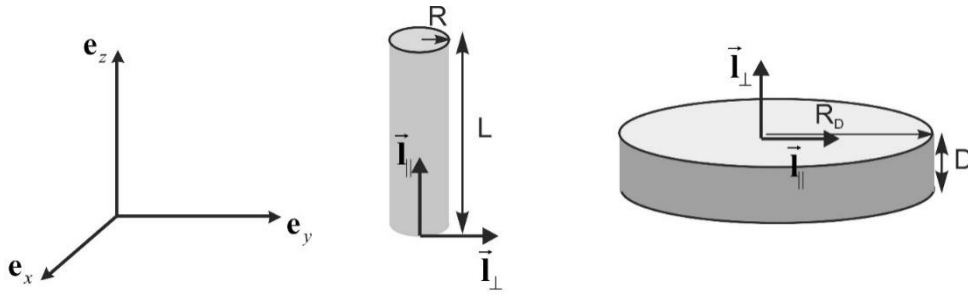


Fig. S6 Different shapes used for SAXS-pattern calculation. Definition of directions for cylinders and disks to calculate the longitudinal and cross-sectional formfactors.

Since disks could equivalently be considered to be short cylinders, where the cross-sectional radius R is larger than the length L , the scattering amplitudes can be derived by substituting $\mathbf{L} \rightarrow \mathbf{D}$ and $\mathbf{R} \rightarrow \mathbf{R}_D$ in Equation (3-5) to obtain

$$F_D(\mathbf{q}, \mathbf{D}, \mathbf{R}_D) = F_{D\parallel}(\mathbf{q}, \mathbf{R}_D) F_{D\perp}(\mathbf{q}, \mathbf{D}) \quad (6)$$

where $F_{D\parallel}(\mathbf{q}, \mathbf{R}_D)$ is now the contribution in the lateral direction and $F_{D\perp}(\mathbf{q}, \mathbf{D})$ is the contribution from the cross-section of the disk. The normal and cross-sectional contributions for disks are given by

$$F_{D\parallel}(\mathbf{q}, \mathbf{R}_D) = \frac{2J_1(\mathbf{q}\mathbf{R}_D)}{\mathbf{q}\mathbf{R}_D} \quad (7)$$

$$F_{D\perp}(\mathbf{q}, \mathbf{D}) = \frac{\sin(\mathbf{q}\mathbf{D}/2)}{\mathbf{q}\mathbf{D}/2} \quad (8)$$

For the calculation of the averages over the size distribution of lengths L and radii R the scattering amplitudes can be factorized and integrated with respect to each of the variables $X = L, R$. In many cases, the Schulz-Zimm distribution is a useful size distribution function. Then the measured z-averages of the functions $f(q, X)$ are given by

$$\langle f(q, X) \rangle_X = \int_0^{\infty} f(q, X) X^m h(X) dX \quad (9)$$

with

$$h(X) = \frac{(z+1)^{z+m+1} X^z}{\bar{X}^{z+m+1} \Gamma(z+m+1)} \exp\left[-(z+1) \frac{X}{\bar{X}}\right] \quad (10)$$

with m the weighting factor for the variable X , the average \bar{X} , and the relative standard deviation $\sigma_X = (z+1)^{-1/2}$. The distribution is normalized such that $\int_0^{\infty} X^m h(X) dX = 1$. The weighting factor relates to the measured intensity being the z-average, such that for spheres

$m = 6$, for cylinders $m = 2$ for the length, and $m = 4$ for the cross-sectional radius, and for disks $m = 2$ for the thickness and $m = 4$ for the lateral disk radius.

The orientational distribution of the particles can be obtained by averaging the scattering amplitudes $\langle F(\mathbf{q}, \mathbf{L}, \mathbf{R}) \rangle_{L,R}$, $\langle F^2(\mathbf{q}, \mathbf{L}, \mathbf{R}) \rangle_{L,R}$, $\langle F_D(\mathbf{q}, \mathbf{D}, \mathbf{R}_D) \rangle_{D,R_D}^2$ and $\langle F_1^2(\mathbf{q}, \mathbf{D}, \mathbf{R}_D) \rangle_{D,R_D}$ over a distribution of angles β between the cylinder axis or lateral direction of the disk, \mathbf{l}_\parallel , and the scattering vector \mathbf{q} . The relevant scalar products are $\mathbf{qL} = L\mathbf{q}\mathbf{l}_\parallel = qL\cos\beta$, $\mathbf{qR} = R\mathbf{q}\mathbf{l}_\perp = qR\sin\beta$, $\mathbf{qD} = D\mathbf{q}\mathbf{l}_\perp = qD\cos\beta$, and $\mathbf{qR}_D = R_D\mathbf{q}\mathbf{l}_\parallel = qR_D\sin\beta$. The orientational averages are then calculated as

$$\left\langle \left\langle F_C(\mathbf{q}, \mathbf{L}, \mathbf{R}) \right\rangle_{L,R}^2 \right\rangle_{or} = \int_0^{\pi/2} \langle F_{C\parallel}(qL\cos\beta(\delta)) \rangle_L^2 \langle F_{C\perp}(qR\sin\beta(\delta)) \rangle_R^2 h(\delta) \sin\delta d\delta \quad (11)$$

$$\left\langle \left\langle F_C^2(\mathbf{q}, \mathbf{L}, \mathbf{R}) \right\rangle_{L,R} \right\rangle_{or} = \int_0^{\pi/2} \langle F_{C\parallel}^2(qL\cos\beta(\delta)) \rangle_L \langle F_{C\perp}^2(qR\sin\beta(\delta)) \rangle_R h(\delta) \sin\delta d\delta \quad (12)$$

$$\left\langle \left\langle F_D(\mathbf{q}, \mathbf{D}, \mathbf{R}_D) \right\rangle_{D,R_D}^2 \right\rangle_{or} = \int_0^{\pi/2} \langle F_{D\parallel}(qR_D\sin\beta(\delta)) \rangle_{R_D}^2 \langle F_{D\perp}(qR\cos\beta(\delta)) \rangle_R^2 h(\delta) \sin\delta d\delta \quad (13)$$

$$\left\langle \left\langle F_1^2(\mathbf{q}, \mathbf{D}, \mathbf{R}_D) \right\rangle_{D,R_D} \right\rangle_{or} = \int_0^{\pi/2} \langle F_{D\parallel}^2(qR_D\sin\beta(\delta)) \rangle_{R_D} \langle F_{D\perp}^2(qR\cos\beta(\delta)) \rangle_R h(\delta) \sin\delta d\delta \quad (14)$$

Details of this calculation are outlined in ref.^[16] of the main publication.

For the calculations we need to specify the orientational distribution of the cylinders and disks, $h(\delta)$, which is defined by the angle δ between a director given by the unit vector \mathbf{n} and the direction \mathbf{l}_\parallel . For the distribution $h(\delta)$ simple approximations can be made which involve Gaussian, Onsager, Boltzmann, or Maier-Saupe distribution functions. These functions are given by

$$h(\delta) = \begin{cases} \exp[-\sin\delta/\bar{\delta}] & , \quad \text{Onsager} \\ \exp[-\delta/\bar{\delta}] & , \quad \text{Boltzmann} \\ \exp[(\cos\delta/\bar{\delta})^2] - 1 & , \quad \text{Maier-Saupe} \\ \exp[-(\delta/\bar{\delta})^2] & , \quad \text{Gaussian} \end{cases} \quad (15)$$

with $0 \leq \bar{\delta} < \infty$. A value of 0 corresponds to a uniform orientation of all cylinders in the direction of the director \mathbf{n} , whereas a value of $\bar{\delta} \rightarrow \infty$ corresponds to an isotropic distribution. If the distribution function is known, the orientational order parameter S defined as

$$S = \left\langle \frac{3\cos^2 \delta - 1}{2} \right\rangle \quad (16)$$

For all scattering patterns a Gaussian-type orientation distribution (Figure S7) gave the best agreement between experiment and simulation. The structural parameters used for the simulations are summarized in Table S1-3.

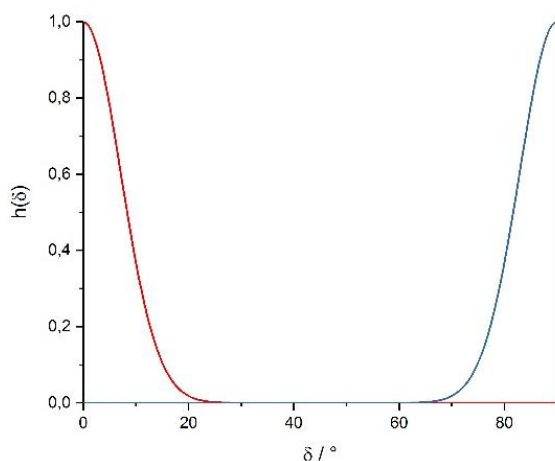


Fig. S7 Gaussian orientational distribution functions. Used for the wormlike micelles and the gold nanorods (red) and the nanoplatelets (blue).

Additionally, 2D-scattering patterns of a pure water microjet with the same diameter and flow rate are shown for the solvent background measurements in Figure S8 to approve that there were no artefacts in the 2D-scattering patterns of the anisotropic particle jets before.

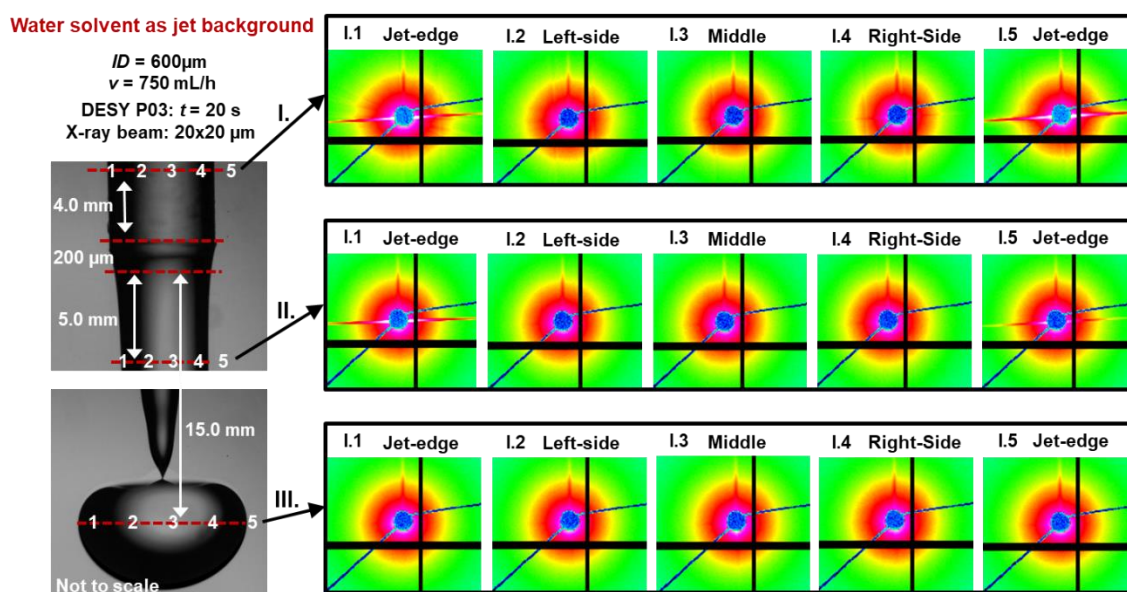


Fig. S8 2D-scattering patterns of a pure water microjet. (I) On the glass capillary 4 mm before outlet, (IV) freejet 5 mm after outlet and (V) droplet region 15 mm after outlet.

Table S1 Parameters for quantitative calculations in Figure 1c and Figure S9b.

3% w/w Hectorite nanoplatelets	I.1	I.4	IV.4	V.4
Disk radius, R ; nm	300	285	160	260
Relative std. deviation, σ_R	0.1	0.1	0.1	0.1
Layer thickness, d ; nm	1.0	1.0	1.0	1.0
Relative std. deviation, σ_d	0.07	0.07	0.07	0.07
Mean deviation, $dbeta$	10	14	65	10
Orientational parameter, f	-0.48	-0.46	-0.14	-0.48
Orientation parameter, S	0.92	0.89	0.20	0.92

Table S2 Parameters for quantitative calculations in Figure S10b.

10% w/w Wormlike micelles	I.1	I.4	IV.4	V.4
Cylinder length, L ; nm	30	20	20	15
Relative std. deviation, σ_L	0.1	0.1	0.1	0.1
Cylinder radius, R ; nm	9	11.5	11.5	12
Relative std. deviation, σ_R	0.07	0.07	0.07	0.07
Unit cell dimension, a ; nm	42	42	42	42
Radial domain size, D_a ; nm	120	55	55	55
Azimuthal coherence length, D_ψ ; nm	5	48	45	48
Displacement, σa , nm	10	6	8	6
Mean deviation, $dbeta$	2	11	55	12
Orientation parameter, S	0.98	0.94	0.31	0.93

Table S3 Parameters for quantitative calculations in Figure S11b.

Gold nanorods	I.1	I.4	IV.4	V.4
Cylinder length, L ; nm	71.4	71.4	71.4	71.4
Relative SD, σL	0.1	0.1	0.1	0.1
Cylinder radius, R ; nm	13	13	13	13
Relative SD, σR	0.07	0.07	0.07	0.07
Mean deviation, $dbeta$	65	95	99	35
Orientation parameter, S	0.23	0.11	0	0.58

Sets of scattering patterns

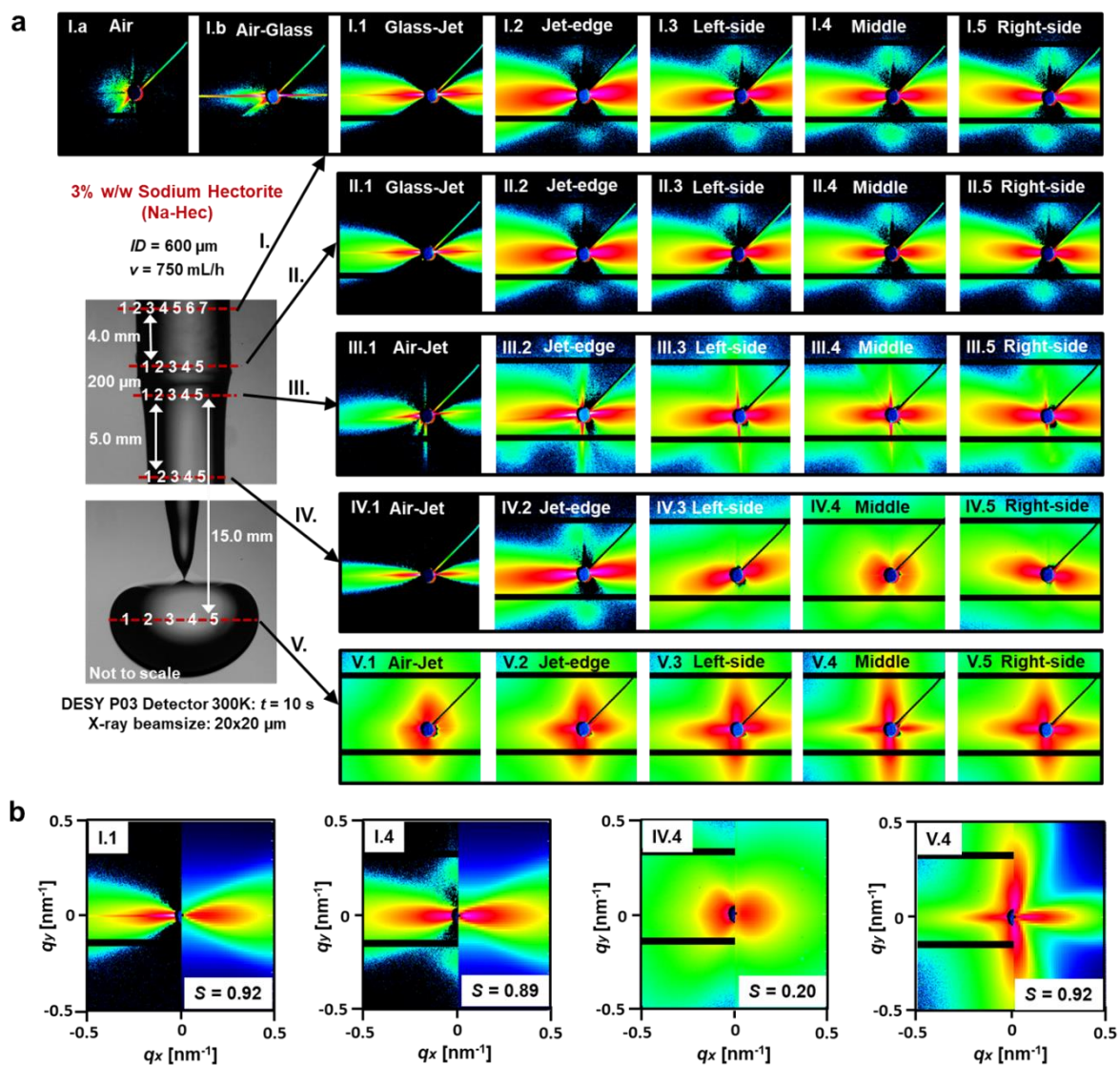


Fig. S9 Sets of measured scattering patterns of the hectorite nanoplatelets. a) At specified scan positions and (b) calculations of scattering patterns as well as their orientation parameter S at four characteristic microjet positions.

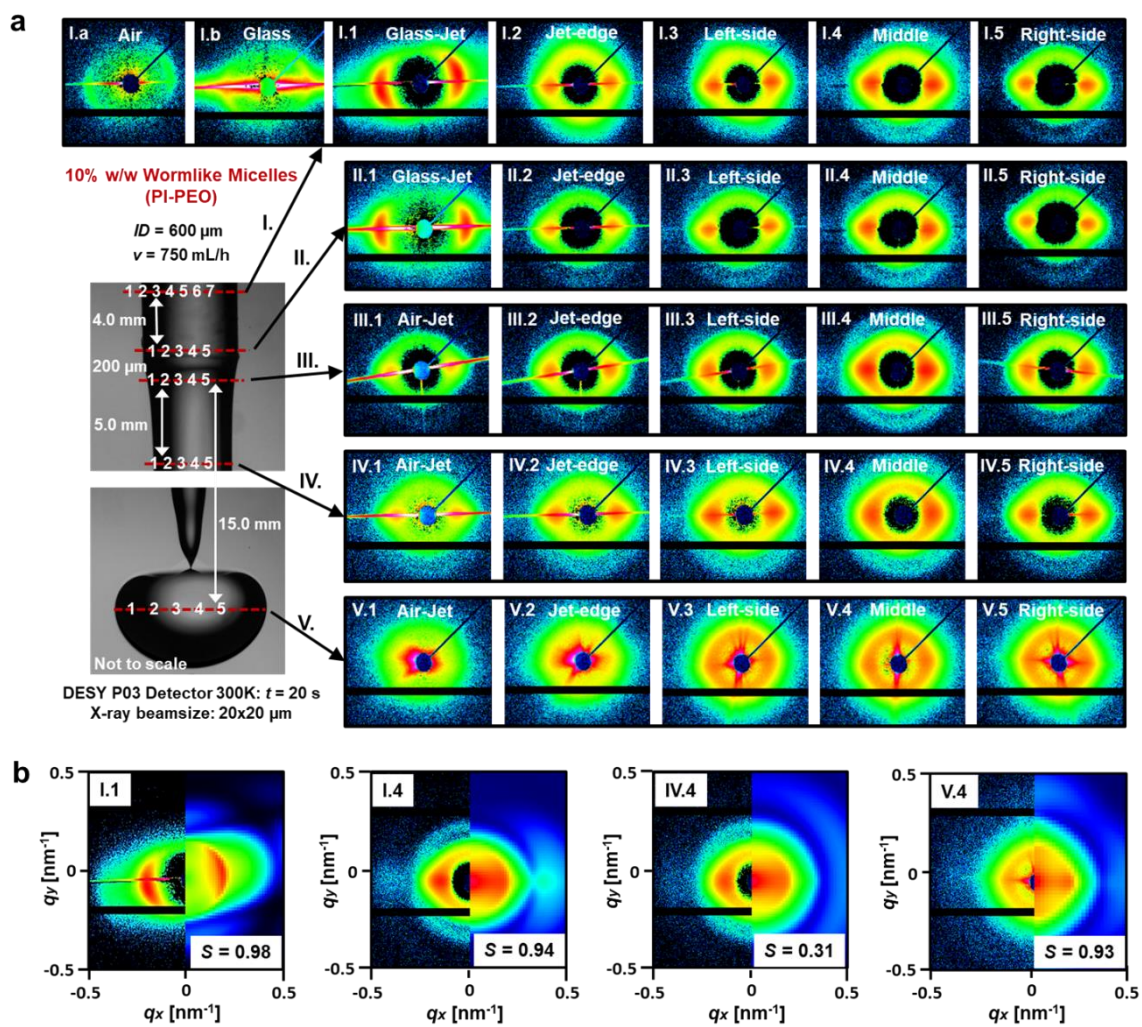


Fig. S10 Sets of measured scattering patterns of the wormlike micelles. a) At specified scan positions and (b) calculations of scattering patterns as well as their orientation parameter S at four characteristic microjet positions.

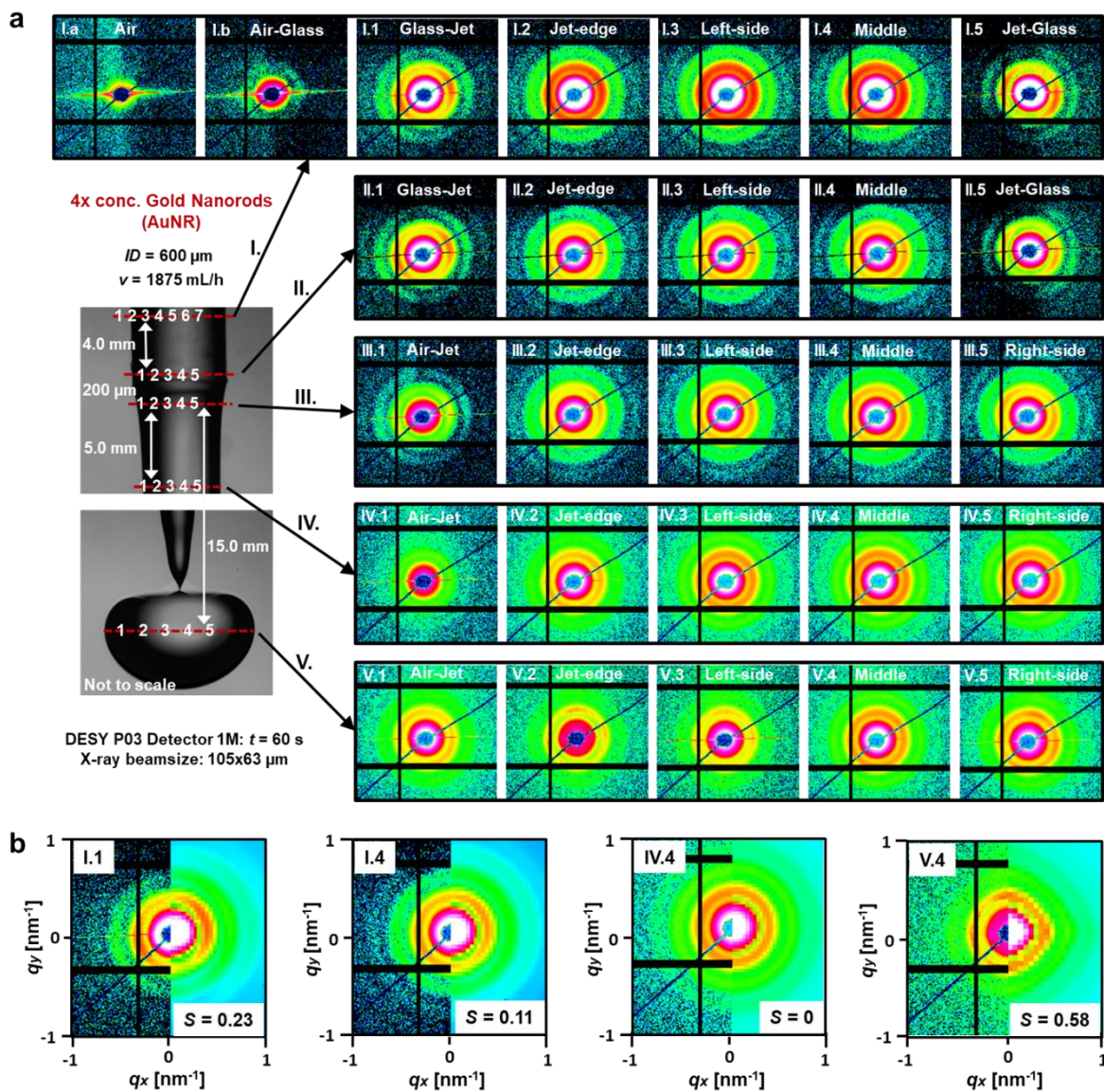
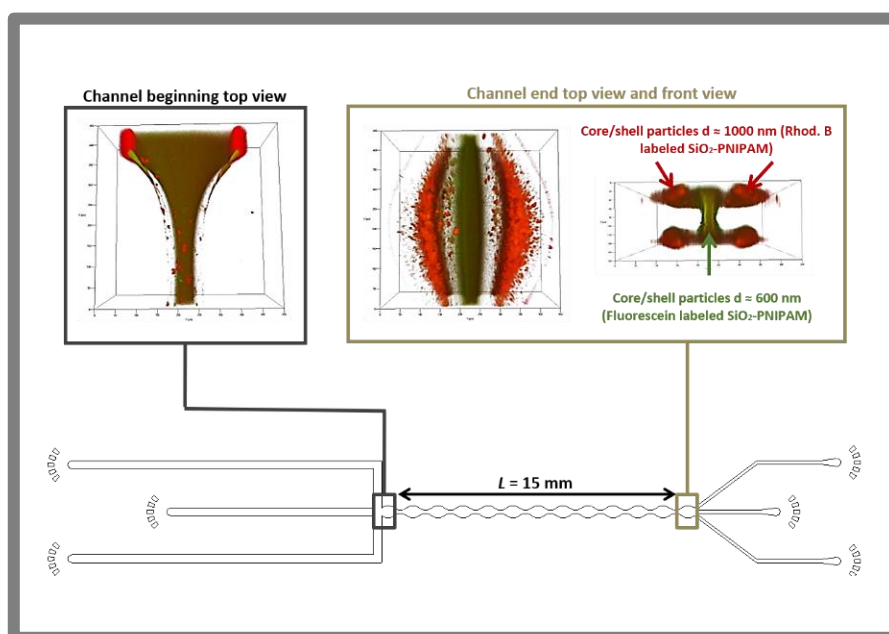


Fig. S11 Sets of measured scattering patterns of the nanorods. a) At specified scan positions and (b) calculations of scattering patterns as well as their orientation parameter S at four characteristic microjet positions.

4.2 Splitting and Separation of Colloidal Streams in Sinusoidal Microchannels



Reproduced with permission from [M. Schlenk](#), M. Drechsler, M. Karg, W. Zimmermann, M. Trebbin, S. Förster published in *Lab on a Chip*, **2018**, *18* (20), 3163-3171.

© 2018 The Royal Society of Chemistry.

Abstract

The control of the distribution of colloidal particles in microfluidic flows plays an important role in biomedical and industrial applications. A particular challenge is to induce cross-streamline migration in laminar flows, enabling the separation of colloidal particles according to their size, shape or elasticity. Here we show that viscoelastic fluids can mediate cross-streamline migration of deformable spherical and cylindrical colloidal particles in sinusoidal microchannels at low Reynolds numbers. For colloidal streams focused into the center of the channel entrance this leads to a symmetric stream-splitting and separation into four substreams. The degree of stream splitting and separation can be controlled via the flow rates, viscoelasticity of the focusing fluid, and the spatial microchannel modulation with an upper limit when reaching the microchannel walls. We demonstrate that this effect can be used to separate flexible particles of different size and shape. This methodology of cross-stream migration has thus great potential for the passive separation of colloids and cells in microfluidic channels.

Introduction

The fundamental understanding and control of particle distribution and separation in micro flows plays an important role in many biomedical, environmental and industrial applications.^{1,2} Microfluidic particle sorting can be achieved via a variety of methods that cause cross-streamline migration. One class are noninvasive methods, which rely on intrinsic hydrodynamic properties of micro flows and particle properties.³ Widely employed examples for particle focusing are based on fluid inertia,⁴⁻⁹ on viscoelastic effects¹⁰ or deformability-selective particle sorting.¹¹⁻¹⁴ It was demonstrated for the first time by Segre *et al.* that rigid particles can migrate to stable off-center positions in pipe flows.⁴ Migration was driven by fluid inertia in the intermediate Reynolds number range ($\sim 1 < Re < \sim 100$) and has been extensively used for particle sorting in Newtonian and viscoelastic fluids.⁵⁻⁹ In contrast, deformable particles like vesicles, capsules or cells show cross-streamline migration already in the limit of Stokes flows at very small values of the Reynolds number. They migrate away from channel walls due to the lift force, as shown at first for Newtonian liquids.¹⁵⁻¹⁷ When separated from the wall deformable particles can migrate further towards the center in Poiseuille flows, driven by the local shear gradient across the particles.¹²⁻¹⁴ Both effects depend on the particle size and their deformability. In shear thinning fluids the center migration of soft particles may be reversed by shear thinning effects¹⁸ or elastic lift forces.¹⁹⁻²² In viscoelastic fluids several types of cross-stream line migration phenomena have been observed for rigid and soft particles.^{3,10,18,23} For example, particle focusing and alignment was achieved over a range of small to medium flow rates to separate solid and deformable particles and cells.²⁴ A spatially varying flow-channel cross-section may lead to center-line focusing of rigid particles in Newtonian fluids²⁵ and Non-Newtonian fluids^{26,27} or to unusual and unexpected reorientations of anisotropic flexible particles in shear thinning fluids.²⁸

So far viscoelastic cross-stream migration of anisotropic or extended chain-like structures has received little attention, although the separation of synthetic or biological macromolecules or anisotropic nanoparticles is an important research field. Thus, we investigated the flow behavior of anisotropic, semiflexible wormlike micelles under conditions that promote cross-stream migration. To control and amplify migration we used sinusoidally modulated microchannels and investigated the flow behavior using fluorescence-, polarization-, and confocal laser scanning-microscopy (CLSM). Streams of the micellar solutions were hydrodynamically focused into the center of the modulated microchannels at low Reynolds numbers using Newtonian and non-Newtonian fluids. We surprisingly discovered that the central stream symmetrically splits into four substreams that separate and further move towards the outer wall of the microfluidic channel with every passage through a channel modulation. We show that stream splitting and

separation can be controlled via flow rates, microchannel geometries, and colloid shape as well as the rheological properties of the focusing fluid. We outline the underlying physical principles for the observed separation effect and furthermore demonstrate that this phenomenon can be generally used to separate colloidal and cellular particles according to their size.

Experimental

4.1 Fabrication of microfluidic devices

The microfluidic chip is initially fabricated by preparing a master device based on a Si wafer via optical lithography.³¹ The microchannel structures are designed in AutoCAD 2013 (Autodesk) and printed on a mask foil with an UV-absorbent ink (JD Photo Data). A black and white drawing of the sinusoidal microchannel design is shown in **Fig. 1A**. Two different masters are finally used to produce the polydimethylsiloxane (PDMS) replicas for a 2D- respectively 3D-focusing chip design via soft lithography which is described in detail in the ESI.³²⁻³⁴ Afterwards, inlet ports are punched into the PDMS microchannels and interfaced with polyethylene (PE) tubes to be able to pump fluids into the devices by using high-precision syringe pumps (Nemysis system; Cetoni GmbH). For all carried out microfluidic experiments, the ratio of the flow rates between main channel and the two side channels was always constant with 1:1.

4.2 Preparation of block copolymer wormlike micelle solution

Polyisoprene₁₁₀-*b*-ethylene oxide₁₉₈ (PI₁₁₀-PEO₁₉₈) with a weight-averaged molar mass of $M_w = 16,000$ g/mol is synthesized by sequential living anionic polymerization, yielding an amphiphilic block copolymer with narrow polydispersity $M_w/M_n = 1.02$ (M_w and M_n are the weight- and number averaged molar mass). The detailed synthesis and characterization of PI₁₁₀-PEO₁₉₈ is described in literature.³⁵ The polymer powder is dissolved in Millipore-quality water to a concentration of 20 wt% and by using an UltraTurrax T8 (IKA Werke GmbH) the solution was finally homogenized. Due to storing three weeks at room temperature the copolymer is able to swell enough in water and self-assemble wormlike micelles. The 20 wt% PI-PEO wormlike micelles stock solution is diluted with MilliQ water down to 1 wt%, 5 wt% respectively 10 wt% and filtered through a polytetrafluorethylene filter with 5 μm pore size. A cryo-transmission electron microscopy (cryo-TEM) image of the wormlike micelles is shown in the ESI (see Fig. S2).

4.3 Preparation of core-shell particle dispersion

Core-shell particles with fluorescently labeled silica cores of approximately 100 nm in diameter and cross-linked poly-*N*-isopropylacrylamide (PNIPAM) shells were synthesized by seeded

precipitation polymerization as previously reported.³⁶ The silica cores were either labeled with fluorescein or rhodamine B using the respective isothiocyanates of the dyes. These cores were then encapsulated in single-step³⁶ or sequential multi-step seeded polymerization³⁷ yielding core-shell particles with overall hydrodynamic diameter of approximately 600 and 1000 nm (swollen state conditions). The final core-shell particles were cleaned by repeated centrifugation and redispersion in water (at least three cycles). Fluorescence microscopy images of two selected samples that were studied in this work (fluorescein-labeled core, overall diameter of 600 nm as well as rhodamine B-labeled core, overall diameter of 1000 nm) are visible in the ESI (Fig. S2). Furthermore, a scanning electron microscopy (SEM) image of the mixture of the SiO₂-PNIPAM core-shell particles in a non-Newtonian 1 wt% polyethylene glycol (PEG) aqueous solution is also shown in the ESI.

4.4 3D-Confocal laser scanning microscopy

The confocal laser scanning microscopy analysis (CLSM) was carried out via Z-scan series of a Zeiss LSM 710 respectively a Leica TCS SP8 that was taken in the x-y-z mode and has been used to reconstruct 3D-images of the flow profiles along the whole microchannel. For the flow experiments, the laser was adjusted to the excitation wavelength of the used fluorescent dyes for the colloids. Thus, the argon laser was used with a wavelength of $\lambda = 514$ nm for Nile red respectively $\lambda = 458$ nm for fluorescein and the helium-neon laser with a wavelength of $\lambda = 543$ nm for rhodamine B. The colloid sample of the dyed wormlike micelles respectively of the core-shell particles was just injected via the middle channel, whereby the focusing fluid (water, glycerine or PEG) was always injected through the two side channels.

4.5 Fluorescence and polarization microscopy

Fluorescence and polarization microscopy was performed with an Axiovert S100 microscope in combination with an Axiocam HRc (Zeiss GmbH) to take pictures and movies. A mercury vapor lamp with specific filters was used to excite the right wavelength of all used fluorescent dyed colloids. The use of a polarization microscope with a quarter wave plate made it also possible to investigate the flow orientation of the colloids within the microchannels (see ESI, Fig. S4).

Results and discussion

2.1 Splitting of colloidal streams by 2D-focusing with non-Newtonian fluids

For our study of the flow behavior of anisotropic colloids, in our case wormlike micelles, we used sinusoidal microchannels with a channel design that is shown schematically in **Fig. 1A**. An aqueous solution of wormlike micelles at a concentration of 1 wt% was focused by two aqueous

side streams into an outlet channel that had periodic sinusoidal variations of the channel width. The wormlike micelles were formed by the self-assembly of poly(isoprene-*b*-ethylene oxide) block copolymers (PI-PEO), which spontaneously occurs when dissolving the block copolymer in water. The channel height ($h = 100 \mu\text{m}$) was the same for all channels. The channel width was $w = 250 \mu\text{m}$ for the central and both side channels and was identical to the average width of the sinusoidal outlet channel. A typical flow rate in the central and side channels were $Q = 200 \mu\text{L/h}$ leading to a total flow rate of $Q = 600 \mu\text{L/h}$ in the outlet channel. We were interested in how the central stream of wormlike micelles respond to spatially periodic flow modulation leading to extension and contraction. For this we labelled the wormlike micelles with a fluorescent dye (Nile Red) to follow the focused stream in the sinusoidal outlet channel using fluorescence microscopy.

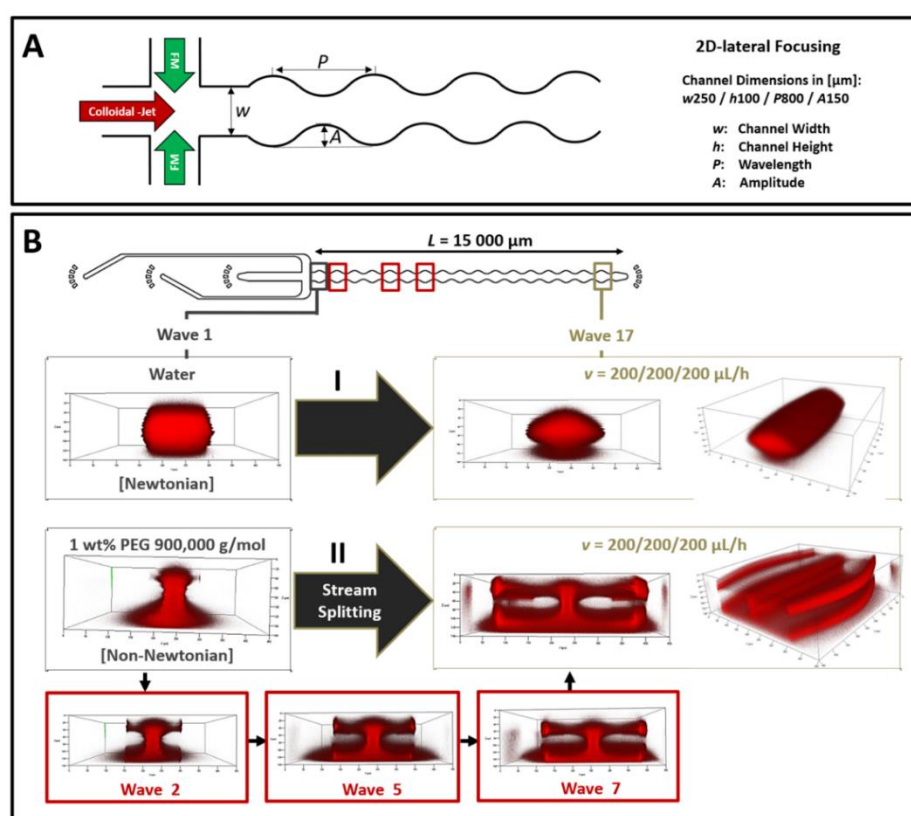


Fig. 1 (A) Scheme of the sinusoidal microchannel design with all parameter dimensions used for 2D-focusing. (B) 3D-CLSM front view images of Nile red labelled 1 wt% solutions of wormlike micelle which are hydrodynamically focused with water as a Newtonian fluid (I) and with a 1 wt% PEO-solution as a non-Newtonian fluid (II). The stream-splitting effect occurs near the microchannel floor and ceiling. The front view images of sine section 2, 5 and 7 illustrate the subsequent increase of the stream-splitting with each sine section.

When using water as a focusing fluid we observed the expected periodic variation of the stream width, which expanded and contracted in proportion to the width of the outlet channel

(**Fig. 1B I**). However, when using a non-Newtonian liquid for flow-focusing, we surprisingly discovered that the stream of wormlike micelles split into four substreams. This is shown in **Fig. 1B II**, where the confocal microscopy image on the left shows the central stream in the first sine section, where it is already slightly extended at the bottom and the floor of the channel. We always observe slight asymmetries between the floor and the ceiling layers in the microfluidic channel due to light scattering from the chip material, which increases from the cover slide and objective towards the center direction of the microfluidic chip device. The two confocal images on the right show the central stream in the 17th sine section, where it has split symmetrically into four substreams which are located close to the left and the right wall at the channel floor and channel ceiling. For flow-focusing we used a 1 wt% solution of a high molecular weight polyethylene glycol (PEG, 900,000 g/mol). Three additional images in **Fig. 1B II** show the increasing separation of the four streams in the 2nd, 5th, and 7th sine section. The part of the central stream that is located in the middle between the floor and the ceiling of the outlet channel does not split.

2.2 Influence of channel geometry

To clarify the conditions that lead to the splitting of the central stream, we compared a sinusoidal channel to a straight channel of the same total length of $L = 1.5$ cm, the same height of $h = 100$ μm , and the same average width $w = 250$ μm . The sinusoidal channel had a period of $P = 800$ μm and an amplitude of $A = 150$ μm . The results are presented in **Fig. 2A I-a**, which shows the CLSM side view and top view images. When using the 1 wt% PEG(900k)-solution for flow-focusing, for the straight channel the central stream width was 75 μm and did not change from the beginning to the end of the channel after 1.5 cm. When using the sine channel, the central stream with an original width of 75 μm splits into four substreams with a separation that increases by ca. 25 μm for each sine wave until the limit of $h = 250$ μm at the channel walls is finally reached. The increasing splitting and separation of the main stream at selected downstream positions is plotted in **Fig. 2A 1-a**.

Fig. 2A I-b shows the effect of the sine period and amplitude on the separation of the substreams. Decreasing each sine-period from $P = 800$ to 400 μm and increasing the amplitude from $A = 150$ to 300 μm lead to a considerably larger separation, e.g. from 200 to 350 μm at the 12th sine section. This demonstrates that the sine-form of the outlet channel is essential for the stream-splitting phenomenon and that by variation of the sine period and amplitude an efficient separation of the substreams can be accomplished over short outlet channel distances.

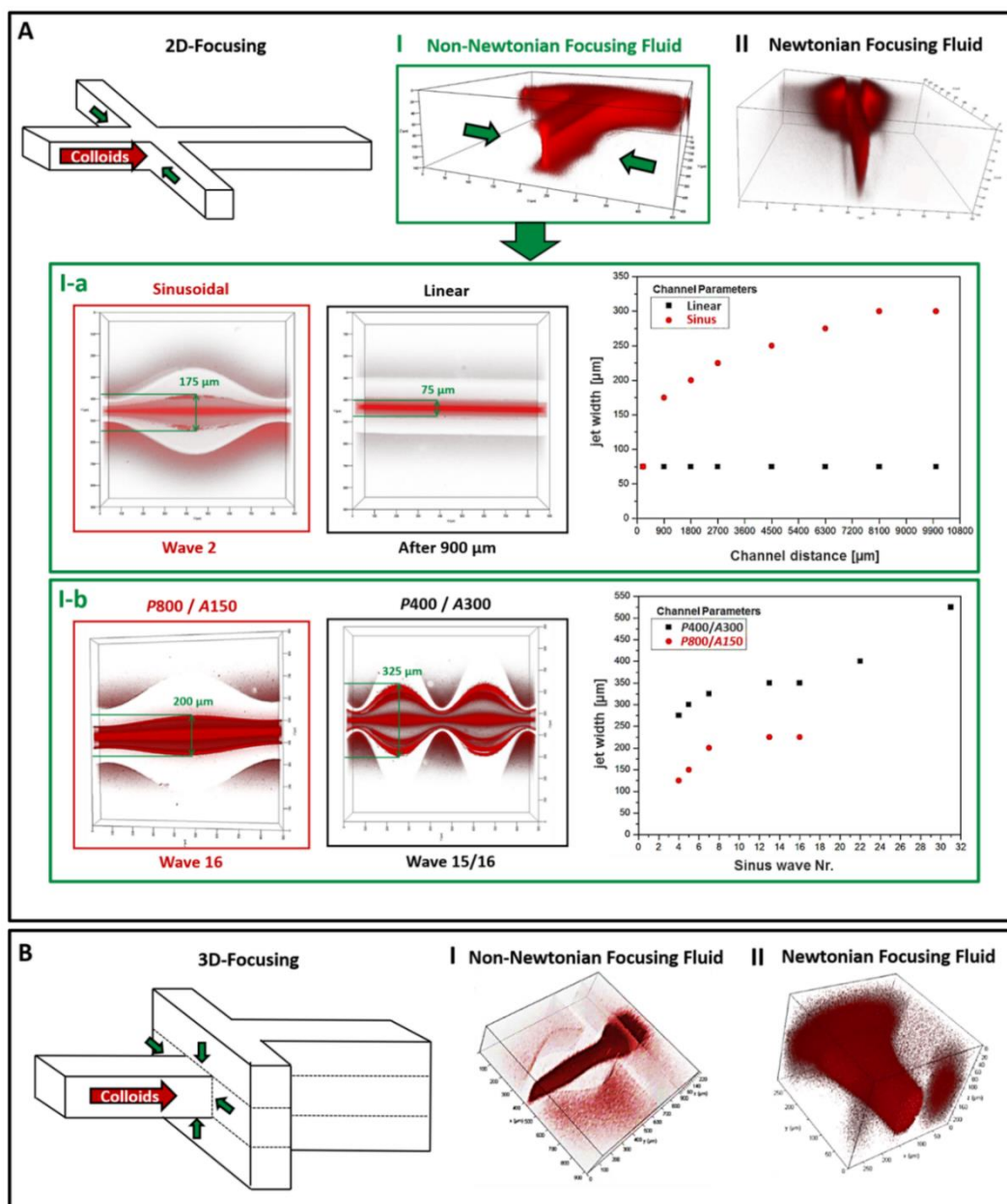


Fig. 2 (A) 3D-CLSM images of the arising stream-splitting effect by using 2D-focusing for a Nile red dyed 1 wt% wormlike micelles solution just in combination with non-Newtonian (I) and not with Newtonian (II) focusing fluids. (I-a) Top view images of the stream-splitting in a sinus-shaped and a linear channel geometry as well as a comparative diagram concerning their sub-stream spreading distances. (I-b) Top view images of stream-splitting in sine-channels comparing half of the periodic wavelength P as well as double of the amplitude A and again a comparative diagram regarding their sub-stream spreading distances. (B) 3D-CLSM images of no emerging stream-splitting by applying a channel design with a 3D-focusing independent from using Newtonian (I) or non-Newtonian (II) focusing fluids.

Next, we considered the influence of the channel floor and ceiling on the splitting of the central stream. To investigate this, we chose a 3D-focusing design such that the central stream was focused into the center of the outlet channel with considerable distance from the channel floor,

ceiling and both side walls. The 3D-focusing channel design is schematically shown in **Fig. 2B**. The confocal microscopy images on the right in **Fig. 2B** clearly show that under these conditions we do not observe any splitting of the central stream. This suggests that the proximity of the channel floor and ceiling is necessary for the splitting and separation of the central stream.

2.3 Effect of molar mass, flow rate and other important parameters

High molecular weight polyethylene oxide (PEO)-solutions are non-Newtonian fluids that show pronounced shear-thinning. We therefore investigated PEOs of smaller molecular weights that show less pronounced shear thinning, eventually becoming near Newtonian at very low molecular weights. The measured flow-curves for each of the investigated polyethylene glycols are shown in the ESI[†] (Fig. S6A). The corresponding experiment with PEOs of different molecular weights were performed under standard conditions with a 1 wt% solution of wormlike micelles, a channel height $h = 100 \mu\text{m}$, an average channel width of $w = 250 \mu\text{m}$, a sine period of $L = 800 \mu\text{m}$, an amplitude of $A = 150 \mu\text{m}$, and a volumetric flow rate of $Q = 600 \mu\text{l/h}$ in the outlet channel. In **Fig. 3A** CLSM-images of the central stream cross-sectional shapes in the first and the 17th sine section are compared for PEO-solutions with molecular weights of 6, 300, and 900 kg/mol. Whereas the 6 kg/mol low molecular weight PEO-solution showed no indications of stream splitting in the 17th sine section, the 300 kg/mol PEO-solution lead to a small, but clearly observable splitting. The 900 kg/mol PEO-solution lead to a very pronounced splitting of the central stream, as already described in **Figs. 1 and 2**. This indicates that the molecular weight of the polymer that is used in the focusing fluid must be sufficiently large to induce stream-splitting.

To investigate whether the observed stream splitting would be due to just a higher viscosity of the focusing stream compared to water, we also investigated glycerin as a Newtonian fluid which has a viscosity that is 1000 times larger compared to water. As visible in the ESI[†] (Fig. S6B), we did not observe any stream splitting with glycerin.

As for shear-thinning non-Newtonian fluids the solution viscosity depends on the shear rate, we investigated the splitting of the central stream for different flow velocities over a range of $Q = 10 - 520 \mu\text{l/h}$, corresponding to mean flow velocities of $v = 0.1 - 6 \text{ mm/s}$. Front view CLSM images and top view fluorescence microscopy images of the streams at the last sine section of the channel are shown in **Fig. 3B**. There is no observable stream splitting at the lowest flow rate of $10 \mu\text{l/h}$. At $80 \mu\text{l/h}$ we observe small but significant splitting, which increases with increasing flow rate of up to $520 \mu\text{l/h}$. Thus, also the flow velocity must be larger than a critical value to induce splitting of the central stream.

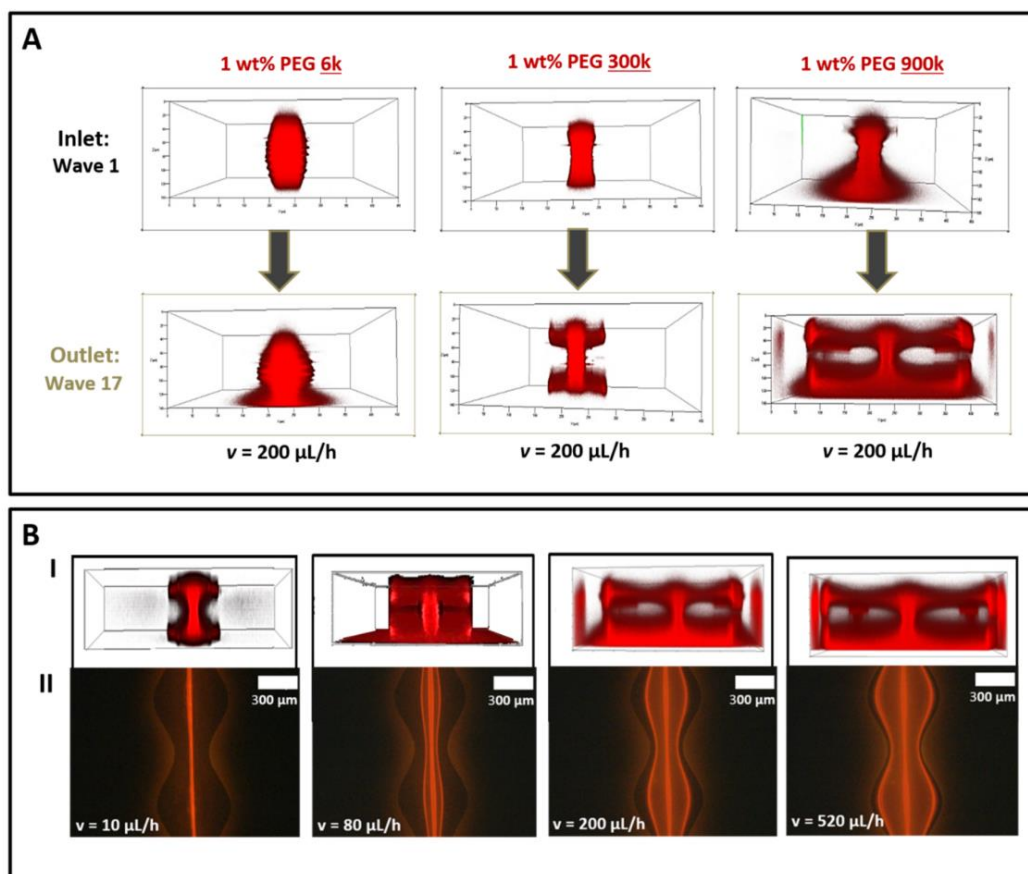


Fig. 3 (A) 3D-CLSM front view images at channel inlet and outlet of the flow profiles of the fluorescent dyed 1 wt% wormlike micelles in water within the standard sinusoidal channel ($w = 250 \mu\text{m}$, $P = 800 \mu\text{m}$, $A = 150 \mu\text{m}$, $L = 100 \mu\text{m}$) by using different molar mass of the non-Newtonian 1 wt% PEG-solution ($M = 6,000 \text{ g/mol}$, $300,000 \text{ g/mol}$ and $900,000 \text{ g/mol}$) as 2D-focusing fluid at a constant flow velocity of $v = 200 \mu\text{L/h}$ for all three inlets. (B) 3D-CLSM front view (I) as well as fluorescent top view (II) images of again the same wormlike micelles solution 2D-focused by the non-Newtonian 1 wt% PEG(900k) solution and this time varying flow rates between $v = 10$ and $520 \mu\text{L/h}$.

These experiments provide first indications on the conditions of the central stream splitting of wormlike micelles. The observation that splitting is observed at PEO molecular weights above $\sim 300 \text{ kg/mol}$ for concentrations of $\sim 1 \text{ wt\%}$ indicates that the effect is related to the overlap concentration c^* of the polymer chains in solution. The PEO overlap concentration can be estimated using the known relation between the hydrodynamic radius and the molecular weight, $R_h = kM^\alpha$, where $k = 0.0145 \text{ nm}$ and $\alpha = 0.571$,²⁹ an exponent which is typical for a polymer under good solution conditions. With a hydrodynamic volume of $V_h = \frac{4\pi}{3} R_h^3$, we can calculate the overlap concentration as $c^* = \frac{M}{N_A V_h}$, where N_A is Avogadro's number. With molecular weights of $M = 6, 300, \text{ and } 900 \text{ kg/mol}$ we calculate $c^* = 26, 1.6 \text{ and } 0.74 \text{ wt\%}$, such that the lowest molecular weight polyethylene glycol at a concentration of 1 wt\% is clearly much below

the overlap concentration, whereas the 300 kg/mol PEG is already close to the overlap concentration. The highest molecular weight 900 kg/mol PEG at a concentration of 1 wt% is clearly above the overlap concentration and thus in the semi-dilute concentration regime where adjacent polymer chains overlap and form a transient network of entangled polymer chains.

The 3D-focusing experiment clearly showed that wall-effects play a major role. The most dominant wall effect is a high wall shear rate, particularly for shear-thinning solutions. Because the channel height ($h = 100 \mu\text{m}$) is smaller than the mean channel width ($w = 250 \mu\text{m}$), the floor and ceiling wall shear rates are expected to have the most pronounced influence. With an average shear rate of $\dot{\gamma} = \frac{2v}{h}$ we obtain values of $\dot{\gamma} = 2.2, 18, \text{ and } 133 \text{ s}^{-1}$ for volumetric flow rates of 10, 80, and 600 $\mu\text{l/h}$. Thus already the average shear rates are of the same order of magnitude or higher compared to the inverse terminal relaxation time of a 1 wt% PEO solution ($\lambda = 50 \text{ ms}$,³⁰), corresponding to Weissenberg numbers of $Wi = \lambda\dot{\gamma} > 1$, such that in the investigated shear rate regime visco-elastic responses are expected to be very pronounced close to the floor and ceiling of the microchannel wall.

A key to the understanding of the stream-splitting is according to our results in **Fig. 1** and **Fig. 2** the interplay between the non-Newtonian focusing fluid and the spatial modulation of the channel cross-section: There is no stream splitting of the suspension of deformable particles for a Newtonian focusing fluid in modulated channels and no stream splitting with viscoelastic fluids in unmodulated, straight channels, but in combination of both.

Possible fluid inertia effects occur for larger values of the Reynolds number $Re = \frac{\rho v D_h}{\eta}$, with ρ is the fluid density, η the shear viscosity, v the average velocity and $D_h = \frac{2wh}{(w+h)}$ the hydraulic diameter with w is the channel width and h is the channel height. This gives for our typical flow conditions, i. e. $\rho = 1.0 \text{ g/cm}^3$, $\eta = 0.001 \text{ Pa}\cdot\text{s}$, $h = 100 \mu\text{m}$, $w = 250 \mu\text{m}$, $Q = 80 \dots 600 \mu\text{l/h}$ in the wide parts of the channel a Reynolds number in the range $Re = 0.2 \dots 1.6$ and in the narrow part $Re = 0.5 \dots 3.75$. Accordingly, inertia effects are expected to be not dominating in agreement with our observations.

In the case of a Newtonian focusing fluid in **Fig. 1** the slight particle depletion near the top and the bottom channel wall is in agreement with the expected lift forces in shear flows near walls¹⁵⁻¹⁷ as well as with the particle-size dependent bulk migration of deformable particles¹¹⁻¹⁴. The slight enhancement of the particle density for a shear thinning focusing fluid near the upper and bottom wall for a straight channel in **Fig. 2 Ia** is also consistent with the observed scenarios reported from previous experiments.²⁸

The shear thinning focusing fluid leads to a flattening for the velocity profile near the center of the flow channel. Complementary, the magnitude of the shear gradient and its spatial variation is enhanced in layers closer to the walls. Accordingly, wavy side-wall boundaries cause wavy streamlines mainly in the two shear thinning regions (STR) close to the upper and lower channel boundary, where the stream splitting is observed. These wavy streamlines are visualized by the wavy particle concentration in **Fig. 2 Ib**. The amplitude of the sinusoidal flow lines increases from zero at the channel center up to the modulated boundaries. In addition, the flow velocity along the flow lines in the STR's decreases with increasing distance from their centers, while the shear rate increases with distance from the centers of the STR's.

A linear shear flow is composed of a rotational and an elongational flow, where the elongational component is oblique to the local stream direction. Accordingly, the mean shape of deformable particles in shear flow is elliptical and the major axis of this ellipse encloses an angle ψ with the local flow direction¹²⁻¹⁴. The dynamics of such deformed particles causes the lift force of soft particles away from flow-channel boundaries¹²⁻¹⁴. Flow fields in channels show nonlinear shear profiles, i. e. the shear rate changes across the finite size of the particles. Therefore, deformable particles migrate across the local streamlines to ranges of smaller shear rates, i. e. in Poiseuille flows to the channel center¹⁵⁻¹⁷. In shear thinning fluids this migration may reverse, and deformable particles migrate under certain condition also away from the center of straight channels³⁷, but this effect is not dominating according to the results in **Fig. 2**. For small molecules like low molecular weight dyes cross-stream migration would not be expected.

Next, we focus on particle migration in the STR's. The particle's inclination angle ψ has the same sign in both halves of a STR at the top and the bottom of the flow channel. The wavy streamlines in each half of the STR's cause an inhomogeneous, spatially modulated elongational flow. This leads to a spatial variation of the particle inclination angles ψ (without sign change). Accordingly, simultaneously the angle ψ and the shapes of flexible particles are different in each of both halves of a modulation wavelength. Therefore, the effects of a variation of the extensional flow acting across differently shaped particles and the overall drag forces cause different forces on the particles in each half of a modulation period. This difference leads to a net drag force per modulation-period and is mainly caused by geometrical factors. For particles in wavy streamlines of Newtonian fluids, this net force points always to the wavy channel boundaries and therefore away from the channel center.

This net force induced by the stream line modulations increases with modulation amplitudes and therefore with the distance from the channel center. Beyond a certain modulation amplitude this induced outward directed net migration outperforms the inward directed migration caused by the

shear gradient variation across a particle, i. e. the direction of net-migration changes its sign beyond a certain distance from the channel center: The sign change never reaches the range near channel center with straight streamlines. As a result, there is in modulated channels always a central particle stream left and therefore stream splitting.

This qualitative model is well in agreement with our experimental observations. The splitting effect is only observed in the high shear regions at the ceiling and floor of the microfluidic channels, where high shear rates lead to particle deformation and alignment. It is further only observed for sinusoidal channels, which are necessary to generate high extensional flow rates. These are highest at the beginning and at the end of each sine section. The extensional flow has different directions in the widening and in the narrowing section of each sine period, i.e. in the widening section in the first half of the sine period it is perpendicular to the flow direction, and in the narrowing section in the second half of the sine period it is parallel to the flow direction. This has been recently demonstrated in ref.²⁸. As the extensional force varies over the size of the particle, and because it has different directions with respect to the local orientation of the particles in the first and the second half of a sine period, it leads to a net migration over a certain distance towards the outer channel boundaries over each sine section. Higher flow rates, larger sine amplitudes and smaller sine periods lead to increased extensional forces and thus larger migration distances, which is well in agreement with our experiments.

2.4 Separation of different colloids

From our explanation it follows that the immersion of colloidal particles in a transient polymer network is a necessary condition for stream splitting and separation. The combination of wormlike PI-PEO micelles in a PEO homopolymer network was chosen because of the mutual thermodynamic miscibility of the PEO polymer components. The miscibility can be affected by an increased viscosity, which prevents interdiffusion within the residence time in the microfluidic channels, and by thermodynamic effects such as depletion-induced demixing, which can particularly occur for mixtures of high molecular weight linear polymers and larger colloids. We therefore increased the concentration of the wormlike micelles from 1 over 5 to 10 wt% and investigated the streams under the standard flow conditions as outlined in **Fig. 1**. The streams were visualized by polarized light microscopy images at the entrance into the sinusoidal channel and at the last sine section. Whereas for the 1 wt% solution we observe a strong stream splitting and separation, for the 5 wt% solution the separation is less pronounced, and finally for the 10 wt% solution we observe no stream splitting at all, as visible in the ESI[†] (Fig. S5). This is related to the much larger viscosity of the concentrated wormlike micellar solution, but also indicates the expected depletion effect.

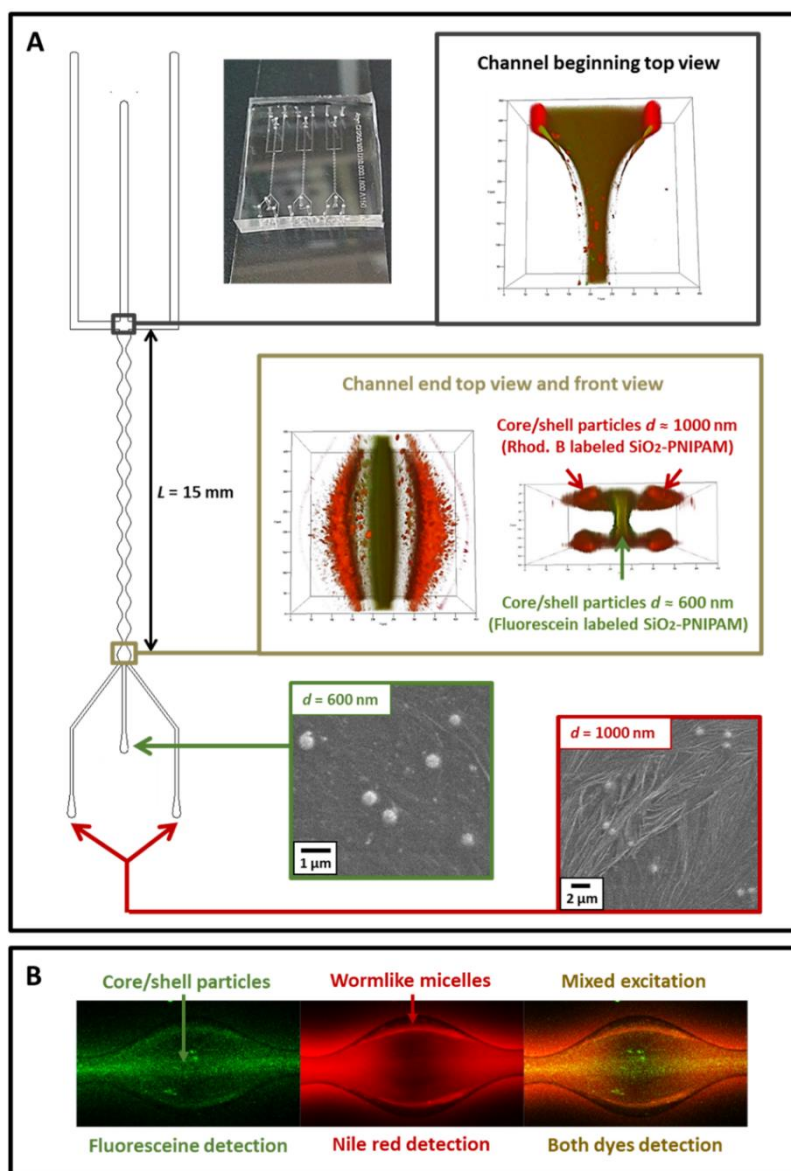


Fig. 4 (A) Sinusoidal microchip with three outlets for particle separation and 3D-CLSM images at channel cross and end. The device is used for non-Newtonian 1 wt% PEG(900 k)-focusing of a bimodal distributed mixture of spherical SiO_2 -PNIPAM core-shell particles with a diameter of $d = 1000$ nm and 600 nm. At the channel end, the two particle sizes are separated into a green center stream with fluorescein (FITC) labeled 600 nm particles and into four red sub-streams at the channel edges with rhodamine B (Rhod B) labeled 1000 nm particles. SEM images of the collected particle sizes are shown, whereby the bigger 1000 nm particles have been collected by the two side channels and the smaller 600 nm particles by the main channel. (B) Tripartite CLSM image at the channel end of the separation of a mixture of spherical core-shell particles $d = 600$ nm (FITC) and anisotropic wormlike micelles $d = 20$ nm (Rhod B) with polydisperse lengths focused by the same PEG-solution. Here, two detected emission wavelengths are shown, just FITC (left) and just Rhod B (mid) but also the overlay from both (right). In (A) we observe the separation of the bimodal distributed mixture of core-shell particles, and in (B) the separation of the wormlike micelles from the core/shell particles, corresponding to purities of $>80\%$ and $>70\%$, respectively, as outlined in the Supporting Information (Fig. S7).

As cross-stream migration is an effective mechanism for particle separation, we investigated the possibility to separate colloids of different size in the splitting streams. We used a binary mixture of spherical silica-PNIPAM core-shell particles with a diameter of 600 nm, which were fluorescently labeled with fluorescein, and a diameter of 1000 nm which were labeled with rhodamine B. We used standard flow conditions ($w = 400 \mu\text{m}$, $h = 100 \mu\text{m}$, $L = 1 \text{ cm}$, $Q = 3 \times 200 \mu\text{L/h}$, 1 wt% PEG900k) with a sinusoidal channel ($P = 800 \mu\text{m}$, $A = 150 \mu\text{m}$) that exits into three outlet channels as shown in **Fig. 4**. The location of the fluorescently labeled colloids could be followed by CLSM. **Figs. 4A** and **S7A** (Supporting Information) demonstrate that purities of $> 80\%$ are achieved after the 12th sine section for each of the 600 and 1000 nm core/shell particles, and $> 70\%$ for each of the wormlike micelles and 600 nm core/shell particles. The purities can be further increased by using channels with a larger number of sine sections.

Conclusion

We observed the splitting of streams of wormlike and spherical colloids into four substreams within sinusoidal microchannels. Splitting occurred when the streams were focused with a viscoelastic polymer solution. This effect could be used to separate spherical colloids of different size and spherical from wormlike colloids. By variation of the experimental conditions such as 2D- vs. 3D-focusing, straight vs. sinusoidal channels, sine period and amplitude, PEO molecular weight, Newtonian vs. non-Newtonian fluids we were able to reveal the essential conditions for the stream splitting effect which are caused by a combination of high extensional and shear rates in the shear-thinning zones of the modulated microchannels. This phenomenon can be generally used to separate colloidal and cellular particles according to their size.

Conflicts of interest

There are no conflicts of interest to declare.

Acknowledgements

This work was financial supported by the German Ministry for Education and Research under Grant 05K13WC5 and the European Research Council Advanced Grant 291211. Prof. Dr. Matthias Karg acknowledges financial support from the German Research Foundation (DFG) via Emmy Noether programme.

References

1. P. Sajeesh and A. K. Sen, *Microfluidics and Nanofluidics*, 2014, **17**, 1-52.
2. D. R. Gossett, W. M. Weaver, A. J. Mach. S. C. Hur, H. T. K. Tse, W. Lee, H. Amini, D. Di Carlo, *Anal. Bioanalyt. Chem.*, 2010, **397**, 3249-3267.
3. A. Karimi, S. Yazdi, A. M. Ardekani, *Biomicrofluidics* 2014, **7**, 021501.
4. G. Segre and A. Silberberg, *Nature*, 1961, **189**, 209-210.
5. J. Zhang, S. Yan, D. Yuan, G. Alici, N.-T. Nguyen, M. Ebrahimi Warkiani and W. Li, *Lab on a Chip*, 2016, **16**, 10-34.
6. D. Di Carlo, *Lab on a Chip*, 2009, **9**, 3038-3046.
7. H. Amini, E. Sollier, W. M. Weaver and D. Di Carlo, *Proceedings of the National Academy of Sciences*, 2012, **109**, 11593-11598.
8. A. A. S. Bhagat, S. S. Kuntaegowdanahalli and I. Papautsky, *Microfluidics and Nanofluidics*, 2009, **7**, 217-226.
9. S. C. Hur, N. K. Henderson-MacLennan, E. R. B. McCabe and D. Di Carlo, *Lab on a Chip*, 2011, **11**, 912-920.
10. D. Yuan, Q. Zhao, S. Yan, S.-Y. Tang, G. Alici, J. Zhang and W. Li, *Lab on a Chip*, 2018, **18**, 551.
11. S. Yang, S. S. Lee, S. W. Ahn, K. Kang, W. Shim, G. Lee, K. Hyun and J. M. Kim, *Soft Matter*, 2012, **8**, 5011-5019.
12. B. Kaoui, G. H. Ristow, I. Cantat, C. Misbah and W. Zimmermann, *Phys. Rev. E* 2008, **77**, 021903.
13. S. K. Doddi and P. Bagchi, *Int. J. Multiphas. Flow* 2008, **34**, 966.
14. G. Couplier, B. Kaoui, T. Podgorski and C. Misbah *Phys. Fluids* 2008, **20**, 111702.
15. I. Cantat and C. Misbah, *Phys. Rev. Lett.* 1999, **83**, 880.
16. U. Seifert, *Phys. Rev. Lett.* 1999, **83**, 876.
17. M. Abkarian, L. Lartigue and A. Viallat, *Phys. Rev. Lett.* 2002, **88**, 068103.
18. F. Del Giudice, S. Sathish, G. D'Avino and A. Q. Shen, *Anal. Chem.* 2017, **89**, 13146-13159.
19. D. Li, X. Lu and X. Xuan, *Anal. Chem.*, 2016, **88**, 12303-12309.
20. C. Raghunath, G. W. Roland and G. Gerhard, *EPL (Europhysics Letters)*, 2010, **91**, 14001.
21. D. Steinhauser, S. Köster and T. Pfohl, *ACS Macro Letters*, 2012, **1**, 541-545.
22. N. Xiang, Q. Dai and Z. Ni, *Applied Physics Letters*, 2016, **109**, 134101.
23. C. Liu, C. Xue, X. Chen, L. Shan, Y. Tian and G. Hu, *Anal. Chem.* 2015, **87**, 6041-6048.
24. T. Go, H. Byeon and S. J. Lee, *Scientific Reports*, 2017, **7**, 41162.
25. C. F. Hewitt and J. S. Marschall, *J. Fluid Mech.* 2010, **660**, 258-281.
26. S. Cha, K. Kang, J. B. You, S. G. Im, Y. Kim and J. M. Kim, *Rheol Acta* 2014, **53**, 927-933.

27. D. Yuan, J. Zhang, S. Yan, C. Pan, G. Alici, N. T. Nguyen and W. H. Li, *Biofluidmechanics* 2015, **9**, 044108.
28. M. Trebbin, D. Steinhauser, J. Perlich, A. Buffet, S. V. Roth, W. Zimmermann, J. Thiele and S. Förster, *Proc. Natl. Acad. Sci. USA*, 2013, **110**, 6706-6711.
29. K. Devanand and J. C. Selser, *Macromolecules*, 1991, **24**, 5943-5947.
30. S. Mukherjee and K. Sarkar, *Physics of Fluids*, 2014, **26**, 103102.
31. N. T. Nguyen and S. Wereley, *Fabrication Techniques for Microfluidics*, Artech House, Norwood, MA, 2002.
32. G. M. Whitesides and Y. Xia, *Annu. Rev. Mater. Sci.*, 1998, **28**, 153-184.
33. S. R. Quake and A. Scherer, *Science*, 2000, **290**, 1536-1540.
34. J. C. McDonald, D. C. Duffy, J. R. Anderson, D. T. Chiu, H. Wu, O. J. A. Schueller and G. M. Whitesides, *Electrophoresis*, 2000, **21**, 27-40.
35. S. Förster and E. Krämer, *Macromolecules*, 1999, **32**, 2783-2785.
36. A. Rauh, M. Rey, L. Barbera, M. Zanini, M. Karg and L. Isa, *Soft Matter*, 2017, **13**, 158-169.
37. S. A. Vasudevan, A. Rauh, L. Barbera, M. Karg and L. Isa, *Langmuir*, 2018, **34**, 886-895.

Supporting Information

Detailed photo- and soft lithographical microchip fabrication

The whole preparation process of polydimethylsiloxane (PDMS) microfluidic devices is shown in Fig. S1. The first step contains the photolithography which is performed in a clean room by spin-coating (Cee 200X, Brewer Science Inc.) a negative photoresist (SU-8 50, Microchem Corp.) onto a 3" silicon wafer, as visible in Fig. S1A. If a so-called 2D-chip design for 2D-focusing is prepared, just one layer of photo resist SU8-50 is spin-coated to build up a channel structure of 100 μm height. For producing a 3D-focusing chip design, two layers about 50 μm and 100 μm as well as two chip parts with channel structures are necessary to finally receive a higher channel height for the two side channels of 250 μm in comparison to the middle channel with 50 μm . The microchannel structures are imparted to the photoresist using a mask aligner (MJB4, SÜSS MicroTec SE). The uncured photoresist is removed in the subsequent development process which yields a one-layered respectively two-layered master. All detailed geometric design parameters of the sinusoidal and linear microchannels are shown in the main publication. The second part of the fabrication process, the soft lithography¹, continues under dust-free conditions by replicating the micro structured master using polydimethylsiloxane (PDMS, Sylgard 184 kit, Dow Corning Corp.) and curing it for $t = 1.5$ h at $T = 75$ °C, as visible in Fig. S1B. The PDMS replica is removed from the master and inlet ports are punched into the polymer using home-made punch needles with an outer diameter of $d = 1$ mm. The PDMS is cut into smaller pieces for better handling whereby the channel design allows preparing several microchannels simultaneously. The final microfluidic device is created by bonding the PDMS replica for a 2D-chip onto a glass slide and the two structured PDMS chip halves to each other for a 3D-device. This is achieved by activating the PDMS and glass surface using air plasma (MiniFlecto-PC-MFC, Gala Instrumente GmbH), respectively the two PDMS chip halves by adding a little drop of pure water (0.2 μm -filtered Millipore) for initially aligning and finally drying at $T = 30$ °C for about $t = 1$ h. The use of a microscope helps during the alignment step and in addition to it the integrated orientation structures of the multi-layer design will snap in and align the microstructures automatically with high precision.

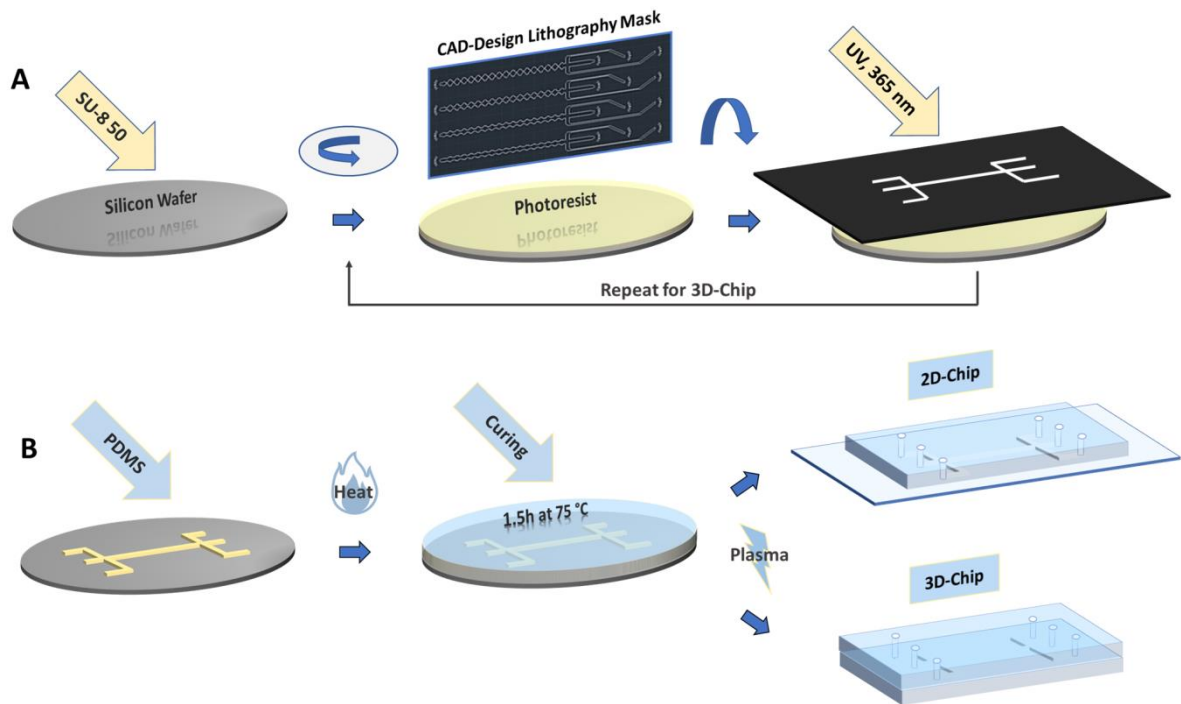


Fig. S1 Fabrication of microfluidic devices made of PDMS. (A) Master device fabrication based on SU-8 50 photoresist using photolithography with UV-exposure whereby the photolithographic master for 3D-chips involves one repeating step to build up a multilayered microstructure. After development, the uncured photoresist is removed. (B) The resulting 2D- respectively 3D-microchannel template is replicated by using soft lithography¹. Therefore, the PDMS is poured onto the master device and cured for $t = 1.5$ h at $T = 75$ °C. Afterwards, the PDMS replica is peeled off the master device, cut into the chip parts and inlet ports for fluids are added. After plasma treatment of the two PDMS halves respectively the glass surface for a 2D-chip, the device is sealed using air plasma treatment.

Characterization of colloids

The microfluidic devices for detailed jet-splitting analysis have been run by focused wormlike micelles which are prepared out of polyisoprene-*b*-polyethylene oxide (PI-PEO) and are polydisperse concerning their length. A solution with a concentration of $c = 0.1$ wt% wormlike micelles is shown by a cryo-transmission electron microscopy (cryo-TEM) image in Fig. S2A. The 2D-microfluidic chips with sinusoidal microchannels have been used to carry out separation experiments on a mixture of two different sizes of silica-poly-*N*-isopropyl-acrylamide (SiO₂-PNIPAM) core-shell particles. The mixture consisted of SiO₂-PNIPAM core-shell particles with a diameter of $d = 600$ nm (polydispersity index, $PDI = 0.03$) labeled with rhodamine B respectively 1000 nm ($PDI = 0.25$) labeled with fluorescein. A sample of the bigger core-shell particles with a diameter of 1000 nm is visible by fluorescent microscopy in Fig. S2B and the sample of the smaller particles with a diameter of 600 nm are shown in the fluorescent microscopic (FlucMic) image of Fig. S2C. The separation experiments have been run by using a 2D-microfluidic chip with sinusoidal microchannels as well as lateral focusing by the side channels via a non-Newtonian solution of polyethylene glycol (PEG) in water. A sample of 1 wt% PEG with a molar mass of $M = 900,000$ g/mol which includes the bimodal size distributed mixture of 600 nm and 1000 nm core-shell particles are displayed by the scanning electron microscopy (SEM) image of Fig. S2D. Here, the prepared sample was dried out at a certain percentage before SEM images could be taken which led to a recrystallization of the polyethylene glycol polymer chains. Thus, bundles of PEG chains could be observed via SEM which verified the expected PEG polymer network.

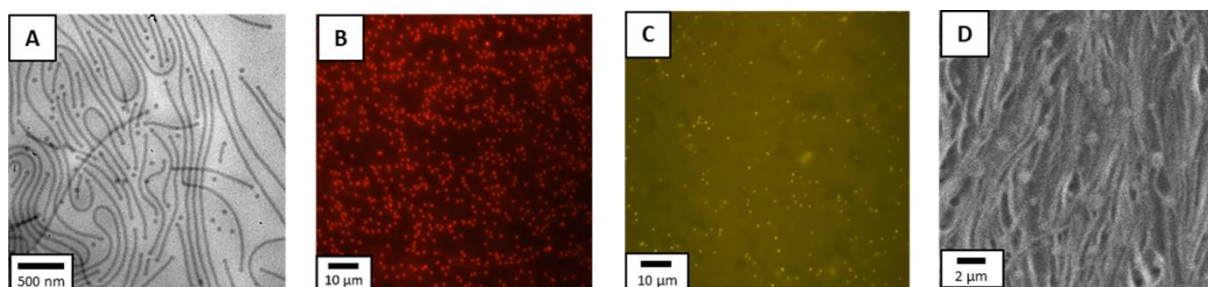


Fig. S2 (A) Cryo-TEM image of a PI₁₁₀-PEO₁₉₈ wormlike micelles solution with a concentration of $c = 0.1$ wt% in water. (B) FlucMic image of rhodamine B-labeled SiO₂-PNIPAM core-shell particles with a total diameter of 1000 nm and a concentration of $c = 0.17$ vol% in water. (C) FlucMic image of fluorescein-labeled SiO₂-PNIPAM core-shell particles with a total diameter of 600 nm and a concentration of $c = 0.13$ vol% in water. (D) SEM image of a sample of 1 wt% PEG with a molar mass of $M = 900,000$ g/mol including the bimodal size distributed mixture of 600 nm and 1000 nm core-shell particles.

Detailed flow profile analysis

In all three parts of Fig. S3 are shown 3-dimensional confocal laser scanning microscopy (3D-CLSM) images for flow profile analysis of focused wormlike micelles (1 wt%) flowing in a sinusoidal microchannel with a width of $w = 250 \mu\text{m}$, a height of $h = 100 \mu\text{m}$ and a distance of $L = 15 \text{ mm}$ as well as a periodic wavelength of $P = 800 \mu\text{m}$ and an amplitude of $A = 150 \mu\text{m}$. In Fig. S3A, a mixture of 1 wt% wormlike micelles dyed with Nile red and 1 wt% PEG with a molar mass of 900,000 g/mol in water was pumped in one inlet through a sinusoidal microfluidic channel of a 2D-chip with varying flow rates. The images for flow rates of $v = 30 \mu\text{L/h}$, $200 \mu\text{L/h}$ and $2000 \mu\text{L/h}$ concerning each of the three inlets show no appearing jet-splitting effect if no colloid focusing by a cross section with side channels is used. Thus, a 2D-device with lateral 2D-focusing of the 1 wt% wormlike micelle solution via non-Newtonian 1 wt% PEG ($M = 900,000 \text{ g/mol}$) from the two side channels is shown in Fig. S3B for a flow rate of $v = 80 \mu\text{L/h}$ for all three inlets. Here, the jet-splitting effect has developed in one main stream and two horizontally divided sub-streams by using the contact of the shear thinning wormlike micelle solution to the top and bottom of the microchannel at the beginning cross section where the highest shear rates appear. As visible, the jet-splitting increases with each sine wave due to the existing expansion zones with higher extension rates after each narrowing section which leads to a shear thinning and sideward pulling of the PEG polymer network entangled wormlike micelles. In Fig. S3C, there is displayed a 3D-chip with a fully-surrounded 3D-focusing for the wormlike micelle solution with the same flow rate of $v = 80 \mu\text{L/h}$ which leads to no jet-splitting effect anymore due to the missing wall contact of the wormlike micelles.

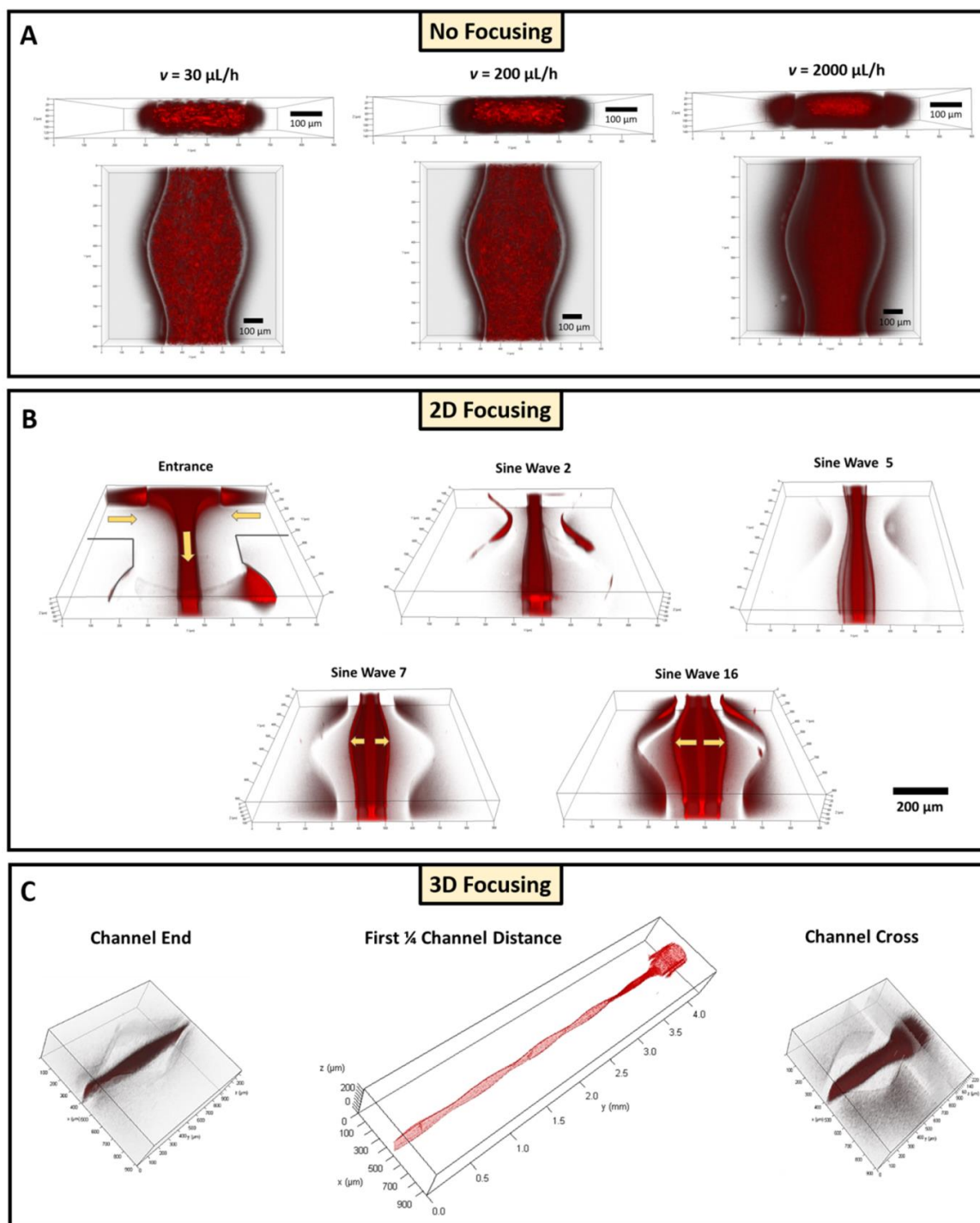


Fig. S3 3D-CLSM flow profile images of Nile red dyed wormlike micelles (1 wt%) within the standard sinusoidal microchannel ($w = 250$, $P = 800$, $A = 150$, $h = 100$, $L = 15.000 \mu\text{m}$). (A) 2D-chip with a mixture of 1 wt% wormlike micelles and 1 wt% PEG(900k) that is pumped with three various flow rates ($v = 30 \mu\text{L/h}$, $200 \mu\text{L/h}$, $2000 \mu\text{L/h}$) and without any focusing through one inlet channel whereby no jet-splitting effect appears. (B) 2D-chip with 2D-focusing of a wormlike micelles solution by two side channels via 1 wt% PEG(900k) that leads to rising jet-splitting within the sine channel. (C) 3D-chip with 3D-focusing of a wormlike micelle solution by two higher side channels does again not create a jet-splitting effect within the whole sinusoidal channel.

In following Fig. S4, there is shown a detailed analysis of the appeared jet-splitting effect of a 2D-laterally focused 1 wt% wormlike micelle solution with a flow rate of $\nu = 200 \mu\text{L/h}$ for each of the three inlets of the sine channel ($w = 250$, $P = 800$, $A = 150$, $h = 100$, $L = 15.000 \mu\text{m}$) based on 3D-CLSM as well as polarization microscopy (PolMic) images. Fig. S4A illustrates the 3D-CLSM images with a front view of the flow profiles within the beginning cross section and after the third, seventh and ninth sinus wave along the sinusoidal microchannel. After the channel entrance, the jet-splitting starts directly at the cross section by existing extension rates and afterwards it increases within the first and all following sine waves due to further rising extension rates within each sine wave. It is clearly visible that the created sub-streams are pulled from the center towards the channel side walls just near to the channel top and bottom. Moreover, we can also observe that the two sub-streams are horizontally divided and forming four sub-streams which move subsequently after each sine wave more near to the channel edges.

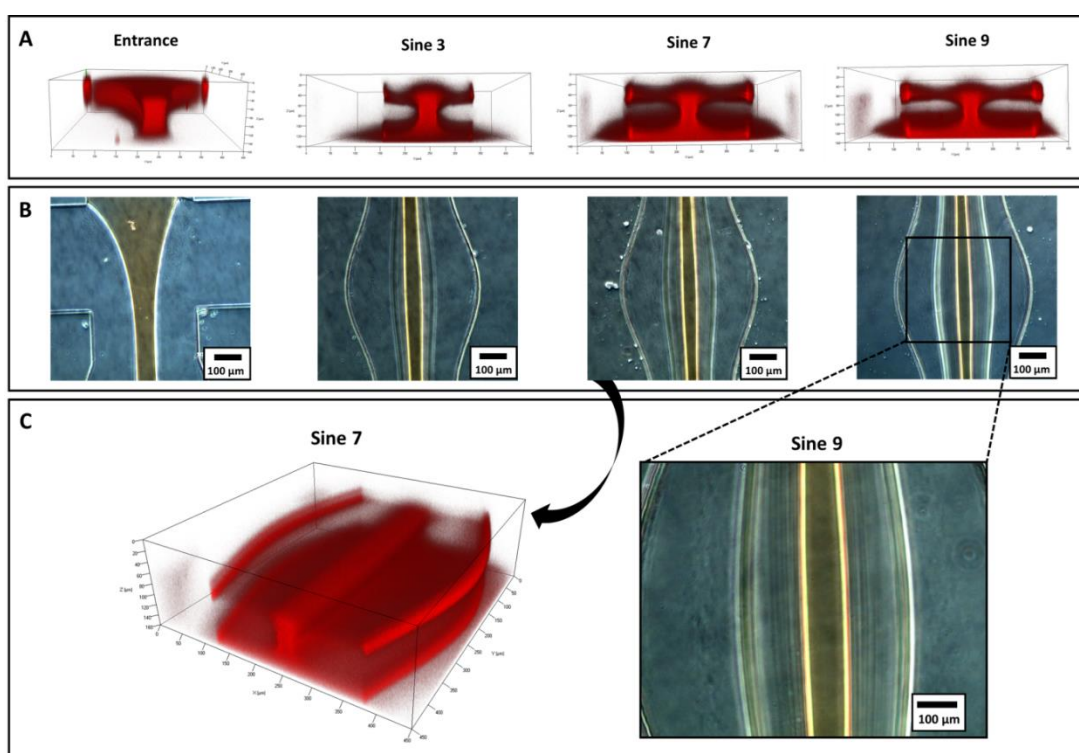


Fig. S4 (A) 3D-CLSM front view images of flow profiles from 1 wt% PEG ($M = 900,000 \text{ g/mol}$) 2D-laterally focused Nile red dyed wormlike micelles (5 wt%) within the beginning cross section as well as after the third, seventh and ninth sinus wave along the sinusoidal microchannel. The flow rate amounts to $\nu = 200 \mu\text{L/h}$ for all three inlets. (B) PolMic top view images to the upper 3D-CLSM images: Orange areas indicate orientation of wormlike micelles in flow direction y , and blue areas would indicate orientation in x axis which means perpendicular to the flow direction.

For each of the 3D-CLSM front view images also the matching polarized optical microscopy images from the top view are taken and displayed in Fig. S4B. PolMic makes it possible to analyze the flow orientation of the wormlike micelles within the microchannel. Here, the used quarter wave plate allows us to distinguish between an orange interference color for the vertically oriented micelles in flow direction and

a blue color for the horizontally orientated micelles perpendicular to the flow. Consequently, all wormlike micelles within the main mid-stream are orientated in flow direction. The micelles within the two sub-streams are also quite orange and thus mainly aligned in flow direction but are able to turn out more within the sub-streams due to a lower flow velocity which is based on the parabolic flow profile conditions in a microfluidic channel.

Moreover, flow profiles for different wormlike micelle concentrations are shown in ensuing polarization microscopy (PolMic) top view images of Fig. S5. The flow rates for each of the three channel inlets were again constant with $v = 200 \mu\text{L/h}$. The lowest focused wormlike micelle concentration of $c = 1 \text{ wt}\%$ showed the broadest jet-splitting already at lower flow rates with less than $v = 100 \mu\text{L/h}$. With increasing concentration, up to $c = 5 \text{ wt}\%$ the jet-splitting is visible just with higher flow rates more than $v = 150 \mu\text{L/h}$ and the sub-streams can broaden up to the maximum which is limited by the channel side walls by using a flow rate of $v = 1000 \mu\text{L/h}$, shown in Fig. S5A.

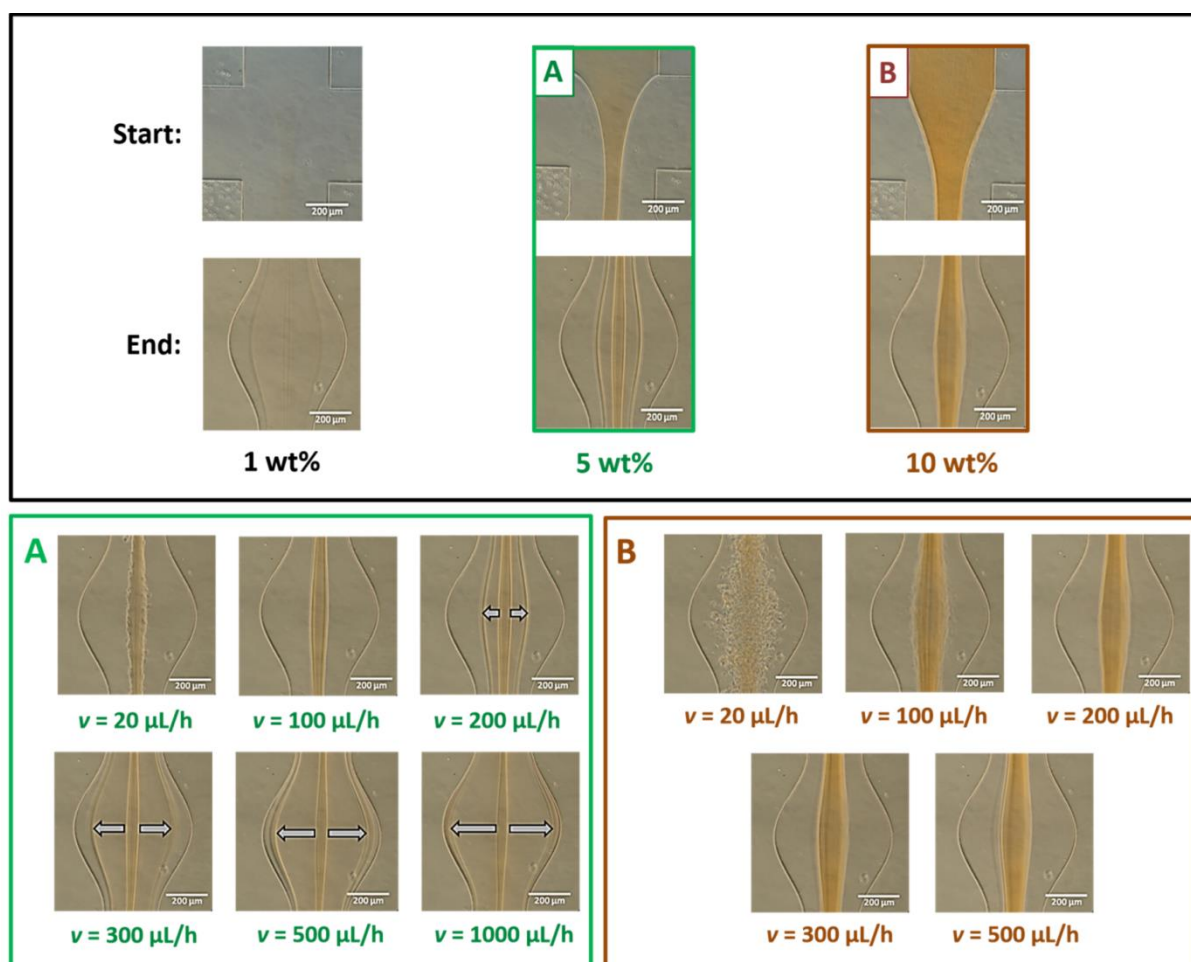


Fig. S5 Polarization microscopy (PolMic) top view images of flow profiles with a constant flow rate of $v = 200 \mu\text{L/h}$ and three different wormlike micelles concentrations (1 wt%, 5 wt%, 10 wt%) again focused with 1 wt% PEG: (A) PolMic flow profiles of the 5 wt% wormlike micelles solution with varying flow rates between $v = 20 \mu\text{L/h}$ and $1000 \mu\text{L/h}$. (B) PolMic flow profiles of the 10 wt% wormlike micelles solution with varying flow rates between $v = 20 \mu\text{L/h}$ and $500 \mu\text{L/h}$.

However, the jet-splitting does not occur anymore with the highest wormlike micelles concentration of $c = 10$ wt%, also for flow rates up to $v = 500$ $\mu\text{L/h}$ as visible in Fig. S5B. The reason for the lower jet-splitting effect with higher wormlike micelles concentration is connected to the higher entanglement and thus viscosity. These properties make it more difficult for the PEG chains to pull the wormlike micelles out of center position via the existing extensional rates within sinusoidal microchannels. Additionally, by using polarization microscopy it was also possible to analyze the flow orientation of the concentrated wormlike micelles within the channel. Here, the used quarter wave plate displays an orange interference color for the vertically oriented micelles in flow direction and a blue color for the horizontally orientated micelles perpendicular to the flow. Thus, all wormlike micelles are orientated in flow direction within the sub-streams and also the main mid-stream. Just for the 5 wt% micelles solution in Fig. 5SA a slight blue coloring of micelles orientated perpendicular to the flow direction is visible at the edge of the channel cross due to the lateral flow focusing.

Rheological Data

The rheological behaviour of the used focusing fluids was experimentally determined by a rheometer (Bohlin Germini HR^{Nano} Rotometric drive 2, Malvin Instruments GmbH). The rheometer was used in combination with a Peltier-plate (MV-4, JULABO USA Inc.) for temperature control and varying sizes of a coaxial cylinder-plate, cone-plate or plate-plate measurement system depending on the viscosity of the analyzed fluid. All measurements have been carried out with the rheometer software (Bohlin v2.0) by using a shear rate setting at a temperature of $T = 25$ °C. Fluids with a very low viscosity like water or the used 1 wt% PEG solution with a low molar mass of $M = 6,000$ g/mol was measured with the coaxial cylinder geometry C25 which has a diameter of $d = 25$ mm. For all other samples with much higher viscosity, like pure glycerin or 1 wt% PEG with a molar mass of $M = 300,000$ g/mol respectively 900,000 g/mol was measured with the cone-plate system CP4 /40 that has a diameter of $d = 40$ mm. All measured liquids which have been used as focusing fluids for the wormlike micelles respectively for the core-shell particles are visible in the rheological diagram of Fig. S5. Here, the Newtonian fluids, like the measured glycerin with a dynamic viscosity of $\eta = 956$ mPa·s or water with $\eta = 0.9$ mPa·s at $T = 25$ °C according to literature², show naturally constant viscosities with the tested shear rates from $\dot{\gamma} = 1\text{E-}4$ s⁻¹ up to 1.000 s⁻¹. These shear rates also include the shear rates which appear within a microfluidic channel. By evaluating the non-Newtonian solutions of 1 wt% PEG with different molar mass, a strong reduction of the viscosity is verified whereby the smallest viscosity for all three of them is always reached with a minimum shear rate of at least about $\dot{\gamma} = 1$ s⁻¹. All of these PEG's have an initial viscosity of about $\eta \approx 100,000$ mPa·s and with a shear rate higher than $\dot{\gamma} = 1$ s⁻¹ the viscosity for the PEG with a molar mass of $M = 900,000$ g/mol is decreased to a constant value of $\eta = 26$ mPa·s, respectively to $\eta = 12$ mPa·s for the PEG with $M = 300,000$ g/mol and to $\eta = 4$ mPa·s for the PEG with $M = 6,000$ g/mol. This evidenced shear thinning behavior here is the foundation for the explanation of the discovered jet-splitting effect and is based on the entangled polymer network of the non-Newtonian PEG focusing fluid which disconnects itself by the higher shear rates near to the channel walls.³

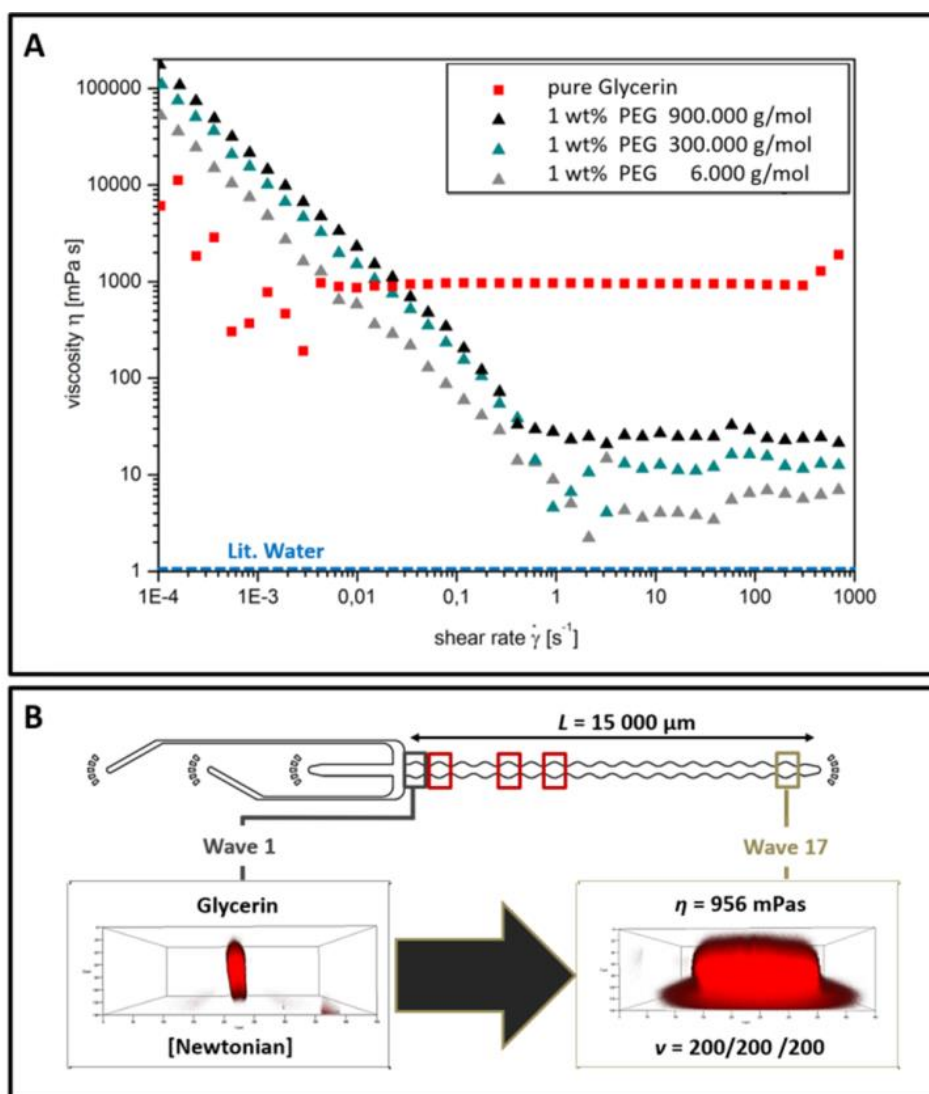


Fig. S6 (A) (A) Rheological diagram about the viscosity curves of Newtonian glycerin, water and non-Newtonian 1 wt% PEG with different molar mass ($M = 6,000\ \text{g/mol}$, $300,000\ \text{g/mol}$ and $900,000\ \text{g/mol}$) in dependence from the shear rates. (B) 3D-CLSM front view images of the flow profiles of fluorescent dyed 1 wt% wormlike micelles in water within the standard sinusoidal channel ($w = 250$, $P = 800$, $A = 150$, $h = 100$, $L = 15\ \text{mm}$) by using high-viscous Newtonian glycerin. The scatter of the data for glycerin at low shear rates and at shear rates $>200\ \text{s}^{-1}$ is due to limitations of the force sensor of the rheometer.

Separation and Purity

To calculate we purity of the sine channel-separated particles we chose the CLSM-images in Fig. 4 to quantitatively determine the fluorescence intensities for each of the particles across the channel as indicated in the regions of interest shown in Fig. S7. The background-subtracted fluorescence intensities shown in the lower panel of Fig. S7A show three peaks, two from the $1000\ \text{nm}$ SiO_2 -PNIPAM core/shell particles (rhodamine-B-labelled, red) in the outer streams, and one from the $600\ \text{nm}$ SiO_2 -PNIPAM core/shell particles (fluorescein-labelled, green) in the central stream. The purities were calculated

according to ref. ⁴ as $P_{1000} = \frac{A(\text{red})}{A(\text{red})+A(\text{green})} 100\%$ for the 1000 nm core/shell particles, where $A(\text{red})$ and $A(\text{green})$ are the integrated intensities over the peaks in the outer streams, indicated by the red scale bars, and as $P_{600} = \frac{A(\text{green})}{A(\text{red})+A(\text{green})} 100\%$ for the 600 nm core/shell particles, where $A(\text{red})$ and $A(\text{green})$ are the integrated intensities over the peak in the central stream, indicated by the green scale bar. We observe that after the 12th sine section there is a small fraction of 600 nm particles in the outer streams of the 1000 nm particles, and of 1000 nm particles in the central stream of the 600 nm particles. From the integrated peak areas, we calculate purities of $P_{1000} = 84\%$ for the 1000 nm particles in the left stream, and of 81% in the right stream. For the purity of the 600 nm particles in the central stream we obtain a value of 83%.

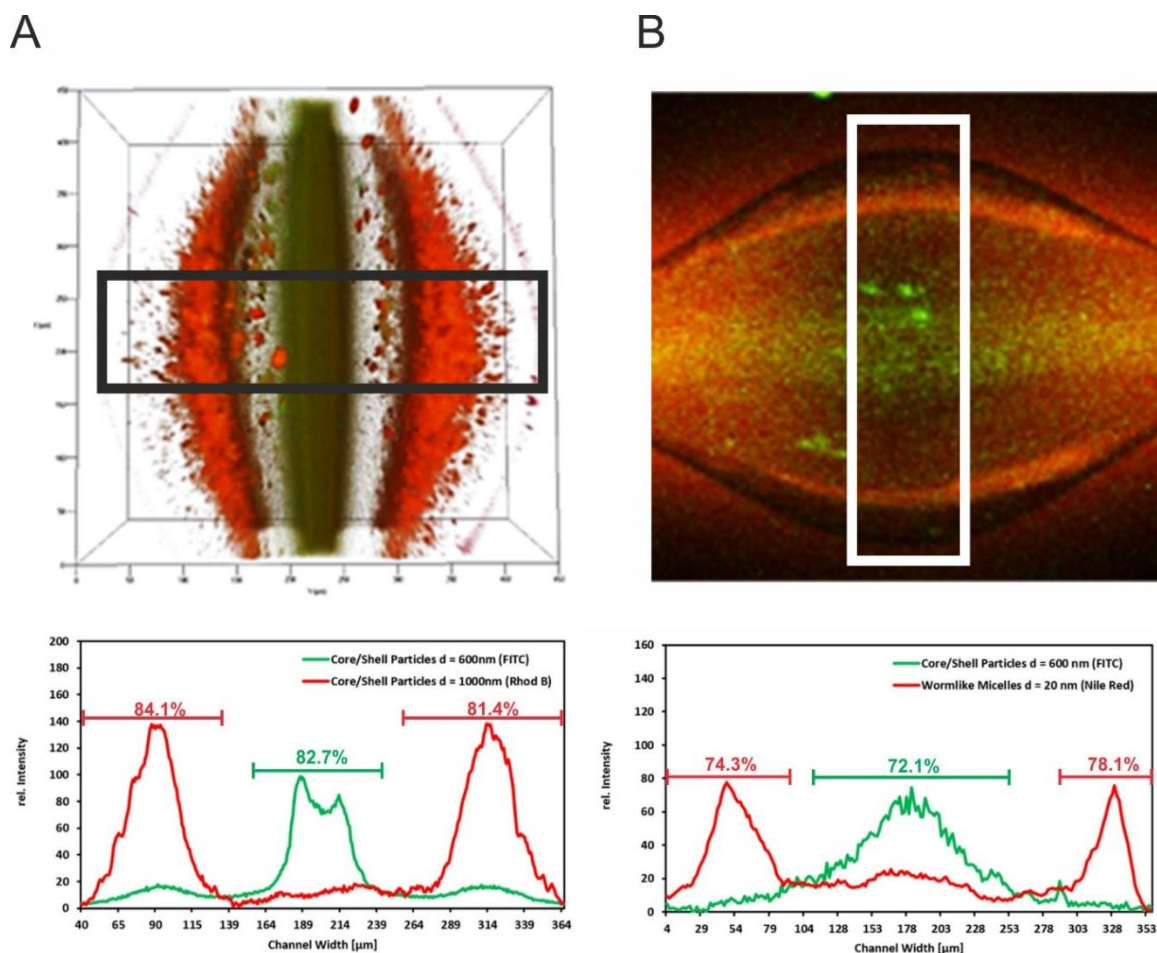


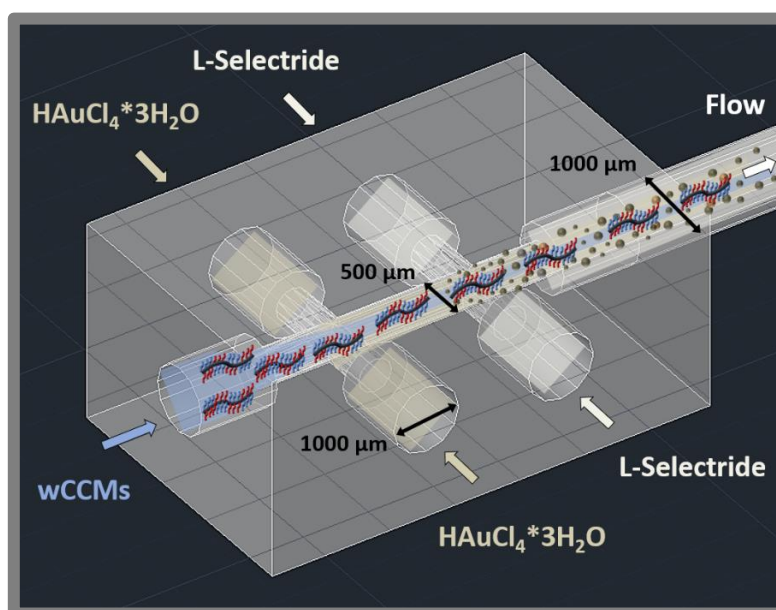
Fig. S7 (A) Section across the channel, indicated by the black rectangle (upper panel), with the corresponding fluorescence intensity profiles (lower panel), from which the purities for each of the separated 1000 nm SiO₂-PNIPAM core/shell particles (rhodamine-B-labelled, red) and 600 nm SiO₂-PNIPAM core/shell particles (fluorescein-labelled, green) was calculated. (B) Section across the channel, indicated by the white rectangle (upper panel), with the corresponding fluorescence intensity profiles (lower panel), from which the purities for each of the separated wormlike micelles (Nile red-labelled, red) and 600 nm SiO₂-PNIPAM core/shell particles (fluorescein-labelled, green) was determined. The scale bars indicate the integrated peak areas. The confocal images are reproduced from Fig. 4.

The background-subtracted fluorescence intensities shown in the lower panel of Fig. S7B similarly show three peaks, two from the wormlike micelles (Nile red-labelled, red) in the outer streams, and one from the 600 nm SiO₂-PNIPAM core/shell particles (fluorescein-labelled, green) in the central stream. The purities were similarly calculated as $P_{600} = \frac{A(\text{red})}{A(\text{red})+A(\text{green})} 100\%$ for the wormlike micelles, where $A(\text{red})$ and $A(\text{green})$ are the integrated intensities over the peaks in the outer streams, indicated by the red scale bars, and as $P_{600} = \frac{A(\text{green})}{A(\text{red})+A(\text{green})} 100\%$ for the 600 nm core/shell particles, where $A(\text{red})$ and $A(\text{green})$ are the integrated intensities over the peak in the central stream, indicated by the green scale bar. We observe that there is a small fraction of 600 nm particles in the outer streams of the wormlike micelles, and of wormlike micelles in the central stream of the 600 nm particles. From the integrated peak areas, we calculate purities of $P_{1000} = 74\%$ for the wormlike micelles in the left stream, and of 78% in the right stream. For the purity of the 600 nm particles in the central stream we obtain a value of 72%.

References

1. G. M. Whitesides and Y. Xia, *Annu. Rev. Mater. Sci.*, 1998, **28**, 153-184.
2. J. F. Coe and T. B. Godfrey, *Journal of Applied Physics*, 1944, **15**, 625-626.
3. M. Cross, *J Colloid Sci*, **20**, 417-437.

4.3 Strategies for the Selective Loading of Patchy Worm-Like Micelles with Functional Nanoparticles



Reproduced with permission from J. Schöbel, C. Hils, A. Weckwerth, **M. Schlenk**, C. Bojer, M.C.A. Stuart, J. Breu, S. Förster, A. Greiner, M. Karg, H. Schmalz published in *Nanoscale*, **2018**, *10* (38), 18257-18268. © **2018** The Royal Society of Chemistry.

Abstract

Block copolymer self-assembly in solution paves the way for the construction of well-defined compartmentalized nanostructures. These are excellent templates for the incorporation and stabilisation of nanoparticles (NPs), giving rise to highly relevant applications in the field of catalysis or sensing. However, the regio-selective incorporation of NPs in specific compartments is still an issue, especially concerning the loading with different NP types. Using crystallisation-driven self-assembly (CDSA), functional worm-like crystalline-core micelles (wCCMs) with a tailor-made, nanometre-sized patchy corona were prepared as versatile templates for the incorporation and stabilisation of metal and metal oxide NPs. Different strategies, like ligand exchange or co-precipitation of polymer stabilised NPs with one surface patch, were developed that allow the incorporation of NPs in specific regions of the patchy wCCM corona. Independent of the NP type and the incorporation method, the NPs showed no tendency for agglomeration and were fixed within the corona patches of the wCCMs. The binary loading of patchy micelles with metal and metal oxide NPs was realised by combining different loading strategies, yielding hybrids with homogeneously dispersed NPs guided by the patchy structure of the template.

Introduction

A major challenge of today's materials science is the developing miniaturisation, demanding precisely tuneable micro- and nanostructures. The self-assembly of amorphous block copolymers (BCPs) in solution proved to be an excellent tool to meet these demands, as a myriad of tailor-made micellar morphologies is accessible.¹ Spherical, cylindrical and helical micelles as well as vesicles are easily obtained by the use of selective solvents.²⁻⁶ More complex preparation steps involving crosslinking or guided hierarchical self-assembly protocols enable the formation of Janus, patchy and multicompart ment micelles (MCMs).⁷⁻¹⁴ Among the MCMs, common examples include clover-, hamburger-, raspberry- and football-like micelles, as well as one-dimensional supracolloidal polymer chains.¹⁵⁻¹⁸ Moreover, MCMs serve as building blocks for the formation of hierarchical superstructures, opening the way for applications in optoelectronic devices, in drug delivery or as templates for selective nanoparticle (NP) incorporation.^{9,19-22}

Although these state-of-the-art methods give access to manifold micelle morphologies, the preparation of well-defined cylindrical or worm-like micelles remains a challenge, as in general the length of the micelles cannot be precisely controlled, leading to broad length distributions.

To overcome these limitations in length control, crystallisation-driven self-assembly (CDSA) gained increasing attention since it is a powerful and very flexible method.^{15,23} Similar to living polymerisation, CDSA can be conducted in a living manner, i.e., the ends of the cylindrical micelles remain active for the addition of unimers (molecularly dissolved BCPs bearing a crystallisable block). This was first reported by Manners and Winnik et al. who self-assembled poly(ferrocenyldimethylsilane) (PFS) containing BCPs.^{24,25} Using a seeded- growth protocol, living CDSA enables a precise length control and opens the way for different micellar architectures like block comicelles (in analogy to BCPs), branched micelles, gradient block comicelles and hierarchical self-assemblies.²⁶⁻³⁶ In addition to PFS containing BCPs, a variety of other semi-crystalline polymers were reported to undergo CDSA, e.g. polyethylene (PE),^{37,38} poly(L-lactide),^{39,40} poly(3-hexylthiophene)^{41,42} and poly(ϵ -caprolactone).^{43,44} Recently, we have shown that worm-like crystalline-core micelles (wCCMs) with a patch-like microphase-separated corona can be prepared by CDSA of polystyrene-block-polyethylene-block-poly(methyl methacrylate) (SEM) triblock terpolymers.^{45,46} Here, the micellar corona is made of alternating nanometre-sized polystyrene (PS) and poly-(methyl methacrylate) (PMMA) patches and the semi-crystalline PE block forms the core. The concept of living CDSA was successfully transferred to the self-assembly of SEM triblock terpolymers employing spherical crystalline-core micelles (sCCMs) as seeds, giving access to patchy micelles with controlled length and length distribution as well as more complex architectures like patchy block comicelles.⁴⁷

Compartmentalised micelles are ideal templates for hybrid materials with inorganic NPs, as the structural complexity allows for a regio-selective incorporation of the NPs.^{20,48} This opens the way for applications in the biomedical sector (drug delivery, imaging), in the optoelectronic sector (nanodevices, photovoltaics) or in sensing and catalysis.^{49–58} Different hybrid materials derived from amorphous MCMs as well as crystalline- core micelles have been reported.^{52,53,55,57,59–65} However, these publications are mainly focused on the incorporation of only one type of NP, as the binary loading of compartmentalised micelles still remains a challenge and is hardly reported.^{66,67} The unique patchy structure of the SEM wCCM corona provides an excellent platform for the construction of tailor-made binary loaded hybrid materials, but this demands the efficient functionalisation of at least one of the corona forming blocks. Recently, we have reported the postpolymerisation amidation of the PMMA block of SEM triblock terpolymers using a 30-fold excess of different N,N-dialkylethylenediamines (alkyl = methyl, ethyl, iso-propyl).⁶⁸ This method showed some disadvantages regarding the harsh reaction conditions (≥ 60 h at 130 °C), the formed side products and the required large excess of amine. In particular, the formation of a large fraction of imide units (ca. 50 mol% with respect to the consumed PMMA units) resulted in low functionalisation degrees and limited solubility in organic solvents, especially for more polar N,N-dialkylethylenediamines (alkyl = methyl, ethyl). The limited solubility affected the CDSA and led to ill-defined, short wCCMs for degrees of functionalisation above 20% for the dimethyl derivative. Thus, only for nonpolar, sterically hindered alkyl substituents (iso-propyl groups) well-defined patchy wCCMs with a reasonable degree of functionalisation ($f = 55\%$) could be obtained. As a result, the first loading experiments with NPs revealed only a partial and inhomogeneous loading, most probably due to the insufficient functionalisation of the amidated patches.

Here, we report the use of functionalised patchy wCCMs as versatile templates for the regio-selective incorporation of NPs. This is realised by amidation of the PMMA block of SEM triblock terpolymers with activated N,N-dimethylethylenediamine (DMEDA), resulting in a nearly quantitative amidation. CDSA of the amidated SEM triblock terpolymers produces the desired patchy wCCMs, featuring highly functionalised corona patches for NP stabilisation. Different strategies for the regioselective loading of the amidated as well as non-functional PS patches with metal and metal oxide NPs are employed to yield the defined hybrid micelles. Finally, we present the successful binary loading of the patchy wCCMs with two different types of NPs (gold/zinc oxide and gold/silver).

Experimental

Materials

All chemicals were purchased from Sigma-Aldrich unless otherwise noted. Tetrahydrofuran (THF) was dried over calcium hydride and potassium prior to use and DMEDA (Acros Organics) over calcium hydride. Ethanol (99.5%), n-heptane, acetic acid (99.9%), L-Selectride (1 M in THF), n-butyllithium (n-BuLi, 2.5 M in hexane), PMMA ($M_w = 35 \text{ kg mol}^{-1}$, Acros Organics), tetrachloroauric acid trihydrate ($\text{HAuCl}_4 \cdot 3\text{H}_2\text{O}$, Alfa Aesar), silver trifluoroacetate (AgTFA), zinc acetate dihydrate, copper acetate, sodium hydroxide and lithium hydroxide monohydrate were used as received.

SEM triblock terpolymer

The SEM triblock terpolymers were synthesised by a combination of living anionic polymerisation and catalytic hydrogenation, as published elsewhere.⁶⁸ The composition of the employed SEM triblock terpolymers is $\text{S}_{40}\text{E}_{21}\text{M}_{39}^{108}$ and $\text{S}_{48}\text{E}_{27}\text{M}_{25}^{141}$. In this notation, the subscripts describe the mass fraction of the corresponding block in wt% and the superscript denotes the overall molecular weight in kg mol^{-1} .

Amidation of SEM

The PMMA block of the SEM triblock terpolymers was amidated under an inert argon atmosphere. First, DMEDA (2 equivalents with respect to MMA units of SEM) was dissolved in 20 mL dry THF and cooled to $-78 \text{ }^\circ\text{C}$ by using an acetone/ dry ice bath. To this solution, n-BuLi (equimolar amount with respect to DMEDA) was added dropwise under stirring followed by heating to room temperature. In another flask, 1 g SEM (3.9 mmol MMA units for $\text{S}_{40}\text{E}_{21}\text{M}_{39}^{108}$ and 2.5 mmol for $\text{S}_{48}\text{E}_{27}\text{M}_{25}^{141}$, 1 equivalent) was dissolved in 80 mL anhydrous THF at $65 \text{ }^\circ\text{C}$ for 30 min. Subsequently, the solution was cooled to $40 \text{ }^\circ\text{C}$ and the activated amine solution was added. The reaction was allowed to proceed for 24 h at $40 \text{ }^\circ\text{C}$ under stirring. Then, 1 mL of deionised water was added to deactivate excess amine and the obtained amidated SEM triblock terpolymers (SEDMA) were isolated by precipitation from pentane. For purification, the product was dissolved in THF at $65 \text{ }^\circ\text{C}$ ($c = 10 \text{ g L}^{-1}$) and centrifuged at $40 \text{ }^\circ\text{C}$ and 5000 rpm for 15 min in order to remove residual lithium hydroxide. The supernatant was precipitated from pentane and dried in a vacuum oven (yield: 1 g (83%)).

Formation of patchy wCCMs

The functional, patchy wCCMs were prepared by CDSA of the amidated SEDMA triblock terpolymers in THF. To this end, the triblock terpolymers were dissolved in THF ($c = 10 \text{ g L}^{-1}$) at $65 \text{ }^\circ\text{C}$ for 30 min and subsequently cooled to $T_c = 20 \text{ }^\circ\text{C}$ (s-SEDMA) or $T_c = 25 \text{ }^\circ\text{C}$ (as-SEDMA) in a thermostated shaker unit (HLC-MKR 13, Ditabis). The self-assembly process was allowed to proceed for 24 h at a shaking rate of 200 rpm.

Synthesis of zinc oxide (ZnO) and copper oxide (CuO) NPs

The synthesis of ZnO and CuO NPs was conducted according to previously published protocols.^{69,70} For the preparation of ZnO NPs, 0.04 mol zinc acetate (1 equivalent) was added to 400 mL boiling ethanol in order to dissolve the salt. After cooling the solution to room temperature, a lithium hydroxide monohydrate solution in ethanol (400 mL, $c = 140 \text{ mM}$, 1.4 equivalents) was added and the reaction mixture was immediately cooled to $0 \text{ }^\circ\text{C}$. The ZnO NPs were precipitated from n-heptane and redispersed in ethanol to yield a final concentration of $c = 3.8 \text{ g L}^{-1}$. The average diameter obtained from transmission electron microscopy (TEM) was $D = 2.7 \pm 0.4 \text{ nm}$. The CuO NPs were synthesised by dissolving 5 mmol copper acetate (1 equivalent), 20 mmol sodium hydroxide (4 equivalents) and 10 mmol acetic acid (2 equivalents) in 500 mL ethanol. The reaction mixture was heated to $78 \text{ }^\circ\text{C}$ for 1 h to yield the CuO NPs. The CuO NP dispersion was precipitated from n-heptane and redispersed in ethanol to yield a final concentration of $c = 1 \text{ g L}^{-1}$. The average diameter of the CuO NPs was determined to be $D = 3.8 \pm 0.6 \text{ nm}$ by TEM. The full characterisation of the NPs can be found in the ESI (Fig. S1†).

In situ synthesis of gold (Au) and silver (Ag) NPs in patchy wCCMs

To 2 mL of a wCCM dispersion ($c = 1 \text{ g L}^{-1}$, THF) 40 μL of the corresponding acid ($\text{HAuCl}_4 \cdot 3\text{H}_2\text{O}$) or metal salt (AgTFA) dissolved in THF ($c = 0.1 \text{ M}$) were added. Immediately, 20 μL of L-Selectride ($c = 1 \text{ M}$, THF) were added and the successful formation of the respective metal NPs was indicated by a characteristic colour change. For as-SEDMA the employed amounts of AgTFA and L-Selectride were reduced by half.

Continuous in situ loading of SEDMA wCCMs with Au NPs

The continuous, in situ loading of s-SEDMA wCCMs was accomplished by a PTFE based microfluidic chip with one main channel and four separate side channels for controlled fluid double focusing. The microfluidic channels of the inner mixing part had a diameter of $D = 500 \text{ }\mu\text{m}$. The outer chip holes were bigger with a diameter of $D = 1000 \text{ }\mu\text{m}$ in order to connect the five inlets via polyethylene (PE) tubes to the syringe pumps. The outlet was fixed to a glass

capillary, which was used to run and investigate the laminar flow-controlled synthesis at a distance of 5 cm via optical microscopy. In a typical experiment, the main channel was fed with an s-SEDMA wCCM dispersion ($c = 1 \text{ g L}^{-1}$, THF) at a flow rate of $2000 \text{ }\mu\text{L h}^{-1}$. The first two side channels were run with a $\text{HAuCl}_4 \cdot 3\text{H}_2\text{O}$ solution ($c = 2 \text{ mM}$, THF) at a flow rate of $2000 \text{ }\mu\text{L h}^{-1}$ and the second two side channels with an L-Selectride solution ($c = 20 \text{ mM}$, THF) at a flow rate of $1000 \text{ }\mu\text{L h}^{-1}$.

Synthesis of PS-stabilised Au NPs (PS@Au)

PS@Au NPs were prepared via ligand exchange starting from citrate-stabilised Au NPs ($D = 7.9 \pm 0.7 \text{ nm}$), synthesised via a seeded growth method reported by Piella et al.⁷¹ A detailed characterisation of the citrate-stabilised Au NPs can be found in the ESI (Fig. S2†). A trithiocarbonate terminated PS (PS-TTC, $M_n = 10\,400 \text{ g mol}^{-1}$, $D = 1.05$, determined by gel permeation chromatography (GPC), ESI Fig. S3A†) was synthesised via reversible addition–fragmentation chain transfer (RAFT) polymerisation according to a previously published protocol.⁷² UV-Vis spectroscopy confirmed the presence of the characteristic TTC absorption at $\lambda = 315 \text{ nm}$ (ESI Fig. S3B†). 120 mL of the aqueous dispersion of citrate-stabilised Au NPs were overlaid with 40 mL of the PS-TTC solution in toluene ($c = 10 \text{ mM}$). After 2 h of vigorous stirring, the phase-transfer of the Au NPs was completed, i.e., the aqueous phase was clear and colourless, whereas the toluene phase showed a deep red colour, indicating a successful ligand exchange. The toluene phase was separated and centrifuged at 12 000–14 000 rpm for 12 h to isolate the PS@Au NPs. The PS@Au NPs were purified from the remaining free PS-TTC ligand by eight washing and centrifugation cycles with 2 mL toluene, respectively. The absence of the free PS-TTC ligand was confirmed by GPC (ESI Fig. S4A†). The hydrodynamic radius of the PS@Au NPs was determined with dynamic light scattering to $R_h = 14.9 \pm 0.7 \text{ nm}$ (ESI Fig. S4B†). The concentration after final dispersion in toluene was determined by UV-Vis spectroscopy to $c = 5.3 \times 10^{17} \text{ NP L}^{-1}$ (see the ESI† for further details).

Loading of SEDMA wCCMs with PS@Au NPs by co-precipitation

10 μL of s-SEDMA wCCMs ($c = 10 \text{ g L}^{-1}$, THF), 37 μL PS@Au NPs ($c = 5.3 \times 10^{17} \text{ NP L}^{-1}$, toluene) and 53 μL THF were mixed in a vial. To this solution, 40 μL of acetone were added in 4 steps under stirring with an equilibration time of 30 min, respectively. Subsequently, 860 μL of acetone were added to achieve an overall acetone fraction of 90 vol%. The solution was stirred for at least 2 h before analysis. In a second experiment, 50 μL of PS@Au NPs and 40 μL THF were employed. All other reaction conditions were kept constant.

Binary loading of SEDMA wCCMs

In a vial, 70 μL THF, 10 μL s-SEDMA wCCMs ($c = 10 \text{ g L}^{-1}$, THF) and 7.5 μL ZnO NPs ($c = 3.8 \text{ g L}^{-1}$, ethanol) were mixed and stirred for 1 h, followed by the addition of 27 μL PS@Au NPs ($c = 5.3 \times 10^{17} \text{ NP L}^{-1}$, toluene). To this solution, 40 μL of acetone were added in 4 steps with an equilibration time of 30 min, respectively. Subsequently, 845 μL of acetone were added to obtain an overall acetone fraction of 90 vol% and the solution was stirred for 2 h before analysis.

For the binary loading with Ag and PS@Au NPs, 100 μL of preformed s-SEDMA/Ag hybrid micelles in THF ($c = 1 \text{ g L}^{-1}$), prepared by in situ reduction of AgTFA, were used. The loading with PS@Au NPs was done according to the procedure described for ZnO/PS@Au NP hybrid micelles.

Instruments

For the microfluidic experiments, syringe pumps (Nemysis Systems, Cetoni GmbH) were used and connected via PE tubes (Scientific Commodities, Inc.) to a home-made PTFE chip. A glass capillary (Hilgenberg GmbH) with an inner diameter of $D = 980 \mu\text{m}$ was connected to the end of the PTFE chip to elongate the reaction pathway. The Au NP formation was followed with an optical microscope IX71 (Olympus Co.) equipped with a D7000 digital camera (Nikon GmbH). $^1\text{H-NMR}$ spectroscopy was conducted on a Bruker Ultrashield 300 system using deuterated chloroform as the solvent at 300 MHz.

FT-IR spectroscopy was performed on a Digilab Excalibur Series FTS system with a Miracle ATR unit of Pike Technologies. The spectra were recorded with a resolution of 4 cm^{-1} and 16 scans were averaged per sample.

For GPC in THF, SDV gel columns ($300 \times 8 \text{ mm}$, 5 μm particle size, PSS Mainz) with pore sizes of 10^5 , 10^4 , 10^3 and 10^2 \AA were used, together with a refractive index detector (RI 101, Techlab Shodex) and a UV detector operating at $\lambda = 254 \text{ nm}$ (Knauer). The applied flow rate was 1 mL min^{-1} at $40 \text{ }^\circ\text{C}$. Narrowly distributed PS standards and toluene as the internal reference were used for calibration.

GPC in hexafluoroisopropanol with potassium trifluoroacetate (8 g L^{-1}) was conducted on PFG gel columns ($300 \times 8 \text{ mm}$, 7 μm particle size, PSS Mainz) with 100 and 300 \AA pore sizes using a flow rate of 0.5 mL min^{-1} at $23 \text{ }^\circ\text{C}$. The signals were detected by using a Gynkotec SE-61 refractive index detector. For calibration, narrowly distributed PMMA standards and toluene as the internal reference were used.

For GPC in N,N-dimethylformamide with lithium bromide (5 g L^{-1}), GRAM columns ($300 \times 8 \text{ mm}$, $10 \mu\text{m}$ particle size, PSS Mainz) with 100 and 3000 \AA pore sizes were used. The sample was analysed at a flow rate of 0.5 mL min^{-1} at $23 \text{ }^\circ\text{C}$ using a DAD VL + G1315C diode array UV detector (Agilent Technologies) operated at $\lambda = 270 \text{ nm}$ and 525 nm . Narrowly distributed PS standards and toluene as the internal reference were employed for calibration.

The thermal properties of the SEDMA wCCM dispersions were analysed by using a SETARAM micro-DSC III system. The samples ($c = 10 \text{ g L}^{-1}$ in THF) were measured in closed batch cells at a scanning rate of 0.5 K min^{-1} and THF was used as the reference.

For UV-Vis measurements a JASCO V630 spectrophotometer and fused quartz cuvettes (Hellma, $d = 0.2 \text{ cm}$) were used. The samples were analysed in THF ($c = 0.1 \text{ g L}^{-1}$) and acetone at room temperature, using the corresponding pure solvent for background subtraction, respectively. For the binary loaded sample pure acetone was used as the reference.

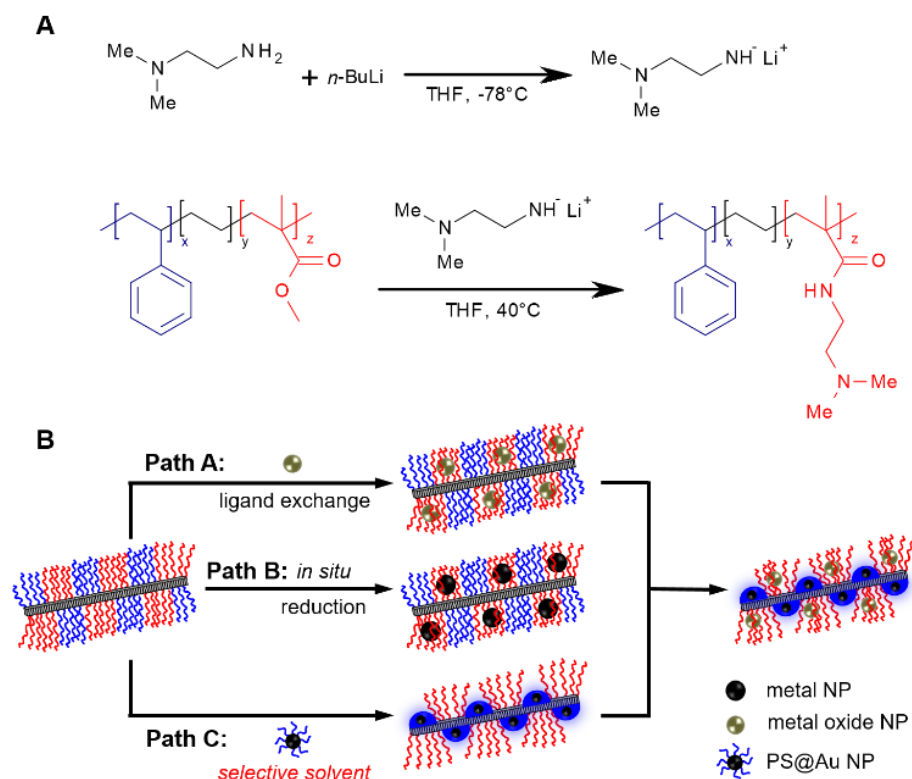
Elastic bright-field TEM was conducted on a Zeiss 922 Omega EFTEM (Zeiss NTS GmbH, Oberkochen, Germany) electron microscope operating at an acceleration voltage of 200 kV . A bottom mounted CCD camera system (Ultrascan 1000, Gatan) recorded the zero-loss filtered images, which were processed by the imaging software Gatan Digital Micrograph 3.9 for GMS 1.4. For high-angle annular dark field scanning transmission electron microscopy (HAADF-STEM), a Tecnai T20 system (FEI, Eindhoven, The Netherlands) was used operating at 200 keV . Energy dispersive X-ray (EDX) spectra were recorded with an Xmax 80 (Oxford Instruments) detector. The samples were diluted to 0.1 g L^{-1} and drop-coated onto carbon-coated copper grids. The solvent was blotted with filter paper and the samples were dried in a vacuum oven at 0.2 mbar and room temperature before staining with ruthenium tetroxide (RuO_4). The software ImageJ was used to determine particle sizes, wCCM lengths and patch sizes. At least 100 measurements were done to obtain representative average values.

Results and discussion

Functional wCCMs with amino group containing patches

The formation of hybrid materials of patchy wCCMs and NPs demands an efficient functionalisation of one of the corona blocks of the employed SEM triblock terpolymers. To this end, we chose an amidation of the PMMA block with N,N-dimethylethylenediamine (DMEDA), utilizing a prior activation of the amine with n-butyllithium (**Scheme 1A**).⁷³ Due to the activation, the amount of DMEDA could be decreased to a 2-fold excess with respect to the amount of methyl ester units in the PMMA block (in comparison with the 30-fold excess used in our previous report⁶⁸) and nearly quantitative conversion was obtained after 24 h under mild

conditions (40 °C). The functionalisation proceeds without degradation of the polymer backbone, as shown by gel permeation chromatography (GPC) of an amidated PMMA homopolymer, which was functionalised under identical conditions as the SEM triblock terpolymers (ESI Fig. S5†).



Scheme 1 Amidation of the SEM triblock terpolymers with prior activation of the amine by *n*-BuLi (A). Strategies for the regio-selective and binary loading of patchy wCCMs with metal and metal oxide NPs (B).

The amidated SEM triblock terpolymers were characterised by $^1\text{H-NMR}$ and FT-IR spectroscopy, as discussed exemplarily for the amidation of $\text{S}_{40}\text{E}_{21}\text{M}_{39}^{108}$ (the subscripts describe the mass fraction of the corresponding block in wt% and the superscript denotes the overall molecular weight in kg mol^{-1}). The signals in the $^1\text{H-NMR}$ spectrum can be clearly assigned to the typical proton signals of the amide (**Fig. 1A**). There is only a weak signal of not consumed PMMA ester units at 3.6 ppm. From the integral of this signal, calibrated by the aromatic polystyrene protons (5, 5 H), a degree of amidation of 95% results. Consequently, the composition and overall molecular weight of the functionalised triblock terpolymer changes to $\text{S}_{33}\text{E}_{17}\text{DMA}_{50}^{131}$. A signal for imide formation, which would be expected at 3.7–4 ppm,⁶⁸ is hardly observable. This indicates that the amidation proceeds without significant side reactions. The successful amidation is further confirmed by FT-IR spectroscopy (ESI Fig. S6†), showing the characteristic amide I and amide II vibrations at 1660 cm^{-1} and 1526 cm^{-1} , respectively, and

only a very weak C=O vibration of the remaining PMMA units. The negligible fraction of imide units in $S_{33}E_{17}DMA_{50}^{131}$ is supported by its solubility in tetrahydrofuran (THF) and chloroform ($CHCl_3$), as in the case of large fraction of imide units the triblock terpolymer would be insoluble in both solvents.⁶⁸

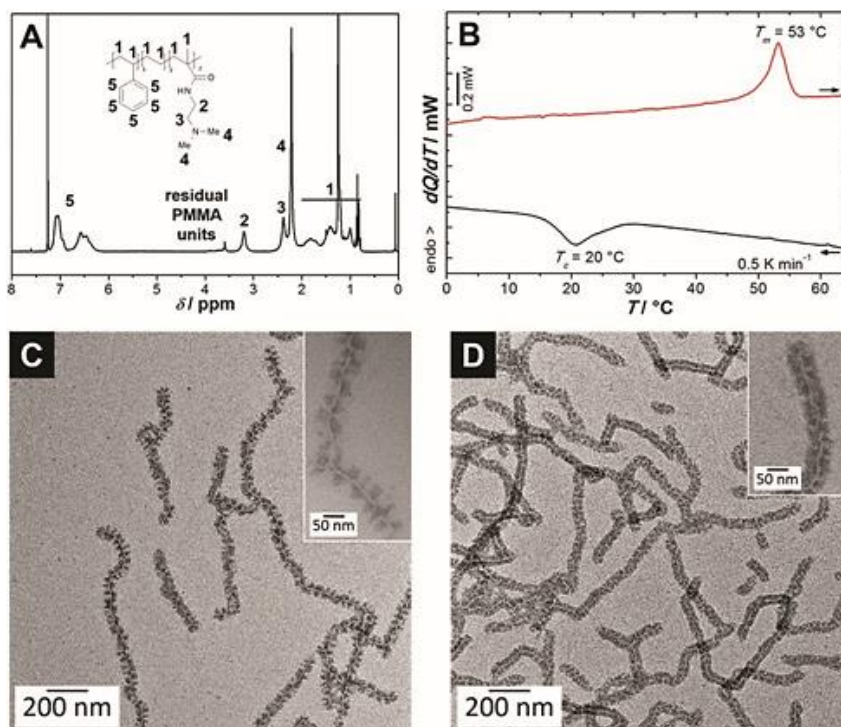


Fig. 1 ¹H-NMR spectrum measured in $CDCl_3$ (A), μ DSC heating and cooling traces ($c = 10\text{ g L}^{-1}$, THF (B)) of *s*-SEDMA as well as TEM micrographs of SEDMA (C) and *as*-SEDMA (D) wCCMs, selectively stained with RuO_4 .

The successful amidation is further confirmed by FT-IR spectroscopy (ESI Fig. S6), showing the characteristic amide I and amide II vibrations at 1660 cm^{-1} and 1526 cm^{-1} , respectively, and only a very weak C=O vibration of the remaining PMMA units. The negligible fraction of imide units in the SEDMA triblock terpolymer is supported by its solubility in tetrahydrofuran (THF) and chloroform ($CHCl_3$), as in case of a high fraction of imide units the triblock terpolymer would be insoluble in both solvents.⁶⁹

The solubility of the SEDMA triblock terpolymers in THF, which is used for CDSA, is crucial for the formation of welldefined patchy wCCMs. Recently, we have shown that the crystallisation temperature (T_c) of the PE middle block in solution is a very sensitive parameter to probe the solubility of the amidated triblock terpolymers.⁶⁸ With decreasing solubility an increase in the T_c of the PE block is observed with respect to that of the corresponding $S_{40}E_{21}M_{39}^{108}$ precursor ($T_c = 21\text{ }^\circ\text{C}$). For T_c values above $30\text{ }^\circ\text{C}$ only ill-defined and strongly aggregated wCCMs are formed. This is attributed to aggregation caused by the limited solubility

of the amidated PMMA block, which results in a higher PE segment density and, thus, a better nucleation of PE crystallisation. Micro-differential scanning calorimetry (μ DSC) shows a T_c at 20 °C for the synthesised $S_{33}E_{17}DMA_{50}^{131}$ triblock terpolymer ($c = 10 \text{ g L}^{-1}$ in THF, **Fig. 1B**), i.e., almost identical to the SEM precursor underlining its good solubility in THF. Consequently, CDSA of $S_{33}E_{17}DMA_{50}^{131}$ in THF at 20 °C resulted in the formation of well-defined wCCMs with an average length of $L = 540 \pm 310 \text{ nm}$ (**Fig. 1C**), as revealed by transmission electron microscopy (TEM). The sample was stained with RuO_4 , which is known for selective staining of the PS domains. Therefore, the PS patches in the corona appear dark and the amidated PMMA (PDMA) patches appear bright, both being arranged in an almost alternating manner. The corona patches exhibit a similar width of $18 \pm 5 \text{ nm}$ for PS and $17 \pm 5 \text{ nm}$ for PDMA, respectively.

Selective loading of patchy wCCMs with NPs

The unique alternating structure of the functional patchy corona of SEDMA wCCMs offers the possibility to incorporate two different types of NPs. The patchy morphology guarantees an efficient separation and at the same time a dense packing of single NPs. We developed three different strategies for the selective loading of the patches with metal and metal oxide NPs (**Scheme 1B**). Path A is based on selective interactions between the PDMA corona patch and the metal oxide NP, which are known to undergo ligand exchange if amino groups are offered.⁷⁴ Path B deals with the in situ synthesis of metal NPs within the PDMA patch of the SEDMA wCCMs, which provides tertiary amino groups as anchor groups for the efficient stabilisation of different metal NPs like gold (Au) or silver (Ag).⁷⁵ Path C is based on polymer–polymer and polymer–solvent interactions. The addition of a selective solvent for one of the corona patches leads to the collapse of the other corona patch. Thus, NPs that are stabilised with the same polymer as the collapsing corona patch are incorporated into the collapsing patch upon selective solvent addition. Combination of path A and C finally leads to binary loaded wCCMs.

Following path A, we investigated the ligand exchange for zinc oxide (ZnO) and copper oxide (CuO) NPs. Both types of NPs were synthesised in ethanol with acetate ligands for stabilisation and have average diameters of $D = 2.7 \pm 0.4 \text{ nm}$ for ZnO and $D = 3.8 \pm 0.6 \text{ nm}$ for CuO (determined by TEM, ESI Fig. S1†). The obtained NPs are phase pure according to the powder X-ray diffraction patterns (ESI Fig. S1A†) and exhibit a narrow particle size distribution (ESI Fig. S1B†). The concentration of the NP dispersions was adjusted to 1–4 g L^{-1} , which ensures that the total amount of added NP dispersion is less than 10 vol% with respect to the employed THF dispersion of SEDMA wCCMs. For higher volume fractions of ethanol the wCCMs are insoluble and agglomerate before the ligand exchange is completed. The NP incorporation was finished after 1 d and the *s*-SEDMA wCCMs were highly loaded with both types of NPs as

revealed by TEM (ZnO: **Fig. 2A** and C; CuO: **Fig. 2E**), pointing to a successful ligand exchange, i.e., acetate ligands vs. amino groups in the PDMA patch. The absence of free NPs in the TEM micrographs points to a complete incorporation of the ZnO and CuO NPs in the micellar corona.

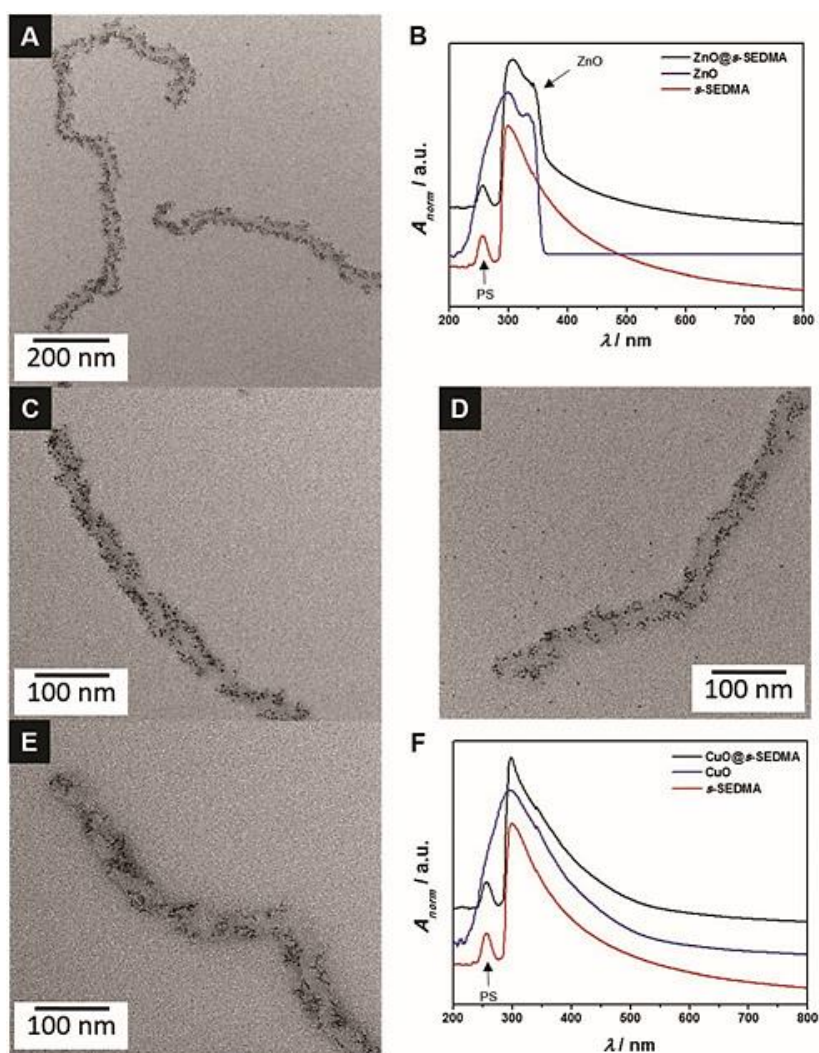


Fig. 2 TEM micrographs and corresponding UV-Vis spectra for the hybrid materials of SEDMA wCCMs with ZnO (A, B, D) and CuO NPs (C, E).

The theoretical ZnO and CuO contents in the hybrid micelles, assuming a complete incorporation of the NPs in the micellar corona, are 12 wt% and 7 wt%, respectively. Both the ZnO and CuO NPs are homogeneously distributed within the PDMA patches of the *s*-SEDMA wCCMs without agglomeration and the “empty” PS patches are still clearly discernible. Here, it has to be noted that in contrast to the neat *s*-SEDMA wCCMs the hybrid micelles were analysed without prior staining with RuO_4 , as the incorporated NPs provide an intrinsic staining of the patches. The UV-Vis spectra of the neat wCCMs show a continuous increase in absorbance with decreasing wavelength, which is attributed to scattering from the wCCMs (**Fig. 2B** and **F**). This is supported by the blue colour of the neat wCCM dispersion (Tyndall effect). The low

wavelength part of the spectrum is dominated by a relatively weak absorption maximum at $\lambda_{\max} = 250$ nm, deriving from the absorption of the PS units of the wCCMs. The UV-Vis spectra of the pure ZnO (**Fig. 2B**) and CuO (**Fig. 2F**) NPs show absorption maxima at approximately 300 nm, which overlap with the scattering contribution of the wCCMs. Consequently, the UV-Vis spectrum of the CuO NP hybrid micelles is similar to the spectrum of the neat *s*-SEDMA wCCMs (**Fig. 2F**). In contrast, the ZnO NPs show a pronounced shoulder at $\lambda = 333$ nm, which is also observable in the UV-Vis spectra of the ZnO NP loaded wCCMs (**Fig. 2B**), confirming the successful incorporation of the NPs in the patchy corona.

To study the effect of patch size on the NP incorporation, we transferred the ligand exchange with ZnO NPs to the *as*-SEDMA wCCMs, keeping the amount of ZnO NPs constant. TEM clearly shows a decreased loading capacity for the smaller PDMA patches, supported by the observation of free ZnO NPs around the wCCMs (**Fig. 2D**, corresponding UV-Vis spectra in ESI Fig. S8A†). To further strengthen the effect of patch size, we added acetone as a selective solvent for the PDMA patch. This leads to a collapse of the PS patches and a swelling of the PDMA patches (ESI Fig. S9†). Due to the swelling, more ZnO NPs were incorporated into the corona and the PS patches are hardly observable.

In path B we utilised the functionalised corona patches as nanoreactors for the simultaneous stabilisation and *in situ* syntheses of different metal NPs via reduction of the corresponding acids and metal salts, i.e., tetrachloroauric acid trihydrate ($\text{HAuCl}_4 \cdot 3\text{H}_2\text{O}$) and silver trifluoroacetate (AgTFA), with L-Selectride (lithium tri-*sec*-butylborohydride). We chose L-Selectride since it is a mild reduction agent that does not reduce ester or amide groups.⁷⁶ After the addition of L-Selectride, the typical colour change of all solutions indicated a successful NP formation, which is further proven by the TEM micrographs shown in **Fig. 3**. The Au and Ag NPs show a spherical shape and are selectively incorporated into the patchy corona of the *s*-SEDMA (**Fig. 3A and B**) and *as*-SEDMA wCCMs (**Fig. 3E and F**). The diameters of the formed NPs are $D_{\text{Au}} = 4.7 \pm 1.2$ nm and $D_{\text{Ag}} = 2.9 \pm 0.8$ nm for the *s*-SEDMA and $D_{\text{Au}} = 4.0 \pm 1.3$ nm and $D_{\text{Ag}} = 2.2 \pm 0.6$ nm for the *as*-SEDMA hybrid micelles, respectively, as determined by TEM image analysis. The rather high size dispersity of the NPs might be attributed to the *in situ* reduction process, which does not allow a precise size control as nucleation and growth of the NPs happen almost simultaneously.

The PDMA patches in the SEDMA/Au hybrid micelles are highly loaded with Au NPs without showing any significant agglomeration. This can be ascribed to the nearly quantitative amidation of the PMMA block, resulting in a high density of amino anchor groups in the PDMA patches. We exemplarily analysed the loading capacity of the *s*-SEDMA wCCMs with Au NPs by

inductively-coupled plasma optical emission spectroscopy (ICP-OES) and thermogravimetric analysis (TGA), which resulted in 652 μg and 787 μg Au, respectively. This equals to 25–28 wt% Au in the final hybrid micelles. Taking into account that the accuracy of ICP-OES fluctuates between 10–20%, the incorporation of Au by in situ synthesis can be regarded as nearly quantitative.⁷⁷ The high loading again provides an intrinsic staining of the PDMA patches, as already observed for the hybrid micelles prepared by ligand exchange. However, due to the similar width of both patch types the PS patches appear comparably small for the *s*-SEDMA based hybrid micelles, which makes it more difficult to discern the patchy structure of the corona. Nevertheless, for the *as*-SEDMA hybrid micelles the patches are clearly distinguishable, which can be attributed to the significantly smaller size of the PDMA patches (14 ± 4 nm) with respect to that of the PS patches (20 ± 6 nm) in the *as*-SEDMA wCCM corona. This underlines the excellent selectivity of the NP incorporation.

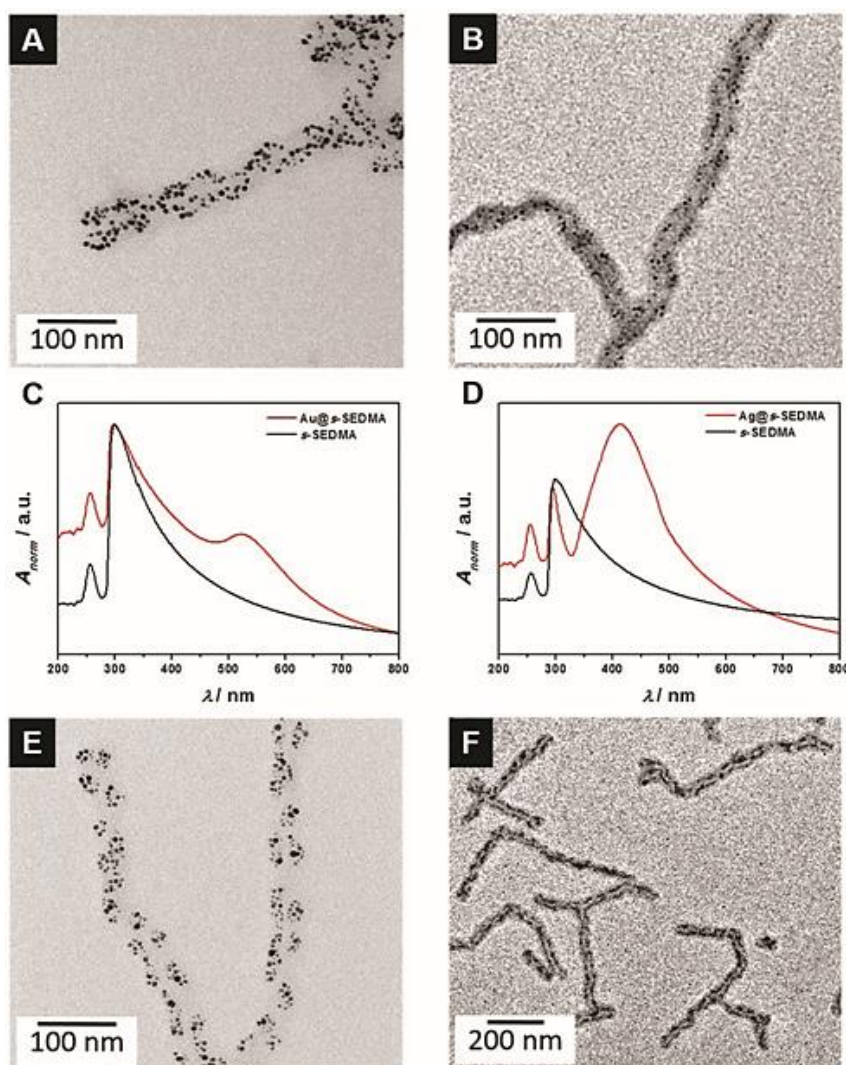


Fig. 3 TEM micrographs and corresponding UV-Vis spectra for the hybrid materials of SEDMA wCCMs with Au (A, D), Ag (B, E) and Pt (C, F) NPs.

Fig. 3C and S8B (ESI†) compare the UV-Vis spectra of the SEDMA wCCMs prior to and after the *in situ* synthesis of Au NPs. All absorbance spectra show the same spectral characteristics except for a peak at approximately $\lambda_{\max} = 523$ nm that appears only for the Au NP loaded wCCMs. This peak can be assigned to absorption due to the localised surface plasmon resonance (LSPR) of the Au NPs, which is characteristic for small, spherical Au NPs.⁷⁸ The low absorbance at wavelengths of $\lambda \geq 700$ nm manifests the good stabilisation and distribution of the Au NPs by the wCCMs and the absence of Au NP aggregates.

Similar to the Au NPs, the Ag NPs are well distributed within the *s*-SEDMA and the *as*-SEDMA wCCMs without agglomeration (**Fig. 3B** and **F**). ICP-OES reveals a loading capacity of 103 μg Ag in the *s*-SEDMA wCCMs, which equals to 5 wt% in the final hybrid micelles (applied amount of Ag: 431 μg). The corona of both Ag hybrid micelles, i.e., based on *s*- and *as*-SEDMA, again shows a patchy structure due to intrinsic staining of the PDMA patches by the incorporated Ag NPs. To highlight the selectivity of NP incorporation in the SEDMA wCCMs, we employed the *in situ* reduction method on the pure $\text{S}_{48}\text{E}_{27}\text{M}_{25}^{141}$ wCCMs (ESI Fig. S10†). The lack of functional groups in these wCCMs causes a statistical distribution of the Ag NPs over the whole TEM grid and almost no Ag NPs are located within the patchy corona. Furthermore, agglomeration of the Ag NPs is observed, which proves that functional groups for NP stabilisation are inevitable.

The UV-Vis spectra of the Ag NP loaded *s*-SEDMA (**Fig. 3D**) and *as*-SEDMA (ESI Fig. S8C†) wCCMs show a strong peak in absorbance at $\lambda_{\max} = 415\text{--}426$ nm, superimposed to the wCCM absorbance. This peak is related to the LSPR of small, spherical Ag NPs.⁷⁹ Compared to the spectra of the Au NP loaded wCCMs, the Ag NP containing systems show a much stronger LSPR contribution, which is attributed to the higher absorption cross-section of Ag as compared to Au NPs of similar size. The narrow width of the LSPR resonance and the absence of significant absorbance at higher wavelengths again underline the good stabilisation and distribution of the Ag NPs by the wCCMs.

In order to study whether mixing effects have an influence on the *in situ* synthesis of NPs, we transferred the batch reduction to a continuous loading process, employing a microfluidic chip with a double-focusing cross and four side channels that allows for a controlled and fast mixing of the reactants (ESI Fig. S11A, B†). The advantage of microchannels is the presence of a laminar flow without turbulences and therefore a diffusion-controlled reaction process for the reactants.^{80,81} In a continuous flow, the *s*-SEDMA wCCM dispersion was pumped through the main channel and at the same time, $\text{HAuCl}_4 \cdot 3\text{H}_2\text{O}$ and L-Selectride were fed via the side channels (ESI Fig. S11C†). The flow rates were adjusted in a way that allows a direct

comparison with the batch in situ process as the employed molar ratio of reactants is identical. The flow rate also determines the residence time $t = \pi R^2/Q$, where s is the length of the capillary ($s = 50$ mm), R the crosssectional radius of the capillary ($R = 490$ μm), and Q the total volumetric flow rate. Here, the total volumetric flow rate is $Q = 8000$ $\mu\text{L h}^{-1}$, which corresponds to a residence time of $t = 17.0$ s. The TEM micrograph reveals that the PDMA patches of the wCCMs are homogeneously and densely loaded with Au NPs, showing an average diameter of $D = 4.3 \pm 1.4$ nm (ESI Fig. S11D†). This is comparable to the size of the Au NPs synthesised by the batch in situ reduction ($D = 4.7 \pm 1.2$ nm, **Fig. 3A**). This indicates that the residence time is sufficiently large to allow for complete reduction of the gold precursor and that the slower mixing in the batch process does not seem to have a major influence on the NP size and homogeneity of the loading. Besides, employing the continuous loading approach the flow rates can be easily varied, which allows a facile tuning of the loading density of the micelles with Au NPs without the need to prepare new reactant solutions (ESI Fig. S11E†).

Binary loading of patchy SEDMA wCCMs

For binary loading of the patchy SEDMA wCCMs with two different types of NPs also the non-functional PS patches need to be loaded. Therefore, we developed a co-precipitation method that offers the possibility to incorporate preformed, PS-stabilised NPs with precisely tailored dimensions within the PS patches of the SEDMA wCCMs without the need for a preceding functionalisation of the patch (**Scheme 1B, path C**). This method is based on polymer–polymer and polymer–solvent interactions. We chose PS-stabilised Au NPs (PS@Au NPs), which were synthesised by a facile ligand exchange method starting from an aqueous dispersion of citrate-stabilised Au NPs with an average diameter of $D = 7.9 \pm 0.7$ nm (determined by TEM, ESI Fig. S2†) and trithiocarbonate-terminated PS (PS-TTC) in toluene, prepared by RAFT polymerisation (ESI Fig. S3†). After the biphasic ligand exchange, the PS@Au NPs were found to be well dispersed in the organic phase. The TEM micrograph shown in **Fig. 4A** reveals that the PS@Au NPs are homogeneously distributed on the TEM grid without agglomeration and show a spherical shape. The PS shell is only visible as a pale-grey shell in the TEM micrograph due to the high electron density of the Au NPs.

The PS@Au NPs show a characteristic LSPR at $\lambda_{\text{max}} = 527$ nm in toluene (**Fig. 4B**), which is red-shifted by 12 nm with respect to the LSPR of the citrate-stabilised Au NPs in water ($\lambda_{\text{max}} = 515$ nm). This red-shift is caused by the change in refractive index from the aqueous phase ($n = 1.33$) to the toluene phase ($n = 1.50$). DMF-GPC using a UV-Vis diode array detector with two different wavelengths, characteristic for PS ($\lambda = 270$ nm) and the Au NPs ($\lambda = 525$ nm), shows that the PS-TTC is efficiently bound on the Au NP surface and there is only a small amount of

residual free PS ligand (ESI Fig. S4A†). The hydrodynamic radius of the PS@Au NPs was determined by dynamic light scattering to $R_h = 14.7 \pm 0.1$ nm, confirming the PS shell around the Au NPs. First, we investigated the aggregation behaviour of neat PS@Au NPs in THF upon addition of acetone in order to identify suitable conditions for the incorporation of PS@Au NPs in the SEDMA wCCMs via coprecipitation. Acetone will be used as the selective solvent for the PDMA patch in the co-precipitation process and, thus, is expected to induce the collapse of the PS ligands. Due to the high sensitivity of the LSPR to particle stability, UV-Vis spectroscopy could be used to follow the solvent induced aggregation (ESI Fig. S12†). Analysis of the spectra reveals that a volume fraction of 33 vol% acetone is sufficient to induce the collapse of the PS shell around the Au NPs, indicated by a broadening of the LSPR, and upon further addition of acetone no significant changes in the UV-Vis absorption maximum were observed.

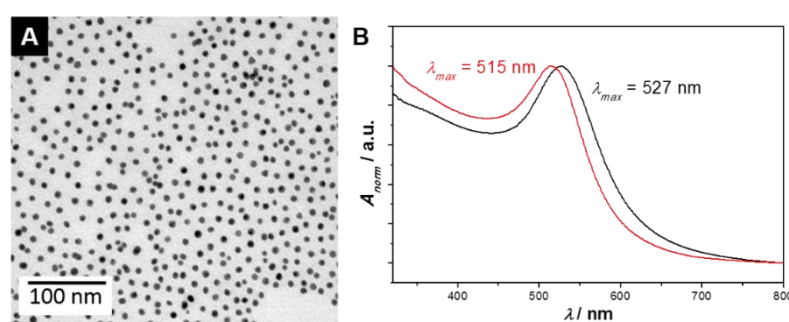


Fig. 4 TEM micrograph (A) and UV-Vis spectrum of the PS@Au NPs in toluene ($c = 8.8 \cdot 10^{15}$ NP L⁻¹, black trace in (B)). The red spectrum in (B) corresponds to the citrate-stabilised Au NPs in water ($c = 1.2 \cdot 10^{16}$ NP L⁻¹) measured prior to the ligand exchange with PS-TTC.

For co-precipitation, the PS@Au NP dispersion in toluene was mixed with the *s*-SEDMA wCCMs in THF, a good solvent for both the PS and PDMA patches. The details on the used amounts can be found in the Experimental section. The addition of acetone was done in two steps. First, 40 μ L acetone (28 vol% with respect to the overall volume) were added in 10 μ L portions, employing an equilibration time of 30 min after each addition. Until this point, the PS@Au NPs do not aggregate. However, the solvent quality for PS is slowly decreasing and the PS@Au NPs start to interact with the PS patches of the *s*-SEDMA wCCMs. In the second addition step, the volume fraction of acetone was increased to 90 vol% to ensure a complete co-precipitation of the PS@Au NPs within the PS corona patches. The TEM micrograph of the loaded wCCMs reveals the successful incorporation of the Au NPs within the corona of the *s*-SEDMA wCCMs and shows a clearly visible patch-like arrangement of the Au NPs (**Fig. 5A**). The PS shell around the Au NPs prevents agglomeration of the NPs even if they are in close proximity to each other. The UV-Vis spectrum clearly shows the LSPR of the Au NPs with a maximum absorbance at $\lambda_{\max} = 530$ nm (**Fig. 5C**), which is close to the position of the LSPR of

the neat PS@Au NPs ($\lambda_{\max} = 527$ nm, **Fig. 4B**). Furthermore, the resonance width did not change significantly and the absorbance quickly drops to values close to zero, which supports the absence of aggregates.

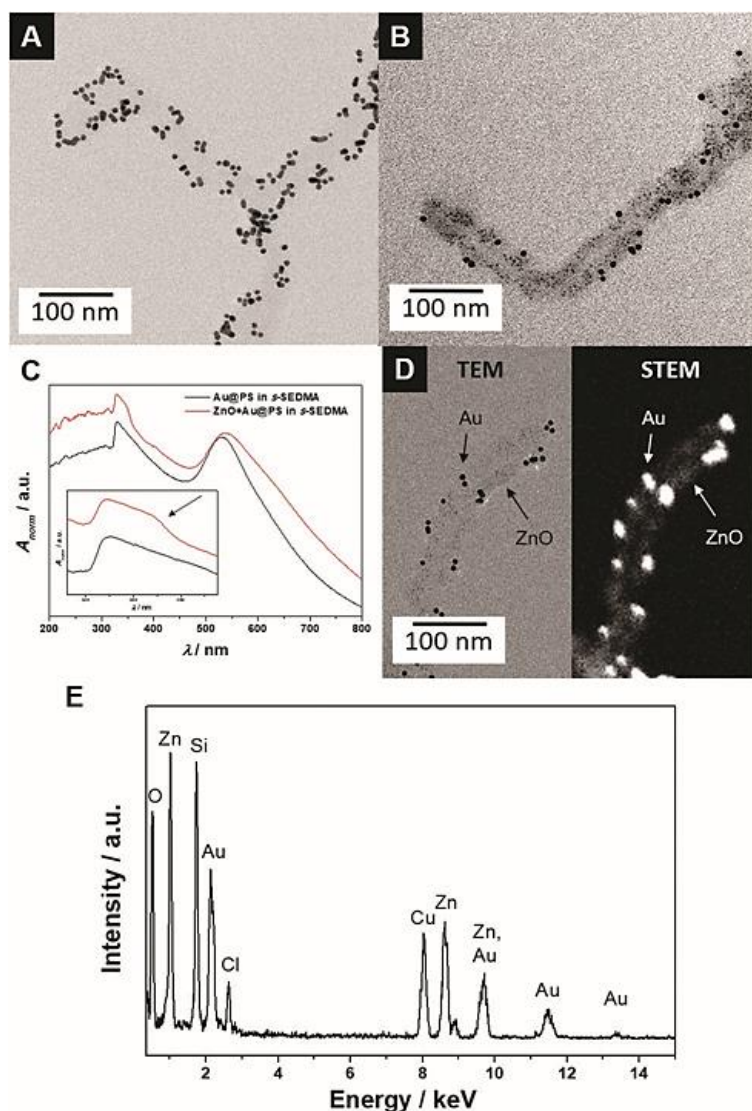


Fig. 5 Hybrid micelles of *s*-SEDMA with PS@Au NPs prepared by coprecipitation (A) and binary loaded *s*-SEDMA wCCMs with PS@Au and ZnO NPs (B). The corresponding UV-Vis spectra are displayed in (C) and the traces were shifted vertically for clarity. Bright-field and HAADF-STEM image (D) and EDX analysis (E) of the binary loaded *s*-SEDMA wCCMs.

Combining path A and C, binary loading of the patchy wCCMs with ZnO and PS@Au NPs is possible (**Scheme 1B**). First, the ligand exchange route was employed to incorporate acetate-stabilised ZnO NPs in the PDMA patches of the *s*-SEDMA wCCMs. Subsequently, the PS@Au NPs were loaded into the PS patches by co-precipitation. The overall amount of acetone was adjusted to 90 vol%, as this leads to complete incorporation of the PS@Au NPs. The employed loading sequence is crucial for a successful binary loading of the wCCMs, since the acetate-

stabilised ZnO NPs show aggregation in acetone. By exchanging the acetate ligands to PDMA before acetone addition, we prevent the aggregation as shown exemplarily for ZnO loaded s-SEDMA wCCMs (ESI Fig. S13†). Consequently, the binary loaded hybrid micelles show no agglomeration of both NP types, but a homogeneous distribution over the whole SEDMA wCCMs, contouring the bright appearing semi-crystalline polyethylene core (**Fig. 5B**). We intentionally decreased the amount of incorporated PS@Au NPs in comparison with the sample shown in **Fig. 5A** to obtain a higher contrast for the ZnO NPs in the TEM micrograph (small dark grey spots within the corona). ICP-OES analysis results in a loading capacity of 56 μg Au and 20 μg ZnO, which corresponds to 43 wt% of inorganic material in the binary loaded wCCMs. These values are similar to the applied amounts of NPs, i.e., 74 μg Au and 28 μg ZnO, respectively.

The UV-Vis spectrum (**Fig. 5C**) shows the typical LSPR of Au NPs at $\lambda_{\text{max}} = 538$ nm as well as a signal for the ZnO NPs at $\lambda_{\text{max}} = 333$ nm, as already observed for the single loaded hybrid micelles (**Fig. 2B**). The binary loading is further confirmed by high-angle annular dark field scanning transmission electron microscopy (HAADF-STEM, **Fig. 5D**) and energy dispersive X-ray (EDX) analysis (**Fig. 5E**). The ZnO NPs in the corona of the binary loaded wCCMs are hardly observable by conventional bright-field TEM (**Fig. 5B** and **D**). In HAADF-STEM the contrast is obtained by elastic scattering, only. Thus, the atomic number Z of the elements directly affects the contrast of the image. Therefore, the Au NPs appear brighter than the ZnO NPs. Both types of NPs are clearly visible in the HAADF-STEM micrograph (**Fig. 5D**, marked with arrows) and confirmed by EDX analysis (**Fig. 5E**) of the same region. As already observed in the bright-field TEM micrograph, the HAADF-STEM image confirms the homogeneous distribution of the Au NPs along the corona of the micelle. The slightly darker appearing ZnO NPs are found in between the Au NPs supporting the patch-like morphology of the corona. The PE core of the SEDMA wCCMs appears as a dark core in between the NP loaded corona, indicating the presence of the polymer template.

The binary loading is not limited to a combination of path A and C. To show the versatility of this method, we combined path B and C to obtain binary loaded wCCMs. To this end, Ag NP loaded hybrid micelles, synthesised by the *in situ* method (same sample like **Fig. 3B**), were used for subsequent co-precipitation of PS@Au NPs. Due to the significantly different sizes of the NPs ($D_{\text{Ag}} = 2.9 \pm 0.8$ nm, $D_{\text{Au}} = 7.9 \pm 0.7$ nm), a differentiation of the two NP types in the TEM image is possible (ESI Fig. S14†). Both NP types are well distributed within the wCCM corona and show no agglomeration, underlining the versatility of patchy wCCMs as templates for the preparation of binary loaded hybrid materials.

Conclusion

In this work, we demonstrated that worm-like micelles with a patch-like microphase-separated corona are highly versatile templates for the regio-selective incorporation of inorganic NPs. Introducing specific anchor groups in one of the corona patches allows to direct the incorporation of metal and metal oxide NPs exclusively in the functionalised patches, either by in situ synthesis of the NPs within the patches or by ligand exchange with preformed NPs. In addition, NPs that are stabilised by the same polymer as one of the corona patches can be selectively incorporated by co-precipitation employing selective solvents. The combination of different loading strategies even allows the formation of binary loaded hybrid micelles with two types of NPs placed in different compartments of the patchy wCCM corona. The patchy corona of the worm-like micelles provides an excellent stabilisation of the incorporated NPs. This in turn results in a high and easily accessible catalytically active NP surface area, which is highly favourable for heterogeneous catalysis.⁵⁸ The binary loaded hybrid micelles are considered as promising materials for catalytic applications, since the homogeneous distribution of different NPs in the micellar corona ensures a high interface between the NPs. This could enhance synergistic effects on catalysis, as for example reported for the combination of ZnO and Au NPs in the photocatalytic degradation of dyes and antibiotics.^{82,83}

Conflicts of interest

There are no conflicts of interests to declare.

Acknowledgements

We thank the German Research Foundation for financial support within the framework of the Collaborative Research Center SFB 840 (project A2). We appreciate support of the Keylab for Optical and Electron Microscopy of the Bavarian Polymer Institute (BPI). The authors thank B. Uch and R. Schneider for GPC and M. Drechsler for help with TEM. J.S. acknowledges the support of the Graduate School of the University of Bayreuth.

References

1. J.-F. Lutz, J.-M. Lehn, E. W. Meijer and K. Matyjaszewski, *Nat. Rev. Mater.*, 2016, **1**, 16024–16037.
2. J. Rodríguez-Hernández, F. Chécot, Y. Gnanou and S. Lecommandoux, *Prog. Polym. Sci.*, 2005, **30**, 691–724.
3. J.-F. Gohy, *Adv. Polym. Sci.*, 2005, **190**, 65–136.

4. Y. Mai and A. Eisenberg, *Chem. Soc. Rev.*, 2012, **41**, 5969–5985.
5. J. Dupont, G. Liu, K. I. Niihara, R. Kimoto and H. Jinnai, *Angew. Chem. Int. Ed.*, 2009, **48**, 6144–6147.
6. S. Zhong, H. Cui, Z. Chen, K. L. Wooley and D. J. Pochan, *Soft Matter*, 2008, **4**, 90–93.
7. I. S. Jo, S. Lee, J. Zhu, T. S. Shim and G. R. Yi, *Curr. Opin. Colloid Interface Sci.*, 2017, **30**, 97–105.
8. A. O. Moughton, M. A. Hillmyer and T. P. Lodge, *Macromolecules*, 2012, **45**, 2–19.
9. J. Du and R. K. O'Reilly, *Chem. Soc. Rev.*, 2011, **40**, 2402–2416.
10. A. Walther and A. H. E. Müller, *Chem. Rev.*, 2013, **113**, 5194–5261.
11. D. J. Pochan, J. Zhu, K. Zhang, K. L. Wooley, C. Miesch and T. Emrick, *Soft Matter*, 2011, **7**, 2500–2506.
12. D. J. Pochan, *Science*, 2004, **306**, 94–97.
13. H. Cui, Z. Chen, S. Zhong, K. L. Wooley and D. J. Pochan, *Science*, 2007, **317**, 647–650.
14. A. H. Gröschel and A. H. E. Müller, *Nanoscale*, 2015, **7**, 11841–11876.
15. U. Tritschler, S. Pearce, J. Gwyther, G. R. Whittell and I. Manners, *Macromolecules*, 2017, **50**, 3439–3463.
16. Z. Li, M. A. Hillmyer and T. P. Lodge, *Langmuir*, 2006, **22**, 9409–9417.
17. A. H. Gröschel, A. Walther, T. I. Löbbling, F. H. Schacher, H. Schmalz and A. H. E. Müller, *Nature*, 2013, **503**, 247–251.
18. T. I. Löbbling, O. Borisov, J. S. Haataja, O. Ikkala, A. H. Gröschel and A. H. E. Müller, *Nat. Commun.*, 2016, **7**, 12097–12106.
19. J. Hu, G. Liu and G. Nijkang, *J. Am. Chem. Soc.*, 2008, **130**, 3236–3237.
20. F. H. Schacher, P. A. Rugar and I. Manners, *Angew. Chem. Int. Ed.*, 2012, **51**, 7898–7921.
21. R. K. O'Reilly, C. J. Hawker and K. L. Wooley, *Chem. Soc. Rev.*, 2006, **35**, 1068–1083.
22. T. H. Epps, III and R. K. O'Reilly, *Chem. Sci.*, 2016, **7**, 1674–1689.
23. J. Schmelz, F. H. Schacher and H. Schmalz, *Soft Matter*, 2013, **9**, 2101–2107.
24. X. Wang, G. Guerin, H. Wang, Y. Wang, I. Manners and M. A. Winnik, *Science*, 2007, **317**, 644–647.
25. J. B. Gilroy, T. Gädt, G. R. Whittell, L. Chabanne, J. M. Mitchels, R. M. Richardson, M. A. Winnik and I. Manners, *Nat. Chem.*, 2010, **2**, 566–570.
26. T. Gädt, N. S. Jeong, G. Cambridge, M. A. Winnik and I. Manners, *Nat. Mater.*, 2009, **8**, 144–150.
27. F. He, T. Gädt, I. Manners and M. A. Winnik, *J. Am. Chem. Soc.*, 2011, **133**, 9095–9103.
28. P. A. Rugar, L. Chabanne, M. A. Winnik and I. Manners, *Science*, 2012, **337**, 559–562.
29. J. Qian, Y. Lu, A. Chia, M. Zhang, P. A. Rugar, N. Gunari, G. C. Walker, G. Cambridge, F. He, G. Guerin, I. Manners and M. A. Winnik, *ACS Nano*, 2013, **7**, 3754–3766.
30. J. R. Finnegan, D. J. Lunn, O. E. C. Gould, Z. M. Hudson, G. R. Whittell, M. A. Winnik and I. Manners, *J. Am. Chem. Soc.*, 2014, **136**, 13835–13844.

31. Z. M. Hudson, D. J. Lunn, M. A. Winnik and I. Manners, *Nat. Commun.*, 2014, **5**, 3372–3379.
32. Z. M. Hudson, C. E. Boott, M. E. Robinson, P. A. Rupar, M. A. Winnik and I. Manners, *Nat. Chem.*, 2014, **6**, 893–898.
33. H. Qiu, Y. Gao, V. A. Du, R. Harniman, M. A. Winnik and I. Manners, *J. Am. Chem. Soc.*, 2015, **137**, 2375–2385.
34. H. Qiu, Z. M. Hudson, M. A. Winnik and I. Manners, *Science*, 2015, **347**, 1329–1332.
35. X. Li, Y. Gao, C. E. Boott, M. A. Winnik and I. Manners, *Nat. Commun.*, 2015, **6**, 8127–8134.
36. X. Li, Y. Gao, C. E. Boott, D. W. Hayward, R. Harniman, G. R. Whittell, R. M. Richardson, M. A. Winnik and I. Manners, *J. Am. Chem. Soc.*, 2016, **138**, 4087–4095.
37. H. Schmalz, J. Schmelz, M. Drechsler, J. Yuan, A. Walther, K. Schweimer and A. M. Mihut, *Macromolecules*, 2008, **41**, 3235–3242.
38. B. Fan, L. Liu, J.-H. Li, X.-X. Ke, J.-T. Xu, B.-Y. Du and Z.-Q. Fan, *Soft Matter*, 2016, **12**, 67–76.
39. L. Sun, A. Pitto-Barry, A. W. Thomas, M. Inam, K. Doncom, A. P. Dove and R. K. O'Reilly, *Polym. Chem.*, 2016, **7**, 2337–2341.
40. L. Sun, A. Pitto-Barry, N. Kirby, T. L. Schiller, A. M. Sanchez, M. A. Dyson, J. Sloan, N. R. Wilson, R. K. O'Reilly and A. P. Dove, *Nat. Commun.*, 2014, **5**, 5746–5754.
41. J. Qian, X. Li, D. J. Lunn, J. Gwyther, Z. M. Hudson, E. Kynaston, P. A. Rupar, M. A. Winnik and I. Manners, *J. Am. Chem. Soc.*, 2014, **136**, 4121–4124.
42. J. Li, X. Li, D. Ni, J. Wang, G. Tu and J. Zhu, *J. Appl. Polym. Sci.*, 2014, **131**, 41186–41196.
43. G. Rizis, T. G. M. van de Ven and A. Eisenberg, *Soft Matter*, 2014, **10**, 2825–2835.
44. J. Wang, W. Zhu, B. Peng and Y. Chen, *Polymer*, 2013, **54**, 6760–6767.
45. J. Schmelz, M. Karg, T. Hellweg and H. Schmalz, *ACS Nano*, 2011, **5**, 9523–9534.
46. S. Rosenfeldt, F. Lüdel, C. Schulreich, T. Hellweg, A. Radulescu, J. Schmelz, H. Schmalz and L. Harnau, *Phys. Chem. Chem. Phys.*, 2012, **14**, 12750–12756.
47. J. Schmelz, A. E. Schedl, C. Steinlein, I. Manners and H. Schmalz, *J. Am. Chem. Soc.*, 2012, **134**, 14217–14225.
48. Y. Mai and A. Eisenberg, *Acc. Chem. Res.*, 2012, **45**, 1657–1666.
49. S. Suárez-Suárez, G. A. Carriedo and A. P. Soto, *Chem. Eur. J.*, 2015, **21**, 14129–14139.
50. B. Nandan and A. Horechyy, *ACS Appl. Mater. Interfaces*, 2015, **7**, 12539–12558.
51. M. Changez, N.-G. Kang, D. W. Kim and J.-S. Lee, *Nanoscale*, 2013, **5**, 11554–11560.
52. K. H. Ku, J. M. Shin, M. P. Kim, C. H. Lee, M. K. Seo, G. R. Yi, S. G. Jang and B. J. Kim, *J. Am. Chem. Soc.*, 2014, **136**, 9982–9989.
53. F. Schacher, E. Betthausen, A. Walther, H. Schmalz, D. V. Pergushov and A. H. E. Müller, *ACS Nano*, 2009, **3**, 2095–2102.
54. R. J. Hickey, Q. Luo and S. J. Park, *ACS Macro Lett.*, 2013, **2**, 805–808.
55. M. P. Kim, K. H. Ku, H. J. Kim, S. G. Jang, G. R. Yi and B. J. Kim, *Chem. Mater.*, 2013, **25**, 4416–4422.

56. A. Walther, J. Yuan, V. Abetz and A. H. E. Müller, *Nano Lett.*, 2009, **9**, 2026–2030.
57. Y. Guo, S. Harirchian-Saei, C. M. S. Izumi and M. G. Moffitt, *ACS Nano*, 2011, **5**, 3309–3318.
58. J. Schöbel, M. Burgard, C. Hils, R. Dersch, M. Dulle, K. Volk, M. Karg, A. Greiner and H. Schmalz, *Angew. Chem. Int. Ed.*, 2017, **56**, 405–408.
59. H. Wang, W. Lin, K. P. Fritz, G. D. Scholes, M. A. Winnik and I. Manners, *J. Am. Chem. Soc.*, 2007, **129**, 12924–12925.
60. H. Wang, X. Wang, M. A. Winnik and I. Manners, *J. Am. Chem. Soc.*, 2008, **130**, 12921–12930.
61. H. Wang, A. J. Patil, K. Liu, S. Petrov, S. Mann, M. A. Winnik and I. Manners, *Adv. Mater.*, 2009, **21**, 1805–1808.
62. F. H. Schacher, T. Rudolph, M. Drechsler and A. H. E. Müller, *Nanoscale*, 2011, **3**, 288–297.
63. S. G. Jang, D. J. Audus, D. Klinger, D. V. Krogstad, B. J. Kim, A. Cameron, S. W. Kim, K. T. Delaney, S. M. Hur, K. L. Killops, G. H. Fredrickson, E. J. Kramer and C. J. Hawker, *J. Am. Chem. Soc.*, 2013, **135**, 6649–6657.
64. L. Jia, G. Zhao, W. Shi, N. Coombs, I. Gourevich, G. C. Walker, G. Guerin, I. Manners and M. A. Winnik, *Nat. Commun.*, 2014, **5**, 3882–3889.
65. J. Xu, H. Zhou, Q. Yu, I. Manners and M. Winnik, *J. Am. Chem. Soc.*, 2018, **140**, 2619–2628.
66. S. H. Jo, H. W. Kim, M. Song, N. J. Je, S. H. Oh, B. Y. Chang, J. Yoon, J. H. Kim, B. Chung and S. Il Yoo, *ACS Appl. Mater. Interfaces*, 2015, **7**, 18778–18785.
67. S. Mei, J. Cao and Y. Lu, *J. Mater. Chem. A*, 2015, **3**, 3382–3389.
68. J. Schöbel, M. Karg, D. Rosenbach, G. Krauss, A. Greiner and H. Schmalz, *Macromolecules*, 2016, **49**, 2761–2771.
69. C. Bojer, J. Schöbel, T. Martin, M. Ertl, H. Schmalz and J. Breu, *Appl. Catal. B Environ.*, 2017, **204**, 561–565.
70. T. Kida, T. Oka, M. Nagano, Y. Ishiwata and X. G. Zheng, *J. Am. Ceram. Soc.*, 2007, **90**, 107–110.
71. J. Piella, N. G. Bastús and V. Puentes, *Chem. Mater.*, 2016, **28**, 1066–1075.
72. G. Moad, J. Chiefari, Y. K. Chong, J. Krstina, R. T. A. Mayadunne, A. Postma, E. Rizzardo and S. H. Thang, *Polym. Int.*, 2000, **49**, 993–1001.
73. A. C. Henry, T. J. Tutt, M. Galloway, Y. Y. Davidson, C. S. McWhorter, S. A. Soper and R. L. McCarley, *Anal. Chem.*, 2000, **72**, 5331–5337.
74. S. Ehlert, S. M. Taheri, D. Pirner, M. Drechsler, H. W. Schmidt and S. Förster, *ACS Nano*, 2014, **8**, 6114–6122.
75. M. R. Jones, K. D. Osberg, R. J. MacFarlane, M. R. Langille and C. A. Mirkin, *Chem. Rev.*, 2011, **111**, 3736–3827.
76. S. W. B. Schonecker, *Makromol. Chem.*, 1996, **338**, 759–762.
77. T. Hendel, M. Wuihschick, F. Kettemann, A. Birnbaum, K. Rademann and J. Polte, *Anal. Chem.*, **86**, 11115–11124.
78. N. R. Jana, L. Gearheart and C. J. Murphy, *Langmuir*, 2001, **17**, 6782–6786.

79. H. Pletsch, L. Peng, F. Mitschang, A. Schaper, M. Hellwig, D. Nette, A. Seubert, A. Greiner and S. Agarwal, *Small*, 2014, **10**, 201–208.
80. G. M. Whitesides, *Nature*, 2006, **442**, 368–373.
81. R. Karnik, F. Gu, P. Basto, C. Cannizaro, L. Dean, W. Kyei-Manu, R. Langer and O. C. Farokhzad, *Nano Lett.*, 2008, **8**, 2906–2912.
82. C. Bojer, J. Schöbel, T. Martin, T. Lunkenbein, D. R. Wagner, A. Greiner, J. Breu and H. Schmalz, *Polymer*, 2017, **128**, 65–70.
83. L. Sun, D. Zhao, Z. Song, C. Shan, Z. Zhang, B. Li and D. Shen, *J. Colloid Interface Sci.*, 2011, **363**, 175–181.

Supporting Information

1. Characterisation of ZnO and CuO NPs

The ZnO and CuO NPs were analysed by powder X-Ray diffraction to confirm the phase purity (Fig. S1A). For both types of NPs, the measured peaks can be clearly assigned to ZnO (PDF: 00-036-1451) and CuO (PDF: 45-0937), respectively. For CuO NPs only the two most intense peaks can be found as reported by Kida *et. al.*¹ The peaks of both NP types show a high full width at half maximum (FWHM), confirming the formation of NPs. Dynamic light scattering (DLS) reveals narrow particle size distributions (Fig. S1B) with average hydrodynamic diameters of 3.2 ± 0.1 nm for ZnO and 5.8 ± 1.4 nm for CuO NPs, respectively. From TEM image analysis (Fig. S1C, D) average diameters of 2.7 ± 0.4 nm for ZnO NPs and 3.8 ± 0.6 nm for CuO NPs were obtained. As expected, the sizes from DLS are slightly higher compared to that determined by TEM, as DLS probes the hydrodynamic diameters.

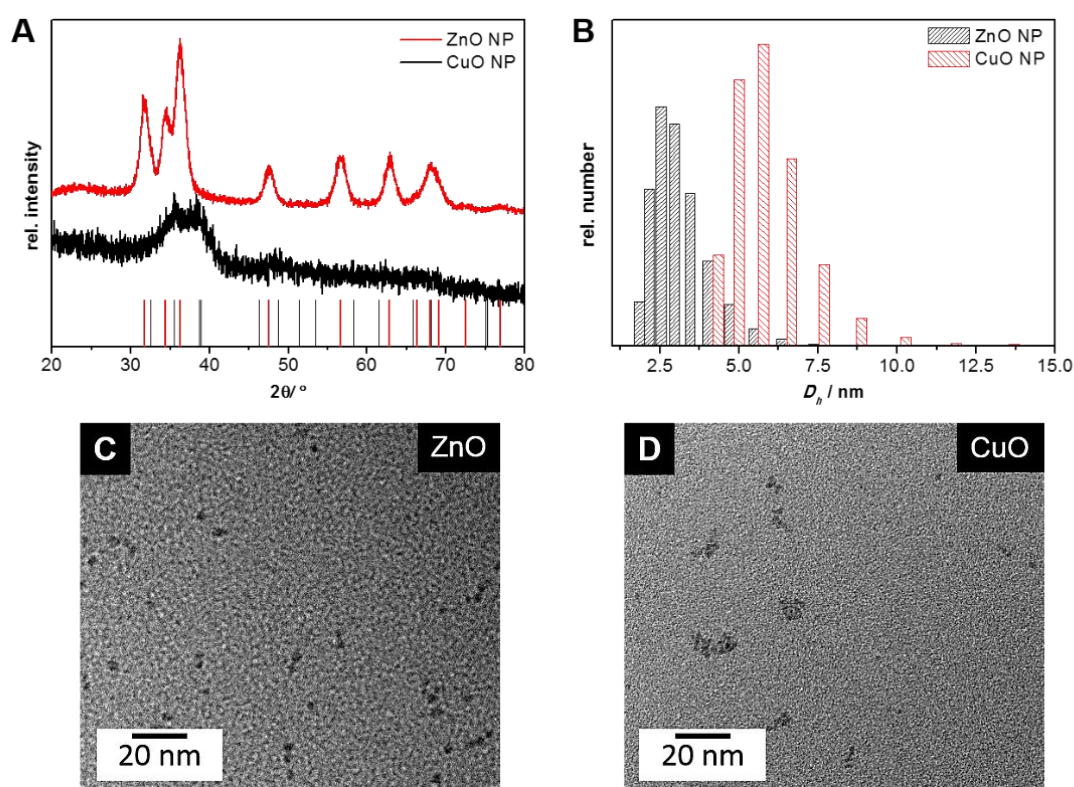


Fig. S1. PXRD pattern (A), particle size distribution obtained from DLS measurements (B) and TEM micrographs of the ZnO and CuO NPs (C, D).

2. Characterisation of citrate-stabilised Au NPs

Au NPs were synthesised according to a seeded-growth protocol by Piella *et al.*² In a first batch, citrate-stabilised seed particles ($D = 4 \pm 0.6$ nm) were produced. In two consecutive steps, these seed particles were grown to $D = 7.9 \pm 0.7$ nm, as revealed by TEM (Fig. S2A, B). These spherical Au NPs showed a characteristic LSPR at $\lambda_{\max} = 515$ nm (Fig. S2C).

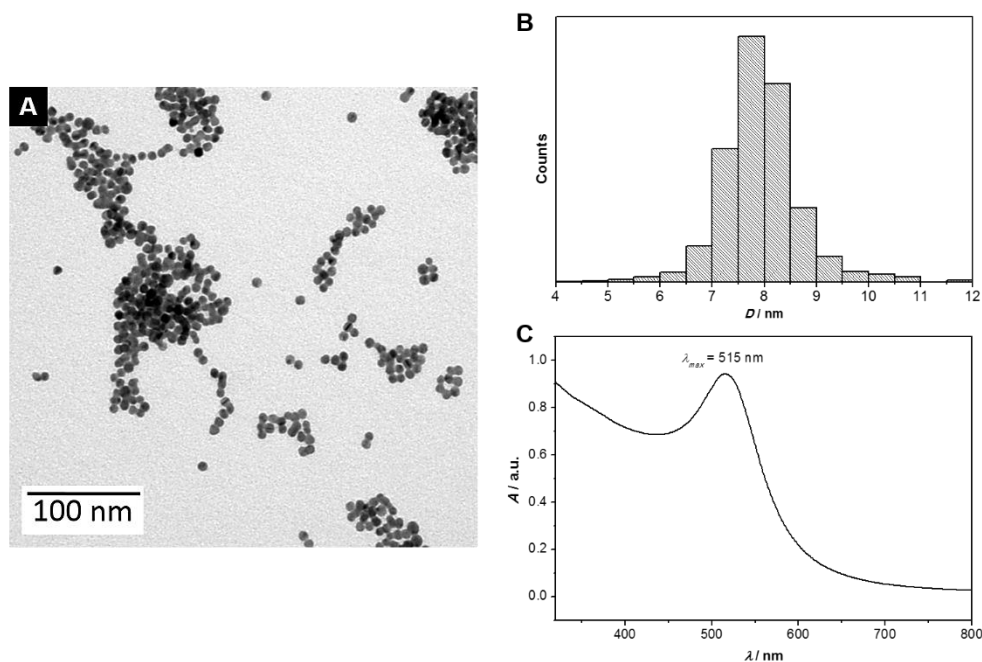


Fig. S2. TEM micrograph (A), size distribution (B) and UV-Vis spectrum ($c = 1.2 \cdot 10^{16}$ NP L⁻¹ in water, (C)) of citrate-stabilised AuNPs.

3. Characterisation of trithiocarbonate-terminated PS

Trithiocarbonate-terminated PS (PS-TTC) was synthesised by reversible addition-fragmentation chain transfer (RAFT) polymerisation according to a protocol of Moad *et al.*³ To this end, styrene and 2-cyano-2-propyl dodecyl trithiocarbonate (8.55 mM L⁻¹) were mixed in a ratio of 169:1. The reaction mixture was degassed for 20 min with nitrogen and subsequently heated to 110 °C for 46 h in an oil bath. The polymerisation was terminated by quenching to 0 °C with an ice bath. The product was dissolved in THF and precipitated from cold methanol.

The molecular weight of the trithiocarbonate-terminated PS was determined by THF GPC to $M_n = 10.4$ kg mol⁻¹ with a dispersity of $\mathcal{D} = 1.05$ (Fig. S3A). The monomodal distribution and the low dispersity prove the controlled polymerisation of styrene. The UV-Vis spectrum shows the typical absorbance of the PS-TTC. The PS shows an absorbance maximum at about $\lambda = 250$ nm, whereas the TTC end group shows a maximum at $\lambda = 315$ nm (Fig. S3B).

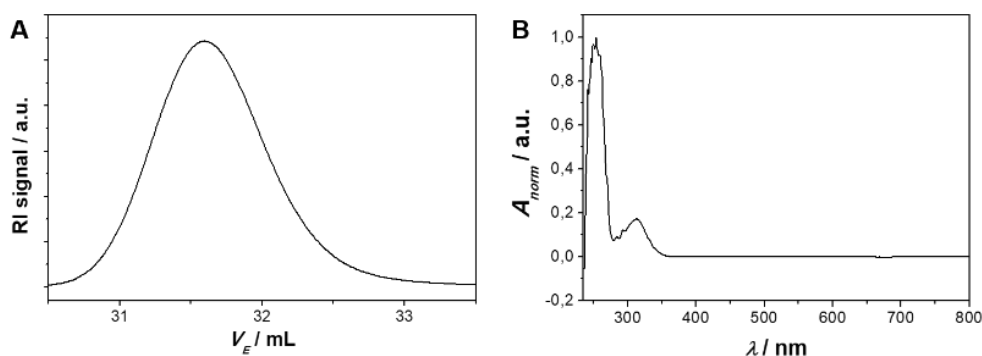


Fig. S3. THF-GPC trace (A) and UV-Vis spectrum of PS-TTC ($c = 0.1$ mg mL⁻¹ in chloroform, (B)).

4. Characterisation of PS-stabilised Au NPs

DMF GPC using a UV-Vis diode-array-detector was performed to show whether the PS ligands are completely bound to the Au NP surface or if free PS ligands are still present (Fig. S4A). Two different wavelengths were selected for detection, being characteristic for the PS ligand ($\lambda = 270$ nm) as well as the Au NPs ($\lambda = 525$ nm). The peak elution volume of the Au NPs is at $V_E = 19$ min (detection at $\lambda = 525$ nm). The corresponding GPC trace for $\lambda = 270$ nm, i.e. specific to PS, shows a bimodal distribution. The main peak at $V_E = 19$ min corresponds to the PS ligands bound to the Au NPs' surface and the minor peak at $V_E = 23$ min to some residual free PS ligands. Dynamic light scattering (DLS) results in an average hydrodynamic radius of $R_h = 14.7 \pm 0.1$ nm, proving the PS shell around the Au NPs (Fig. S4B). The small standard deviation indicates the absence of agglomerates in solution.

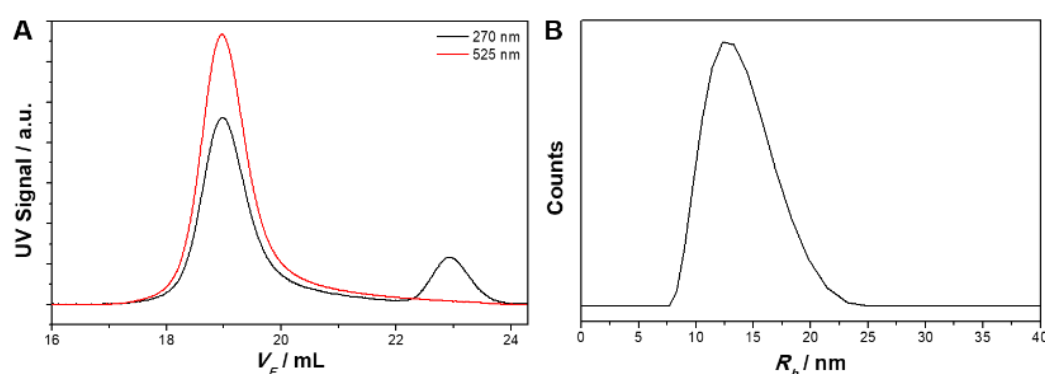


Fig. S4. DMF-GPC traces (A) and particle size distribution obtained by DLS in toluene (B) of PS@Au NPs.

5. Determination of Au NP concentration

The concentration of the PS@Au NPs in the final toluene dispersion was determined using a method reported by Hendel *et al.*⁴ To this end, the absorbance of the PS@Au NP dispersion at 400 nm before normalisation of the spectrum and the corresponding dilution factor f were used to calculate the concentration of elemental Au (equation 1).

$$[Au] = \frac{A_{400} \cdot f \cdot 1.25 \cdot 10^{-4} \text{ mol L}^{-1}}{0.3} \quad (1)$$

The absorbance measured for the PS@Au NP in toluene was $A_{400} = 0.5584$ with a dilution factor of $f = 60$. To calculate the concentration of Au NPs in the dispersion, the radius of the Au NPs from TEM measurements ($R_{TEM} = 4$ nm), the molar mass of Au ($M_{Au} = 196.97$ g mol⁻¹) and the density of Au ($\rho_{Au} = 19.3 \cdot 10^6$ g m⁻³) is needed. Equation 2 is used to calculate the final Au NP concentration.

$$[Au \text{ NP}] = \frac{[Au] \cdot M_{Au}}{\frac{4}{3} \cdot R_{TEM}^3 \cdot \pi \cdot \rho_{Au}} \quad (2)$$

This yields in an Au NP concentration of $[Au \text{ NP}] = 5.3 \cdot 10^{17}$ NP L⁻¹.

6. Characterisation of the amidated PMMA homopolymer

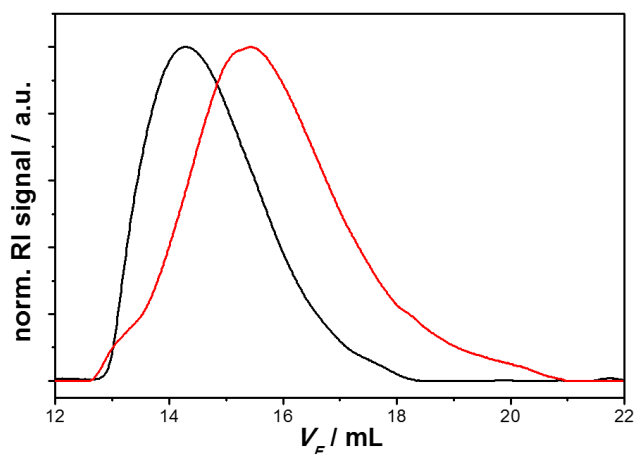


Fig. S5. HFIP GPC traces of PMMA (red) and amidated PMMA (black).

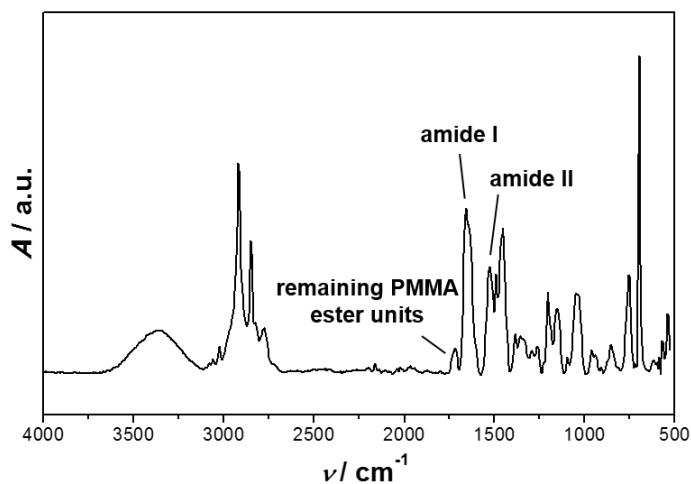
7. Characterisation of the *s*-SEDMA triblock terpolymer

Fig. S6. FT-IR spectrum of SEDMA.

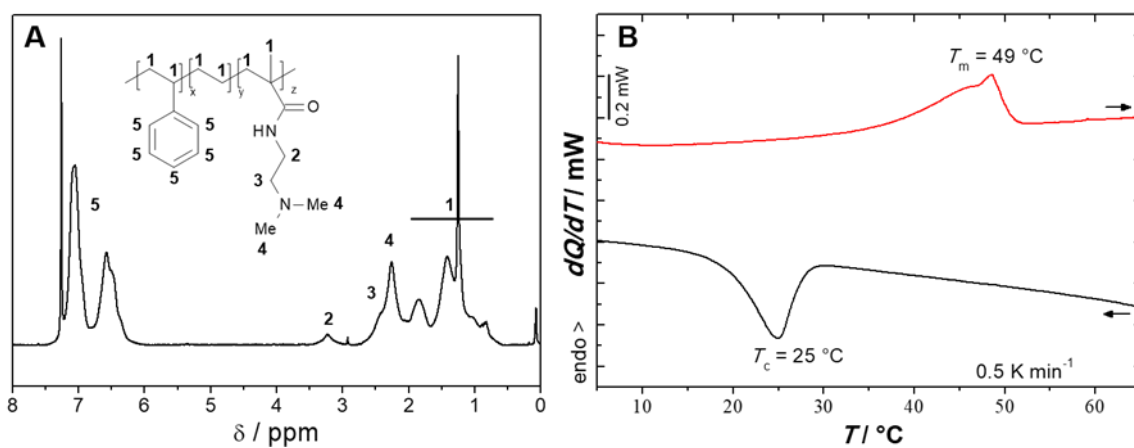
8. Characterisation of *as*-SEDMA

Fig. S7 $^1\text{H-NMR}$ spectrum measured in CDCl_3 (A) and μDSC heating and cooling traces ($c = 10 \text{ g L}^{-1}$ in THF, (B)) of *as*-SEDMA.

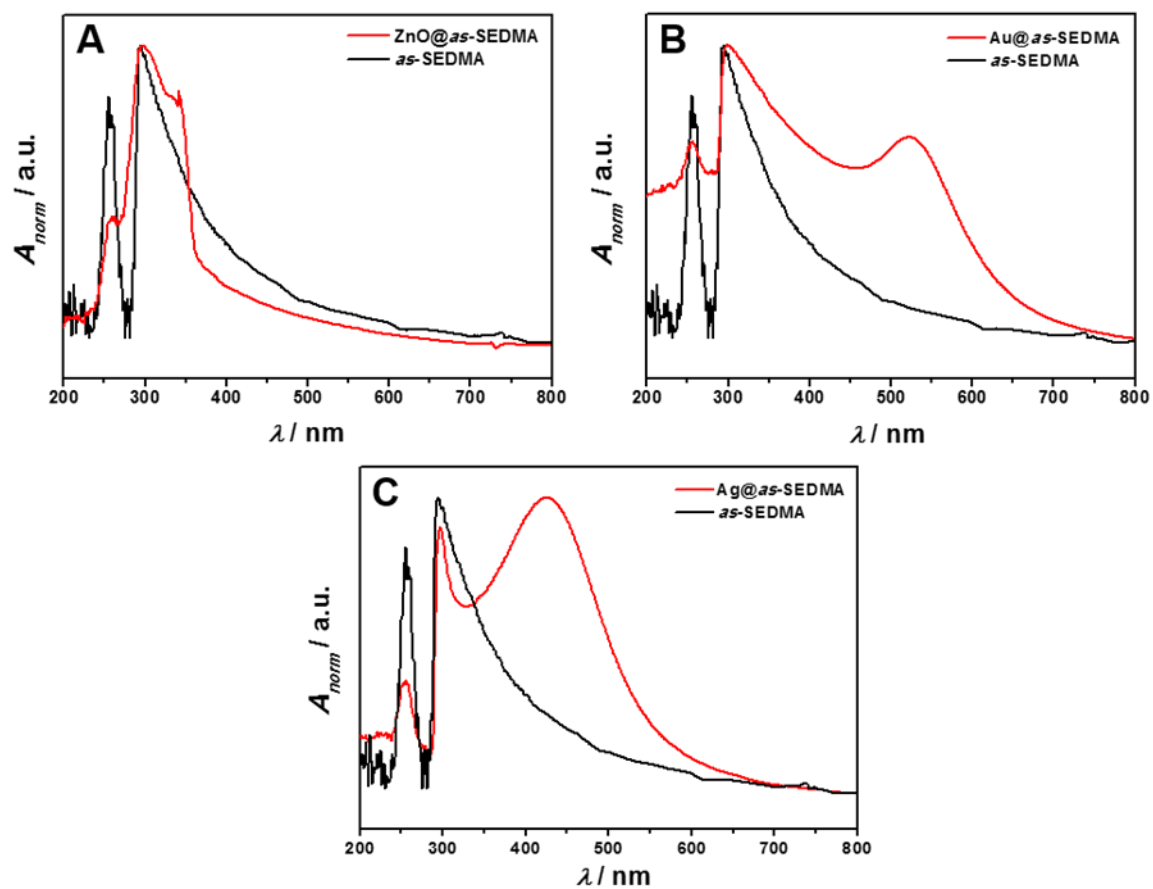
9. Optical properties of the *as*-SEDMA hybrid micelles

Fig. S8 UV-Vis spectra of *as*-SEDMA hybrid micelles with ZnO (A), Au (B) and Ag (C) NPs.

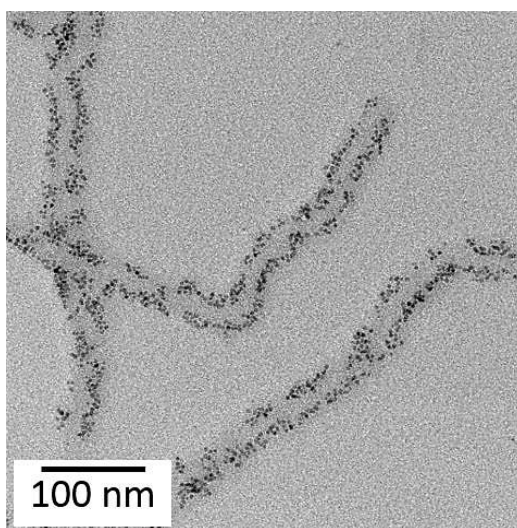
10. ZnO/*as*-SEDMA hybrid wCCMs in acetone

Fig. S9 TEM micrograph of *as*-SEDMA/ZnO NP hybrid wCCMs (dispersion in THF/acetone = 10/90 (v/v)).

11. *In situ* synthesis of Ag NPs in the presence of non-functionalized $S_{48}E_{27}M_{25}^{141}$ wCCMs

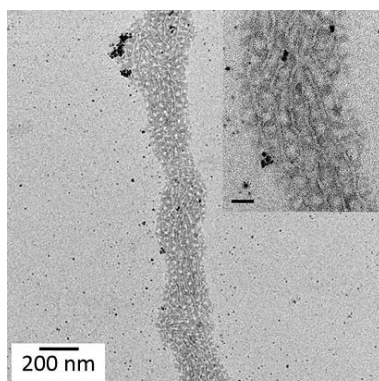


Fig. S10 Blend of Ag NPs and $S_{48}E_{27}M_{25}^{141}$ wCCMs. The absence of functional groups for the incorporation of Ag NPs in the wCCM corona leads to a statistical distribution of free Ag NPs and several agglomerates over the whole copper grid. The scale bar in the inset corresponds to 50 nm.

12. Continuous loading by microfluidics

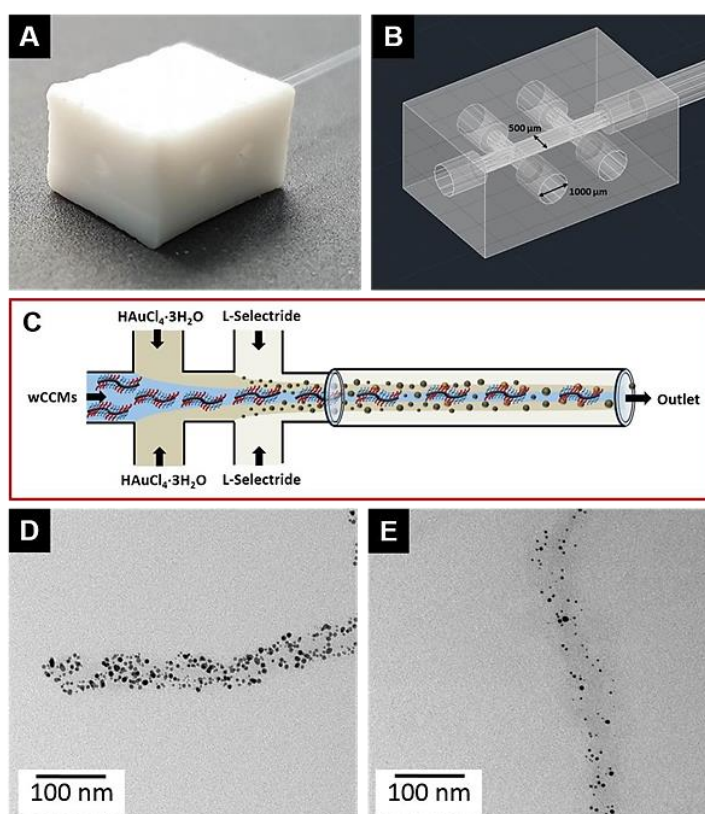


Fig. S11 For optimum mixing of the educts, we fabricated an individually designed microfluidic device based on a home-made PTFE chip (A) with a double-focusing cross that is made of four side channels and finally connected to a glass capillary (inner diameter $D = 980 \mu\text{m}$) *via* the central main channel, as visible in the detailed CAD-design (B). Illustration of the fluid focusing within the tailor-made microfluidic device (C). TEM micrograph (D) of the *s*-SEDMA/Au hybrid micelles prepared at following flow rates: *s*-SEDMA wCCMs: $2000 \mu\text{L h}^{-1}$, $\text{HAuCl}_4 \cdot 3\text{H}_2\text{O}$: $2000 \mu\text{L h}^{-1}$ and L-Selectride: $1000 \mu\text{L h}^{-1}$ ($Q = 8000 \mu\text{L/h}$, $t = 17.0 \text{ s}$).

13. Aggregation behaviour of PS@Au NPs

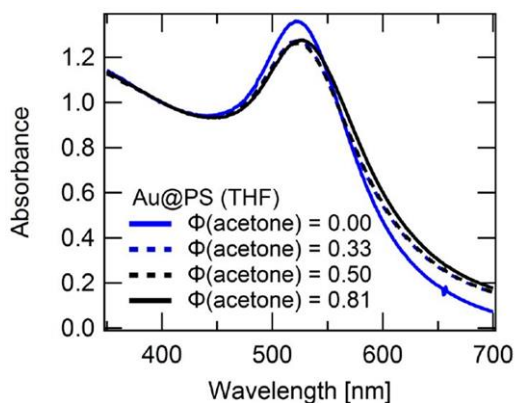


Fig. S12 UV-Vis spectra of PS@Au NPs in different solvent mixtures of THF and acetone.

14. ZnO/*s*-SEDMA hybrid wCCMs in acetone

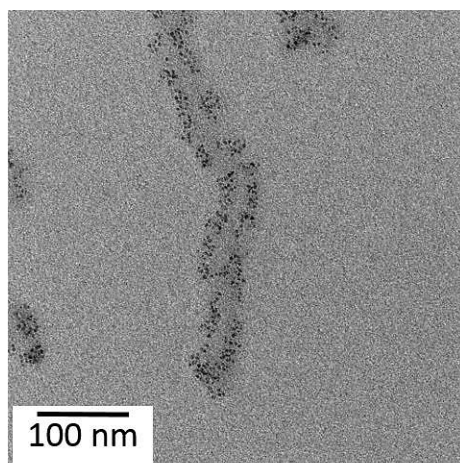


Fig. S13 TEM micrograph of the *s*-SEDMA/ZnO NP hybrid wCCMs (dispersion in THF/acetone 10/90 (v/v)).

15. Binary loading of *s*-SEDMA wCCMs with Ag and PS@AuNPs

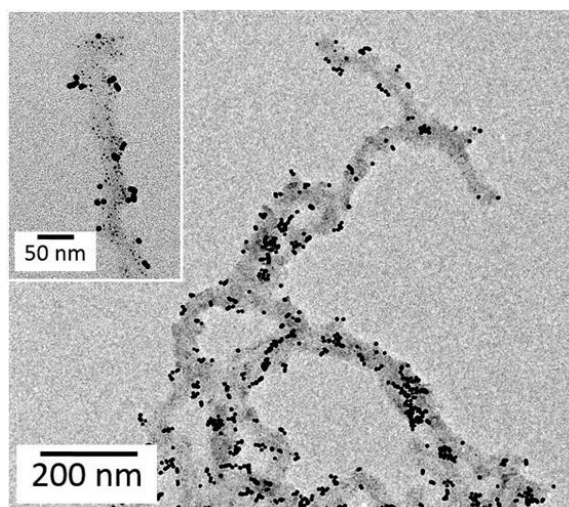


Fig. S14 TEM micrograph of binary loaded *s*-SEDMA wCCMs with Ag and PS@Au NPs.

9. References

1. T. Kida, T. Oka, M. Nagano, Y. Ishiwata and X. G. Zheng, *J. Am. Ceram. Soc.*, 2007, **90**, 107–110.
2. J. Piella, N. G. Bastús and V. Puentes, *Chem. Mater.*, 2016, **28**, 1066–1075.
3. G. Moad, J. Chiefari, Y. K. Chong, J. Krstina, R. T. A. Mayadunne, A. Postma, E. Rizzardo and S. H. Thang, *Polym. Int.*, 2000, **49**, 993–1001.
4. T. Hendel, M. Wuihschick, F. Kettemann, A. Birnbaum, K. Rademann and J. Polte, *Anal. Chem.*, 2014, **86**, 11115–11124.

Acknowledgements/Danksagung

Die letzten Zeilen, die ich im Rahmen dieses Dokumentes schreibe, möchte ich ausschließlich all denjenigen Menschen widmen, die zum Gelingen dieser Arbeit maßgeblich beigetragen haben.

Zuallererst gilt mein besonderer Dank meinem Doktorvater Prof. Dr. Stephan Förster, dass er mir die Möglichkeit gegeben hat auf so einem interessanten sowie anspruchsvollen Thema zu arbeiten und ich dennoch die Freiheiten genießen konnte zu lernen, eigene Ideen zu verfolgen und daran zu wachsen. Ich danke dafür, dass er in schwierigen Phasen mit Rat und Tat zur Seite stand und stets die Probleme des Alltags sowohl mit Expertise als auch mit Menschlichkeit zu lösen vermochte und dabei immer den nötigen Motivationsschub mit auf den Weg gab. Ganz besonders möchte ich ihm aber dafür danken, dass er mir ermöglicht hat drei Monate am Solvay Institut der Université de Bordeaux zu arbeiten und zu lernen. Ich habe vieles aus dieser Zeit mitgenommen, sowohl fachlich als auch persönlich, indem ich interessante Menschen treffen, neue Freunde gewinnen und sogar die Liebe finden durfte, und das schätze ich zutiefst.

Zusätzlich möchte ich mich aber auch bei Frau Jennifer Hennessy und Frau Elisabeth Dünfelder bedanken, für die vielen schönen Gespräche und die Hilfe bei den kleinen Dingen, die einen manchmal so unbeschreiblich schwer erscheinen. An dieser Stelle gilt aber insbesondere mein Dank Herrn Karlheinz Lauterbach, dem Urgestein des Lehrstuhls der „Physikalischen Chemie“ an der Universität Bayreuth. Denn für ihn ist die Universität als auch die Arbeitsgruppe genauso wie für mich zur zweiten Heimat geworden, war Zufluchtsort und gab halt zu gleich. Ohne unseren Kral Heinz wäre der Forschungsalltag wohl nur halb so lustig und schön gewesen, da nichts mehr funktioniert und seine erfrischende Art einfach gefehlt hätte.

Ein herzliches Dankeschön richte ich an Prof. Dr. Georg Papastavrou für das Anfertigen des Zweitgutachtens. Prof. Dr. Matthias Karg danke ich für die Zurverfügungstellung der Kern-Schale-Partikel, Prof. Dr. Josef Brey für die Schichtsilikate und Prof. Dr. Fery für die Benutzung des Konfokal-Laser-Scanning Mikroskops. Prof. Dr. Markus Retsch danke ich im Besonderen für seine zutiefst menschliche Art und die unglaublich erfrischenden Gespräche.

Benedikt Neugirg bin ich zudem sehr dankbar für das konstruktive Korrekturlesen dieser Arbeit.

Zudem möchte ich mich im Speziellen bei Martin Trebbin für die erste freundliche Einführung in die Mikrofluidik und die vielen hilfreichen Diskussionen bedanken. Ein ganz besonderer Dank gilt meinem kongenialen Büro- wie Laborkollegen, aber vor allem Leidensgenossen Eddie Hofmann, mit dem ich den langen sowie interessanten Weg der Promotion mit all seinen Höhen und Tiefen von Anfang bis Ende gegangen sind.

Aber auch möchte ich mich bei allen meinen anderen Kollegen aus der Arbeitsgruppe bedanken, die unseren Lehrstuhl erst zu dem gemacht haben, was er am Ende war, nämlich das blühendste und abwechslungsreichste Leben was man sich vorstellen kann. Stephan Hauschild mit seiner hilfsbereiten und zuvorkommenden Art habe ich als unermüdlichen und einen der nettesten Menschen kennen gelernt. Daniela Pirner, Tobias Güttler, Maria Michaelis, Miriam Mauer, Kirsten Volk, Christian Stelling, Pia Ruckdeschl, Fabian Nutz, Tobias Jurczyk und Kilian Krüger haben das Leben in der Arbeitsgruppe einzigartig gemacht. Maria Ritter, Carolin Fürst und Susanne Seibt danke ich zusätzlich für die schöne gemeinsame Zeit in Melbourne und Sascha Ehlert, Corinna Stegelmeier, Jan Schröder sowie Sarah Mehdizadeh haben mir die schönsten Plätze in ihrer wunderschönen Heimatstadt Hamburg gezeigt. Martin Dulle möchte ich danken für seine ausgeglichene Art, stetige Hilfsbereitschaft und die anschaulichen Erklärungen, Sabine Rosenfeldt für die gute Zeit am ESRF/ILL. Meinen Praktikanten Andreas Karg, Rebecca Suckfüll, Tobias Lauster, Nico Carl und Tobias Bubmann möchte ich für deren Stehvermögen im Angesicht der sehr anspruchsvollen Mikrofluidik Experimente danken.

Ein ganz besonderer Dank gilt jedoch Sebastian With, für seine freundliche Einführung in die Mikrofluidik und AutoCAD, aber vor allem für seine Freundschaft. Denn seine Unterstützung sowie die Abwechslung im und außerhalb des Unialltags gerade in einer meiner schwersten Lebensphasen, werde ich ihm nie vergessen.

Ein spezieller Dank gilt in diesem Zusammenhang natürlich auch meinen Kommilitonen und guten Freunden Daniel Forberg, Benedikt Neugirg, Thomas Wittmann, Toni Hille, Georg Lochner, Christian Schulz und Jonas Schubert für die gute Zeit während der Promotion und die fachübergreifenden Diskussionen an unserem legendären Chemiestammtisch, sowie den unzähligen mitunter waghalsigen Aktivitäten. Mein Dank gilt hier zudem meiner ehemaligen Praktikumskollegin und Promotionsleidensgenossin Inna Dewald mit der ich in diversen Salsa Abenden den Unialltag hinter mir lassen konnte. Einen weiteren Dank möchte ich an dieser Stelle auch allen helfenden Mitgliedern der CSG e.V. und JCF Bayreuth entrichten, mit denen ich gemeinsam viel Arbeit in die Organisation einiger großer Events wie dem Graduiertentag, dem Dr. Donna Nelson Vortrag oder das Sommerfest der Chemie gesteckt und natürlich viel Spaß gehabt hatte. Hier sei selbstverständlich auch die gesamte Chemiker Fußballmannschaft CSB nicht zu vergessen, mit der zusammen ich viele Schlachten, manchmal auch sehr aussichtslose, aber dennoch immer sehr schöne, in der Wilden Liga bestritten hatte. Ebenfalls sei hier Nikolai Zimmermann erwähnt, auf den bei Spielen der CSB und Veranstaltungen der CSG, aber auch beim abendlichen Essen in der Mensa und den vernichtenden Übungen bei MaxxF immer Verlass war.

Ich habe darüber hinaus die wunderbare Möglichkeit gehabt einige Monate am Solvay Institut der Université de Bordeaux zu verbringen und möchte Prof. Dr. J.-B. Salmon sehr herzlich danken, dass er mich so freundlich in der Arbeitsgruppe aufgenommen hat, mir die Möglichkeit gegeben hat mich einem interessanten Forschungsthema zu widmen und sich viel Zeit für Fragen und Diskussionen genommen hat. Ich habe in Frankreich in allen Lebenslagen viel lernen dürfen. In diesem Sinne danke ich daher dem gesamten Arbeitskreis für den herzlichen Umgang und dabei insbesondere meinen Bürokollegen Jérémy Decock, Serhii Mytnyk, Laura Romasanta, Benôit Joffres, Charles Loussert, Tristan Aillet, Alexandre Turani and Swati Kaushik. Über Serhii Mytnyk wurde ich zudem zu einem legendären Abend eingeladen, der mein Leben maßgeblich beeinflussen sollte, denn er nahm mich gleich am ersten Wochenende mit zu Philip Schäfer, bei dem ich weitere interessante Menschen kennen lernen durfte. Hier sei gerade Frank Bokeloh, Pedro Mateus, Kars de Vet, Marco Felipe und Leire Gartzia Rivero genannt, mit denen ich in Bordeaux viele schöne und lustige Abende verbrachte. Wie natürlich gleich am besagtem ersten Abend des Kennenlernens, als wir noch lange durch die Stadt zogen und ich in der letzten berüchtigten Bar meine wunderbare Liebe, Lucinda Langlands-Perry, gefunden habe.

Schlussendlich bin ich einfach sehr dankbar dafür, was mir durch die Promotion ermöglicht wurde, nämlich nicht nur unglaublich interessante Forschung zu betreiben, sondern auch mit dem ersten selbst verdienten Geld Dinge und Momente zu erleben, die so einzigartig sind wie das Leben selbst. Erst dadurch war es für mich möglich an so besondere Orte zu reisen wie 2014 zur Fussball Weltmeisterschaft in Brasilien um dort in Rio de Janeiro wiederum unglaublich offenherzige Menschen zu treffen oder aber auch bis an das andere Ende der Welt nach Australien zu fliegen um dort mit den Chemikern aus Bayreuth Lisa Zappe, Tina Weller, Tobias Klein und Mara Klara den Kontinent zu erkunden. Alles das machte die Zeit der Doktorarbeit zu einer der wohl spannendsten, aufregendsten und kreativsten Abschnitte meines Lebens.

Nun bleibt mir am Ende noch den wichtigsten Menschen in meinen Leben zu danken: meinen Eltern, Großeltern und meiner Schwester, dafür dass sie mir eben dieses Studium ermöglicht haben und immer liebevoll für mich da sind, auch wenn es mal nicht so läuft, dafür dass sie mir halt geben, mich unterstützen und motivieren. Mein tiefster Dank gilt meiner einzigartigen wie außergewöhnlichen Loulou für das Leben mit ihr und die wunderschönen Momente, die wir zusammen beschreiten, für ihre Nähe in der Ferne und die dennoch grenzenlose Liebe, die unendlichen Freuden und den Rückhalt auch in schwierigen Phasen.

„Glück heißt, seine Freude in der Freude des anderen zu finden.“

Georges Bernanos

„Per aspera ad astra.“

Seneca

Declaration/Erklärung

(§ 9 Satz 2 Nr. 3 PromO BayNAT)

Hiermit erkläre ich eidesstattlich, dass ich diese Arbeit selbständig verfasst und keine anderen als die von mir angegebenen Quellen und Hilfsmittel benutzt habe (vgl. Art. 64 Abs 1 Satz 6 BayHSchG).

(§ 9 Satz 2 Nr. 3 PromO BayNAT)

Hiermit erkläre ich, dass ich die Dissertation nicht bereits zur Erlangung eines akademischen Grades eingereicht habe und dass ich nicht bereits diese oder eine gleichartige Doktorprüfung endgültig nicht bestanden habe.

(§ 9 Satz 2 Nr. 4 PromO BayNAT)

Hiermit erkläre ich, dass ich Hilfe von gewerblichen Promotionsberatern bzw. -vermittlern oder ähnlichen Dienstleistern weder bisher in Anspruch genommen habe noch künftig in Anspruch nehmen werde.

(§ 9 Satz 2 Nr. 7 PromO BayNAT)

Hiermit erkläre ich mein Einverständnis, dass die elektronische Fassung meiner Dissertation unter Wahrung meiner Urheberrechte und des Datenschutzes einer gesonderten Überprüfung unterzogen werden kann.

(§ 9 Satz 2 Nr. 8 PromO BayNAT)

Hiermit erkläre ich mein Einverständnis, dass bei Verdacht wissenschaftlichen Fehlverhaltens Ermittlungen durch universitätsinterne Organe der wissenschaftlichen Selbstkontrolle stattfinden können.

.....
Ort, Datum, Unterschrift